Universiteit
Leiden
The Netherlands

Distant star formation in the faint radio sky

Algera, H.S.B.

Citation
Algera, H. S. B. (2021, October 27). *Distant star formation in the faint radio sky*. Retrieved from https://hdl.handle.net/1887/3221280

Version:	Publisher's Version
License:	Licence agreement concerning inclusion of doctoral thesis in the Institutional Repository of the University of Leiden
Downloaded from:	https://hdl.handle.net/1887/3221280

Note: To cite this publication please use the final published version (if applicable).

Distant Star Formation in the Faint Radio Sky

Proefschrift

ter verkrijging van
de graad van doctor aan de Universiteit Leiden,
op gezag van rector magnificus prof. dr. ir. H. Bijl,
volgens besluit van het college voor promoties
te verdedigen op woensdag 27 oktober 2021
klokke 11:15 uur

door

Hiddo Sunny Bouwe Algera

geboren te Sneek, Nederland
in 1995

Promotor:	Prof. dr. Huub Röttgering	
Co-promotor:	Dr. Jacqueline Hodge	
Promotiecommissie:	Prof. dr. Serena Viti	
	Prof. dr. Paul van der Werf	
	Prof. dr. Ian Smail	Durham University
	Prof. dr. Vernesa Smolčić	University of Zagreb
	Dr. Rychard Bouwens	
	Dr. Dominik Riechers	Cornell University

Cover by Zehui Xu (徐泽慧)

ISBN: 978 94 6419 329 9

Printed by: Gildeprint

Mar as de sinne no in stjer is
Like lyts as alle oaren
Dan freegje ik my ôf
Wa is de skepper fan de skepper
– Skepper fan de Skepper, Reboelje (1989)

Contents

1 Introduction **1**
1.1 The Beginning . . . 1
1.2 The Evolution of Galaxies . . . 2
1.2.1 Star Formation in Galaxies . . . 5
1.2.2 Star Formation Rates . . . 8
1.2.3 Dusty Star-forming Galaxies . . . 10
1.2.4 The Star-forming Population . . . 11
1.3 Radio Emission in Galaxies . . . 13
1.3.1 Synchrotron Emission . . . 14
1.3.2 The Far-infrared/radio Correlation . . . 15
1.3.3 Free-free Emission . . . 20
1.3.4 The Radio Spectrum . . . 21
1.4 The Spectral Energy Distribution of Galaxies . . . 23
1.4.1 An Inventory of Star formation Rate Tracers . . . 23
1.4.2 The Cosmic Star Formation Rate Density . . . 28
1.5 Active Galaxy Nuclei . . . 29
1.6 The Radio Revolution . . . 31
1.6.1 The Faint Radio Sky . . . 32
1.6.2 The Faint Radio Population . . . 35
1.7 This Thesis . . . 37
1.8 The Future . . . 39

2 The Nature of the Ultra-faint Radio Population **41**
2.1 Introduction . . . 42
2.2 Data . . . 46
2.2.1 Radio Data . . . 46
2.2.2 Near-UV to far-IR data . . . 49

2.2.3 Spectroscopic Redshifts . . . 51
2.2.4 X-ray data . . . 52
2.3 Multi-Wavelength Cross-Matching . . . 52
2.3.1 Radio Cross-Matching . . . 54
2.3.2 Additional Cross-Matching . . . 54
2.3.3 Redshifts of the Radio Sample . . . 56
2.4 AGN Identification . . . 60
2.4.1 HLAGN . . . 63
2.4.2 MLAGN . . . 67
2.4.3 AGN Identification Summary . . . 73
2.5 Composition of the Ultra-Faint Radio Population . . . 74
2.5.1 The Ultra-faint Radio Population . . . 74
2.5.2 Euclidean-normalized Number Counts . . . 76
2.5.3 Optically dark Sources . . . 83
2.5.4 Implications for Next-Generation Radio Surveys . . . 89
2.6 Summary & Future . . . 91
2.A AGN Diagnostics from SED Fitting . . . 93
2.B Comparison to 3 GHz VLA-COSMOS . . . 94
2.B.1 Radio-excess AGN . . . 95
2.B.2 SED-fitted AGN . . . 96
2.B.3 Red, quiescent AGN . . . 97
2.C Incompleteness in the Multi-wavelength Photometry . . . 98
2.C.1 X-ray AGN . . . 98
2.C.2 MIR AGN . . . 98
2.C.3 Radio-excess AGN . . . 99
2.C.4 Summary . . . 100
2.D Final Counterpart Catalog . . . 101

3 The Far-infrared/Radio Correlation for Dusty Star-forming Galaxies 105
3.1 Introduction . . . 106
3.2 Observations & Methods . . . 108
3.2.1 Submillimeter Observations . . . 108
3.2.2 Radio Observations . . . 109
3.2.3 Additional Multi-wavelength Data . . . 110
3.2.4 SMG Redshifts and Physical Properties . . . 111
3.2.5 Radio Stacking . . . 113
3.3 Results . . . 114
3.3.1 Radio Properties of AS2UDS . . . 114

3.3.2 AGN in AS2UDS . . . 119
3.3.3 (A lack of) Redshift Evolution in the FIRRC . . . 121
3.3.4 Correlations with Physical Properties . . . 125
3.4 Discussion . . . 127
3.4.1 Previous Studies of the FIRRC . . . 127
3.4.2 The FIRRC for SMGs . . . 130
3.5 Conclusions . . . 143
3.A Stacking . . . 144
3.B Radio AGN in submm and radio-selected Samples . . . 147
3.C The FIRRC in Radio-selected Samples . . . 149

4 Free-free Emission in High-redshift Star-forming Galaxies 153
4.1 Introduction . . . 154
4.2 Observations & Data Reduction . . . 156
4.2.1 COLD*z* . . . 156
4.2.2 Ancillary Radio Observations . . . 158
4.2.3 Ultra-violet to Submillimeter Observations . . . 161
4.2.4 X-ray Observations . . . 162
4.3 Continuum Sources . . . 163
4.4 Multi-Wavelength Properties . . . 168
4.4.1 Multi-wavelength Counterparts and Redshifts . . . 168
4.4.2 Spectral Energy Distributions . . . 171
4.4.3 X-ray and Mid-infrared AGN Signatures . . . 171
4.5 34 GHz Source Counts . . . 172
4.6 34 GHz Continuum Source Properties . . . 177
4.6.1 Radio AGN . . . 177
4.6.2 Radio Spectral Decomposition for Star-forming Galaxies . . . 179
4.6.3 Line and Dust Continuum Subtraction . . . 182
4.6.4 The Radio Spectra of High-redshift Star-forming Galaxies . . . 183
4.6.5 Free-Free Star-Formation Rates . . . 190
4.7 Free-free Emission with the SKA and ngVLA . . . 193
4.8 Conclusions . . . 195
4.A Image Properties . . . 197
4.A.1 Completeness . . . 197
4.A.2 Peak versus Integrated Fluxes . . . 198
4.A.3 Flux Boosting . . . 199

4.B Spectral Energy Distributions 201

5 Probing Cosmic Star Formation With Radio Free-free Emission 205
5.1 Introduction 206
5.2 Data 209
5.2.1 Radio Data 209
5.2.2 Optical/FIR Data 211
5.3 Methods 212
5.3.1 Radio Stacking 212
5.3.2 Radio Spectral Decomposition 215
5.4 Results 216
5.4.1 The Typical Radio Spectrum of Radio-selected Galaxies216
5.4.2 Free-free Emission in Optically-selected Galaxies . . 218
5.5 Discussion 223
5.5.1 Radio Star-formation Rates 223
5.5.2 A Lack of High-frequency Emission 225
5.5.3 The Cosmic Star-formation History 234
5.6 Conclusions 238
5.A Stacking 240
5.B The COSMOS $z = 5.3$ Protocluster 244

Bibliography 246

Summary 258

Samenvatting 265

Publications 272

Curriculum Vitae 275

Acknowledgements 277

1 Introduction

Nothing became something
Turned itself inside out
Subatomic particles became atoms, became stars, became galaxies
– Jens Lekman on How We Met, The Long Version (2017)

1.1 The Beginning

At the time of writing, we live on planet Earth, the third planet around a relatively typical star we call the Sun. The Sun, like a few hundred billion other stars, resides in what we call a galaxy. In fact, this particular galaxy is so important to us that it is sometimes referred to as *the* Galaxy, although more typically it is known as the Milky Way. It may come as a surprise that until just about a century ago, it was still not known whether the Milky Way was the only galaxy in the Universe. It took new observations from American astronomer Edwin Hubble to conclusively show that the so-called "spiral nebulae" that had been observed over the years were, in fact, galaxies themselves, existing far beyond the outskirts of the Milky Way (Hubble 1926).

Much has happened since within astronomy. In the late 1920s, astronomers Georges Lemaître and Hubble[1] independently observed that distant galaxies all appear to move away from us, at a speed directly proportional to their distance (Lemaître 1927; Hubble 1929). From this observation, it follows that the Universe must be expanding, and in turn must have been smaller in the past. Indeed, the Universe can be traced back in time to a single point – known as the *Big Bang* – which has been reliably calculated to have occurred some 13.8 billion years ago (Planck Collaboration et al. 2020). Our current physical models are unable to fully explain nor

[1]Yes, the same Edwin Hubble – it turns out that breakthrough findings like these are a surefire way to get a space telescope named after you.

describe this beginning of the Universe, but begin to apply within the first second following the Big Bang. The particles that we know, and also the particles that we don't know, were formed.

At this point in time, the Universe was a hot soup consisting of ionized hydrogen and helium, and copious free electrons – the basic building blocks of all the visible matter around us. We have no direct observations of this early epoch, as the Universe remained far too dense for light to travel freely. Instead, all the light within the Universe would be constantly scattered around by the free electrons. As the Universe expanded, however, it gradually cooled down while its density dropped. The free electrons and ions were finally able to combine into neutral particles, and light could now freely traverse the Universe. Some of this light was able to make its way to Earth unimpeded, and is directly observable with our telescopes.

This *primordial* light provides the very first picture of the infant Universe, and is shown in Figure 1.1. It portrays what is known as the *Cosmic Microwave Background* (CMB), which is the low-energy radiation that permeates the entire Cosmos. Because the Universe has expanded substantially since the emission of the CMB, the wavelength of its photons has expanded with it. In turn, the CMB is much less energetic now than it was in the past, and radiates at a temperature of less than three degrees above absolute zero (Bennett et al. 2003). The CMB is therefore not visible with the human eye, but can instead be observed using dedicated radio telescopes.

One crucial observation about the CMB is that it is not perfectly smooth. Mind you, it is still really smooth, with any variations being on the order of just 0.01%, but it is not *perfectly* smooth. This has monumental consequences. Some regions are ever so slightly denser, and have ever so slightly more gravity than others. Over the course of a few hundred million years (e.g., Bromm & Yoshida 2011), more and more material will therefore slowly be pulled into these regions due to gravity. Here, the first galaxies form.

1.2 The Evolution of Galaxies

A *galaxy* is the collection of many millions or billions of stars amidst a tenuous reservoir of cosmic gas, dust and a mysterious substance known as dark matter, all of which is holding itself together via gravity. While a satisfactory definition in an astronomical sense, it is somewhat abstract. As a picture is known to speak a thousand words, some examples of galaxies

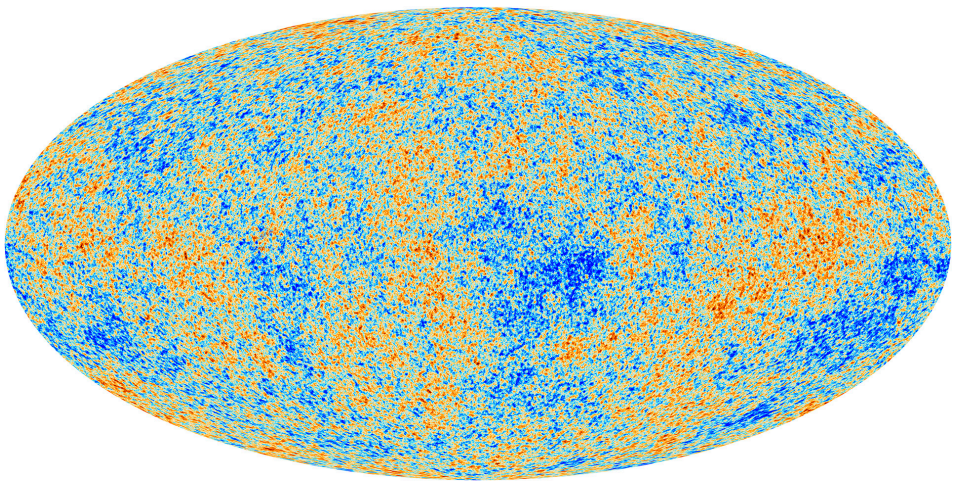

Figure 1.1: The cosmic microwave background, as observed by the *Planck* satellite. The CMB represents relic radiation from the Big Bang, and constitutes the earliest observable light from the Universe. The CMB is highly uniform, and the colour scale has been enhanced to show small deviations from this uniformity. Slightly overdense regions in the CMB give rise to future sites of galaxy formation. Credit: ESA and the Planck Collaboration.

are shown in Figure 1.2. Galaxies, clearly, come in a wide variety of shapes and sizes. Some galaxies, our Milky Way included, are flat spiral disks that appear blue when observed in visible light. Others appear as large, elliptical collections of stars with a relatively red colour. Even others are enshrouded in large amounts of dust, and are very difficult to detect at the wavelengths visible to the human eye. One of the main objectives in astronomy is to explain the large variety of galaxies that we observe, and to understand how galaxies may evolve from one type into another.

Understanding the evolution of galaxies, however, is complicated by one simple fact: a galaxy evolves very, very slowly. Individual stars that make up a galaxy, for example, have lifetimes from a few million years to many tens of billions of years – the latter being much longer than the current age of the Universe. In addition, our Sun is currently traveling through the Milky Way at a velocity of roughly 220 kilometers per second (Gunn et al. 1979). At this rate, it takes roughly 220 million years for the Sun to complete a single orbit through the Galaxy. All these timescales, from the evolution of individual stars to the motions of stars within galaxies, are much larger than a human lifespan. As a result, we cannot simply observe a galaxy for a few years, or even for a few decades or centuries, and infer how it evolves. Instead, we need to observe many galaxies at different

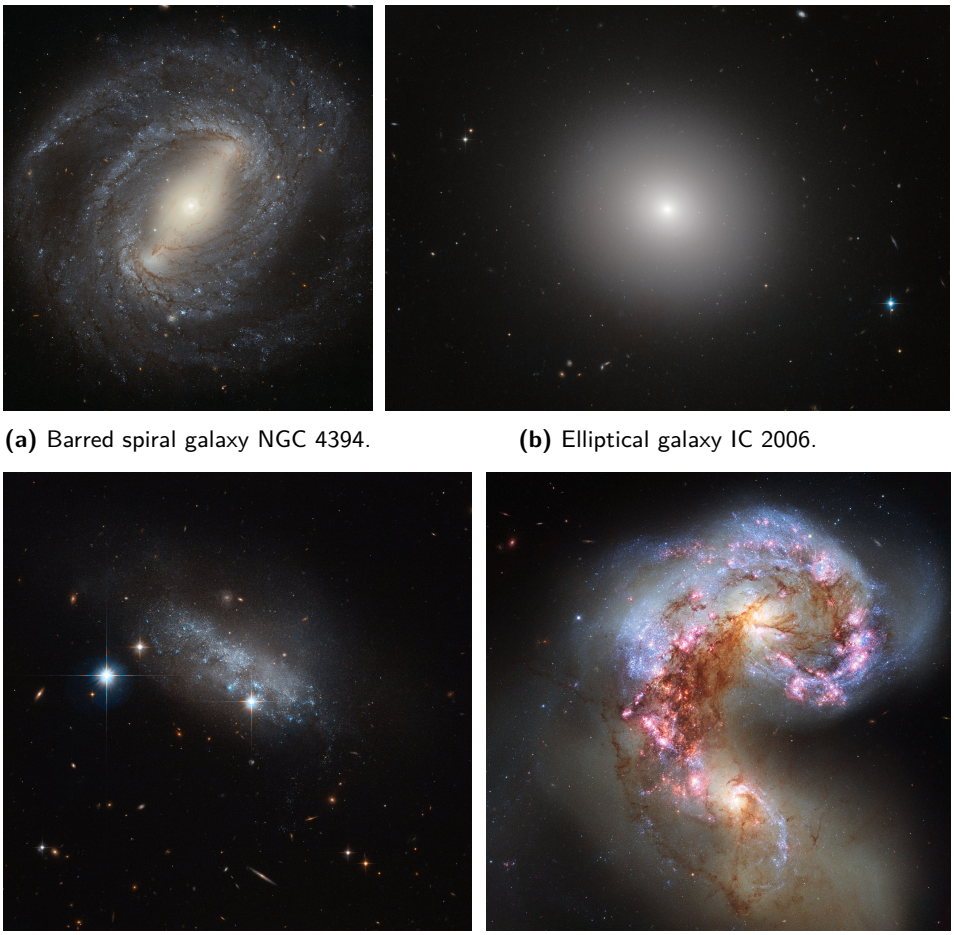

(a) Barred spiral galaxy NGC 4394.

(b) Elliptical galaxy IC 2006.

(c) Irregular galaxy IC 3583.

(d) The two colliding Antennae Galaxies.

Figure 1.2: Several examples of nearby galaxies, highlighting the diversity of the galaxy population. Our galaxy, the Milky Way, is a spiral galaxy likely not too dissimilar from the barred spiral shown in panel **a)**. Spiral galaxies such as the example shown here generally form stars within their spiral arms, which emit blue light. Elliptical galaxies, such as the example in panel **b)**, on the other hand, typically show very little star formation, and appear redder. Panel **c)** shows an irregular galaxy, with no clear discernible structure, while panel **d)** shows the chaotic collision of what previously were two normal spiral galaxies. Collisions such as these are often paired with a surge in star formation within the merging galaxy, as evidenced by the abundant blue star-forming regions within the Antennae (Credit: ESA/Hubble & NASA).

stages in their lives – young ones or old ones – and compare the way they look. All these individual galaxies form the puzzle pieces that have to be combined into a full theory of galaxy evolution.

Owing to the finite speed of light, finding the youngest galaxies in the Universe is equivalent to finding the most distant ones. Measuring accurate distances is crucial in astronomy, as our telescopes namely only provide information on the *apparent* brightness of the observed galaxy population. Only when distances are known, can their *intrinsic* brightness be inferred. In the field of galaxy evolution, distances are customarily expressed via the parameter *redshift*, notated as the letter z. As the Universe is constantly expanding, so is the wavelength of light emitted by distant galaxies. Since longer wavelengths appear redder to the human eye, a galaxy at a higher redshift is more distant. In particular, redshift is directly related to the size of the Universe: at a redshift $z = 1$, the Universe was half its current size, and the wavelength of light has in turn since expanded by a factor of two. At a redshift of $z = 2$, the Universe was a third its current size, while wavelengths emitted at this time are now observed to be three times larger, and so forth. We will later see that galaxies emit light across the full *electromagnetic spectrum*, including X-rays, ultraviolet and infrared light, and radio waves. As the light from more distant galaxies becomes increasingly redshifted, observations in, for example, the infrared part of the spectrum may in fact probe the visible light emitted by distant galaxies, or even their ultraviolet light in even more distant ones.

Since the size of the Universe increases with time as it expands, redshift is also often used to express the age of the Universe. At the present time, we define the redshift to be $z = 0$, while the Universe is roughly 13.8 billion years old. On this scale, the Big Bang, marking the beginning of the Universe, occurred at a redshift of infinity. The CMB was emitted around $z \approx 1100$ (Bennett et al. 2003), and the first stars and galaxies already formed a few hundred million years after the Big Bang, around a redshift of $z \sim 15 - 20$ (e.g., Bromm & Loeb 2004; Hashimoto et al. 2018). The formation of stars and the subsequent build-up of galaxies form the topic of the next Section.

1.2.1 Star Formation in Galaxies

When observed from a dark location on Earth, the Milky Way appears as a large, white band of stars stretched across the night sky. Stars are, indeed, the most readily visible constituents of galaxies, and understanding how

galaxies evolve therefore requires some understanding of the evolution of the individual stars that comprise them.

Stars form when clouds of dense molecular gas collapse under their own gravity. This process, like many in astronomy, takes a long time – on the order of a few million years (Krumholz & Tan 2007) – and as a result it is not possible to watch star formation happen in real time. In addition, stars generally do not form alone. Instead, massive nebulae of gas, such as the famous and well-studied Orion nebula, are large stellar nurseries forming a multitude of stars over the course of a few tens of millions of years (e.g., Murray 2011). Such a collection of recently formed stars is known as a *simple stellar population*, or SSP for short. The "simple" in this name stems from the fact that the stars are assumed to be born at roughly the same time, and also from the same gas, meaning they have the same initial composition (e.g., Bruzual 2010).

The notion of an SSP is very useful in extragalactic astronomy, because in distant galaxies we cannot observe single stars even with powerful telescopes. Instead, what is typically observed is the combined light of all the stars within many individual SSPs. It is therefore illuminating to first examine an SSP in its purest form – without any intervening dust or other complexities – in some detail. The light emitted by an SSP is most readily characterized through its *spectral energy distribution*, which is a measure of the total energy emitted as a function of wavelength. An example spectral energy distribution of an SSP at various ages is shown in Figure 1.3. The youngest SSP shown has an age of 10 million years, while the oldest one has an age of 10 billion years. The difference between these SSPs is stark, in particular at short wavelengths (indicated by the Greek letter λ). At a wavelength of 0.1 μm, which lies in the ultraviolet part of the spectrum, the young SSP is nearly a million times brighter than its aged counterpart. However, at longer wavelengths, beyond roughly one micron, the difference is reduced to less than a factor of one hundred.

This difference in energy emitted between young and old SSPs is directly related to the types of stars that comprise these populations, as the lifetime of any star is strongly dependent on its mass. Massive stars use up their available fuel much more quickly than their low-mass counterparts, and as such live much shorter lives. For example, a star of 30 solar masses has a typical lifetime of only 10 million years. However, a star such as the Sun, which by definition consists of one solar mass, lives roughly 10 billion years, or one thousand times as long. This means that, if one observes a young SSP, the most massive stars are still alive. However, older SSPs will

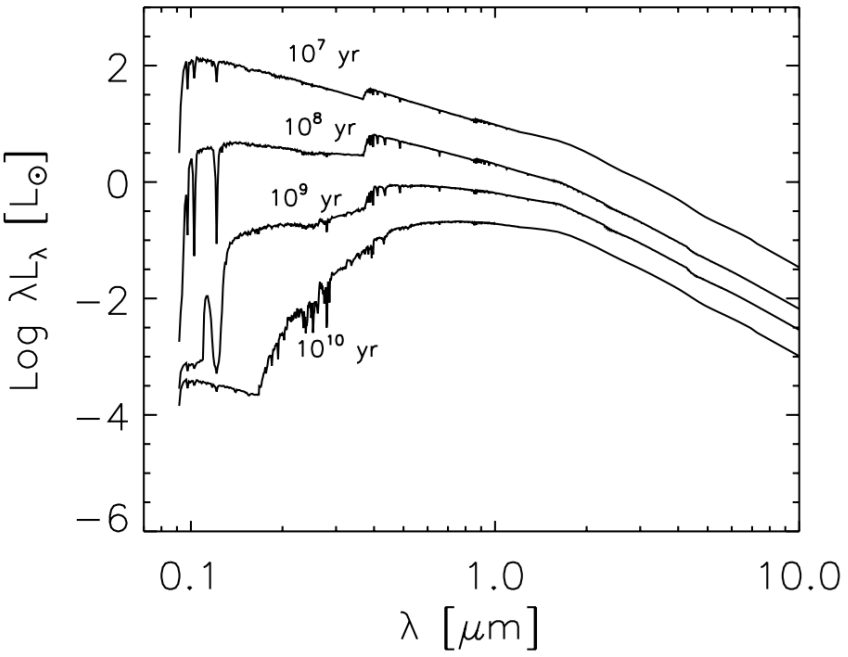

Figure 1.3: Spectral energy distributions of four simple stellar populations of various ages. The vertical axis shows the energy output in solar luminosities, as a function of wavelength in micron. Younger SSPs emit significantly more ultraviolet radiation than their aged counterparts. Figure taken from Takagi et al. (2003).

only have low-mass stars left – the massive ones will have ended their lives in powerful *supernova* explosions.

Because massive stars burn through their fuel very quickly, they are also significantly hotter than low-mass stars such as the Sun. Therefore, massive stars emit light at more energetic wavelengths, such as in the ultraviolet part of the spectrum, whereas low-mass stars are mostly limited to the less energetic optical and infrared wavelength regimes.[2] Young SSPs will therefore emit copious amounts of energetic ultraviolet radiation, whereas older ones will emit much smaller amounts. This fact can be inverted: if one measures a lot of ultraviolet radiation coming from a galaxy, this

[2]The wavelength where a star emits most of its energy is inversely proportional to the temperature of a star – a fact known as Wien's displacement law. However, all stars emit radiation across a broad wavelength range. This is part of the reason why, even for a not particularly massive star like the Sun, wearing sunscreen is recommended.

must mean that it harbors a young stellar population.[3] In fact, the precise amount of ultraviolet radiation holds valuable clues on how many young, luminous stars exist. In turn, ultraviolet observations can measure a galaxy's recent *star formation rate*.

1.2.2 Star Formation Rates

The star formation rate (SFR) of a galaxy is a fundamental quantity describing its evolution. Expressed in $M_\odot\,\mathrm{yr}^{-1}$, the SFR describes how quickly a galaxy is forming stars over time. The Milky Way, for example, has an SFR of roughly $1 - 2\,M_\odot\,\mathrm{yr}^{-1}$ (Licquia & Newman 2015). This number should not be directly interpreted as one or two Sun-like stars forming in the Milky Way each year. As previously mentioned, the formation of a single star is a lengthy process, and instead the SFR is a measure of the *average* yearly mass formed in stars within some recent history. We will see later on that this "recent history" can be anywhere from a few million years to more than a hundred million years for the various different ways astronomers use to measure star formation rates.

One important topic that we have until now neglected is the actual *composition* of a simple stellar population. If we can only measure the combined light of an SSP in distant galaxies, can we actually say something about how many stars have formed, and how massive these stars are? In the distant Universe, the answer is actually most generally "no". Instead, astronomers use observations of nearby SSPs, where it is still possible to observe and count individual stars, and adopt these results for galaxies in the early Universe. The number of stars that form at a given stellar mass is a distribution known as the *initial mass function*, or IMF (e.g., Salpeter 1955). A variety of determinations for the IMF exist in the astronomical literature, though they all share a common feat: low-mass stars are abundant, while massive stars are rare. This fact has an interesting consequence. Simple stellar populations are most readily identified by the high-mass stars they produce, as these are short lived and produce strong ultraviolet radiation, while most of the actual stellar mass that has formed is hidden in low-mass stars.

Given an IMF, and a model for the light produced by an SSP, the total observed light at ultraviolet wavelengths L_{UV} can directly be used to in-

[3] The critical reader will note that this (incorrectly) assumes no other mechanisms are able to generate significant ultraviolet radiation in galaxies. We discuss this in Section 1.5.

fer a galaxy's star formation rate ($\mathrm{SFR_{UV}}$). We will not concern ourselves here with the explicit conversion factor between these quantities, but simply state they are linearly related (e.g., Kennicutt 1998):

$$\mathrm{SFR_{UV}} \propto L_{\mathrm{UV}} \,. \tag{1.1}$$

Some of the most powerful telescopes, such as the *Hubble Space Telescope*, are able to observe at ultraviolet wavelengths, and have been used to observe UV radiation from galaxies within the first billion years of the Universe (e.g., Bouwens et al. 2016).

One important caveat, however, affects the accuracy with which ultraviolet radiation can be used as a tracer of star formation in galaxies. A galaxy, namely, is more than just a collection of simple stellar populations. In addition to stars, galaxies contain potentially large amounts of gas and dust within them, and any radiation emanating from an SSP may encounter these contents along its way to our telescopes.[4] Dust, in particular, has a significant impact on ultraviolet and optical light. Upon absorbing energetic radiation from stars, dust will be heated and subsequently radiate its energy at longer wavelengths, generally in the infrared and (sub)millimeter parts of the spectrum.

Dust itself is, in fact, a byproduct of star formation. It is predominantly produced by supernovae and a particular late evolutionary stage of low to intermediate mass stars known as the *AGB phase* (Michałowski 2015). Since the most massive stars will explode as supernovae in only a few million years, dust buildup in galaxies can happen quite rapidly, and dust has been shown to exist in some of the earliest galaxies that have formed within a billion years after the Big Bang (Bouwens et al. 2021; Schouws et al. 2021).

Since dust is capable of attenuating ultraviolet light, star formation rates inferred from ultraviolet emission may be strongly underestimated in dusty galaxies. In this case, we refer to the missing star-formation as being *dust obscured*. Various studies (e.g., Whitaker et al. 2017) have indicated that most galaxies with star formation rates in excess of $\mathrm{SFR} \gtrsim 10\,M_\odot\,\mathrm{yr}^{-1}$ have over half of their star formation obscured by dust. For a complete picture of galaxy formation, it is therefore crucial to understand the prevalence and effects of dust in galaxies.

[4] When astronomers talk about "dust", they refer to mostly carbon- and silicon-based pebbles with a typical size of, roughly, a nanometer to a micron (Draine 2003).

The shift of optical and ultraviolet light to longer wavelengths due to dust is occasionally referred to as *dust reddening*. The presence of dust in galaxies can therefore be inferred observationally as a deficit in emission at short ("blue") wavelengths, or – typically more readily – by observing significant emission at "red" wavelengths, including the infrared and submillimeter regimes. Owing to the brightness of newly formed massive stars, galaxies that are actively star-forming will have most of their dust heated by these young stellar populations. As a result, the observed total dust emission from galaxies is a direct measure of the attenuated ultraviolet luminosity of young stars, and hence measures a galaxy's (dust-obscured) star formation rate. As for ultraviolet SFRs (Equation 1.1), star formation rate and infrared luminosity $L_{\rm IR}$ are directly related through a linear calibration (Kennicutt 1998):

$$\mathrm{SFR}_{\rm IR} \propto L_{\rm IR} \tag{1.2}$$

If a galaxy contains both obscured and unobscured star formation, its total star formation rate is given by $\mathrm{SFR} = \mathrm{SFR}_{\rm IR} + \mathrm{SFR}_{\rm UV}$, that is, by summing the infrared and ultraviolet contributions. As we will discuss in the next Section, dust-obscured star formation forms a crucial part of any full theory of galaxy evolution.

1.2.3 Dusty Star-forming Galaxies

When the *Infrared Astronomical Satellite* (IRAS) was launched in 1983, and performed an all-sky survey at infrared wavelengths, it quickly made a surprising discovery (e.g., Soifer et al. 1987). The satellite, operating at wavelengths between $12-100\,\mu$m (Neugebauer et al. 1984), observed thousands of bright galaxies that had not previously been seen in optical surveys. These galaxies were among the most actively star-forming hitherto observed, but were so dust-obscured that nearly all of their stellar light was attenuated and re-emitted at infrared wavelengths. While certainly an interesting population, the bright dust-obscured galaxies observed by IRAS – designated (Ultra) Luminous Infrared Galaxies; (U)LIRGs for short – make up only a small fraction of the local galaxy population, and only a few percent of the total amount of star formation happening nearby (Sanders & Mirabel 1996).

However, around the turn of the 21st century, infrared telescopes had become powerful enough that more distant galaxies could be probed. Using

the *James Clerk Maxwell Telescope*, operating at a wavelength of $850\,\mu$m, Smail et al. (1997) presented the first evidence that bright dust-obscured starburst galaxies were more prevalent in the early Universe, which was quickly confirmed by subsequent studies (see Blain et al. 2002 for a review). Recent estimates indicate that more than half of all star formation from redshift $z \sim 4$ to the present day is obscured by dust (e.g., Zavala et al. 2021), with a significant fraction due to bright dust-obscured starbursts. Owing to their discovery at $850\,\mu$m – a much longer wavelength than probed with IRAS – these distant starbursts were dubbed *submillimeter galaxies* (SMGs). Many thousands of SMGs have been observed to date, with the brightest among them reaching star formation rates in excess of $1000\,M_\odot\,\mathrm{yr}^{-1}$. The physical conditions in these galaxies that lead to such extravagant star formation rates remain a topic of much research in astronomy (see e.g., Hodge & da Cunha 2020 for a review).

1.2.4 The Star-forming Population

At this point, it is illuminating to take a step back, and place these dusty galaxies in a broader context. In fact, a simple yet revealing illustration of the overall galaxy population requires only two parameters, one of which we have previously introduced: star formation rate and *stellar mass*. These two quantities are naturally related: while the star formation rate is a measure of a galaxy's current evolution, the stellar mass represents its past evolution. Indeed, stellar mass may simply be understood as the integral of a galaxy's star formation rate across time.[5]

Figure 1.4 shows a sample of galaxies in the nearby Universe on the star formation rate versus stellar mass plane. The galaxy population roughly divides into three different subsets: the bulk of the galaxies fall onto a (nearly) linear relation between star formation rate and stellar mass, known as the *star formation main sequence* (e.g., Brinchmann et al. 2004; Noeske et al. 2007). The main sequence constitutes a tight correlation with a scatter of roughly $0.3\,$dex, and has been shown to already be in place at high redshift (at least $z \sim 4-5$; Speagle et al. 2014; Schreiber et al. 2015). In addition, the normalization of the main sequence increases with increasing redshift, implying that – at fixed stellar mass – typical galaxies were more strongly star-forming in the past.

[5]This is somewhat of an oversimplification, as a fraction of the mass formed during star formation is later returned to the interstellar medium. As such, the true stellar mass of a galaxy is different from the total mass formed in stars (e.g., Bruzual & Charlot 2003).

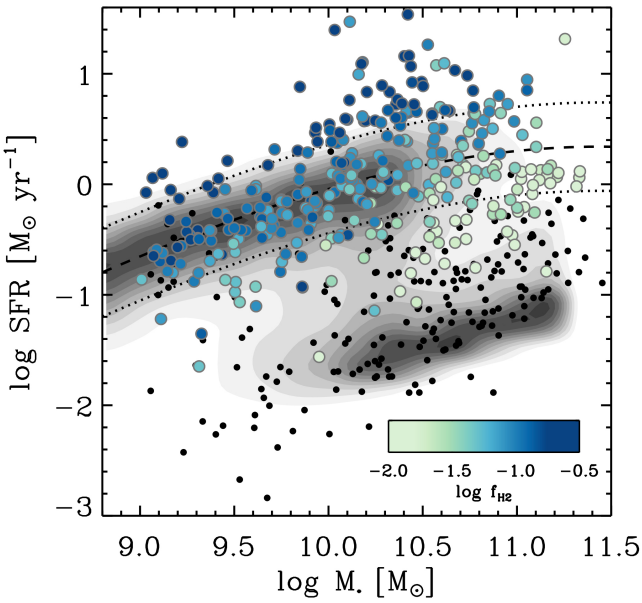

Figure 1.4: Galaxies (from the xCOLD GASS survey) on the star formation rate versus stellar mass plane. At fixed stellar mass, galaxies can have a variety of star-formation rates: most galaxies lie on the star formation main sequence, where – at least at low and intermediate masses – stellar mass and SFR are roughly linearly related. A small fraction of galaxies has star formation rates in strong excess with respect to the main sequence; these form the starburst population. In contrast, a fraction of predominantly massive galaxies shows very little star formation, and makes up the quiescent population. Galaxies in this figure are colored by their molecular gas contents, which constitutes the fuel for star formation. High gas fractions typically correspond to higher star formation rates. (Figure credit Amélie Saintonge, based on data from Saintonge et al. (2016); `http://www.star.ucl.ac.uk/~amelie/research.html`).

Not all galaxies, however, lie on the main sequence. A fraction of galaxies contains very little ongoing star formation, despite being relatively massive. This population is known as the *quiescent population*. Quiescent galaxies must have had significant star formation in the past in order to assemble their current stellar mass, though their star formation has since mostly ceased by the as of yet not fully understood mechanism of *quenching*. Quenching, most likely, involves either expelling or heating of gas within galaxies, which in turn inhibits future star formation (e.g., Kereš et al. 2005; Croton et al. 2006). In order to shed further light on the precise mechanisms and timescales involved in quenching, significant obser-

vational efforts are focused on detecting quiescent galaxies in the early Universe, where their number densities were significantly smaller compared to the present day (e.g., Ilbert et al. 2013).

In contrast to the quenched population, some galaxies have significantly higher star formation rates than would be expected based on the main sequence; this highly star-forming population constitutes what are known as *starburst galaxies*. Starburst activity may be triggered via galaxy mergers, as is commonly observed for local starbursts (Sanders & Mirabel 1996), or alternatively by an increase in their cold gas contents, or an increased efficiency of star formation from the available gas (Santini et al. 2014; Elbaz et al. 2018; Liu et al. 2019). Starburst galaxies overlap in part with the submillimeter galaxies introduced earlier, as high star formation is accompanied by significant dust build-up, although some SMGs may fall onto the upper end of the main sequence and may not formally be classified as starbursts (e.g., Michałowski et al. 2012; Birkin et al. 2021).[6] Nearly all massive galaxies are thought to go through one or multiple starburst phases (e.g., Dudzevičiūtė et al. 2020), and, similarly, less massive galaxies may also often rise above or dip below the main sequence (Sparre et al. 2015; Matthee & Schaye 2019) As such, while the star-forming main sequence may be regarded as an average trajectory for galaxy evolution, it should not be regarded as an evolutionary sequence for any individual galaxy.

Having established an inventory of the full galaxy population, the next few Sections will focus on their multi-wavelength emission, beginning with the longest wavelengths.

1.3 Radio Emission in Galaxies

A large fraction of this thesis concerns itself with a wavelength regime we have yet to explore: the radio window. Radio waves from an astronomical origin were originally discovered in 1931 by American engineer and physicist Karl Jansky, using a radio telescope he himself constructed. The legacy of Jansky's work remains reflected in the unit of flux density that is ubiquitously used in radio astronomy, the *Jansky*, defined as $1\,\mathrm{Jy} = 10^{-26}\,\mathrm{W\,m^{-2}\,Hz^{-1}}$. In addition, the famous collection of linked radio telescopes near Socorro, New Mexico in the United States was renamed the *Karl G. Jansky* Very Large Array in his honor in 2012.

[6] It must be noted that stellar masses tend to be quite uncertain for dust-obscured populations such as SMGs, see for example Michałowski et al. (2012).

Radio emission in galaxies can be produced in a variety of ways. Here, continuing our discussion from the previous sections, we will focus on radio emission originating from star formation, while we discuss other origins in Section 1.5.

As we have established in Section 1.2.2, measuring star formation rates in distant galaxies typically revolves around probing the emission originating from young stars. While some stars do emit radio waves, and in fact the Sun is the brightest object in the radio sky due to its proximity to us, direct stellar radio emission is not used as a tracer of star formation. Most stars are, indeed, radio-faint. Using radio observations from the Very Large Array across more than half of the entire sky, supplemented by similar all-sky observations at optical wavelengths, Kimball et al. (2009) did not conclusively detect any radio emission from a stellar origin. Instead, the radio emission produced by star-forming galaxies stems from two main sources: supernovae shocks and ionized plasma. The radio waves emitted by these sources are produced by, respectively, *synchrotron emission* and *free-free emission*.

1.3.1 Synchrotron Emission

Synchrotron radiation is produced by the acceleration of charged particles in a magnetic field. The exact origin of magnetic fields in galaxies remains debated (e.g., Beck 2012), and it is unclear whether they are generated in the early Universe, or instead arise later through astrophysical phenomena. Nevertheless, magnetic fields are ubiquitous in galaxies, and have been directly observed in nearby galaxies through polarized emission at various wavelengths, as well as Zeeman splitting (Robishaw et al. 2008). Magnetic fields further appear to be particularly strong in local starburst galaxies (McBride et al. 2014, 2015), where they may attain strengths of several milliGauss (mG). More typical spiral galaxies have magnetic field strengths that are generally on the order of $10\,\mu$G (Beck 2012; Tabatabaei et al. 2017).

The charged particles generating synchrotron emission are created in the shock waves that accompany the violent death of massive stars ($\gtrsim 8\,M_\odot$) in supernova explosions. Such massive stars are short lived, and as such their supernova rate is related to a galaxy's recent star formation rate, albeit with a short delay ($\lesssim 30\,$Myr; Bressan et al. 2002). However, from a theoretical point of view, it is far from trivial to use radio observations as a means of determining star formation rates, as this process involves

understanding many key ingredients, such as the physics of supernovae, the acceleration of cosmic rays in their remnants, the propagation of such cosmic rays through the host galaxy, and the magnetic field in which they radiate their energy (e.g., Condon 1992).

However, nature lends her helping hand. Early observations by Van der Kruit (1971, 1973) already indicated the existence of a correlation between the infrared and radio luminosities of galaxies, a result which was soon extended to larger galaxy samples (De Jong et al. 1985; Helou et al. 1985). Since then, this so-called *far-infrared/radio correlation* has been shown to hold across many orders of magnitude in galaxy luminosity, from small dwarf galaxies to bright starbursting systems (e.g., Yun et al. 2001; Bell 2003). In turn, this surprisingly robust and tight correlation undoubtedly masks a plethora of underlying physical phenomena, which we explore in the following Section.

1.3.2 The Far-infrared/radio Correlation

The Theory

For the far-infrared/radio correlation to exist, naively these two statements must hold: 1) a large and roughly fixed fraction of star formation within galaxies is dust-obscured, and 2) the supernova-induced cosmic rays radiate a roughly fixed fraction of their energy through synchrotron emission (e.g., Völk 1989; Lisenfeld et al. 1996). This second condition, in turn, encompasses two related effects: cosmic rays should not escape the galaxy prior to losing the bulk of their energy, and the magnetic fields in galaxies should be sufficient that synchrotron emission contributes significantly to cosmic ray energy loss. As we will outline below, these conditions are expected to be fulfilled in relatively massive galaxies, which form the main focus of this thesis. In low-mass galaxies, however, these conditions are not necessarily expected to hold (e.g., Murphy 2009a; Lacki et al. 2010). A significant fraction of star-formation in low-mass systems may not be enshrouded in dust (Whitaker et al. 2017), resulting in infrared emission not being a robust star formation rate indicator in these galaxies. However, in what Bell (2003) dub "a conspiracy", radio synchrotron emission similarly fails to account for all star formation in low-mass galaxies, by virtue of cosmic rays being able to escape these typically smaller systems prior to losing all their initial energy. In turn, the far-infrared/radio correlation appears to be preserved even in faint, low-mass galaxies (Bell 2003; Delvecchio et al. 2021). In what follows, however, we will focus mostly

on massive galaxies, as these constitute the general population detected in high-redshift radio surveys (Section 1.6).

As a start, let us examine the nature of synchrotron emission in galaxies in some detail. The synchrotron *spectrum* of a typical star-forming galaxy, defined as its flux density as a function of frequency, is often well-characterized by a single power-law that may be written as $S_\nu \propto \nu^{\alpha_{\rm NT}}$. Observations indicate that $\alpha_{\rm NT} \approx -0.85$ (e.g., Niklas et al. 1997; Murphy et al. 2012; Tabatabaei et al. 2017), for a typical cosmic ray energy distribution (e.g., Lacki et al. 2010). In addition, this value appears to be typical for both normal star-forming galaxies and high-redshift starbursts, albeit with substantial scatter (e.g., Ibar et al. 2009; Thomson et al. 2014; Smolčić et al. 2017b; Gim et al. 2019).[7]

However, it was quickly recognized that the strong magnetic fields in starburst galaxies imply very short *cooling times* for cosmic rays, given that the timescale for synchrotron emission $\tau_{\rm syn}$ depends strongly on the magnetic field strength ($\tau_{\rm syn} \propto B^{-3/2}$; Thompson et al. 2006). Cooled synchrotron emission is expected to produce a spectral slope steeper than the canonical $\alpha_{\rm NT} \approx -0.85$, potentially reaching values of $\alpha_{\rm NT} \approx -1.3$ (Kardashev 1962). However, such steep spectra are not typically observed in star-forming galaxies at GHz frequencies.

As a result, it became apparent that the physics underpinning the far-infrared/radio correlation may be more complex than previously thought. (Thompson et al. 2006) proposed that, in dense starburst environments, other effects were at play that could flatten the synchrotron spectrum from its cooled value back to the canonical $\alpha_{\rm NT} \approx -0.85$. These two effects are *ionization cooling* and *bremsstrahlung*. Ionization cooling involves cosmic rays colliding with the ambient interstellar medium in galaxies (generally atomic or molecular hydrogen), whereby they lose energy. Such collisions are most efficient for relatively low-energy cosmic rays, whereas synchrotron cooling is most effective for their high-energy counterparts. As such, Thompson et al. (2006) argued these two processes could balance each other and in turn reconstruct what appears to be a typical uncooled synchrotron spectrum. Bremsstrahlung losses, which similarly occur from the interaction of relativistic cosmic rays with the neutral interstellar medium, have no such energy dependence, but serve as an additional process competing with synchrotron cooling.

[7] Local ULIRGs, however, may show somewhat shallower spectra, see e.g., Clemens et al. (2008) and the discussion in **Chapter three**.

With the introduction of additional mechanisms of energy loss, however, a new problem arises. If the cosmic rays that drive the far-infrared/radio correlation lose *too much* of their energy through processes other than synchrotron emission, the correlation should disappear. Lacki et al. (2010) carefully model the relative importance of synchrotron, ionization and bremsstrahlung losses, in addition to *inverse Compton cooling* involving the energy loss of cosmic rays upon their interaction with the local radiation field. They determine that, while synchrotron emission is indeed suppressed in starburst galaxies due to the various competing processes, collisions of cosmic rays with the interstellar medium should generate *secondary cosmic rays*, such as secondary electrons and positrons. These newly created charged particles will then, in turn, continue to emit synchrotron emission, thereby augmenting the synchrotron radiation produced by the primary cosmic rays. This careful balancing of energy loss mechanisms with the additional synchrotron radiation produced by secondary cosmic rays, in turn, is expected to preserve the far-infrared/radio correlation in massive starbursts.[8]

As radio telescopes were becoming capable of probing more distant galaxy populations, it became paramount to additionally assess the nature of the far-infrared/radio correlation in the high-redshift Universe. As the cosmic microwave background was more energetic in the past, inverse Compton losses on the CMB should become increasingly dominant further back in cosmic time (e.g., Murphy 2009a). Eventually, inverse Compton cooling is therefore expected to result in a breakdown of the far-infrared/radio correlation (Schleicher & Beck 2013), although the exact redshift where this breakdown should occur depends on the magnetic field strength of individual galaxies. Starburst galaxies, fortified by their strong magnetic fields, are expected to be most resilient to this breakdown (Murphy 2009a). In addition, Lacki et al. (2010) argue that their strong magnetic should further increase their synchrotron luminosities, as these will enhance the radiative losses of the less energetic, yet more numerous, cosmic ray population. In turn, starburst galaxies form powerful laboratories for studies of the far-infrared/radio correlation in the early Universe. Indeed, Lacki & Thompson (2010) argue that "puffy" starbursts – being bulkier than their local, more compact starbursting counterparts – may, in fact, show enhanced radio emission at high redshift due to their high star formation

[8] In fact, the prediction that the correlation is preserved in starbursts was *also* labeled a conspiracy by Lacki et al. (2010).

rates. We provide strong evidence for this prediction in **Chapter three**.

The Observations

While a fully satisfactory theoretical interpretation may remain somewhat elusive, the importance of the far-infrared/radio correlation in observational studies cannot be overstated. Since infrared emission from galaxies constitutes a probe of dust-obscured star formation, this correlation provides the recipe for converting radio emission into star formation rates. As a result, the precise nature of the far-infrared/radio correlation is widely explored also in the observational realm, and generally involves defining the 'q' parameter first introduced by Helou et al. (1985):

$$q_{\rm IR} = \log_{10}\left(\frac{L_{\rm IR}}{3.75\times10^{12}\,{\rm W}}\right) - \log_{10}\left(\frac{L_{1.4}}{{\rm W\,Hz^{-1}}}\right)\,. \tag{1.3}$$

Parameter $q_{\rm IR}$, as such, constitutes the logarithmic difference of the infrared and radio luminosity of a galaxy, with an appropriate normalization to turn it into a dimensionless quantity. The radio luminosity is defined at a frequency of $1.4\,$GHz, which has historically been a popular frequency for performing radio surveys. In the local Universe, $q_{\rm IR}$ attains a typical value of $q_{\rm IR} = 2.64$, with a modest scatter of roughly $0.2-0.3\,$dex (e.g., Yun et al. 2001; Bell 2003). Given a value of $q_{\rm IR}$, star formation rates may be determined from radio synchrotron emission via

$$\mathrm{SFR}_{\rm radio} \propto L_{1.4} \propto 10^{q_{\rm IR}} L_{\rm IR}\,. \tag{1.4}$$

The importance of $q_{\rm IR}$ for determining radio-based star formation rates has lead to significant interest in exploring its potential dependence on either redshift, or galaxy physical parameters from an observational perspective. Early work by Garrett (2002) in the well-studied *Hubble Deep Field North* indicated the correlation seemed to persist out to $z\sim1$, albeit for a small sample of just 20 galaxies. Ivison et al. (2010b), used observations from the *Herschel Space Telescope* to probe the correlation out to $z\sim2$, and found a slight redshift-dependence, which was corroborated by subsequent studies (e.g., Thomson et al. 2014; Magnelli et al. 2015; Delhaize et al. 2017). Most intriguingly, this apparent redshift evolution contradicted the evolution predicted by theoretical studies: instead of high-redshift galaxies becoming radio-dim due to inverse Compton losses on the cosmic microwave

background, galaxies in the early Universe appeared to become increasingly radio-bright.

One caveat that perhaps remained underappreciated in these early studies of the far-infrared/radio correlation at high redshift (though see Sargent et al. 2010), was that selection effects may be a source of bias. For example, observations at far-infrared wavelengths benefit from what is known as the *negative k-correction*: while naively distant galaxies should appear dimmer than their more close by counterparts, this effect is compensated for by virtue of probing shorter rest-frame wavelengths in these more redshifted systems, where dusty galaxies tend to be brighter (Casey et al. 2014). In turn, observations at far-infrared wavelengths (e.g., $850\,\mu$m) have a rather uniform sensitivity to star formation at high redshift ($z \sim 1.5 - 6$). Radio observations, however, suffer from a *positive k-correction*, whereby more distant galaxies become increasingly faint quickly (Section 1.3.4). If not precisely accounted for, this leads to biases whereby at high redshift only the brightest radio sources are detected. This, in turn, will induce artificial evolution in the correlation, consistent with the evolution seen in observations (Sargent et al. 2010).

In addition, radio surveys may probe emission from a non-star-forming origin. Radio emission produced by supermassive holes in the center of galaxies – the topic of Section 1.5 – may form a source of contamination, and bias studies of the far-infrared/radio correlation. Upon carefully weeding out such contaminants, Molnár et al. (2018) argue that the correlation does not evolve with redshift, at least out to $z \sim 1.5$. Furthermore, if the far-infrared/radio correlation is non-linear, this too can induce artificial redshift evolution (Basu et al. 2015; Molnár et al. 2021).

Puzzled by an apparent (lack of) redshift evolution, and armed with deep multiwavelength ancillary observations, recent studies have begun exploring alternative dependencies of the far-infrared/radio correlation. In a detailed analysis, Delvecchio et al. (2021) find that the correlation likely depends on stellar mass, while any redshift dependence is secondary (see also Smith et al. 2020). Such evolution, however, remains difficult to explain from a theoretical point of view, and is in apparent disagreement with the models from Lacki et al. (2010) and Lacki & Thompson (2010). On the other hand, some recent studies of the sizes of radio galaxies support their predictions of secondary cosmic ray generation in galaxies (e.g., Varenius et al. 2016; Thomson et al. 2019). As such, despite its importance, the far-infrared/radio correlation remains a rather nebulous manifestation of

a variety of competing physical processes – a conspiracy, if you will.

1.3.3 Free-free Emission

While the mechanism generating synchrotron radiation in galaxies has proven to be quite complex, the opposite is true for the second process generating emission at radio frequencies: *free-free emission*. Free-free emission is produced during an interaction between charged particles, most commonly between free electrons and protons. The resulting free-free luminosity, in turn, is directly proportional to the rate of such interactions, and hence depends on the square of the ionized particle density ($N_{\mathrm{FF}} \propto n_e n_p \propto n_e^2$, where n_e and n_p are, respectively, the electron and proton density). As a result, the bulk of the free-free emission in galaxies is produced in dense, ionized regions.

Upon the formation of a sufficiently massive star from an initial cloud of dense molecular gas, the stellar radiation will proceed to ionize its surroundings. The resulting dense ionized regions, known as H II regions, produce the majority of free-free emission in galaxies. The lifetime of such H II regions is short, typically on the order of a few million years, as the cloud is rapidly dispersed by the young stars it harbors (Chevance et al. 2020). As a result, free-free emission provides a measure of massive ($\gtrsim 10 - 15\,M_\odot$; Kennicutt & Evans 2012; Byler et al. 2017) star formation on a timescale much shorter than ultraviolet, infrared or radio synchrotron emission.

Similar to the aforementioned tracers, free-free emission has been calibrated as a tracer of star-formation, as given by Murphy et al. (2011):

$$\mathrm{SFR}_{\mathrm{FF}} \propto T_e^{-0.45} \nu^{0.10} L_{\mathrm{FF}}(\nu)\,. \tag{1.5}$$

Here $L_{\mathrm{FF}}(\nu)$ is the free-free luminosity at a frequency ν and T_e is the typical electron temperature of the H II regions, upon which the star formation rate weakly depends.

The spectrum of free-free emission is remarkably simple. An analytical treatment of the Coulomb interactions in an ionized plasma, such as an H II region, shows that free-free emission should give rise to flat spectrum, though some minor quantummechanical corrections are required for a complete description. Taking these into account, the spectrum of free-free emission may be written as $S_\nu \propto \nu^{\alpha_{\mathrm{FF}}}$, where $\alpha_{\mathrm{FF}} = -0.10$ is the known,

fixed spectral index (e.g., Condon 1992; Murphy et al. 2012). The combination of free-free and synchrotron emission then provides a description of the *radio spectrum* of star-forming galaxies.

1.3.4 The Radio Spectrum

Having introduced the two main ingredients that make up radio emission in star-forming galaxies, as well as their frequency dependencies, we may now examine their relative contributions to the radio spectrum. To this end, let us introduce the *thermal fraction*, which quantifies the contribution of thermal free-free emission to the total radio emission (e.g., Murphy et al. 2012):[9]

$$f_\nu^{\mathrm{th}} = \frac{S_\nu^{\mathrm{FF}}}{S_\nu^{\mathrm{FF}} + S_\nu^{\mathrm{NT}}} \,. \tag{1.6}$$

Given the different spectral indices of free-free and synchrotron emission, the thermal fraction naturally depends on frequency. Indeed, the thermal fraction is expected to increase towards higher frequencies, due to the flat spectrum of free-free emission. What remains, then, is to anchor the thermal fraction at some reference frequency ν_0, from whereon it may be scaled to other frequencies. Observations of local galaxies indicate a thermal fraction of roughly 10% at a frequency of 1.4 GHz (Condon 1992; Tabatabaei et al. 2017). The total radio spectrum may then be written as the combination of synchrotron and free-free emission, and is of the form

$$S_\nu = S_{\nu_0} \left[\left(1 - f_{\nu_0}^{\mathrm{th}}\right) \left(\frac{\nu}{\nu_0}\right)^{\alpha_{\mathrm{NT}}} + f_{\nu_0}^{\mathrm{th}} \left(\frac{\nu}{\nu_0}\right)^{-0.1} \right] . \tag{1.7}$$

A model of the radio spectrum, adopting a thermal fraction of $f_{\mathrm{th}}(1.4\,\mathrm{GHz}) = 0.10$ and $\alpha_{\mathrm{NT}} = -0.85$, is shown in Figure 1.5. As a result of the dominant synchrotron contribution at GHz frequencies, the overall spectral index (i.e., averaging free-free and synchrotron emission) of the radio spectrum is typically $\alpha \sim -0.70$ in this regime, which is a value that is commonly adopted in the literature (Condon 1992; Smolčić et al. 2017b).

[9] A brief elaboration on the subscripts used: NT stands for non-thermal, as synchrotron as synchrotron emission does not involve particles with a thermal (i.e., Maxwell-Boltzmann) distribution of velocities. Free-free emission, denoted by subscript FF, on the other hand, is a thermal process. This nomenclature will be used interchangeably throughout this thesis.

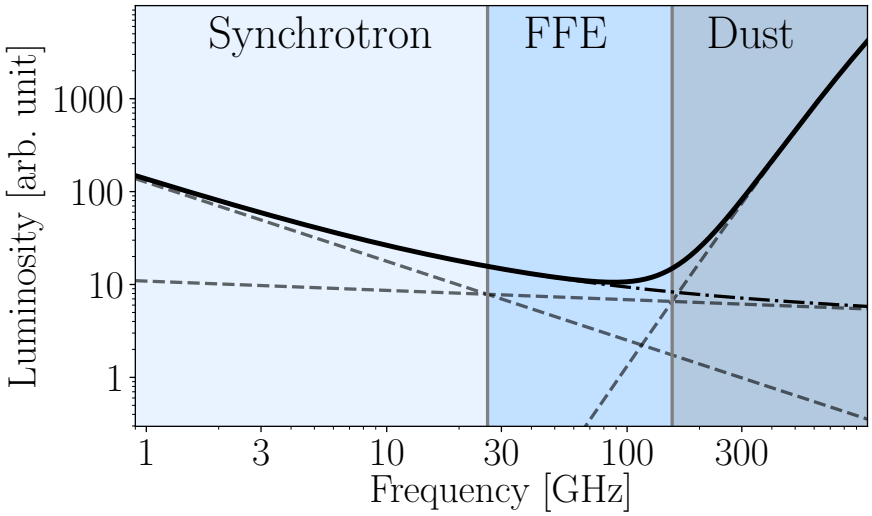

Figure 1.5: A simple model for the radio spectrum of a star-forming galaxy. At low frequencies, the steep synchrotron component is dominant, while at $\nu \gtrsim 30$ GHz, free-free emission overtakes the synchrotron contribution. At even higher frequencies, $\nu \gtrsim 200$ GHz, dust overtakes free-free emission. In this thesis, when referring to the radio spectrum, we consider the region where free-free and synchrotron dominate the emission, unless stated otherwise.

Around $\nu \sim 30$ GHz, however, the thermal fraction reaches upwards of 50%, and free-free emission takes over as the main emission mechanism. Eventually, around $\nu \gtrsim 200$ GHz, thermal emission from dust grains overtakes free-free emission as we start probing the millimeter regime. In reality, there is considerable scatter about these values, which may depend on a variety of factors, such as the precise synchrotron slope, the age of the starburst and the star-formation history, and the dust mass and temperature of the galaxy. A more detailed exploration of the radio spectrum of star-forming galaxies is provided in **Chapters 4 & 5**.

It is important to note that the model of the radio spectrum presented in Equation 1.7, combining just free-free and synchrotron emission, is a simplification in its own right. The radio spectrum typically does not extend as a power law to the lowest frequencies ($\nu \lesssim 1$ GHz), where it instead flattens or turns over due to a non-negligible optical depth (Condon 1992). In addition, older starbursts will show a deficit in synchrotron emission at high

frequencies due to spectral ageing (e.g., Thomson et al. 2019). However, more complex prescriptions of the radio spectrum naturally require more and better data, which is generally not available for distant galaxies. As a result, the radio spectrum is often approximated by either a single power law, or by the combination of two power laws describing free-free and synchrotron emission.

1.4 The Spectral Energy Distribution of Galaxies

In the previous sections, we have introduced a variety of ways galaxies produce light. At ultraviolet and optical wavelengths, we measure the direct emission from stars, while at infrared wavelengths this is predominantly starlight that has been reprocessed by cold dust. Radio wavelengths, instead, measure either supernovae through synchrotron emission, or dense ionized gas through free-free emission.[10]

A typical spectral energy distribution of a (dusty) star-forming galaxy, spanning ultraviolet to radio wavelengths, is shown in Figure 1.6. Of course, this figure is just a single example that cannot possibly encompass the variety of the full galaxy population. More dust-rich galaxies will be fainter in the optical and ultraviolet regimes, while their emission at (far-)infrared wavelengths is boosted. On the other hand, galaxies that have little ongoing star formation will predominantly shine at optical and near-infrared wavelengths, by virtue of their older stellar populations.

1.4.1 An Inventory of Star formation Rate Tracers

Having introduced a plethora of star formation rate indicators (and having omitted a plethora more), we here discuss them jointly and compare the advantages and disadvantages of each.

Ultraviolet Emission

Ultraviolet emission is produced directly by relatively young stars and traces star formation across a timescale of $\sim 10 - 200\,\mathrm{Myr}$ (Kennicutt & Evans 2012), corresponding to the lifetime of stars that produce significant UV emission. For some of the earliest known galaxies, this is the only star formation rate indicator available, owing to the sensitivity of telescopes such

[10] For now, we have conveniently left X-ray emission out of our discussion. X-rays, too, may be generated by star formation (e.g., Symeonidis et al. 2014), but are often of a non-star-forming origin – see Section 1.5 for more details.

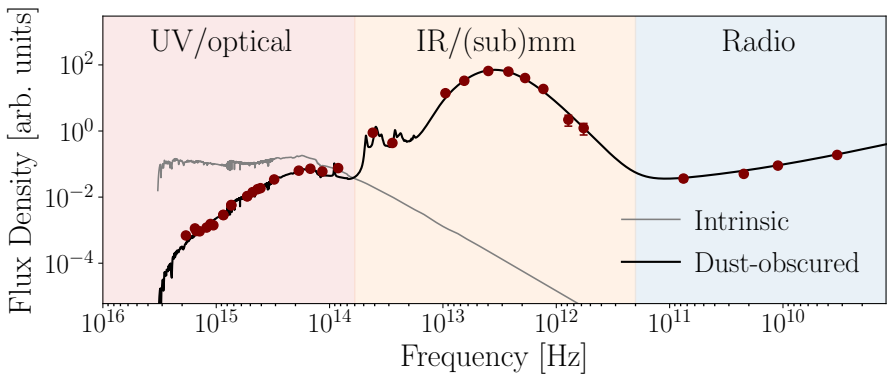

Figure 1.6: Example spectral energy distribution of a (dusty) galaxy. The rough extent of the various multiwavelength regimes in their colloquial astronomical definition are indicated. The grey line shows the intrinsic stellar spectrum, while the black line indicates the dust-reprocessed emission. The red circles represent a variety of multiwavelength measurements, and are shown to indicate the extent of the typical sampling of a galaxy's spectral energy distribution.

as the *Hubble Space Telescope*. However, in the absence of additional long wavelength information, ultraviolet star formation rates will always constitute a lower limit on the true star formation rate, as dust attenuation reduces a galaxy's UV luminosity. As infrared observations are generally not available, average dust corrections are often assumed to incorporate any contribution from dust-obscured star formation (e.g., Oesch et al. 2013), though these are inherently uncertain for individual galaxies.

In addition, while targeting the rest-frame ultraviolet emission in distant galaxies provides a powerful way of detecting and characterizing these faint systems, this emission will be redshifted to longer wavelengths due to the expansion of the Universe. In fact, the emission at wavelengths shortward of the Lyman α transition, ($\lambda < 1216\,$Å) is generally fully extincted by neutral hydrogen both within the galaxy and along the line of sight towards us (e.g., Steidel et al. 1996). In turn, optical and near-infrared telescopes are required to study the UV properties of the earliest galaxies.

Infrared emission

Infrared emission is emitted when dust in galaxies reprocesses the light from massive stars. Infrared emission, as such, traces dust-obscured star

formation across a timescale of ~ 100 Myr (Kennicutt & Evans 2012) – similar to the timescale of ultraviolet emission. Infrared emission, however, is not a direct tracer of star formation, as it does not directly probe stellar light, and relies on the presence of dust within the galaxy. From a theoretical perspective, this complicates its use as a star formation tracer, as any older stellar populations may also contribute to the heating of dust. Nevertheless, for highly star-forming galaxies, the contribution of older stellar populations to the infrared luminosity is generally negligible ($\lesssim 10\%$; Kennicutt & Evans 2012).

From a practical point of view, measuring the infrared emission in distant galaxies is complicated by the limited sensitivity and resolution of most infrared and submillimeter telescopes. The *resolution* of a telescope defines the smallest detail it can observe. Any objects smaller than this smallest observable size will be *unresolved*, and therefore blended together. The resolution with which a telescope can observe a galaxy, or any object for that matter, is strongly wavelength-dependent. It is typically measured in arcseconds, and depends on the ratio λ/D, where λ is the observing wavelength, and D the diameter of the telescope.[11] In order to obtain the same resolution, an infrared telescope must therefore be significantly larger than an ultraviolet telescope. In practice, this is generally not feasible, and as a result, most infrared-based telescopes have a relatively modest resolution, much larger than the size of individual galaxies at cosmological distances. As an example, the *Herschel Space Observatory* has a resolution spanning $5'' - 36''$ depending on the wavelength used for observing. The James Clerk Maxwell Telescope has a similarly modest resolution of $15''$ at a wavelength of $850\,\mu$m. The *Hubble Space Telescope*, on the other hand, can attain a resolution as high as $0''.05$. For comparison, the typical size of a distant galaxy is on the order of one arcsecond – the precise value of course varying with distance, galaxy type, as well as with observing wavelength (e.g., van der Wel et al. 2014; Gullberg et al. 2019; Jiménez-Andrade et al. 2019). Infrared telescopes are therefore oftentimes unable to separate closely neighboring galaxies, which remain blended together. This, in turn, makes it significantly more difficult to observe distant galaxies, and infer their dust-obscured star formation rates. In addition, infrared-based telescopes are generally limited by either the cooling of their instruments, which itself may provide thermal emission at infrared wavelengths, or by the bright, omnipresent infrared background light (e.g., Farrah et al. 2019). These factors, in turn, complicate probing the earliest galaxies at infrared

[11] An arcsecond is defined as $1/3600^{\text{th}}$ of a degree.

wavelengths. One notable exception to either of these limitations is the *Atacama Large Millimeter Array* (ALMA), which can attain both a high resolution and sensitivity. Within the last decade, ALMA has indeed revolutionized infrared-based studies of distant star formation, and has provided the first window on dust at the highest redshifts (Hodge & da Cunha 2020).

Radio Synchrotron Emission

Radio Synchrotron Emission is produced by supernova-induced shocks, and can be used as a tracer of star formation through its tight correlation with the infrared luminosities of galaxies (Section 1.3). Given the long wavelength nature of synchrotron emission, it traces star formation in a dust-unbiased manner. However, as it relies on stellar deaths, synchrotron emission is a highly indirect tracer of star formation, lagging behind other tracers by $\sim 30\,\mathrm{Myr}$ (Bressan et al. 2002). However, when star formation has ceased, it lingers for a similar timescale as ultraviolet and infrared emission – roughly $\sim 100\,\mathrm{Myr}$. As the radio and infrared luminosities of galaxies are known to correlate, there is no obvious benefit in using the less direct synchrotron emission as a star formation rate tracer from a theoretical point of view. In practice, however, radio telescopes are generally more sensitive than infrared/submillimeter telescopes, and as such they are able to probe more distant galaxies. This is due to the powerful technique of *radio interferometry*. Instead of having a single radio telescope observe the sky, a radio interferometer is a collection of telescopes all working together. Having a large number of individual telescopes increases the area across which radio waves are collected, and as such allows for the detection of fainter objects. In addition, the resolution of a radio interferometer is not dependent on the size of the individual radio dishes, but instead on the *separation* between its dishes. The Very Large Array (VLA), for example, consists of 27 radio dishes, each with a diameter of 25 meter. However, the maximum separation between the dishes can be up to 36 kilometers – far larger than the size of any single telescope!

Powerful interferometers capable of probing dust emission exist as well, such as the aforementioned ALMA operating at (sub)millimeter wavelengths. However, compared to radio telescopes such as the VLA, submillimeter interferometers have a much smaller field of view, owing to their shorter observing wavelengths. From a practical standpoint, therefore, radio synchrotron emission is a very powerful and efficient tracer of star formation in the early Universe, being capable of probing a large number of faint galax-

ies in feasible amounts of observing time.

The main drawback of using synchrotron emission to probe distant star formation, however, is the somewhat nebulous theoretical underpinning of the far-infrared/radio correlation on which it relies, as discussed in Section 1.3.2. It remains debated if, or to what extent, the correlation is modified in distant galaxies, with a variety of recent studies indicating that the correlation may evolve with redshift (Magnelli et al. 2015; Delhaize et al. 2017) or galaxy physical parameters such as stellar mass (e.g., Delvecchio et al. 2021). In **Chapter Three**, we further provide evidence that the far-infrared/radio correlation depends on the physical conditions within galaxies, by studying the correlation for a large sample of highly star-forming dusty galaxies.

Radio Free-free Emission

Radio free-free emission is emitted by the ionized bubbles created by young, massive stars. The short lifetime of these H II regions ensures free-free emission traces star formation on a near-instantaneous timescale of $\sim 3 - 10$ Myr (Kennicutt & Evans 2012). Similar to synchrotron radiation, free-free emission is a dust-unbiased tracer of star formation. Its key benefits, however, are its direct nature as a star formation rate tracer, and the fact that free-free emission can be observed with powerful radio telescopes providing high resolution observations. In theory, free-free emission is therefore one of the best star formation rate tracers available for distant galaxies.

In practice, however, free-free emission has remained mostly unexplored in the early Universe, with observations by and large having been limited to local galaxies. This is a result of the relative faintness of free-free emission compared to synchrotron emission (Figure 1.5), and the high-frequency nature of the former. High radio frequencies are more difficult to observe due to more stringent weather constraints, and also provide a significantly smaller field of view than low-frequency observations. In addition, the precise contribution of free-free emission to the measured radio flux density – the thermal fraction introduced in Section 1.3 – depends on a variety of factors, such as the star formation history of the galaxy (Bressan et al. 2002) and the non-thermal synchrotron slope. As such, detecting free-free emission generally requires deep, multi-frequency observations designed to disentangle the free-free component from the synchrotron emission which dominates the radio spectrum at low frequencies (e.g., Tabatabaei et al. 2017). In turn, observations aimed at detecting free-free emission are expensive. Nevertheless, free-free emission is set to be a key tracer of distant

star formation when improved radio facilities come online in the (near) future, warranting its exploration already with current telescopes. **Chapters four and five** present two pioneering studies of radio free-free emission in the early Universe, and discuss its potential as a star formation rate tracer in further detail.

1.4.2 The Cosmic Star Formation Rate Density

Armed with this variety of star formation rate indicators, astronomers are able to measure the *cosmic star formation rate density* (SFRD) – one of the most fundamental quantities in the field of galaxy evolution. The cosmic star formation rate density is a measure of the *average* star formation rate across all galaxies, at a given moment in cosmic history. A compilation of various ultraviolet and infrared-based measurements of the SFRD from Madau & Dickinson (2014) is shown in Figure 1.7. The ultraviolet observations have been corrected for extinction by dust, though these corrections are – particularly at high redshift – very uncertain.

In the early Universe, the SFRD rapidly rose, peaking around a redshift of $z \sim 2$ (10 Gyr ago). The SFRD subsequently entered a decline towards the present day, which is expected to continue into the future (Walter et al. 2020). Besides accurately measuring the shape of the SFRD, it is also crucial to understand why its shape is as observed. Since stars form out of clouds of molecular gas, parallel efforts are underway to measure the cosmic molecular gas density, which have determined a similar evolution across cosmic time (Decarli et al. 2019; Riechers et al. 2019).

The wealth of constraints on the SFRD compiled in Figure 1.7 may suggest that the history of cosmic star formation is, for the most part, fully understood. This, however, is not the case. At high redshift ($z \gtrsim 3$), nearly all constraints on cosmic star formation are from ultraviolet observations, which require the aforementioned uncertain dust corrections. In addition, these observations are by construction incomplete, as they miss galaxies that are (nearly) fully dust-obscured. Recent studies of the SFRD at far-infrared and radio wavelengths have hinted towards an excess in star formation at $z \gtrsim 3$ compared to the Madau & Dickinson (2014) compilation (e.g., Novak et al. 2017; Gruppioni et al. 2020), which may indicate the early Universe being significantly more dust-rich than previously thought (e.g., Casey et al. 2018). Several recent detections of large samples of dust-obscured galaxies at very high redshift ($z \gtrsim 6$) with ALMA (e.g., Bouwens et al. 2021) will provide a much improved census of dust at early cosmic epochs in the near future. In addition, there is substantial room

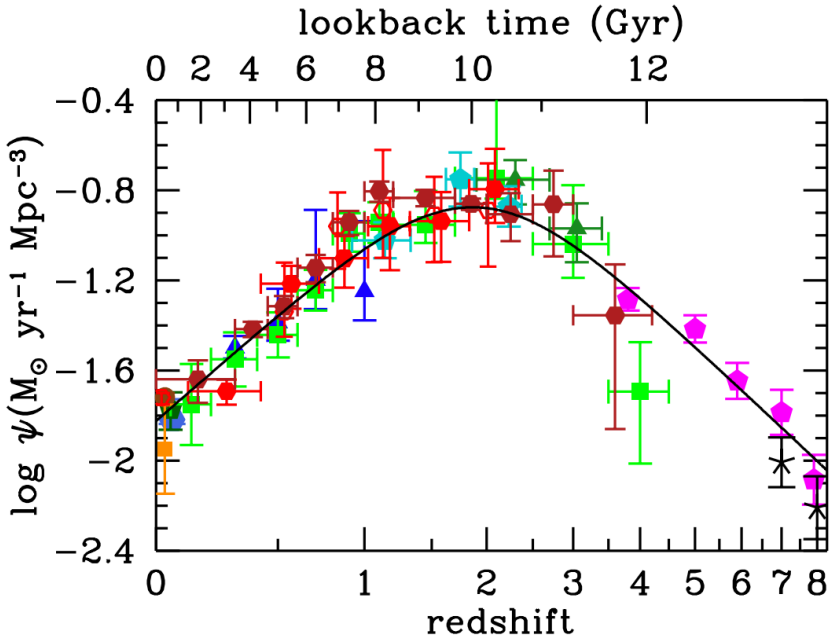

Figure 1.7: A compilation of the cosmic star formation rate density by Madau & Dickinson (2014), with the various colours representing different studies. The vertical axis shows the SFRD parameterized by the Greek letter ψ, as a function of redshift (lower x-axis) or time (upper x-axis). Starting with the formation of the first galaxies at high redshift ($z > 10$), the SFRD rises rapidly up to $z \sim 2$. Since then, the SFRD has been on the decline.

for improvement also in the way star formation rates are measured, as the canonical tracers of star formation suffer from various uncertainties (Section 1.4.1). In **Chapter five**, we therefore place the first constraints on the cosmic star formation rate density using the powerful radio free-free emission as a tracer.

1.5 Active Galaxy Nuclei

In the previous sections, we have discussed how star formation imprints its signature on the spectral energy distribution of galaxies. However, in a fraction of galaxies this emission of star-forming origin is outshined – potentially by orders of magnitude – by an *active galactic nucleus* (AGN).

In the early 1960s, Dutch astronomer Maarten Schmidt took an optical spectrum of a star that appeared to coincide with the bright radio source 3C 273 that had been observed a few years prior with an array of radio telescopes located near Cambridge, England. In a surprising find, Schmidt observed the spectral lines to have shifted from their intrinsic wavelength, placing the "star" at a redshift of $z = 0.158$; a distance of several hundred megaparsecs (Schmidt 1963). This vast distance, in turn, suggested 3C 273 to be an extremely luminous object, while its "quasi-stellar" nature implied it was compact, with the emission being generated within its nuclear region. It was quickly postulated (e.g., Lynden-Bell 1969) that accretion of material onto a supermassive black hole, hosted in the center of galaxies, could provide this enormous luminosity.

It has since become well-accepted that nearly all galaxies host such massive black holes in their centers (Richstone et al. 1998), with those subject to significant accretion emanating as active galactic nuclei. Most galaxies are thought to go through multiple AGN phases (e.g., Kormendy & Ho 2013), though only when the galaxy is active at the time of observations will it be classified as an AGN. From the perspective of galaxy evolution, AGN play an important role. The cosmic star formation history is seen to correlate strongly with the cosmically averaged accretion rate of AGN (Shankar et al. 2009), which is indicative of gas fueling both star formation and the central black hole. Furthermore, the existence of the so-called Magorrian relation (Magorrian et al. 1998), which describes the correlation between the mass of central galaxy bulges and that of their supermassive black holes, indicates some form of co-evolution between the black holes and the galaxy as a whole, despite the vastly different physical scales involved. These findings are generally attributed to feedback processes from the central AGN, via the launch powerful winds or jets that may trigger or alternatively impede star formation in galaxies (e.g., Best et al. 2006; Wang et al. 2010).

The wavelength at which AGN emission can be observed may vary from galaxy to galaxy. In particular, Heckman & Best (2014) distinguish two types of AGN with different observational signatures, related to their particular accretion mechanisms. *Radiative-mode* AGN are characterized by significant accretion – generally in excess of 1% of the Eddington luminosity – and are fed by a surrounding accretion disk.[12] Radiative-mode AGN

[12]The Eddington luminosity scales linearly with the mass of the central black hole, and is given by $L_{\rm Edd} = 3 \times 10^4 \, (M_\bullet / M_\odot) \; L_\odot$, while the accretion luminosity simply follows from

generally emit strong X-ray and ultraviolet emission, originating from the accretion disk and surrounding hot corona (Brandt & Alexander 2015). In addition, such AGN are thought to be surrounded by a clumpy, dusty torus, which, upon being heated by the central black hole, provides additional emission at mid-infrared wavelengths (e.g., Lacy et al. 2004).

Jet-mode AGN, on the other hand, are thought to be fueled not directly by an accretion disk, but via an accretion flow dominated by advection (Heckman & Best 2014). Their accretion rates tend to be lower than those of radiative-mode AGN, being less than a percent of the Eddington rate. In addition, a dusty torus is often absent in jet-mode AGN, and instead these sources are most readily characterized by the radio synchrotron emission they produce, generally in the form of powerful radio jets extending far beyond the outskirts of the galaxy.

Some overlap between these two classes of sources exists, however, as a fraction of AGN emit strongly in both the radio and X-ray regimes (Ceraj et al. 2018; Delvecchio et al. 2018). In turn, various classifications of AGN remain common in astronomical literature, with Padovani et al. (2017) going as far as describing this categorization as an "AGN zoo". Radio astronomers, for example, tend to distinguish two main AGN populations: radio-loud and radio-quiet AGN, which, as their names imply, differ based on their observed level of nuclear radio emission. Radio-loud AGN, in turn, may exhibit a variety of morphologies, leading to the often-used Fanaroff & Riley (1974) classification scheme. Among the most powerful AGN are the *quasars*, which have been detected already as far back as $z \sim 7$ (e.g., Wang et al. 2019). However, only roughly 10% of quasars appear to be radio-loud (e.g., Bañados et al. 2015). In turn, it is clear that a detailed study of the full AGN population involves a multiwavelength perspective, which constitutes the topic of **Chapter two**.

1.6 The Radio Revolution

The single most straightforward thing one can do upon the completion of a new radio survey, is determining the distribution of radio sources as a function of flux density. Perhaps somewhat surprisingly, even this simple counting exercise can have far-reaching implications. The number of sources one expects to measure in a radio survey is namely a function of the *cosmology* of the Universe, and depends, for example, on whether the Uni-

Einstein's famous mass-energy equivalence, with an added efficiency factor $\epsilon \sim 0.1$ (King & Pounds 2015), via $L_{\rm acc} = \epsilon \times \dot{M}_\bullet c^2$. Here, $\dot{M}_\bullet$ is the mass accretion rate of the black hole.

verse is static or evolving (Kellermann & Wall 1987). Back when the first dedicated radio interferometers saw extensive use in astronomy, building upon the rapid development of radar technology during the Second World War, the *steady state theory* of the Universe remained a popular concept. This model involves a Universe that, while expanding, is non-evolving, and has no beginning or end (Bondi & Gold 1948; Hoyle 1948). While the discovery of the cosmic microwave background (Dicke et al. 1965) proved to be the definitive nail in the coffin for the steady state model, radio number counts had already provided strong evidence of its inconsistency with observations (Priester 1958; Ryle & Clarke 1961).

Returning to the present day, the cosmology of the Universe has naturally been constrained to an accuracy beyond what radio number counts can provide. Nevertheless, it remains customary to determine the number counts for any large new radio survey, even if only to ensure the (rather technical process of) data reduction was performed successfully. As the capabilities of radio telescopes continue to improve, new regimes of faint galaxies are beginning to be unraveled – the *faint radio sky*.[13]

1.6.1 The Faint Radio Sky

Observational astronomy, of course, is a field that is constantly driven by technological advancements. As telescopes become bigger, or expand their observable wavelength ranges, new discoveries arise without exception. In that regard, the present is an exciting time for any radio astronomer. Indeed, at the heart of this thesis lies the "revolution" that is currently taking place within radio astronomy: the Very Large Array – the telescope that has without a doubt been most instrumental to this thesis – was constructed in the 1970s, but received a major upgrade in 2012 enhancing its sensitivity by an order of magnitude (Kellermann et al. 2020). Just a few years ago, the *Giant Meterwave Radio Telescope* (GMRT) in India, which saw its first light in 1995, received an upgrade of a similar magnitude. With the aim of probing even longer wavelengths than the GMRT, the *Low Frequency Array* (LOFAR) was constructed in The Netherlands, taking its first observations of the radio sky in 2010. In the decade following, LOFAR has expanded into a multitude of other European countries, further enhancing both its sensitivity and resolution.

[13] What any one astronomer refers to as "faint" is, of course, somewhat subjective. Furthermore, the notion of faintness will even change over time. Some quantitative discussion in the following section is warranted.

The observations provided by this radio revolution allow for significant advances in our understanding of the faint radio sky. As outlined in Section 1.5, the bulk of the bright radio population is composed of active galactic nuclei (e.g., Condon 1984), which can be observed out to cosmological distances. Star-forming galaxies, however, are significantly fainter and require more powerful radio telescopes to be detected at early cosmic times. Owing to the on average increased brightness of radio sources at low observing frequencies, we begin by discussing recent progress in radio observations of star-forming galaxies in the GHz frequency regime.

Quantifying the Faint Radio Sky

One of the first radio surveys capable of probing the *microjansky* radio population over a relatively large area was undertaken in the extragalactic COSMOS field (Schinnerer et al. 2007, 2010). Carried out with the VLA at 1.4 GHz, the VLA-COSMOS survey reached a sensitivity of, roughly $10 - 15\,\mu$Jy across an area of two square degrees. At these depths, bright AGN, with radio powers of $L_{1.4} = 10^{25}\,\mathrm{W\,Hz^{-1}}$, are detectable out to high redshift ($z \sim 5$). However, even with these deep (and only decade-old) observations, just the very brightest star-forming galaxies – the tip of the iceberg – were detectable beyond $z \gtrsim 1$.

The vastly improved capabilities of the current VLA are illustrated by a comparison of the pre-upgrade VLA-COSMOS survey with a more recent example: the 3 GHz COSMOS-XS survey (Figure 1.8; van der Vlugt et al. 2021; Chapter 2).[14] While the former was limited to probing ULIRGs and HyLIRGs, with star formation rates in excess of $\mathrm{SFR} = 100\,M_\odot\,\mathrm{yr^{-1}}$ and $\mathrm{SFR} = 1000\,M_\odot\,\mathrm{yr^{-1}}$, respectively, the COSMOS-XS survey is capable of probing such galaxies out to $z \sim 3$ and $z \gg 5$. [15]

In addition, as outlined in Section 1.2.4, the normalization of the star forming main sequence increases rapidly with redshift, such that at a fixed stellar mass, high-redshift galaxies are more strongly star-forming. In turn, it is illustrative to focus on a galaxy at a constant mass of $M_\star = 10^{10.5}\,M_\odot$, corresponding to roughly half the mass of the Milky Way (Licquia & New-

[14] While carried out at 3 GHz, we converted the relevant COSMOS-XS flux densities to 1.4 GHz with a spectral index of $\alpha = -0.70$; Section 1.3.4.

[15] However, note that the 1.4 GHz VLA-COSMOS survey targets the full COSMOS field across 23 separate pointings (Schinnerer et al. 2007), while COSMOS-XS focuses on a single, deep pointing at 3 GHz. Nevertheless, recent observations with the upgraded VLA across the full field at 3 GHz (Smolčić et al. 2017b) improve upon the depth at 1.4 GHz by a factor of $3\times$, when adopting $\alpha = -0.70$.

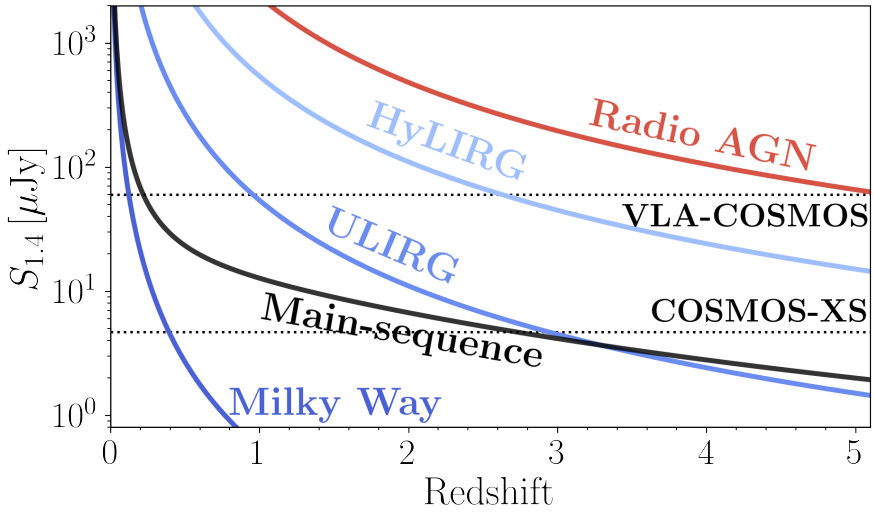

Figure 1.8: The typical 1.4 GHz flux density of various types of radio sources as a function of redshift. A luminous AGN ($L_{1.4} = 10^{25}\,\mathrm{W\,Hz^{-1}}$) remains brighter than $S_{1.4} \gtrsim 100\,\mu$Jy out to $z \sim 4$, and is therefore detectable even in relatively shallow radio surveys, such as the 1.4 GHz VLA-COSMOS survey (5σ detection limit of $S_{1.4} \approx 60\,\mu$Jy). However, Milky Way-like galaxies are virtually undetectable in such surveys, and even ULIRGs (SFR $= 100\,M_\odot\,\mathrm{yr^{-1}}$) can only be observed out to $z \lesssim 1$. Deeper surveys such as COSMOS-XS ($5\sigma \approx 2.5\,\mu$Jy; Chapter 2), made possible by the 2012 upgrade of the Very Large Array, can probe ULIRGs out to $z \sim 3$ and HyLIRGs (SFR $= 1000\,M_\odot\,\mathrm{yr^{-1}}$) across the entire history of the Universe. In addition, due to the rapid evolution of the star forming main sequence with redshift, COSMOS-XS allows for the detection of $M_\star = 10^{10.5}\,M_\odot$ main sequence galaxies out to $z \sim 3$ (black line), while such galaxies are virtually undetectable in the VLA-COSMOS observations.

man 2015; black line in Figure 1.8). The star formation rate of such a galaxy is expected to be similar to that of a ULIRG at $z \gtrsim 3$ (Speagle et al. 2014), while being significantly lower at the present day. In turn, even at this relatively high stellar mass, main-sequence galaxies are virtually undetectable in previous radio surveys at all but the lowest redshifts. The improved sensitivity of the *Karl G. Jansky* Very Large Array, however, provides the ability of detecting such main sequence star-forming galaxies out to $z \sim 3$, or roughly across 80% of cosmic history. As such, the current "revolution" allows for the detection of *representative* galaxies at high redshift with radio telescopes.

1.6.2 The Faint Radio Population

Having established that deep radio surveys are capable of probing faint star-forming galaxies in the early Universe, the question remains to what extent it is indeed truly star formation being probed. Answering this question requires the combination of deep radio observations with equally sensitive observations across the full electromagnetic spectrum, in order to distinguish between star formation and AGN activity. While initially it was thought that star-forming galaxies started dominating the radio sky at flux densities below ~ 1 mJy at 1.4 GHz, subsequent studies (e.g., Bonzini et al. 2013; Padovani et al. 2015) indicated that both radio-quiet and radio-loud AGN still made up a relatively large fraction of the sub-mJy sky.

As multiwavelength data are crucial for the classification of the radio population, an efficient strategy entails targeting well-studied extragalactic fields with deep radio observations. The aforementioned two square-degree COSMOS field, indeed, has seen tremendous efforts from radio and non-radio astronomers alike (e.g., Scoville et al. 2007; Laigle et al. 2016 and references therein). Recently, sensitive 3 GHz observations from Smolčić et al. (2017b) have mapped the entire field down to a detection limit of $\sim 12\,\mu$Jy, with Smolčić et al. (2017a) subsequently providing a detailed view on the incidence of AGN in the radio sky at flux densities down to only a few tens of microjanskies. **Chapter two** introduces the Very Large Array COSMOS-XS survey, which targets a subset of the COSMOS field at two frequencies – 3 and 10 GHz – in a traditional *wedding cake* design: while limited to a smaller area, the COMSOS-XS 3 GHz observations improve upon the depth of the existing 3 GHz data by a factor of five. This combination of large-area but shallower observations with deep data across a smaller field of view is common in radio astronomy as it provides a detailed view of the full radio population.

In addition to this observational perspective, theoretical models for the radio sky have seen rapid development as well, generally with the aim of providing predictions for next-generation radio facilities. These simulations, by their very nature, consist of a complex mixture of observationally determined number densities of the various radio populations, imprinted upon the large scale structure of the Universe as provided by theoretical N-body simulations. Some of the earliest simulations of the radio sky were presented by Wilman et al. (2008), while a recent, improved set of simulations is provided by Bonaldi et al. (2019). We briefly discuss the ingredients of such simulations below, and explicitly compare them to the observed ra-

dio sky in Chapters 2 & 4.

The Bonaldi et al. (2019) simulations, for example, rely on the *Planck Millennium* dark matter-only simulations from Baugh et al. (2019). These provide a realistic framework of the structure of the Universe, allowing for an accurate description of the spatial distribution and clustering of radio sources. In these simulations, individual dark matter haloes are identified and subsequently populated by either star-forming galaxies, or (radio-loud) active galactic nuclei. While Wilman et al. (2008) treat radio-loud and -quiet AGN separately, by modelling the latter based on the observed X-ray luminosity function, Bonaldi et al. (2019) opt to include radio-quiet AGN as a subset of the star-forming population. Observationally, it remains unclear whether the radio emission in the high-redshift radio-quiet AGN population is (significantly) enhanced by the nuclear activity, or whether it is produced mainly through star formation (e.g., Panessa et al. 2019 and references therein; see also Chapter two).

Utilizing observational evidence that radio-loud AGN are typically hosted in massive galaxies (e.g., Sabater et al. 2019), as well as the probabilistic *abundance matching* technique used to assign galaxies of a given stellar mass to a typical halo mass, Bonaldi et al. (2019) subsequently populate the dark matter haloes with a realistic AGN population. This, in turn, is built upon the observed luminosity functions of the various types of radio AGN and their observed redshift evolution (e.g., the models from Massardi et al. 2010). This, generally, requires extrapolating the luminosity functions beyond the redshift ranges where they were constrained observationally, in turn inducing some intrinsic uncertainties into the simulated radio skies.

Modelling of star-forming galaxies similarly builds upon existing observational constraints. Wilman et al. (2008) adopt the measured 1.4 GHz luminosity function by Yun et al. (2001), thereby extrapolating it both to faint radio sources and to high redshift. On the other hand, Bonaldi et al. (2019) use the known (albeit uncertain) correlation between radio emission and star-formation rate to predict radio luminosity functions from the cosmic star formation rate density. In turn, such semi-empirical modelling provides direct predictions of star-forming galaxies and AGN down to ~ 1 nJy at 1.4 GHz; beyond what is currently in reach of radio telescopes. In addition, upon assuming spectral index distributions for the various radio populations, these simulations are capable of providing a view of the full radio sky across a wide range of frequencies (e.g., 150 MHz - 20 GHz in the case of Bonaldi et al. 2019).

What remains a clear gap in our understanding, however, is the nature of the faint high-frequency radio sky. Detailed studies of the composition of the high-frequency ($\gtrsim$ 30 GHz) radio populations in the microjansky regime have not been performed, for the simple reason that these depths have been unattainable for radio telescopes until the advent of the upgraded Very Large Array in 2012. Yet, even the sensitive upgraded VLA requires significant amounts of observing time to probe distant star-forming galaxies at high frequencies, owing to the typical faintness of this population (Section 1.3.4). Nevertheless, this regime is of considerable interest, as it harbors radio free-free emission as a powerful tracer of star formation.

At present, high-frequency detections of star-forming galaxies have remained limited to individual bright sources, potentially aided by gravitational lensing (e.g., Thomson et al. 2012; Wagg et al. 2014; Huynh et al. 2017). In addition, as the upcoming Square Kilometer Array Phase-2 will only provide frequency coverage up to 20 GHz, theoretical models of the radio sky have similarly not attempted to explore the higher frequency regimes. Furthermore, this in turn implies that, until the advent of the next generation Very Large Array sometime in the 2030s or 2040s, the current VLA will remain the go-to facility for exploring the high-frequency radio sky.

Some progress has been made at intermediate frequencies, with a recent study by Murphy et al. (2017), carried out at 10 GHz, providing some initial constraints on free-free emission in the early Universe. However, their observations still remained limited to the radio frequencies dominated by synchrotron emission, and lacked the ancillary data to robustly isolate the free-free component. Combined observations spanning both the low and high frequencies are therefore crucial to fully explore free-free emission in the early Universe, and form the topic of **Chapters 4 & 5**.

1.7 This Thesis

The ongoing revolution in radio astronomy and the accompanying wealth of new data are opening up a new window on galaxy evolution. This thesis includes four studies of the galaxy population in the faint radio sky, with the overarching aim of establishing how radio emission may be used to probe their star formation activity. The structure of this thesis is as follows. We begin by studying the composition of the faint radio population, separating it into star-forming galaxies and AGN (Chapter Two). In Chapter Three, we combine the low-frequency radio emission of dusty star-forming galaxies

with their infrared properties in order to explore the elusive origins of the far-infrared/radio correlation. In Chapters Four and Five, we turn to the high-frequency radio emission in star-forming galaxies, and perform a pioneering study of radio free-free emission in the early Universe. We briefly expand upon these studies below.

Chapter Two: With the advent of new, deep radio observations, the natural question arises what powers the radio emission of the faintest galaxy populations. We investigate the composition of the radio population identified in the Very Large Array COSMOS-XS survey, dividing it into star-forming galaxies and active galactic nuclei based on a variety of multiwavelength tracers of AGN activity. We find that the incidence of radio AGN decreases tremendously among the faint radio population, which is therefore predominantly powered through star formation.

Chapter Three: While the far-infrared/radio correlation provides the crucial recipe for measuring star formation rates via radio emission, its origins remain nebulous. We investigate the nature of the correlation for a large sample of dust-obscured star-forming galaxies at high redshift. These galaxies form an ideal laboratory for studies of the far-infrared/radio correlation, as they can be observed in an unbiased manner. We find no evidence for redshift evolution in the correlation, unlike previous (more biased) samples in the literature. In addition, we find that dusty star-forming galaxies are offset from the local correlation, being radio-bright by a factor of three. We argue this offset is the result of the extreme physical conditions present in such starbursting systems.

Chapter Four: Free-free emission constitutes an ideal probe of star formation activity in galaxies, being both a dust-unbiased and direct tracer. However, free-free emission is overshadowed by the brighter synchrotron emission at low radio frequencies, and hence requires expensive high-frequency observations to be robustly detected. We perform the first survey of free-free emission at high redshift, making use of deep 34 GHz observations from the COLDz survey. We detect eighteen galaxies in these observations, including seven that are likely powered through star formation. We determine free-free star formation rates for this star-forming subsample, and show that these are in agreement with canonical tracers of star formation.

Chapter Five: Left wanting more than just the seven star-forming galaxies from Chapter Four, we push the available radio data to their limits via a multi-frequency stacking analysis on optical/infrared-selected galax-

ies. This analysis is aimed at constraining the shape of the radio spectrum of faint, star-forming galaxies, and detecting their typical level of free-free emission. We find a systematic deficit of high frequency emission in the stacked radio spectra, which we interpret as the ageing of the synchrotron component. We additionally provide the first constraints on the cosmic star formation rate density with radio free-free emission, and find these to be in agreement with canonical constraints.

1.8 The Future

As the "radio revolution" is showing no signs of winding down, the future is, well, *faint*. There is significant room even for the current Very Large Array to extend the studies of free-free emission presented in this thesis. While increasing the depth and/or area covered at the highest frequencies ($\gtrsim 30$ GHz) may be prohibitively expensive, opportunities exist at slightly lower frequencies. As an example, we recently extended the ultra-deep 3 and 10 GHz COSMOS-XS survey to 1.4 GHz, allowing for an unprecedented view of the faint star-forming population with sufficient frequency coverage for free-free emission to be robustly disentangled from the low-frequency synchrotron component.[16] This intermediate frequency regime may, indeed, constitute the ideal compromise between field of view, typical source brightness and frequency lever arm for studies of this powerful star formation tracer. With increased sample sizes, free-free emission cannot only be established as a tracer of star formation, it can be used as a means of *calibrating* other tracers.

Perhaps the one tracer that benefits particularly from such calibrations, is radio synchrotron emission. While the galaxy samples used for studying this tracer through the far-infrared/radio correlation grow increasingly larger, an alternative approach is to investigate in detail how the correlation depends on the physical conditions in individual galaxies. Firmly establishing the correlation across varying physical scales in both starburst and main-sequence galaxies may provide key insights into its puzzling origins. The current VLA is already capable of providing such detailed tests in bright, gravitationally lensed systems, which will provide a benchmark for future facilities.

[16] A brief introduction to these new observations is given in Chapter Five, though future works will fully explore these exciting data.

Any outlook towards the future is certainly incomplete without mentioning the *Square Kilometer Array*. While not extending the frequency coverage of the VLA, the SKA will provide an unprecedented survey speed through its combination of field of view and sensitivity. This, in turn, allows for detailed observations of the microjansky galaxy population at low frequencies across much larger areas than presently feasible. In addition, SKA *deep fields* will probe down to sensitivities of several hundred nanojanskies, and reveal the ever fainter galaxy populations. Parallel efforts by non-radio facilities will subsequently be able to characterize these populations in exceptional detail.

The high-frequency capabilities of the SKA should, however, not be underestimated. Reaching up to 15 GHz in Phase-1 – with the aim of being expanded to 20 GHz in the more distant future – SKA surveys of free-free emission are all but unthinkable. As an example, deep surveys with the high-frequency bands of SKA1-Mid, such as Band 5b with a central frequency of 12.5 GHz (Braun et al. 2019), will probe the free-free-dominated regime in star-forming galaxies at $z \gtrsim 1$. Even modestly star-forming galaxies, with star formation rates of only $10\,M_{\odot}\,\mathrm{yr}^{-1}$ at $z = 1$, will be detectable in just 20 hr of observing time. As a result, a COSMOS-XS-like survey can be undertaken with the SKA in just a fraction of the observing time currently required. For detailed observing strategies and time estimates in SKA-based studies of free-free emission, we refer the reader to Chapter four.

The true *game changer*, however, will be the next-generation VLA, which will revolutionize our understanding of the radio spectra of faint, distant galaxies by virtue of its impressive sensitivity and frequency coverage. The ngVLA is expected to span an impressive range of 1.2 - 116 GHz, with a bandwidth reaching up to 20 GHz (Selina et al. 2018). In turn, large-area surveys of free-free emission will become, perhaps, the most powerful tool of measuring star formation in the early Universe.

2 The Nature of the Ultra-faint Radio Population

Abstract

Ultra-deep radio surveys are an invaluable probe of dust-obscured star formation, but require a clear understanding of the relative contribution from radio AGN to be used to their fullest potential. We study the composition of the μJy radio population detected in the *Karl G. Jansky* Very Large Array COSMOS-XS survey based on a sample of 1540 sources detected at 3 GHz over an area of ~ 350 arcmin^2. This ultra-deep survey consists of a single pointing in the well-studied COSMOS field at both 3 and 10 GHz and reaches RMS-sensitivities of 0.53 and 0.41 μJy beam^{-1}, respectively. We find multi-wavelength counterparts for 97% of radio sources, based on a combination of near-UV/optical to sub-mm data, and through a stacking analysis at optical/near-infrared wavelengths we further show that the sources lacking such counterparts are likely to be high-redshift in nature (typical $z \sim 4-5$). Utilizing the multi-wavelength data over COSMOS, we identify AGN through a variety of diagnostics and find these to make up 23.2 ± 1.3% of our sample, with the remainder constituting uncontaminated star-forming galaxies. However, more than half of the AGN exhibit radio emission consistent with originating from star-formation, with only 8.8 ± 0.8% of radio sources showing a clear excess in radio luminosity. At flux densities of ~ 30 μJy at 3 GHz, the fraction of star-formation powered sources reaches ~ 90%, and this fraction is consistent with unity at even lower flux densities. Overall, our findings imply that ultra-deep radio surveys such as COSMOS-XS constitute a highly effective means of obtaining clean samples of star-formation powered radio sources.

H. S. B. Algera, D. van der Vlugt, J. A. Hodge *et al.*
The Astrophysical Journal 903, 139 (2020)

2.1 Introduction

One of the key quests in extragalactic astronomy is to understand how the build-up and subsequent evolution of galaxies proceeds across cosmic time. Deep radio surveys offer an invaluable window onto this evolution, as they are a probe of both recent dust-unbiased star formation activity, as well as emission from active galactic nuclei (AGN). Past radio surveys were mostly limited to probing the latter, as AGN make up the bulk of the bright radio population (e.g. Condon 1989). Current surveys, in large part owing to the increased sensitivity of the upgraded NSF's *Karl G. Jansky* Very Large Array (VLA), are now changing this, and allow for joint studies of star-forming galaxies (SFGs) and faint AGN. This, however, requires these populations be distinguished from each other, necessitating detailed studies of the multi-wavelength properties of the radio-detected population (e.g. Bonzini et al. 2013; Padovani et al. 2017; Smolčić et al. 2017a; Delvecchio et al. 2017).

Radio emission from SFGs is dominated at frequencies below $\lesssim 30$ GHz by non-thermal synchrotron radiation (Condon 1992), which is thought to originate mainly from the shocks produced by the supernova explosions that end the lives of massive, short-lived stars. This conclusion is supported by the existence of the far-infrared-radio correlation (FIRC, e.g. De Jong et al. 1985; Helou et al. 1985; Yun et al. 2001; Bell 2003), which constitutes a tight correlation between the (predominantly non-thermal) radio and far-infrared (FIR) emission of star-forming galaxies. As the FIR-emission is dominated by thermal radiation from dust that has been heated by young, massive stars, this allows for the usage of radio continuum emission as a star-formation tracer through the FIR-radio correlation. Radio observations of the star-forming population are therefore, by definition, dust-unbiased, and hence provide an invaluable probe of cosmic star formation. In particular, radio surveys directly complement rest-frame ultraviolet (UV) studies of the cosmic star formation rate density (SFRD), which, while extending out to very high redshift ($z \sim 10$, e.g. Bouwens et al. 2015; Oesch et al. 2018), are highly sensitive to attenuation by dust. The extent of such dust attenuation remains highly uncertain beyond 'cosmic noon' ($z \gtrsim 3$, e.g. Casey et al. 2018), and necessitates the additional use of dust-unbiased tracers of star formation. Recently, Novak et al. (2017) performed the first study of the radio SFRD out to $z \sim 5$, finding evidence that UV-based studies may underestimate the SFRD by $15 - 20\%$ beyond $z \gtrsim 4$. They attribute this to substantial star formation occurring in dust-obscured

galaxies, which further highlights the value in carrying out deep radio surveys. Their findings are consistent with results from large sub-millimeter surveys, which are predominantly sensitive to this dusty star-forming population (see Casey et al. 2014 for a review).

In the last few decades, it has also become increasingly clear that the evolution of individual galaxies is substantially affected by the presence of supermassive black holes (SMBHs) in their center (e.g. Kormendy & Ho 2013). Among such evidence found locally is the Magorrian-relation (Magorrian et al. 1998) describing the tight correlation between the mass of the central SMBH of a galaxy and of its bulge. In addition, the cosmic history of black hole growth is comparable to the growth in stellar mass (Shankar et al. 2009), suggesting strong co-evolution. This is often explained by the accretion processes onto the black hole regulating star formation through mechanical feedback, either impeding (e.g. Best et al. 2006; Farrah et al. 2012) or instead triggering epochs of star formation and (Wang et al. 2010; Reines et al. 2011). Such AGN feedback is vital in particular for numerical simulations (e.g. Springel et al. 2005; Schaye et al. 2015) in order to recover, for example, galaxy luminosity functions and local scaling relations. Furthermore, direct evidence for mechanical feedback has been observed in local systems (e.g. McNamara & Nulsen 2012; Morganti et al. 2013). These results exemplify the importance of studying both galaxies and AGN jointly, instead of as separate entities.

Typically, two populations of AGN can be distinguished in radio surveys: sources which can be identified through an excess in radio emission compared to what is expected from the FIRC (henceforth referred to as radio-excess AGN) and sources which have radio emission compatible with originating from star formation, but can be identified as AGN through any of several multi-wavelength diagnostics (Padovani et al. 2011; Bonzini et al. 2013; Heckman & Best 2014; Delvecchio et al. 2017; Smolčić et al. 2017a; Calistro Rivera et al. 2017).[1] The latter class generally exhibit AGN-related emission throughout the bulk of their non-radio spectral energy distribution (SED), in the form of, e.g., strong X-ray emission or mid-infrared dust emission from a warm torus surrounding the AGN (e.g. Evans et al. 2006; Hardcastle et al. 2013). This distinction illustrates the importance of using multi-wavelength diagnostics for identifying AGN activity, which forms the focus of this work.

[1]These sources are also often referred to as radio-loud and radio-quiet AGN respectively (e.g. Heckman & Best 2014), though we follow here the terminology from Delvecchio et al. (2017) and Smolčić et al. (2017a).

The distribution of the star-forming and AGN populations has been well-established to be a strong function of radio flux density. At high flux densities, the radio-detected population is dominated by radio-excess AGN (Kellermann & Wall 1987; Condon 1989), followed by a flattening of the number counts around ~ 1 mJy. This flattening was initially interpreted as the advent of purely star-forming galaxies, but subsequent studies (e.g. Gruppioni et al. 1999; Bonzini et al. 2013; Padovani et al. 2015) probing down to a few hundreds to tens of μJy at 1.4 GHz revealed that a substantial part of the sub-mJy population remains dominated by non-radio excess AGN, with the current consensus being that SFGs only start dominating the radio source counts below ~ 100 μJy (Padovani et al. 2011; Bonzini et al. 2013; Padovani et al. 2015; Maini et al. 2016; Smolčić et al. 2017a), which is also in fairly good agreement with predictions from semi-empirical models of the radio source counts (Wilman et al. 2008; Bonaldi et al. 2019). This faint regime is of great interest for studies of star-formation, but has not been widely accessible yet to present-day radio telescopes.

With the upgraded VLA in particular, the radio population at the μJy level can now reliably be probed, which will help constrain the relative contributions of the various radio populations to unprecedented flux densities. Historically, a 'wedding-cake approach' has been the tried-and-tested design for radio surveys, incorporating both large-area observations and deeper exposures of smaller regions of the sky. By combining such observations, a clear consensus on both the bright and faint end of the radio population can be reached, which is crucial for understanding the different classes of radio-detected galaxies, as well as for the accurate determination of the radio source counts, luminosity functions and the subsequent radio-derived cosmic star-formation history.

The COSMOS-XS survey (van der Vlugt et al. 2021, henceforth Paper I) was designed to explore the faint radio regime and, by construction, constitutes the top of the wedding cake, making it the natural complement to large-area surveys such as the 3 GHz VLA-COSMOS project (Smolčić et al. 2017a,b). By going a factor of ~ 5 deeper than this survey, we directly probe two of the most interesting populations, namely the poorly-understood radio-quiet AGN and the faint star-forming galaxies. While radio surveys were historically limited by their inability to probe the typical star-forming population, being sensitive mostly to starburst galaxies (typical star-formation rates in excess of $\gtrsim 100\,M_{\odot}\,\mathrm{yr}^{-1}$), the COSMOS-XS survey reaches sub-μJy depths and allows for the detection of typical star-forming sources out to redshifts of $z \lesssim 3$. For this reason, the survey

is well-suited to bridge the gap between the current deepest radio surveys and those of the next-generation radio telescopes.

COSMOS-XS targets a region of the well-studied COSMOS field (Scoville et al. 2007), such that a wealth of multi-wavelength data are available for optimal classification of the radio population. Such ancillary data is crucial to place the survey into a wider astronomical context, and allows for the connection of the radio properties of the observed galaxy population to observations in the rest of the electromagnetic spectrum. With the combined COSMOS-XS survey and multi-wavelength data, we ultimately aim to constrain the faint end of the high-redshift radio luminosity functions of both SFGs and AGN, and use these to derive the corresponding dust-unbiased cosmic star formation history, as well as the AGN accretion history. Additionally, the unprecedented depth at multiple radio frequencies allows for the study of the high-redshift radio spectral energy distribution in great detail, and allows for the systematic isolation of the radio free-free component in star-forming galaxies, to be used as a robust star formation rate tracer (e.g Murphy et al. 2012, 2017). All of these science goals require a good understanding of the origin of the observed radio emission and hence depend on whether it emanates from star formation or instead from an AGN, and will be tackled in forthcoming papers.

In this paper, the second in the series describing the COSMOS-XS radio survey, we address this question by studying the composition of the ultra-faint radio population detected at 3 GHz in an ultra-deep single pointing over the COSMOS field (reaching an RMS of $\sim 0.53\,\mu$Jy beam^{-1}). We additionally present a catalog containing the multi-wavelength counterparts of the radio sources selected at 3 GHz, utilizing the wealth of X-ray to radio data available over COSMOS. The paper is structured as follows. In Section 2.2 we summarize the COSMOS-XS observations, the radio-selected catalog as well as the multi-wavelength ancillary data. In Section 2.3 we describe the association of counterparts to the radio sample. The decomposition of the radio population into SFGs and AGN is laid out in Section 2.4, and we present the multi-wavelength counterpart catalog in Section 2.D. Finally, we present the ultra-faint radio soure counts, separated into SFGs and AGN, in Section 2.5 and we summarize our findings in Section 2.6. Throughout this work, we assume a flat Λ-Cold Dark Matter cosmology with $\Omega_m = 0.30$, $\Omega_\Lambda = 0.70$ and $H_0 = 70\,\mathrm{km\,s^{-1}\,Mpc^{-1}}$. Magnitudes are expressed in the AB system (Oke & Gunn 1983), and a Chabrier (2003) initial mass function is assumed. The radio spectral index, α, is defined through $S_\nu \propto \nu^\alpha$ where S_ν represents the flux density at frequency ν.

2.2 Data

2.2.1 Radio Data

The COSMOS-XS survey consists of a single ultra-deep VLA pointing in the well-studied COSMOS field at both 3 and 10 GHz of ~ 100 and ~ 90 h of observation time, respectively. The full survey is described in detail in Paper I, but we summarize the key procedures and parameters here. The 3 GHz observations (also known as the S-band) were taken in B-array configuration, and span a total bandwidth of 2 GHz. The effective area of the pointing – measured up to 20 per cent of the peak primary beam sensitivity at the central frequency – is approximately 350 arcmin^2. The 10 GHz pointing (X-band) was taken in C-array configuration, and spans a frequency range of 4 GHz around the central frequency. The total survey area is approximately 30 arcmin^2 at 10 GHz. At both frequencies, roughly 20% of the bandwidth was lost due to excessive radio frequency interference.

Imaging of both datasets was performed using standalone imager WSclean (Offringa et al. 2014), incorporating $w-$stacking to account for the non-coplanarity of our baselines. Both images were created via Briggs weighting, with a robust parameter set to 0.5. This resulted in a synthesized beam of $2\farcs14 \times 1\farcs81$ at 3 GHz and $2\farcs33 \times 2\farcs01$ at 10 GHz. The near-equal resolution of $\sim 2\farcs0$ was chosen to be large enough to avoid resolving typical faint radio sources, which are generally sub-arcsecond in size at the μJy-level (Bondi et al. 2018; Cotton et al. 2018). In turn, this resolution allows for the cleanest measurement of their radio flux densities, while ensuring that confusion noise remains negligible (Paper I).

The final root-mean-square (RMS) noise levels of the S- and X-band images are 0.53 μJy beam^{-1} and 0.41 μJy beam^{-1} at their respective pointing centres. For the S-band, the RMS-noise corresponds to a brightness temperature of $T_B \simeq 20$ mK. This implies we are sensitive even to face-on star-forming spiral galaxies, which have a typical $T_B = 0.75 \pm 0.25$ K (Hummel 1981).

The locations of both the S- and X-band pointings within the COSMOS field are shown in Figure 2.1, and were explicitly chosen to match the pointing area of the COLDz survey (Pavesi et al. 2018; Riechers et al. 2019). A zoomed-in view of the radio maps themselves are presented in Paper I.

Source extraction on both images was performed with PyBDSF (Mohan & Rafferty 2015), down to a 5σ peak flux threshold. PyBDSF operates through identifying islands of contiguous emission around this peak value, and fitting such islands with elliptical Gaussians to obtain peak and inte-

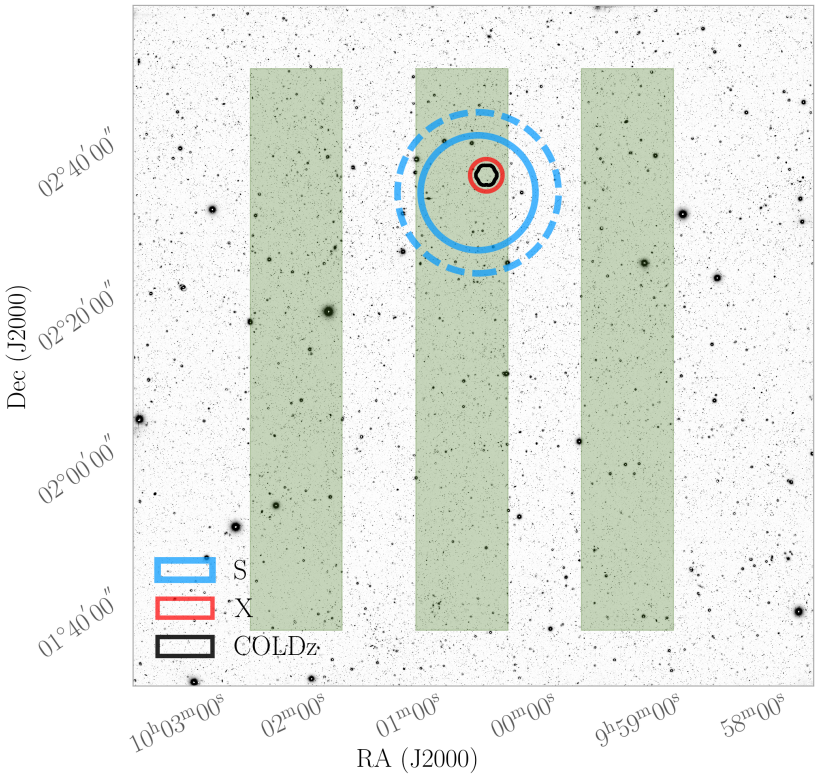

Figure 2.1: Layout of the S- (blue) and X-band (red) pointings, out to the half-power point of the primary beam (solid circles). For the S-band, we further highlight the field-of-view out to 20 per cent of the peak primary beam sensitivity (dashed circle), which defines our total survey area, over the two square degree COSMOS field. Also shown is the 34 GHz COLDz mosaic (Pavesi et al. 2018), which overlaps in its entirety with the X-band field of view. The background image consists of Subaru observations in the $i+$ filter, with the UltraVISTA ultra-deep stripes overlaid in green. For a zoomed-in view of the radio maps themselves, see van der Vlugt et al. (2021).

grated flux measurements. In total, we obtain 1498 distinct radio sources within 20% of the peak primary beam sensitivity, of which 70 ($\sim 5\%$) consist of multiple Gaussian components. While our survey is far from being confusion limited, a fraction of islands deemed robustly resolved in the source detection are in fact artificially extended as a result of source blending. In order to disentangle true extended sources from blended ones, we examined whether the Gaussian components making up an island can be individually cross-matched to separate sources in the recent Super-deblended catalog over COSMOS (Jin et al. 2018, see Section 2.2.2), which contains mid-IR to radio photometry based on positional priors from a combination of K_s, *Spitzer*/MIPS 24μm and VLA 1.4 and 3 GHz observations. As these radio data are both shallower and higher resolution than our observations, they are suitable for assessing any source blending. Furthermore, radio sources such as FR-II AGN (Fanaroff & Riley 1974) are not expected to have mid-IR counterparts for their individual lobes as these sources – by definition – have their radio emission spatially offset from the host galaxy. Hence, when all components can be individually associated to different multi-wavelength counterparts, we deem these associations robust, and define the Gaussian components to be separate radio sources. Altogether, we find that 40 of the initial 70 multi-Gaussian sources separate into 82 single 'deblended' components. In total, our radio survey therefore consists of 1540 individual sources detected at 3 GHz, within 20 per cent of the peak primary beam sensitivity. Altogether, this results in a $\sim 4\%$ increase in the number of radio sources that is cross-matched to a multi-wavelength counterpart (Section 2.3). This is the result of two effects: firstly, we find an overall larger number of radio sources now that blended ones have been separated, and secondly we find a larger fractional number of cross-matches, as blended sources were assigned a flux-weighted source center that could be substantially offset from the true centers of the individual Gaussian components, preventing reliable cross-matching. We note that this procedure slightly deviates from that in Paper I, where we focused instead on the radio properties of this sample and therefore refrained from invoking multi-wavelength cross-matching.

In addition to the 1540 S-band detections, a total of 90 sources are detected at 10 GHz within 20% of the maximum primary beam sensitivity at $\geqslant 5\sigma$ significance (948 and 60 sources lie within the half power point of the primary beam, respectively).[2] The S-band sample comprises the main

[2]With the adopted primary beam cut-off of 20%, the COSMOS-XS survey is deeper than the ($\sim 5\times$ shallower) 3 GHz VLA-COSMOS survey (Smolčić et al. 2017a,b) across the entire

radio sample used in the subsequent analysis described in this paper. We assign the radio sources detected at 3 GHz either their peak or integrated flux density, following the method from Bondi et al. (2008) described in detail in Paper I. We then ensure that we take the same flux density measurement for the X-band sources, as all sources detected at 10 GHz can be cross-matched to an S-band counterpart (Section 2.3) and the radio data have a similar resolution at both frequencies. In Paper I, we additionally investigated the completeness and reliability of the radio sample, for which we repeat the main conclusions here. We found that the catalogues are highly reliable with a low number of possible spurious detections ($\lesssim 2\%$). We further investigate possible spurious sources by visually inspecting all detections within $30''$ of a bright (SNR $\geqslant 200$) radio source. From these we flag, but do not remove, eight sources that are potentially spurious or have their fluxes affected as result of the characteristic VLA dirty beam pattern around the nearby bright object. The S-band sample was further determined to be $\gtrsim 90\%$ complete above integrated flux densities of $15\,\mu$Jy, with the completeness dropping to 50% at $\sim 10\,\mu$Jy due mainly to the primary beam attenuation reducing the survey area. In our derivation of the radio number counts for star-forming sources and AGN (Section 2.5) all of these completeness considerations are taken into account.

Additional radio data over our pointings exists as part of the 1.4 GHz VLA-COSMOS survey (Schinnerer et al. 2007, 2010), which reaches an RMS of $\sim 12\,\mu$Jy beam^{-1}. Accounting for the frequency difference through scaling with $\alpha = -0.70$, our S-band observations are a factor ~ 13 deeper than these lower frequency data, and hence the 1.4 GHz observations are mostly useful for the brightest sources detected at 3 and 10 GHz. Additionally, a seven-pointing mosaic at 34 GHz (RMS $\sim 1.4\mu$Jy beam^{-1}, area ~ 10arcmin^2) exists as part of the COLDz project (Pavesi et al. 2018; Riechers et al. 2019; Algera et al. in prep.). The COSMOS-XS 10 GHz data is directly centered on this mosaic, allowing for a detailed analysis of the long-wavelength spectrum of faint radio sources with up to four frequencies. We defer this analysis to a future paper.

2.2.2 Near-UV to far-IR data

The COSMOS field has been the target of a considerable number of studies spanning the full electromagnetic spectrum. We complement our radio observations with near-UV to FIR-data that has been compiled into vari-

field of view.

ous multi-wavelength catalogs: i) the Super-deblended mid- to far-infrared catalog (Jin et al. 2018) containing photometry ranging from IRAC 3.6μm to 20cm (1.4 GHz) radio observations; ii) the $z^{++}YJHK_s$-selected catalog compiled by Laigle et al. (2016) (hereafter COSMOS2015) and iii) the $i-$band selected catalog by Capak et al. (2007).

The Super-deblended catalog contains the latest MIR-radio photometry for nearly 200,000 sources in the COSMOS field, with 12,335 located within the COSMOS-XS field-of-view. Due to the relatively poor resolution of FIR telescopes such as *Herschel*, blending of sources introduces complications for accurate photometry. Through the use of priors on source positions from higher resolution images (*Spitzer*/MIPS 24μm and VLA 1.4 and 3 GHz observations) in combination with point spread function fitting, the contributions to the flux from various blended galaxies in a low-resolution image can be partly disentangled. This 'Super-deblending' procedure is described in detail in Liu et al. (2018). The Super-deblended catalog contains photometry from *Spitzer*/IRAC (Sanders et al. 2007) and *Spitzer*/MIPS 24μm (Le Floc'h et al. 2009) as part of the S-COSMOS survey, *Herschel*/PACS 100μm and 160μm data from the PEP (Lutz et al. 2011) and CANDELS-*Herschel* (PI: M. Dickinson) programs, *Herschel*/SPIRE images at $250, 350$ and 500μm as part of the HerMES survey (Oliver et al. 2012) and further FIR data at 850μm from SCUBA2 as part of the Cosmology Legacy Survey (Geach et al. 2017), AzTEC 1.1mm observations (Aretxaga et al. 2011) and MAMBO 1.2mm images (Bertoldi et al. 2007), in addition to 1.4 GHz and 3 GHz radio observations from Schinnerer et al. (2007, 2010) and Smolčić et al. (2017b), respectively. However, we use the photometry from catalogs provided directly by Schinnerer et al. (2007, 2010), as they provide both peak and integrated fluxes, whereas the Super-deblended catalog solely provides peak values. In addition, we use our ~ 5 times deeper COSMOS-XS 3 GHz observations described in Section 2.2.1 in favor of those from Smolčić et al. (2017b).

The Super-deblended catalog further includes photometric and spectroscopic redshifts, based on the Laigle et al. (2016) catalog where available, in addition to IR-derived photometric redshifts and star-formation rates.[3]

Since a shallower radio catalog was used for the deblending procedure,

[3]We do not use FIR-derived photometric redshifts in this work, as these values are considerably more uncertain than those derived from near-UV to near-IR photometry (e.g. Simpson et al. 2014), but we comment on the small sample of sources with only FIR photometric redshifts in Section 2.5.3.

this raises the concern that one of the VLA-COSMOS priors for the Super-deblended catalog is, in fact, located near a fainter radio source detected only in COSMOS-XS that contributes partially to the FIR flux at that location. In such a scenario, all the FIR emission would be wrongfully assigned to the brighter radio source, which would have an artificially boosted flux, and the fainter source may be wrongfully assigned no FIR-counterpart. We verified, however, that this is not likely to be an issue, as we see no drop in the fraction of cross-matches between COSMOS-XS and the Super-deblended catalog for radio sources with a nearby neighbor in COSMOS-XS. Hence there is no indication of any boosting in the FIR-fluxes of Super-deblended entries due to a nearby, faint radio source.

The COSMOS2015 catalog contains photometry for upwards of half a million entries over the 2 square-degree COSMOS field, including 37,841 within the COSMOS-XS field-of-view. Sources are drawn from a combined $z^{++}YJHK_s$ detection image, where the deep $YJHK_s$ observations are taken from the second UltraVISTA data release (McCracken et al. 2012). The COSMOS-XS S-band pointing is largely located within one of the UltraVISTA 'ultra-deep' stripes (Figure 2.1), which reaches a 3σ depth in magnitude of $25.8, 25.4, 25.0, 25.2$ in Y, J, H and K_s respectively, as measured in $3''$ apertures. The COSMOS2015 catalog further provides cross-matches with NUV, and MIR/FIR data. The former consists of *GALEX* observations at 1500 Å (FUV) and 2500 Å (NUV) (Zamojski et al. 2007), and the latter ranges from *Spitzer*/MIPS 24μm to *Herschel*/SPIRE 500μm photometry, drawn from the same programs as introduced for the Super-deblended catalog. In addition, photometric redshifts, star-formation rates and stellar masses are provided by COSMOS2015, derived through SED-fitting by LePhare (Ilbert et al. 2006), using photometry spanning the NUV - K_s bands.

Finally, the $i-$band selected catalog compiles photometry from 15 photometric bands between the u-band (0.3μm) and the 2.5μm K_s-band. The 5σ depth in the $i-$band equals 26.2 as determined within a $3''$ aperture. Photometric redshifts were derived from SED fitting with LePhare and were later added to the catalog by Ilbert et al. (2009).

2.2.3 Spectroscopic Redshifts

A substantial fraction of galaxies in the COSMOS field have been targeted spectroscopically, and therefore have a robustly determined redshift. We make use of the 'master spectroscopic redshift catalog' available internally to the COSMOS team (version 01 Sept. 2017, M. Salvato in prep.). It con-

tains ∼100,000 entries, compiled from a large number of spectroscopic surveys over the COSMOS field, including zCOSMOS (Lilly et al. 2007, 2009), the VIMOS Ultra Deep Survey (VUDS; Le Fèvre et al. 2015) and MOSDEF (Kriek et al. 2015). In total, there are 5,074 sources with reliable spectroscopic redshifts in the COSMOS-XS field-of-view (see also Section 2.3.3).

2.2.4 X-ray data

Strong X-ray emission is a vital diagnostic for AGN activity. The most recent X-ray data over the COSMOS field is the 4.6 Ms *Chandra* COSMOS Legacy survey (Civano et al. 2016), covering the full 2.2 deg^2. Marchesi et al. (2016a) present the catalog of the optical and infrared counterparts of the X-ray sources identified by the survey. This catalog includes 200 sources within our S-band field of view, and contains for each the absorption-corrected luminosity in the soft $[0.5-2]$ keV, hard $[2-10]$ keV and full $[0.5-10]$ keV bands, or the corresponding upper limit in the case of a non-detection in a given energy band.[4] Where available, X-ray sources in this catalog were assigned the spectroscopic redshift of their counterparts, taken from the COSMOS master spectroscopic catalog. For the remaining sources, photometric redshifts exist, based on template fitting making use of AGN-specific templates as described in Salvato et al. (2011). X-ray luminosities were calculated by using the best available redshift and an X-ray spectral index of $\Gamma = 1.4$ for the required $K-$corrections, which is a typical value for a mix of obscured and onobscured sources (Marchesi et al. 2016b). Absorption corrections to the X-ray luminosity in each energy band were calculated based on the measured hardness ratio, as described in Civano et al. (2016).

2.3 Multi-Wavelength Cross-Matching

In this section, we elaborate on our multi-wavelength matching process. As a brief summary of the procedure, we cross-match catalogs based on a symmetric nearest neighbour algorithm, whereby we search for counterparts within a given matching radius. A suitable value of this radius is determined through cross-matching with a mock version of the appropriate catalog, which contains the same sources with randomized sky coordinates.

[4] The flux limit of the *Chandra* COSMOS Legacy Survey over the COSMOS-XS S-band pointing is $\sim 2 \times 10^{-15}$ erg cm^{-2} s^{-1} in the full $2-10$ keV range (Civano et al. 2016).

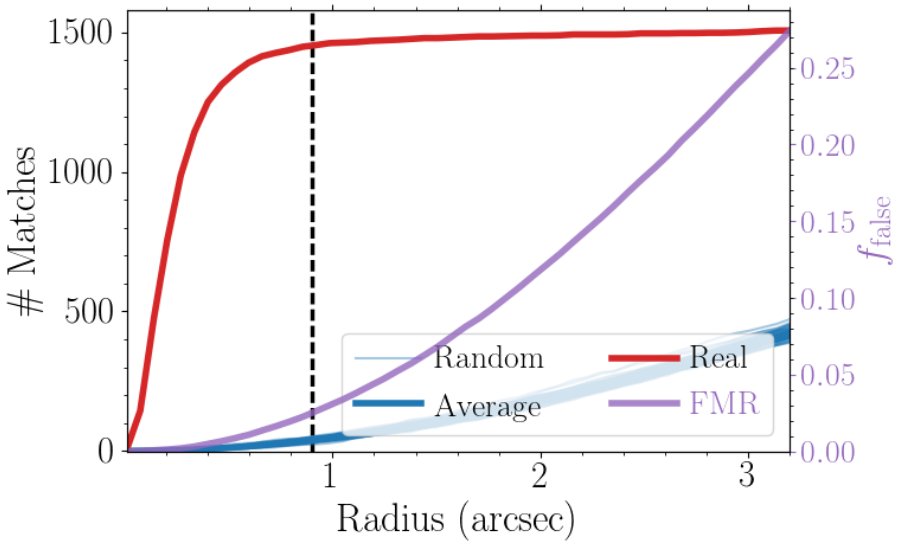

Figure 2.2: Illustration of the cross-matching process, for the radio and Super-deblended catalogs. The red line represents the number of matches obtained within a given matching radius, whereas the blue lines show the number of matches obtained when cross-matching with a catalog with the same source density but randomized sky positions. The purple curve, corresponding to the right ordinate axis, shows the false match fraction obtained at a given matching radius. The vertical black line indicates the typical matching radius of $0\farcs9$ adopted in this work.

As our radio images are not uniformly sensitive across their full field of view as result of the primary beam, we ensure mock sources can only be placed in the region where they can theoretically be detected at $\geqslant 5\sigma$, to mimic the true distribution of sources. Through cross-matching with such mock catalogs, we obtain an estimate of the number of false matches at any given matching radius, and we hence define the false matching rate (FMR) as the average number of cross-matches obtained with the randomized catalogs divided by the total number of catalog entries. The matching radius we adopt is taken to be the radius where the number of matches for the real and mock catalogs is (approximately) equal, which is generally around $0\farcs9$, and coincides with a typical FMR $\lesssim 3\%$ for all our multi-wavelength cross-matching.

2.3.1 Radio Cross-Matching

There are a total of 1540 and 90 radio sources within 20% of the peak primary beam sensitivity for the S- and X-band, respectively. We cross-match these two frequencies using a matching radius of $0\farcs9$, which yields 89 matches (FMR $\lesssim 0.7\%$). The single X-band source that could not be cross-matched to a counterpart at 3 GHz appears to be a lobed radio source where the relative brightness of the two lobes is different in the two images, causing the centre of the source to be appreciably offset between the two images ($\sim 1\farcs25$). Despite this offset, visual inspection verifies that the sources are related, such that all X-band sources are assigned a counterpart at 3 GHz. Due to the relatively low density of radio sources in the VLA COSMOS 1.4 GHz catalog, we utilize a matching radius of $1\farcs2$ when cross-matching with the S-band data (FMR $\lesssim 0.1\%$). This generates 185 matches, with 12 sources being detected at all three frequencies (1.4, 3 and 10 GHz).

2.3.2 Additional Cross-Matching

In order to construct UV/optical – FIR SEDs for the S-band detected sources, we cross-match with three catalogs in order of decreasing priority: Super-deblended (Jin et al. 2018), COSMOS2015 (Laigle et al. 2016) and the $i-$band selected catalog by Capak et al. (2007). The Super-deblended catalog contains the most up-to-date collection of FIR-photometry available over the COSMOS field, but does not include optical and near-IR photometry shortwards of IRAC 3.6μm. We therefore attempt to cross-match S-band sources that have Super-deblended counterparts with either COSMOS2015 or the $i-$band selected catalog, which do contain photometry at these shorter wavelengths.

An overview of the matching process is presented in the form of a flowchart in Figure 2.3. In summary, the procedure is as follows: we first cross-match the S-band selected catalog of 1540 sources with the Super-deblended photometric catalog, obtaining 1454 matches within $0\farcs9$ (FMR $\simeq 2.5\%$, see Figure 2.2). To obtain optical and near-IR photometry, we subsequently cross-match with the COSMOS2015 catalog. As a result of the larger source density compared to the Super-deblended catalog, we use a matching radius of $0\farcs7$ instead of $0\farcs9$ around the radio coordinates, motivated by the number of false matches obtained at larger radii. The theoretical FMR at $0\farcs7$ equals $\sim 4.8\%$, which is substantial. To account for both this and the difference in matching radii between the different catalogs, which may lead to inconsistencies in the overall cross-matching process

where we artificially cannot assign our sources COSMOS2015 counterparts if their offset from the radio coordinates falls into the range $0\farcs7 < r < 0\farcs9$, we therefore also utilize the Super-deblended source coordinates. As these are based in part on IR-detections, they are typically more similar to the near-IR derived COSMOS2015 coordinates. We therefore perform additional cross-matching within $0\farcs2$ around these Super-deblended source positions – since such closely associated sources are likely to be real (FMR $\lesssim 0.4\%$) – under the constraint that the offset between any of the catalog is less than $0\farcs9$. We then acquire 1372 sources with both Super-deblended and COSMOS2015 photometry, which spans the full near-UV to millimetre range. Only 25 of these cross-matches (1.8%) have COSMOS2015 - Super-deblended separations $\geqslant 0\farcs2$, but as the median separation between the radio and Super-deblended coordinates remains small ($\sim 0\farcs3$), we expect a negligible increase in the overall FMR after cross-matching with the COSMOS2015 catalog. We additionally have 82 sources with Super-deblended cross-matches for which we did not obtain COSMOS2015 counterparts. As these sources will greatly benefit from shorter wavelength data in our subsequent analysis, we cross-match them with the i-band selected catalog within $0\farcs9$ and recover an additional 29 matches.[5] We thus obtain full near-UV to radio photometry for 96.4% of sources cross-matched with the Super-deblended catalog.

For the 86 (5.6%) of radio-detected sources for which we could not acquire robust Super-deblended counterparts, we first cross-match with the COSMOS2015 catalog within $0\farcs7$, gaining 12 matches (4 expected false matches). For the remaining sources, we obtain 4 matches with the i-band catalog within $0\farcs9$, containing photometry up to the K_s-band (with 1 expected false match). Overall, we did not obtain any non-radio counterparts for 70/1540 sources (4.5%). Two of these are detected at multiple radio frequencies and are therefore certainly real. Upon cross-matching with the S-COSMOS IRAC catalog from Sanders et al. (2007), we recover 18 additional matches within $0\farcs9$, which further indicates that a substantial number of this sample consists of real radio sources that evade detection at shorter wavelengths. However, as these cross-matches therefore solely have IRAC photometry, they lack redshift information, which is crucial for subsequent AGN identification (Section 2.4). Therefore, we do not further include these sources in the characterization of our radio sample, though

[5]The formal cross-matching radius adopted is $0\farcs9$ for consistency with other catalogs, but all matches lie within $0\farcs5$ of both the Super-deblended and radio sky positions, and as such we estimate the FMR to be $\lesssim 1\%$.

we return to these 'optically dark' detections in Section 2.5.3. When accounting for these additional 18 matches with S-COSMOS, 96.6% of our radio sample can be cross-matched to a non-radio counterpart.

As reliable redshift information is crucial for investigating the physical properties of our radio-detected sources, we further remove 33 galaxies from our sample for which no redshift information was available in any of the catalogs. The majority of these sources are only present in the Super-deblended catalog, and were detected through priors from the 3 GHz VLA COSMOS project (Smolčić et al. 2017b). As for these sources no photometry exists shortwards of MIPS 24μm, no reliable photometric redshift can be obtained. Altogether, we are left with a remainder of 1437 sources (93.3% of the initial 1540 detections at 3 GHz). This constitutes the S-band detected sample that will be used in the subsequent analysis.

We additionally recover 108 cross-matches with X-ray sources taken from the *Chandra* COSMOS Legacy survey (Civano et al. 2016; Marchesi et al. 2016a) based on an adopted cross-matching radius of $1\farcs4$ (theoretical FMR $\simeq 0.1\%$).[6] The 108 X-ray counterparts for the radio sample correspond to $\sim 51\%$ of the X-ray sources within the COSMOS-XS field of view. This is larger than the 32% found for the 3 GHz VLA-COSMOS survey (Delvecchio et al. 2017), which is consistent with the fact that nearly one third of the radio counterparts we associate to X-ray sources lie below the theoretical $5\sigma_{\rm rms} \simeq 11.5\mu$Jy detection limit of that survey.

Overall, we expect a false matching rate of $\lesssim 3\%$ (~ 40 sources, which includes 4 sources flagged as 'potentially spurious' in Section 2.2.1), based on the combined FMRs from the cross-matching of the individual catalogs, as well as a spurious fraction of $\lesssim 2\%$. We hence deem our multi-wavelength catalog to be reliable.

2.3.3 Redshifts of the Radio Sample

Accurate redshift information for our radio sample is vital not only for the classification of AGN, but also for subsequent studies of the star-formation history of the universe. We therefore attempted to assign to each source its most reliable redshift through comparing the various redshifts (photometric or spectroscopic) we obtained from the different catalogs. First of all, we discarded all spectroscopic redshifts from the COSMOS master catalog (M. Salvato in prep.) that have a quality factor $Q_f < 3$, indicating an un-

[6] We adopted a cross-matching radius of $1\farcs4$ as *Chandra* astrometry is accurate to 99% within this radius, see `http://cxc.harvard.edu/cal/ASPECT/celmon/`.

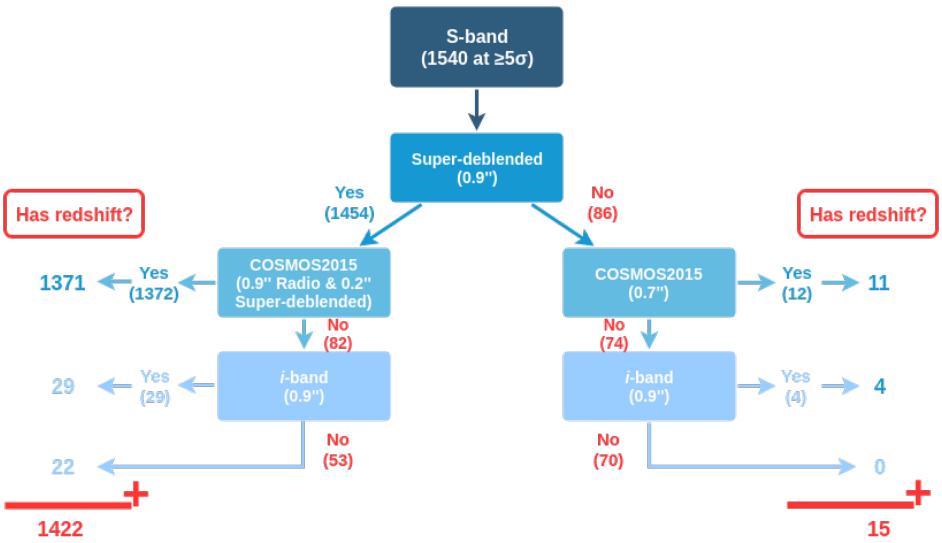

Figure 2.3: Flowchart of the matching process, indicating the priority of catalogs used and number of cross-matches obtained with each. We match a total of 1470/1540 sources (95.5%) to a counterpart in at least one multi-wavelength catalog. From this sample, we keep 1437 sources (93.3%) with reliable redshift information. This represents the main radio sample studied in this work.

certain or poor spectroscopic redshift. All remaining sources for which a robust spectroscopic redshift is available are then assigned this value. The majority of sources additionally have photometrically determined redshifts available, from up to three different studies (e.g. Capak et al. 2007; Laigle et al. 2016; Jin et al. 2018). We prioritize the photometric redshift from the Super-deblended catalog if available, as it is determined using prior photometric redshift information from other catalogs (e.g. COSMOS2015), but is re-computed with the inclusion of longer-wavelength data. However, any differences between these photometric redshifts are small by construction, as Jin et al. (2018) force the Super-deblended redshift to be within 10% of the prior value. If a Super-deblended redshift is unavailable, we instead use the photometric redshift from COSMOS2015 or the $i-$band selected catalog, in that order. We make an exception when the source is X-ray detected, in which case we assign it the photometric redshift from the *Chandra* X-ray catalog (Marchesi et al. 2016a). These redshifts have been determined through SED fitting with the inclusion of AGN templates, and are therefore more appropriate for AGN, which form the bulk of our X-ray detected

sample (Section 2.4.1).

We compute the reliability of our redshifts, defined as $\sigma(z) = |z_{\rm spec} - z_{\rm phot}|/(1+z_{\rm spec})$ for the 584 sources which have both photometric and spectroscopic redshift information available. The normalized median absolute deviation (Hoaglin et al. 1983), defined as 1.48 times the median of $\sigma(z)$, is found to be 0.012, indicating a very good overall consistency between the two redshifts. The fraction of sources with $\sigma(z) > 0.15$, the common threshold for defining 'catastrophic failures', equals 4.8 per cent, with the main region of such failures being the optically fainter sources, as expected. We verified that the distribution of such failures in terms of $i-$band magnitude is similar to that in Figure 11 of Laigle et al. (2016), though with a slightly larger failure fraction at fainter magnitudes $i_{\rm AB} \gtrsim 23$, which can be fully explained by our small sample size at these magnitudes.[7]

In summary, our sample contains 584 sources ($\sim$ 41%) with spectroscopic and 853 sources with photometric redshifts (Figure 2.4). About two-thirds of our $z \lesssim 1$ sample is detected spectroscopically, but the fraction of spectroscopic redshifts drops dramatically towards higher redshift. Additionally, a total of 103 sources have no redshift information. The majority of these (70 sources) were not cross-matched to any multi-wavelength counterpart. Only two sources without redshift information have optical/near-IR photometry, but nevertheless no robust photometric redshift could be obtained for these catalog entries. The median radio flux density (and bootstrapped uncertainty) of the sources without redshift information is $S_{3\,\rm GHz} = 10.5^{+2.0}_{-1.2}\,\mu$Jy, similar to the median of the full sample, which equals $S_{3\,\rm GHz} = 11.3^{+0.4}_{-0.5}\,\mu$Jy. The median flux density of the radio sources detected only in COSMOS-XS, i.e. without cross-matches to the Super-deblended or VLA-COSMOS catalogs, equals $7.2^{+1.4}_{-0.7}\,\mu$Jy – below the formal detection limit of the latter survey, as expected.

We show the detection limit of the COSMOS-XS survey as function of redshift in Figure 2.5. For ease of comparison with previous surveys, which have predominantly been performed at lower frequencies, we show the distribution of rest-frame 1.4 GHz luminosities, computed using a standard spectral index of $\alpha = -0.7$ even where multiple radio fluxes were available (see Section 2.4.2). These luminosities are converted into star-formation rates adopting the conversion from Bell (2003) under the assumption that

[7]While most of our photometric redshifts are from the Super-deblended catalog, and not from COSMOS2015, the former are by construction similar to the redshift adopted for the deblending prior, and as such comparing our photometric redshift accuracy with Laigle et al. (2016) is justified.

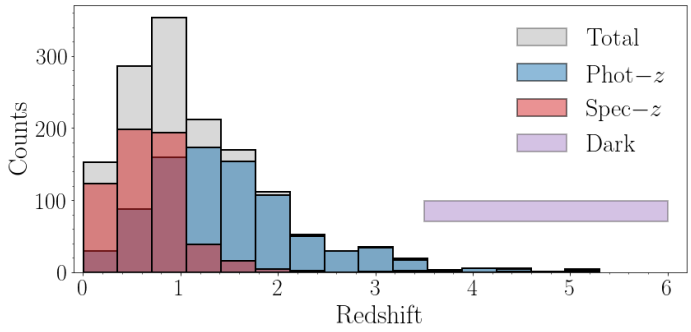

Figure 2.4: Distribution of the radio-selected sample in redshift, for all 1437 sources with redshift information. Red and blue bars indicate spectroscopic and photometric redshifts respectively, and the grey histogram represents the full distribution. We additionally show the expected redshift range populated by the 29 'optically dark' sources – sources without optical counterparts and redshift information, analyzed in Section 2.5.3 – via the purple bar. Out to $z \sim 1$, nearly two-thirds of our redshifts are spectroscopic.

the radio emission is fully powered by star formation. In the following section, we will instead adopt a redshift-dependent conversion factor, as it has recently been shown to evolve with cosmic time (Magnelli et al. 2015; Delhaize et al. 2017; Calistro Rivera et al. 2017).

Finally, in Figure 2.6, we show the overall counterpart completeness of the 1540 S-band sources in twelve flux density bins. Uncertainties on the counting statistics were calculated following Gehrels (1986) for bins with fewer than 10 sources without optical counterparts, and were assumed to be Poissonian otherwise. We adopt these confidence limits for sparsely populated bins throughout this work. The completeness in all bins is upwards of 90%, and no trend with radio flux density can be seen, indicating that the association of counterparts to our radio sources is not limited by the depth of the multi-wavelength photometry. Additionally, this indicates that it is unlikely that there are a substantial number of spurious radio sources within our 3 GHz image, as these would likely populate the low flux density bins and would typically not be associated to a multi-wavelength counterpart. Despite the lack of multi-wavelength counterparts for $\sim 4.5\%$ of radio sources, a substantial fraction of these are simply faint at optical/near-infrared wavelengths, and as such are not spurious (see the discussion in Section 2.5.3).

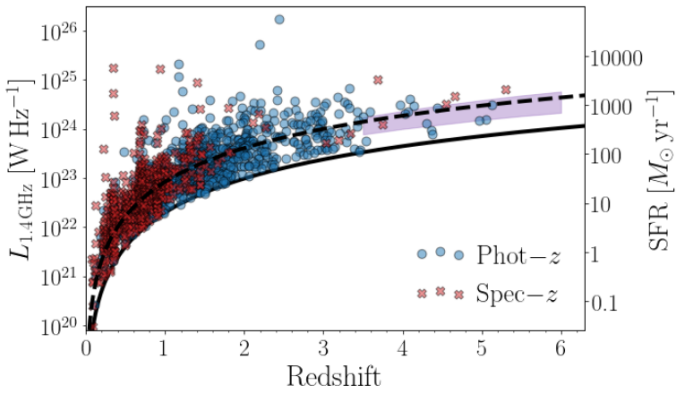

Figure 2.5: Rest-frame 1.4 GHz luminosity versus redshift for the COSMOS-XS 3 GHz-detected sample with reliable redshift information. The flux limit of the survey is indicated through the solid black line. Blue circles and red crosses indicate photometric and spectroscopic redshifts, respectively. The dashed, black line represents the flux limit of the 3 GHz VLA-COSMOS survey (Smolčić et al. 2017b) and is included for comparison. The COSMOS-XS survey constitutes a factor ~ 5 increase in sensitivity compared to these wider radio data. We additionally show the redshift and luminosity range likely populated by the radio-detected sources without optical/near-IR photometry through the shaded purple area (Section 2.5.3). Star-formation rates (right ordinate axis) are computed assuming the radio emission is fully powered by star formation, and adopting a conversion that is independent of redshift, based on the local galaxy sample studied by Bell (2003); see also Section 2.4.2. Radio luminosities are converted to rest-frame 1.4 GHz using a fixed spectral index $\alpha = -0.70$. The theoretical detection limit (solid black line) is computed using 5 times the RMS in the S-band image centre and scaled to 1.4 GHz rest-frame using an identical spectral index.

2.4 AGN Identification

In this section, we outline the criteria used for identifying AGN among our radio-detected sources, making use of the wealth of data available over the COSMOS field. In the literature, numerous such multi-wavelength identifiers exist, based on both broad-band photometry and spectroscopy. In order to avoid potential biases due to incomplete coverage in various bands, we only utilize AGN diagnostics which are available for the vast majority of our radio-selected sample, which are outlined below. This excludes such diagnostics as inverted radio spectral indices (e.g. Nagar et al. 2000), very long baseline interferometry (e.g. Herrera Ruiz et al. 2017) and optical spectra (e.g. Baldwin et al. 1981).[8]

[8]Radio spectral indices are available for 255 sources ($\sim 18\%$ of the sample with redshift information). Eight of these have inverted spectral indices (7 from 1.4 - 3 GHz data, and a

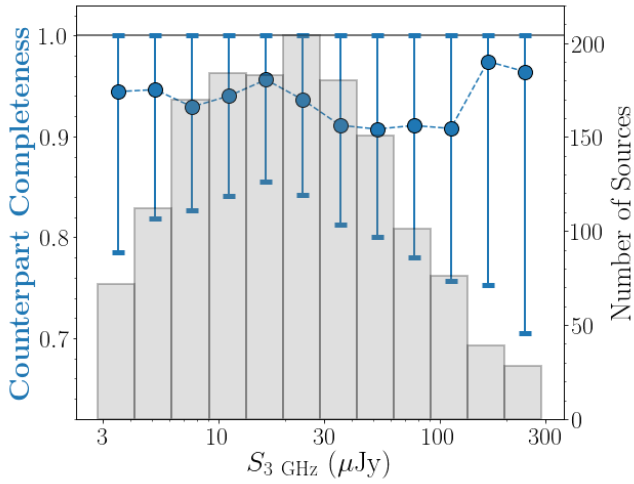

Figure 2.6: Counterpart completeness as a function of flux density for the S-band sample (left ordinate axis). Our S-band selected catalog contains counterparts with reliable redshifts for 93.3% of all S-band detected sources, and all flux density bins are $\gtrsim 90\%$ complete. No clear trend with flux density is seen, making it unlikely that a substantial number of low-SNR S-band sources are spurious, as for these no counterpart would be expected. The background histogram and corresponding right ordinate axis indicate the total number of sources in a given flux density bin.

In our panchromatic approach to AGN identification, we make use of SED fitting code magphys (da Cunha et al. 2008, 2015) to model the physical parameters of our galaxy sample. magphys imposes an energy balance between the stellar emission and absorption by dust, and is therefore well-suited to model the dusty star-forming populations to which radio observations are sensitive. We stress that magphys does not include AGN templates, and is therefore only suitable for modelling sources whose SEDs are dominated by star-formation related emission. However, we can use this to our advantage when identifying AGN based on their radio emission in Section 2.4.2. Additionally, we use AGNfitter (Calistro Rivera et al. 2016, 2017), a different SED-fitting routine appropriate for AGN, in Section 2.4.1 to further mitigate this issue. We fit our full radio sample with magphys, including all FUV to mm data. The radio data is not fitted, as an excess in radio emission is indicative of AGN activity and could therefore bias our

single source detected at 3 and 10 GHz), though seven were previously identified as AGN through other multi-wavelength diagnostics. The inclusion of an inverted spectral index as AGN diagnostic will therefore have a negligible effect on the overall AGN identification.

results (Section 2.4.2).

We will follow the terminology introduced in Delvecchio et al. (2017) and Smolčić et al. (2017a), and divide the radio-detected AGN into two classes: the moderate-to-high luminosity AGN (HLAGN) and low-to-moderate luminosity AGN (MLAGN). These definitions refer to the radiative luminosity of AGN, resulting from accretion onto the supermassive black hole, which traces the overall accretion rate.[9] For efficiently accreting AGN ($\dot{m} \gtrsim 0.01\ \dot{m}_{\rm Edd}$, where $\dot{m}$ is the mass accretion rate and $\dot{m}_{\rm Edd}$ the Eddington rate), the bulk of the radiative luminosity is emitted by the accretion disk (UV) as well as in X-rays (Lusso et al. 2011; Fanali et al. 2013). Depending on both the orientation and the optical depth of the obscuring torus, this radiation may be (partially) attenuated and re-emitted in the mid-infrared (e.g., Ogle et al. 2006). X-ray and MIR-based tracers of AGN activity therefore preferentially select high radiative luminosity AGN, and hence imply higher overall accretion rates. Conversely, low accretion rates ($\dot{m} \ll 0.01\ \dot{m}_{\rm Edd}$) are associated with radiatively inefficient accretion, whereby the accretion disk is generally truncated and advection-dominated accretion takes over in the vicinity of the black hole (e.g. Heckman & Best 2014). As the timescale of such inflows is much shorter than the cooling time of the material, such ineffecient accretion produces little UV and X-ray emission. A recent study by Delvecchio et al. (2018), employing X-ray stacking on the 3 GHz-selected radio-excess AGN sample from VLA-COSMOS, indeed finds that below $z \lesssim 2$ the accretion rates of such AGN are $\dot{m} \lesssim 0.01\ \dot{m}_{\rm Edd}$, with only 16% of this sample being individually X-ray detected, implying overall inefficient accretion for the typical radio-excess AGN. They additionally do not find any correlation between AGN X-ray and radio luminosity at a fixed redshift. Instead, the identification of AGN with lower accretion rates and radiative luminosities, referred to here as MLAGN, thus relies predominantly on radio-based diagnostics. These are effectively based on the fact that, for such AGN, the multi-wavelength star-formation rate indicators are discrepant, as will be clarified in Section 2.4.2. It must be noted, however, that a hard division between high- and moderate-luminosity AGN does not exist, and we therefore follow Delvecchio et al. (2017) by applying the tags 'moderate-to-high' and 'low-to-moderate' to indicate the overlap between the classes. This further serves to illustrate that there is no one-to-one relation between the class an AGN belongs to and its accretion rate. We will study the various sets of AGN in

[9] Delvecchio et al. (2017) further argue that the HLAGN/MLAGN definitions closely resemble the widely used HERG/LERG nomenclature.

more detail in a future paper, and instead focus on the classification in this work.

2.4.1 HLAGN

In the context of this paper, we identify a source as an HLAGN if it satisfies any of the following criteria:

- The source shows a $\geqslant 2\sigma$ excess in X-ray luminosity compared to its FIR-derived star-formation rate, based on the relations from Symeonidis et al. (2014).
- The source exhibits mid-IR IRAC colors that place it within the Donley et al. (2012) wedge, provided it lies at $z \leqslant 2.7$.
- The source shows a significant AGN-component in the form of a dusty torus or accretion disk, based on SED fitting.

We expand on each of these criteria in the following subsections.

X-ray AGN

A subset of HLAGN are characterized by a high X-ray luminosity, which is thought to originate from the accretion disk around the central supermassive black hole (SMBH). In the conventional picture (Heckman & Best 2014), this disk is surrounded by a hot corona, which boosts the energy of the seed photons from the accretion process through inverse Compton scattering into the X-ray regime. The accretion disk is further thought to be obscured by a dusty torus, which – if sufficiently dense – may absorb even the hard X-rays produced by the AGN. Nevertheless, in the scenario of low obscuration, AGN-powered X-ray emission can be orders of magnitude brighter than X-rays expected from star-formation related processes, which arise primarily from high-mass X-ray binaries (Fabbiano 2006). In order to classify our X-ray detected sources as AGN, we make use of the X-ray properties of star-forming galaxies derived by Symeonidis et al. (2014). They found that typical SFGs have a relation between their FIR-luminosity and soft band ($[0.5-2]$ keV) X-ray luminosity given by $\log L_{\mathrm{FIR}} = \log L_{[0.5\text{-}2]} + 4.55$, with a 2σ scatter around this relation of 0.74 dex. We classify sources with an X-ray excess above this 2σ scatter as HLAGN.

For the AGN classification we extract $[0.5-10]$ keV obscuration-corrected X-ray luminosities from the *Chandra* COSMOS Legacy catalog presented

in Marchesi et al. (2016a).[10] We scale X-ray luminosities between different bands with a power law index of $\Gamma = 1.4$, defined such that the X-ray luminosity follows $L_X \propto \nu^{1-\Gamma}$. In the following, we will quote X-ray luminosities in the $[0.5-8]$ keV range. Out of the 108 cross-matches we obtained within $1\farcs4$ with this catalog, we identify 106 sources as X-ray AGN.[11] Had we adopted a fixed X-ray luminosity threshold of $L_{\rm X} = 10^{42}$ erg s^{-1}, as is common in the literature (e.g. Wang et al. 2013; Delvecchio et al. 2017; Smolčić et al. 2017a), we would have missed an additional 7 X-ray sources at low redshift that are only modestly X-ray luminous, but are nonetheless substantially offset from the relations from Symeonidis et al. (2014). Our main motivation for adopting a threshold dependent on $L_{\rm FIR}$ is however to avoid the misclassification of highly starbursting sources, as SFRs upwards of $\sim 300\ M_\odot$ yr^{-1} are expected to generate X-ray luminosities in excess of $L_{\rm X} \sim 10^{42}$ erg s^{-1}. We therefore regard a selection based on the comparison of FIR- and X-ray luminosities to be more robust in general. Based on the discussion in Appendix 2.C.1, where we employ X-ray stacking, we further conclude that we are minimally affected by incompleteness issues, which may arise from the relatively shallow X-ray data, resulting in rather unconstraining upper limits on the X-ray luminosities of the typical high-redshift ($z \gtrsim 2$) source.

MIR AGN

Sources that fall within the class of high-luminosity AGN are believed to be surrounded by a warm, dusty torus, which will absorb and re-radiate emission emanating from the region around the central SMBH. This gives rise to a specific MIR-continuum signature associated to predominantly dusty and obscured AGN. Early work in the identification of AGN based on MIR-colors was done by Lacy et al. (2004), based mostly on the *Spitzer*/IRAC colors of local Seyfert galaxies. Due to intrinsic reddening of high-redshift sources, these criteria are not optimized for galaxies at moderate redshift ($z \gtrsim 0.5$), and we therefore use the adapted criteria from Donley et al. (2012) to identify obscured HLAGN. We locate sources within the Donley et al. (2012) wedge, defined through their equations (1) and (2) and iden-

[10] In case an X-ray source was assigned a different redshift than given in the *Chandra* catalog, we re-computed its X-ray luminosity using the updated value.

[11] Upon adopting a steeper X-ray photon index of $\Gamma = 1.7$, as may be more appropriate for star-forming galaxies (e.g. Lehmer et al. 2010), we instead identify one additional X-ray AGN. However, including this additional source as an X-ray AGN has no impact on our overall conclusions.

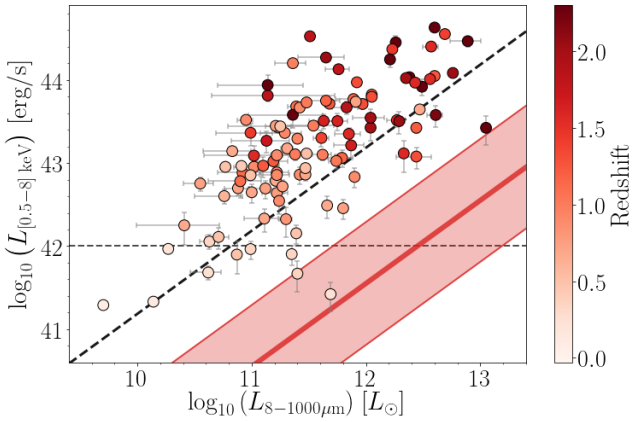

Figure 2.7: X-ray luminosity in the $[0.5-8]$ keV energy band versus total infrared ($8-1000\mu$m) luminosity for our X-ray detected sample, color-coded by redshift. The solid diagonal line represents the X-ray versus total-infrared luminosity relations for star-forming sources from Symeonidis et al. (2014), scaled to a full $[0.5-8]$ keV using a power law exponent $\Gamma = 1.4$. The red, shaded region indicates the 2σ scatter around this relation (equivalent to 0.74 dex). All soures that fall outside of this scatter are identified as X-ray AGN in this work. The diagonal, black line is shown for comparison and represents the AGN luminosity threshold from Alexander et al. (2005), which is more conservative in identifying X-ray AGN than the threshold we adopt here. The dashed, horizontal line indicates a constant X-ray luminosity threshold of 10^{42} erg s^{-1}, which is a typically used threshold for identifying AGN in the literature at low redshift. All but two of our X-ray detected sources are substantially offset from the Symeonidis et al. (2014) relations, including 7 low-redshift sources with $L_X \lesssim 10^{42}$ erg/s.

tify such sources as MIR AGN. As the MIR-colors of dusty star-forming galaxies at high redshift ($z \gtrsim 3$) closely resemble those of obscured AGN (e.g. Stach et al. 2019), we restrict our analysis to $z \leqslant 2.7$, as Donley et al. (2012) are increasingly biased above this redshift. We note these MIR-criteria are somewhat conservative in order to minimize the occurrence of false positives, and the MIR-identification becomes less complete for X-ray faint AGN. Overall, we recover 28 AGN based on their *Spitzer*/IRAC colors. While only $\sim 60\%$ of our sample has reliable IRAC photometry in all four channels, and hence we cannot robustly place the remaining sources within the Donley et al. (2012) wedge, this incompleteness has negligible effect on our overall AGN identification (Appendix 2.C.1).

AGN SED-fitting

HLAGN are expected to show a composite multi-wavelength SED, exhibiting signs of both star-formation and AGN-related processes. A spectral decomposition will therefore detail the relative contribution of these two components, allowing AGN to be identified as such if their emission dominates over the contribution from star formation at certain wavelengths. We use AGNfitter (Calistro Rivera et al. 2016) to fit the far-UV to FIR SEDs of our radio-selected sample. AGNfitter is a publicly available python-based SED-fitting algorithm implementing a Bayesian Markov Chain Monte Carlo method to fit templates of star-forming and AGN components to observed multi-wavelength galaxy photometry. Two such AGN components are fitted: an accretion disk, which predominantly emits at UV- and optical wavelengths, and a warm, dusty torus that contributes mostly to the MIR continuum. The SED-fitting further includes UV/optical emission from direct starlight, as well as dust-attenuated stellar emission in the infrared.

As AGNfitter utilizes a Monte Carlo method in its SED-fitting procedure, its output includes realistic uncertainties on any of its computed parameters, such as the integrated luminosities in the various stellar and AGN components. These uncertainties are particularly informative for galaxies with no or little FIR-photometry, as in this case the long-wavelength SED is largely unconstrained. This is in contrast to SED fitting codes that impose energy balance between the stellar and dust components, such as magphys (da Cunha et al. 2008, 2015) and sed3fit (Berta et al. 2013) which is built upon the former and extended to include AGN templates. We opt for a Bayesian algorithm without energy balance, as it has been shown that dust and stellar emission can be spatially offset in high-redshift dusty galaxies such that imposing energy balance may be inaccurate (e.g. Hodge et al. 2016). In addition, it allows for the comparison of realistic probability distributions for the integrated luminosities of the various galaxy and AGN components, enabling us to separate the populations based on physical properties, rather than based on the goodness of fit. We compare our results with those obtained with sed3fit by Smolčić et al. (2017a) in Appendix 2.B.2.

Prior to the fitting, we account for uncertain photometric zeropoint offsets and further potential systematic uncertainties by adding a relative error of 5% in quadrature to the original error on all photometric bands between U and MIPS 24 μm, similar to e.g. Battisti et al. (2019). This further serves to guide the fitting process into better constraining the spectrum at FIR wavelengths, where photometric uncertainties are generally large.

Without such an adjustment, the fitting would be dominated by the small uncertainties on the short-wavelength photometry, and occasionally fail to accurately model the FIR component.

We then identify AGN via a comparison of the integrated luminosities in both the torus and accretion disk components with, respectively, the stellar-heated dust continuum and the direct optical and near-UV stellar light, taking into account the probability distributions of these integrated luminosities. This comparison then directly takes into account the reliability of the photometry, as large photometric uncertainties will naturally lead to a broad probability distribution in the integrated luminosities of the various components. Therefore, this procedure only includes AGN that can reliably be identified as such, similar to e.g. Delvecchio et al. (2014, 2017), who compare the best-fitting SEDs with and without AGN templates, and require the former to be a better fit at the 99% confidence level in order to identify it as AGN. We slightly modify this procedure for sources without any FIR-photometry, and expand on the exact criteria we employ in Appendix 2.A. Overall, we identify 149 sources as HLAGN based on SED fitting, with 51 (78) being identified solely through a MIR-torus (accretion disk) component. A further 20 sources are classified as an AGN based on both of these features.

We show the overlap between the three different methods utilized for identifying HLAGN in Figure 2.8. As expected, the subset of AGN identified through mid-IR colors largely overlaps with those found through SED-fitting, such that the X-ray and SED-fitted AGN make up the bulk of the total set of HLAGN.

2.4.2 MLAGN

Whereas AGN selected through X-ray emission, MIR-colors and SED-fitting diagnostics preferentially identify HLAGN, which form the subset of AGN powered by efficient accretion, a second, low-luminosity AGN population is most readily detected through its radio properties. We assign sources to the class of low-to-moderate luminosity AGN (MLAGN) if they are not identified as HLAGN and satisfy one of the following criteria:

- The source exhibits radio-emission that exceeds (at the 2.5σ level) what is expected from star formation, based on the radio-FIR correlation.
- The source exhibits red rest-frame $[\mathrm{NUV} - r^{+}]$ colors, corrected for dust attenuation, typically indicating a lack of star formation.

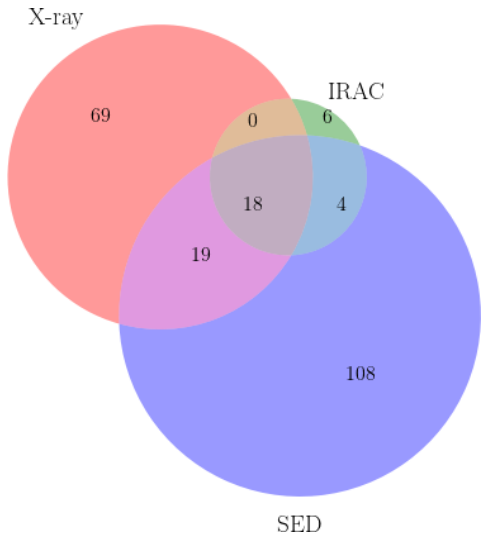

Figure 2.8: Venn diagram showing the overlap between the various AGN diagnostics used for identifying HLAGN. The areas of circles and overlapping regions are roughly proportional to the number of sources within this category.

Radio-excess AGN

The FIR-radio correlation describes a tight interconnection between the dust luminosity of a star-forming galaxy and its low-frequency radio luminosity. This connection arises because the same population of massive stars that heats up dust, causing it to re-radiate its energy in the FIR, produces supernovae that generate relativistic particles emitting synchrotron radiation at radio frequencies. However, galaxies that host an AGN may have their radio emission dominated instead by the active nucleus, and will therefore be offset from the FIRC. To quantify this, we define the correlation parameter q_{TIR} as the logarithmic ratio of a galaxy's total IR-luminosity L_{TIR}, measured between (rest-frame) $8-1000\,\mu$m, and its monochromatic radio luminosity at rest-frame 1.4 GHz, $L_{1.4\mathrm{GHz}}$ (following e.g. Bell 2003; Thomson et al. 2014; Magnelli et al. 2015; Delhaize et al. 2017; Calistro Rivera et al. 2017; Algera et al. 2020a):

$$q_{\mathrm{TIR}} = \log_{10}\left(\frac{L_{\mathrm{TIR}}}{3.75\times10^{12}\,\mathrm{W}}\right) - \log_{10}\left(\frac{L_{1.4\mathrm{GHz}}}{\mathrm{W/Hz}}\right)\,. \tag{2.1}$$

The factor 3.75×10^{12} is the central frequency of the total-IR continuum ($8-1000\,\mu$m) in Hz and serves as the normalization. There is now a grow-

ing consensus that q_{TIR} is a function of redshift (Magnelli et al. 2015; Delhaize et al. 2017; Calistro Rivera et al. 2017), for reasons that are still rather poorly understood. Nevertheless, we utilize a redshift-dependent threshold in terms of q_{TIR} to identify galaxies with radio excess based on what is expected from the FIRC. We show the distribution of q_{TIR} as a function of redshift for our sample of radio-detected sources in Figure 2.9, with the FIR-luminosities obtained from magphys.[12] Rest-frame 1.4 GHz luminosities are determined using the measured spectral index for the required K-corrections if available. When only a single radio flux is available, a spectral index of $\alpha = -0.7$ is assumed instead. The luminosities are then calculated through

$$L_{1.4\,\mathrm{GHz}} = \frac{4\pi D_L^2}{(1+z)^{1+\alpha}} \left(\frac{1.4\,\mathrm{GHz}}{3\,\mathrm{GHz}}\right)^{\alpha} S_{3\,\mathrm{GHz}}\,. \tag{2.2}$$

Here D_L is the luminosity distance at redshift z and $S_{3\,\mathrm{GHz}}$ is the observed flux density at 3 GHz. The uncertainty on the luminosity is computed by propagating the error on the flux density and – if the source is detected at $\geqslant 2$ radio frequencies – the spectral index, i.e. the source redshift is taken to be fixed. The error on q_{TIR} further includes the propagated uncertainty on the FIR-luminosity returned by magphys.

To quantify radio excess, we adopt the redshift-dependent q_{TIR} determined for star-forming galaxies by Delhaize et al. (2017). They determine a best-fitting trend of $q_{\mathrm{TIR,D17}} = 2.86 \times (1+z)^{-0.19}$, with an intrinsic scatter around the correlation of $\sigma_q = 0.31$. Their best fit takes into account the sample selection at both radio and far-infrared wavelengths through a two-sided survival analysis. As such, Delhaize et al. (2017) take into account that radio-faint star-forming galaxies – those with a value of q_{TIR} above the typical correlation – are preferentially missed in radio-selected samples, in particular at high-redshift due to the negative radio $K-$correction. We therefore adopt their median redshift-dependent value for q_{TIR} appropriate for star-forming galaxies, minus $2.5 \times \sigma_q$, as our threshold for identifying radio-excess AGN. That is, our threshold identifies a radio source as an AGN if it lies below the median far-infrared-radio correlation for star-forming galaxies at more than 2.5σ significance. Adopting the Delhaize

[12] Using energy-balance is appropriate here, as it allows us to associate FIR-luminosities even to sources without good photometric coverage at these wavelengths. Adopting a code without energy balance would instead result in artificially low FIR-luminosities and as such biases sources towards being radio-excess AGN. We study the effect of incompleteness in our FIR-photometry and the assumption of energy balance in Appendix 2.C.3.

et al. (2017) results appropriate for star-forming sources, and taking into account the intrinsic scatter about the correlation, minimizes the effect of selection biases and incompleteness in our multi-wavelength photometry on the AGN classification. Overall, we identify a total of 110 radio-excess AGN via this method.

However, this number of AGN may be affected by the fact that we do not have radio spectral indices for ~ 80% of our sample (see also Gim et al. 2019). To test the effect of assuming a fixed spectral index for these sources, we re-compute the number of radio-excess AGN by assigning every source detected solely at 3 GHz a spectral index drawn from a normal distribution, centered around $\alpha = -0.70$, with a standard deviation of $\sigma = 0.30$ (similar to the intrinsic scatter in the radio spectral indices found by Smolčić et al. 2017b in the 3 GHz VLA-COSMOS survey). We then run this procedure 200 times and find the mean number of radio-excess AGN to be $N_{\rm AGN} = 120$, with a standard deviation of 5 sources. It is unsurprising that the typical number of radio-excess AGN increases slightly when a distribution of spectral indices is assumed, as the number of star-forming sources is $\sim 12\times$ greater than the number of AGN. As such, it is more likely for a galaxy classified as star-forming when $\alpha = -0.70$ is assumed to scatter below the AGN threshold than for an AGN to scatter into the star-forming regime. However, the minor increase of ~ 10 radio-excess AGN we find when adopting such a distribution of spectral indices does not change our conclusions that radio-excess AGN make up only a small fraction of the μJy radio population.

While the radio-excess criterion described above constitutes a clear way to identify AGN for sources with well-constrained FIR-luminosities, only 50% of our sample is detected in the far-infrared at $\geqslant 3\sigma$. To improve the completeness of our sample of radio-excess AGN, we utilize the distribution of FIR-luminosities for the sources with at least one 3σ detection at any of the FIR-wavelengths, and compare this with expected FIR-luminosities of the *Herschel*-undetected sources. For each of the latter, we compute the FIR-luminosity through the far-infrared radio correlation, assuming the previously mentioned relation for star-forming sources by Delhaize et al. (2017), again adopting their normalization minus 2.5 times their intrinsic scatter about the correlation. Effectively, we thus compute a conservative FIR-luminosity of our *Herschel*-undetected sample at the 2.5σ level, assuming all radio emission is powered by star formation. We compare the FIR-luminosities derived in this manner with the distribution of luminosities for our sources with well-constrained FIR photometry in

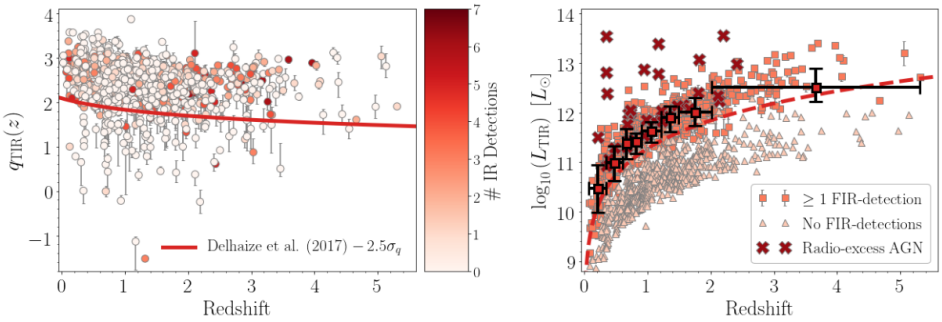

Figure 2.9: Left: FIRC-parameter $q_{\rm TIR}$ as a function of redshift for the S-band detected sample of 1437 sources. Sources are colored by the number of detections in the FIR (including *Herschel*/PACS & SPIRE, as well as SCUBA2, JCMT/AzTEC and IRAM/MAMBO). The solid red line constitutes the redshift-dependent trend of $q_{\rm TIR}(z)$ as determined for star-forming galaxies by Delhaize et al. (2017), minus $2.5\times$ the intrinsic scatter of 0.31 dex, which constitutes our redshift-dependent threshold for radio excess. The 110 sources below this line are then identified as radio-excess AGN. **Right:** Empirically determined sensitivity curve of our *Herschel* observations, showing the redshift-dependent FIR-luminosity of our sample, either computed through magphys (orange squares) or via the FIRC, assuming a conservative $q_{\rm TIR}(z)$ (triangles and crosses). The sources with good FIR-photometry are binned in redshift (large red squares). The empirical detection limit is then determined via a fit through the lower errorbars, and is shown via the dashed red line. Radio sources without far-infrared photometry that fall above this detection threshold are identified as AGN. This diagnostic allows us to quantify radio excess for sources lacking FIR-photometry, and identifies a total of 62 radio-excess AGN.

the lower panel of Figure 2.9. We fit a power law through the $16^{\rm th}$ percentile of the distribution of $\log L_{\rm TIR}$ in each redshift bin for sources with FIR-detections, and thus empirically determine the detection threshold of sources with a given dust luminosity. Sources which fall above the median FIR-luminosity determined for the sample with *Herschel*-detections, yet are themselves undetected in the FIR, are also identified as 'inverse' radio-excess AGN. This constitutes a total of 62 sources, shown via the red crosses in the lower panel of Figure 2.9. A substantial number of these, 46 in total, were previously identified through the normal radio-excess criterion. This substantiates that the energy balance magphys applies to determine far-infrared luminosities is typically a good assumption for these sources (see also Dudzevičiūtė et al. 2020).

Red, quiescent AGN

The class of MLAGN can be further extended by including red galaxies, as – once obscuration by dust has been corrected for – such colors indicate a cessation of star formation. We quantify this through the rest-frame $[\mathrm{NUV} - r^+]$-colors of our sources, which we model through integrating the best-fitting, unattenuated magphys SED over the GALEX NUV 2300 Å and Subaru r^+-band filters. We follow Ilbert et al. (2010) and define sources with $[\mathrm{NUV} - r^+] > 3.5$ as quiescent galaxies, but limit this analysis to sources at $z \leqslant 2$, as we do not accurately measure the rest-frame UV emission for sources at high redshift. As radio emission traces star formation, and quiescent sources by definition lack significant star-formation activity, we identify radio sources with red rest-frame colors as MLAGN. We find 50 such sources and note that 56% of these were already previously identified through the (inverse) radio excess criterion, similar to what is found by Smolčić et al. (2017a). We verified that there is no trend between the NUV/optical colors and redshift, as such a trend may be indicative of an inaccurate extrapolation of a galaxy's SED by magphys to rest-frame NUV wavelengths, resulting in the misclassification of red, quiescent MLAGN.

We show the relation between the FIRC-parameter q_{TIR} and rest-frame $[\mathrm{NUV} - r^+]$-colors for sources at $z \leqslant 2$ in Figure 2.10 (left panel). On average, redder sources exhibit lower values of q_{TIR}, and hence constitute a higher fraction of radio-excess AGN. A total of 22 sources – nearly half of the sources with $[\mathrm{NUV} - r^+] > 3.5$ – nevertheless show radio emission consistent with originating solely from star formation, which may indicate that these sources are in fact low-level (dusty) SFGs without substantial AGN activity in the radio (though five are identified as HLAGN instead). The determination of whether these objects have an AGN contribution is however complicated by the fact that only four of these sources have detections in the far-infrared, such that the modelled dust continuum emission of these objects is determined solely through the energy balance that magphys imposes. This adds an additional layer of uncertainty to their distribution of q_{TIR}. For this reason, as well as the general observation that red, early-type galaxies are typically linked with radio-bright AGN hosts (e.g. Rovilos & Georgantopoulos 2007; Smolčić 2009; Cardamone et al. 2010; Delvecchio et al. 2017), we identify these sources as quiescent (ML)AGN nevertheless. Ultimately, the sample of red rest-frame optical/NUV sources not identified as AGN through other means only concerns a small number of sources (only 1.5% of our radio sample, or 6.6% of all AGN), and their inclusion has a negligible effect on the number counts we derive in Section 2.5, with all

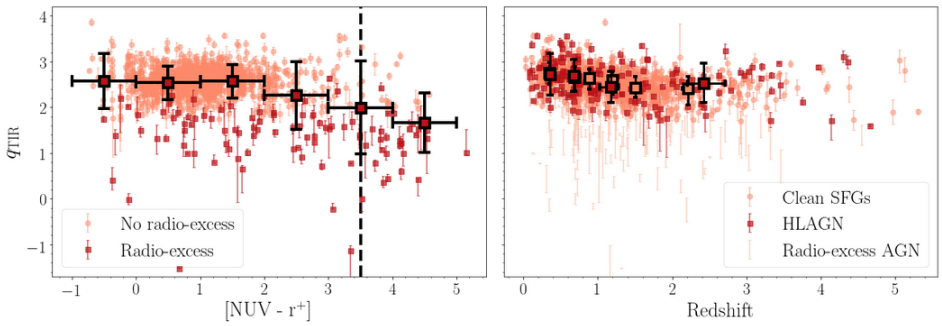

Figure 2.10: Left: The radio-FIR correlation parameter q_{TIR} (Equation 2.1) as a function of rest-frame $[\mathrm{NUV} - r^+]$-colors for all sources at $z \leqslant 2$. The sample is divided into radio-excess AGN (red squares) and sources primarily powered by star formation (orange circles). The dashed black line represents the threshold for identifying sources as red, quiescent MLAGN. The large squares indicate the mean values per bin, and the binwidth is shown through the horizontal errorbars. The vertical errorbars represent the 1σ standard deviation per bin. On average, redder sources show stronger radio emission for a given FIR-luminosity, which is consistent with a substantial fraction of these sources being radio-excess AGN. **Right:** q_{TIR} as a function of redshift for the clean star-forming sample (orange circles) and HLAGN without radio-excess (red squares). The large orange and red squares represent the binned values for the clean SFGs and HLAGN, respectively. No significant difference is present between the distribution of q_{TIR} for the two samples, indicating that AGN without radio-excess have radio properties consistent with arising solely from star formation.

results being consistent within the uncertainties if we include these sources in the clean SFG sample instead. In fact, omitting these sources from the sample of MLAGN further strengthens our conclusions that AGN make up only a small fraction of the μJy radio population.

2.4.3 AGN Identification Summary

The results of the AGN identification process are listed in Table 2.1, and are additionally summarized as a Venn diagram in Figure 2.11. We find a total of 334 AGN in our sample ($23.2 \pm 1.3\%$, where the error represents the 1σ Poissonian uncertainty), using the five different diagnostics detailed in the previous sections. Combined, our AGN sample contains 224 HLAGN and 110 MLAGN. Overall, $\sim 64\%$ of the sample was identified using just a single AGN tracer, whereas the remaining AGN were identified as such with up to four diagnostics. This exemplifies the importance of using various tracers of AGN activity, as the different diagnostics trace intrinsically different populations.

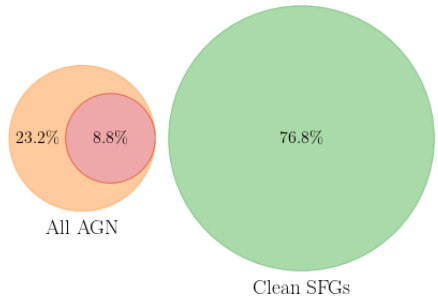

Figure 2.11: Visual representation of the different radio populations examined in this paper. The subset of all AGN is shown in orange, and combines both MLAGN and HLAGN. AGN exhibiting a radio excess are shown in red, and form less than half of the total AGN population. Clean star-forming sources are shown in green, and form the remainder of the radio sample.

Less than half of the AGN we identify show an excess in radio emission with respect to the radio-FIR correlation, as is shown in the Venn diagram in Figure 2.11 by the red circle. We overplot all AGN without radio-excess on the radio-FIR correlation in Figure 2.10 (right panel), which shows that these sources have radio emission that is fully consistent with originating from star formation. Therefore, only $8.8 \pm 0.8\%$ of our radio sample has radio emission that is clearly not from a star-forming origin.

2.5 Composition of the Ultra-Faint Radio Population

2.5.1 The Ultra-faint Radio Population

In Figure 2.12, we show both the fractional and cumulative contribution of the different radio populations as a function of 3 GHz flux density. We restrict our analysis to sources with flux densities $< 100\,\mu$Jy, which constitute $\sim 98\%$ of our sample, because of poor statistics at our bright end. At relatively high flux densities between $50 - 100\,\mu$Jy, the radio population remains fairly equally split among the combination of MLAGN and HLAGN and clean star-forming galaxies, though our modest sample size at these fluxes results in significant uncertainties. Nevertheless, the class of MLAGN dominates the population of AGN at $S_\nu \gtrsim 50 - 100\,\mu$Jy, which is unsurprising as the bulk of this population is made up of sources that show radio excess, and are therefore radio-bright by definition. At flux densities $\lesssim 30\,\mu$Jy, which constitutes 86% percent of our sample, we observe a clear increase in star-forming sources, reaching a fractional contribution

Table 2.1: Summary of the AGN identification.

Method	HLAGN	Fraction	MLAGN[a]	%age
X-ray	106	7.4%	-	-
IRAC	28	1.9%	-	-
SED-fitting	149	10.4%	-	-
• Torus	71	4.9%	-	-
• Disk	98	6.8%	-	-
Radio-excess	25	1.7%	85	5.9%
Inverse radio-excess	19	1.3%	43	3.0%
$[\mathrm{NUV} - r^+]$	5	0.3%	45	3.1%
Total[b]	224	15.6%	110	7.7%

[a]MLAGN are, by definition, not identified through the X-ray, IRAC or SED-fitting criteria.

[b]The total does not equal the sum of all rows, as a single AGN may be identified through multiple diagnostics.

of $\gtrsim 80\%$ in the lowest flux density bins. Cumulatively, our sample reaches 50% star-forming sources at flux densities $\sim 10\mu$Jy, and overall is made up for $\sim 75\%$ by sources with no hints of AGN activity. At our detection limit of $\sim 2.7\mu$Jy, approximately 85% of the sample is made up of clean SFGs.

Instead of adopting the MLAGN and HLAGN terminology, which includes sources with signs of AGN activity across their full SED, we consider in Figure 2.13 the fractional contribution of sources with and without radio excess. The latter class includes galaxies that exhibit AGN-like activity in their X-ray to mid-infrared SEDs, but show no sign of AGN activity at radio wavelengths. While at fluxes above $\gtrsim 100\mu$Jy sources with radio-excess dominate the population, their fractional contribution declines steeply towards lower flux densities, and below $\lesssim 20\mu$Jy the contribution of galaxies without any radio-excess is $\gtrsim 95\%$. If we adopt the definition that – despite any other AGN signatures – galaxies without any radio-excess are star-forming, this implies that the fraction of star-forming galaxies is nearly unity below $\lesssim 20\mu$Jy. Overall, the fraction of sources without AGN signatures in the radio in the COSMOS-XS survey equals $91.2 \pm 0.8\%$. We verify in Appendix 2.C.4 that there is no dependence of any of the AGN diagnostics as function of flux density, indicating that the increased fractional contribution of star-forming sources with decreasing flux density is robust.

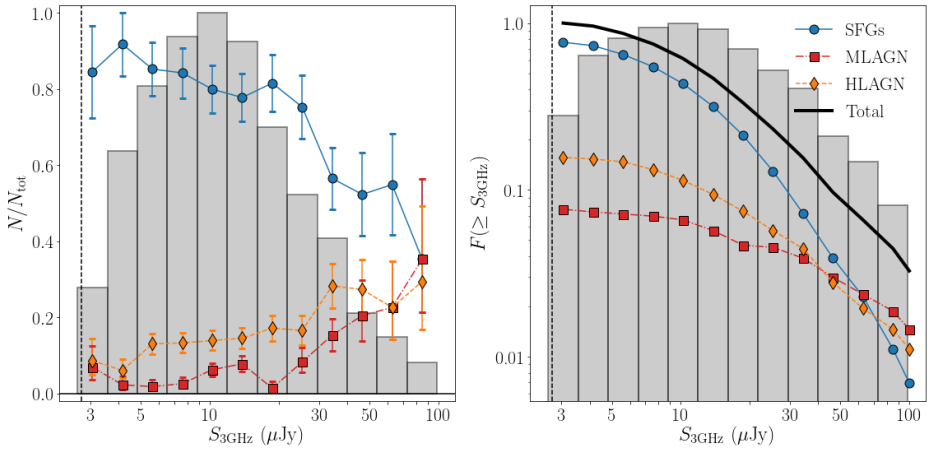

Figure 2.12: Left: the fraction of sources of a given type (SFGs, MLAGN and HLAGN) as a function of flux density. Errorbars represent the Poissonian uncertainties for > 10 sources per bin, or the confidence limits from Gehrels (1986) otherwise. In both panels, the vertical dashed grey line indicates the 5σ detection limit of the COSMOS-XS survey, and the grey histogram shows the normalized number of sources in a given logarithmic 3 GHz flux density bin. **Right:** the cumulative fraction of sources as a function of flux density, defined to increase towards lower flux densities. Overall, $\sim 75\%$ of sources make up the sample of clean, star-forming galaxies, while below $\sim 30\,\mu$Jy, the fraction of such SFGs increases to $\gtrsim 80\%$.

In Figure 2.14, we show the distribution of the sample with redshift, and the fractional contribution of each population per redshift bin. The median redshift for all populations is approximately $z \sim 1$, illustrating the well-known result that the redshift distribution of radio sources is near-independent of flux density (Condon 1989). In addition, the overall fraction of the various source populations remains fairly constant with redshift. This likely indicates that there are no obvious biases in the AGN selection as a function of redshift, which we investigate further for each of the AGN diagnostics individually in Appendix 2.C.4.

2.5.2 Euclidean-normalized Number Counts

In this section, we translate our observed sample, which may be parametrized as N_i radio-detected sources within the $i^{\rm th}$ flux density bin $S_{\nu,i}$, into the completeness-corrected Euclidean-normalized number counts. The completeness corrections are required to reconstruct the intrinsic number density of radio sources from our observed sample. Our modus operandi has

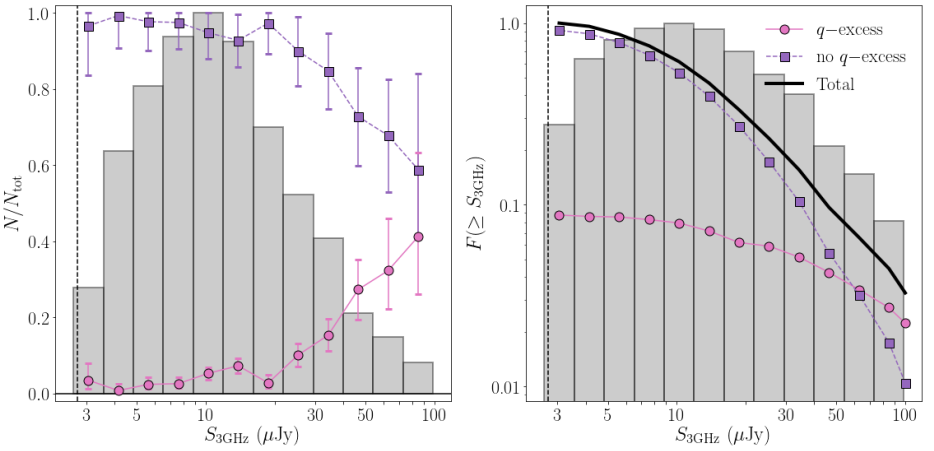

Figure 2.13: Left: the fraction of sources with (without) radio excess in pink (purple) as a function of 3 GHz flux density. The datapoints are shown with Poissonian uncertainties when there are > 10 sources per bin. The confidence limits from Gehrels (1986) are adopted otherwise. In both panels, the grey histogram shows the normalized number of sources in a given logarithmic flux density bin and the vertical dashed grey line indicates the 5σ detection limit of the COSMOS-XS survey. **Right:** the cumulative fraction of sources with and without radio excess versus flux density, defined to increase towards lower flux densities. The fraction of sources powered by star formation reaches near-unity below $\sim 20\,\mu$Jy. Cumulatively, $\sim 90\%$ of our sample shows radio emission that is star-formation powered.

been to cross-match the 3 GHz detected radio population with various multi-wavelength catalogs, and to use this information to classify this radio sample into AGN and star-forming sources. The main source of incompleteness is the primary beam attenuation, decreasing our sensitivity to faint radio sources towards the edge of the pointing. We additionally correct for spurious detections in the original 3 GHz map, as well as our incompleteness in assigning multi-wavelength counterparts to real radio sources. The magnitude of the former two completeness corrections are detailed in Paper I, and the incompleteness in counterpart association was determined in Section 2.3.3 (see also Figure 2.6).

In the following, we will assume that the completeness corrections we have derived apply uniformly to the various radio populations - that is, these corrections are a function of observed flux density only, and not of any additional source properties. The full completeness correction C_i applied to the $i^{\rm th}$ flux density bin is then given by

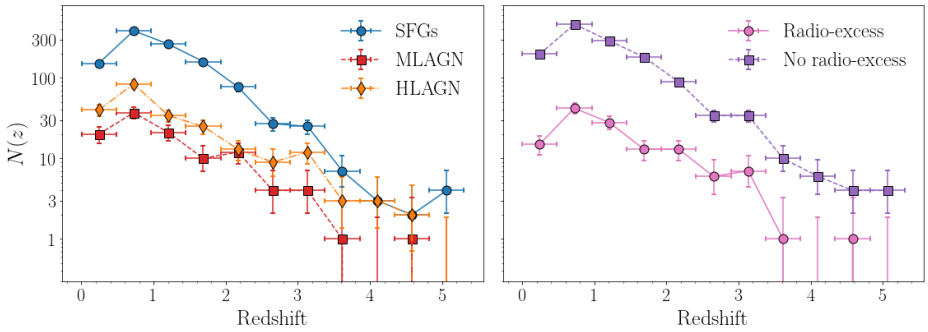

Figure 2.14: Left: distribution of SFGs, MLAGN and HLAGN with redshift. **Right:** distribution of radio-excess AGN and sources without radio excess with redshift. Errorbars represent the uncertainties on the counting statistics in each bin. The median redshift of the sample is $z \sim 1.0$, and the fractional contribution of the SFGs and various types of AGN remains roughly constant as a function of redshift.

$$C_i\left(S_{\nu_i}\right) = \frac{1 - f_{\text{spurious}}(S_{\nu_i})}{f_{\text{flux}}(S_{\nu_i}) \times f_{\text{ctrpt}}(S_{\nu_i})}. \tag{2.3}$$

Here f_{spurious} is the fraction of spurious sources expected in the given flux density bin, f_{flux} is the fractional flux density completeness of our sample, taking into account our declining sensitivity to sources away from the primary beam centre, and f_{ctrpt} is the fraction of sources in the given flux density bin for which we have obtained reliable non-radio counterparts. The Euclidean source counts in the i^{th} bin are then computed via

$$S_{\nu,i}^{5/2} n(S_{\nu,i}) = \frac{C_i N_i}{\Delta S_{\nu,i} \Omega} S_{\nu,i}^{5/2}, \tag{2.4}$$

where $\Omega \sim 350$ arcmin^2 is the field of view of the S-band survey area, out to 20% of the maximum primary beam sensitivity and $\Delta S_{\nu,i}$ is the width of the i^{th} flux density bin. The normalization with $S_\nu^{5/2}$, applied to the center of the bin, has historically been used, and translates into a flat slope of the number counts with flux density for a fully Euclidean universe. The completeness-corrected Euclidean source counts for the different radio populations are shown in Figure 2.15 and tabulated in Table 2.2. The total uncertainties on our measurements combine uncertainties on the counting

statistics with the propagated errors on the various completeness corrections. The effects of cosmic variance are not included in the uncertainties, but we quantify its contribution in Section 2.5.2 and overplot the results as shaded regions in the figure.

We compare our results with the number counts from Smolčić et al. (2017a), who cover a larger area to shallower depths. Focusing first on the sample of MLAGN, HLAGN and clean SFGs (the upper panel of Figure 2.15), we observe a good match between the number counts of the two types of AGN between our data and the Smolčić et al. (2017a) sample at the flux densities we have in common ($25 \lesssim S_\nu \lesssim 100\,\mu$Jy), whereas we find a slight increase in clean SFGs at the fainter flux densities. This may be explained by cosmic variance (Section 2.5.2), or by uncertainties in the completeness corrections at the faint end of the VLA-COSMOS survey ($\lesssim 50\,\mu$Jy).

In the lower panel of Figure 2.15, we compare our number counts for sources with and without radio-excess with the VLA-COSMOS sample. We find an overall agreement, although our fraction of sources without radio-excess at flux densities $\lesssim 50\,\mu$Jy is slightly larger than what is found by Smolčić et al. (2017a), similar to our increase in the counts for clean SFGs. The number counts of radio-excess AGN are further in good agreement at the flux densities the two surveys have in common. Combined, this is fully consistent with our results from Paper I, where we find a slight increase in the overall radio number counts compared to the 3 GHz VLA-COSMOS sample. Similar to the above, these differences may be explained by cosmic variance or uncertainties in the completeness corrections. Overall, our 3 GHz source counts are broadly consistent with the VLA-COSMOS data, and as ultimately the population of sources with and without radio excess are used to determine cosmic star-formation rate densities, this agreement is encouraging.

We additionally compare our results to recent simulations from Bonaldi et al. (2019), who simulate the radio continuum emission from radio-excess AGN and star-forming galaxies. They model the star-forming population by converting galaxy luminosity functions from UV, Lyman-α and IR observations from Cai et al. (2013, 2014) – corrected for dust extinction where necessary – into the star-formation history of the universe (SFHU). As star formation is directly coupled to radio emission, this SFHU is sampled and converted into a radio luminosity function using the local calibration from Murphy et al. (2012), slightly adapted to compensate for the over-prediction of the faint end of the local radio luminosity functions (see the discussion in Mancuso et al. 2015). For the radio-excess AGN, Bonaldi

Table 2.2: Euclidean-normalized source counts for the various radio populations.

Flux (μJy)			Completeness				SFGs	MLAGN	HLAGN	No $q-$excess	$q-$excess
$S_{\rm low}$	$S_{\rm high}$	$S_{\rm centre}$	$f_{\rm flux}$[a]	$f_{\rm ctrpt}$[b]	$f_{\rm spurious}$[c]	$C_{\rm full}$[d]	Counts[e]	Counts	Counts	Counts	Counts
2.64	4.82	3.56	0.162	0.909	0.010	$7.11^{+2.37}_{-1.45}$	$0.45^{+0.16}_{-0.10}$	$0.02^{+0.01}_{-0.01}$	$0.03^{+0.02}_{-0.01}$	$0.50^{+0.17}_{-0.10}$	$0.01^{+0.01}_{-0.00}$
4.82	8.82	6.52	0.444	0.935	0.011	$2.45^{+0.41}_{-0.29}$	$0.70^{+0.13}_{-0.09}$	$0.02^{+0.01}_{-0.01}$	$0.11^{+0.02}_{-0.02}$	$0.80^{+0.15}_{-0.10}$	$0.02^{+0.01}_{-0.01}$
8.82	16.12	11.92	0.828	0.938	0.017	$1.28^{+0.17}_{-0.10}$	$0.94^{+0.13}_{-0.09}$	$0.08^{+0.02}_{-0.02}$	$0.17^{+0.03}_{-0.03}$	$1.11^{+0.15}_{-0.10}$	$0.07^{+0.02}_{-0.02}$
16.12	29.49	21.81	0.934	0.947	0.015	$1.13^{+0.14}_{-0.07}$	$1.29^{+0.18}_{-0.13}$	$0.07^{+0.02}_{-0.02}$	$0.28^{+0.05}_{-0.05}$	$1.54^{+0.21}_{-0.15}$	$0.10^{+0.03}_{-0.03}$
29.49	53.94	39.88	0.940	0.900	0.020	$1.17^{+0.19}_{-0.13}$	$1.16^{+0.23}_{-0.19}$	$0.36^{+0.10}_{-0.08}$	$0.59^{+0.14}_{-0.12}$	$1.70^{+0.32}_{-0.26}$	$0.41^{+0.11}_{-0.09}$
53.94	98.65	72.95	1.000	0.920	0.000	$1.09^{+0.20}_{-0.09}$	$0.89^{+0.24}_{-0.20}$	$0.50^{+0.16}_{-0.14}$	$0.46^{+0.16}_{-0.14}$	$1.20^{+0.29}_{-0.24}$	$0.66^{+0.20}_{-0.17}$

[a] Flux completeness of the given flux density bin, including the incompleteness resulting from reduced primary beam sensitivity.

[b] Fraction of radio sources in the given flux density bin assigned a multi-wavelength counterpart with a robustly measured redshift.

[c] Expected fraction of spurious sources in the given flux density bin.

[d] Overall completeness correction applied to the bin, as defined in Equation 2.3, with the propagated uncertainty.

[e] All the number counts are given in units of $\mathrm{Jy}^{3/2}\ \mathrm{sr}^{-1}$.

et al. (2019) start with radio luminosity functions for three different types of AGN (steep-spectrum sources, flat-spectrum radio quasars and BL Lacs), which they evolve through cosmic time using evolutionary parameters motivated by the literature. Additionally, different spectral indices are assumed for the three sets of AGN, including a Gaussian distribution around the mean spectral index per class of AGN. Their resulting definitions of the AGN and star-forming populations are largely consistent with our definition of sources with and without radio-excess, respectively, and hence we show the source counts determined from their simulated catalog in the lower panel of Figure 2.15. For this, we use the $25\,\mathrm{deg}^2$ simulations at 3 GHz that probe down to flux densities of $10\,\mathrm{nJy}$. Our number counts for star-formation powered sources are in excellent agreement with these simulations across the full range of flux densities we cover, including at the faint end, where we are probing a fully new parameter space. Our number counts for radio-excess AGN are additionally consistent with the predictions from Bonaldi et al. (2019), although the last two bins for radio-excess AGN ($S_{3\,\mathrm{GHz}} \lesssim 10\,\mu\mathrm{Jy}$) lie slightly below the expected value from the simulations. However, our number counts are still consistent with the predictions within the 1σ scatter due to cosmic variance, which we quantify in the following section.

Cosmic Variance

To quantify how cosmic variance may influence our observed number counts, we make use of the 5×5 deg^2 simulations by Bonaldi et al. (2019) that model the populations of star-forming and radio-excess galaxies. We draw radio sources from non-overlapping circular regions from their full simulated cosmic volume, whereby we take into account that faint sources can only be recovered in the central regions of the primary beam. For example, a source with a flux density of $10 \times \sigma_{\mathrm{rms}}$ can be detected at 5σ significance out to the half power point of the primary beam. Such sources are therefore drawn from a circular region with a diameter equal to the FWHM of the S-band primary beam. The brightest sources can be detected in the full field of view of our observations, which equals $\Omega \simeq 350$ arcmin^2 out to 20% primary beam sensitivity. As such, our cosmic variance calculation takes into account that faint sources, while more numerous than brighter ones, can only be detected within a smaller region in our pointing.

For each of the resulting 225 regions, we compute the Euclidean number counts and the corresponding 1σ and 2σ confidence intervals, which are shown as the shaded regions in Figure 2.15. These confidence intervals

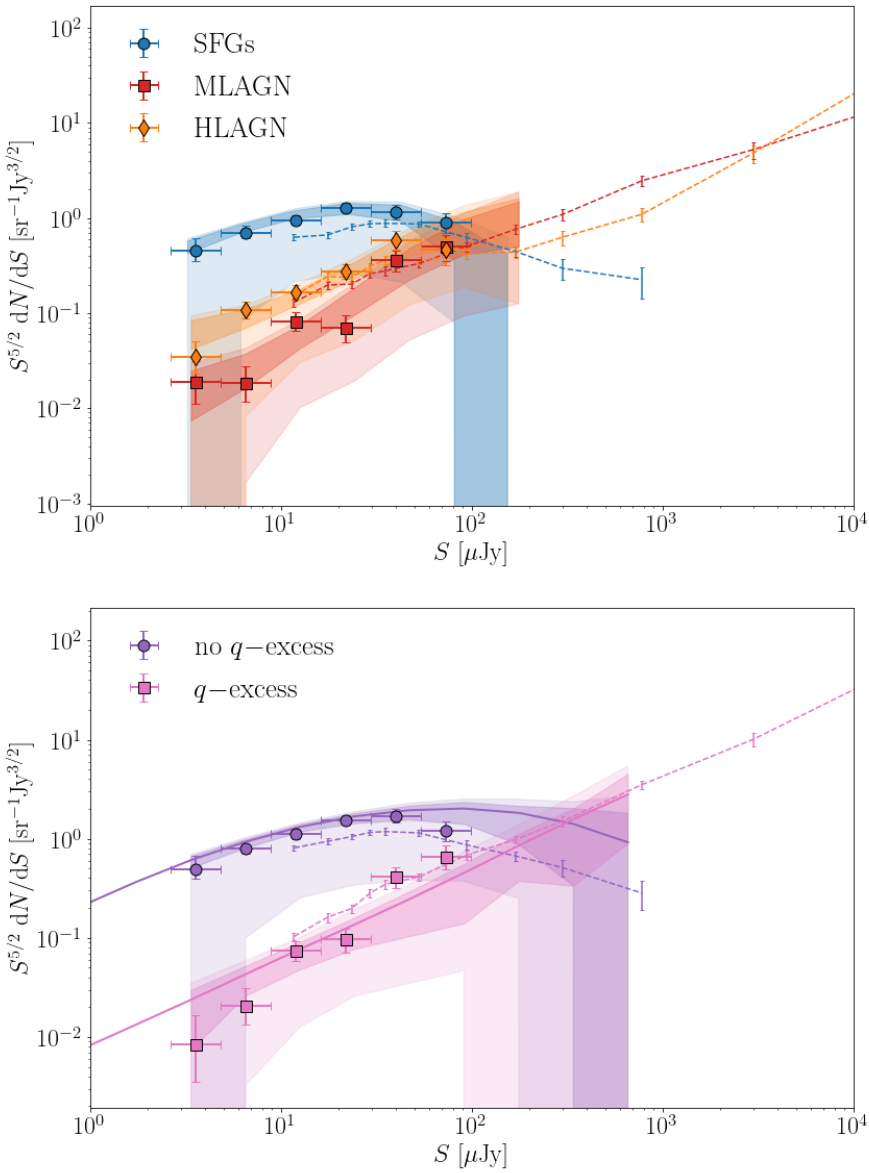

Figure 2.15: Euclidean-normalized source counts for the faint radio population. **Upper:** source counts for the moderate-to-high luminosity AGN (HLAGN, orange), low-to-moderate luminosity AGN (MLAGN, red) and clean star-forming galaxies (blue). Our data are represented by the colored markers, and we compare with the recent 3 GHz VLA-COSMOS observations (Smolčić et al. 2017b,a), represented by the dashed lines. The expected scatter as a result of cosmic variance is shown by the shaded regions (dark: 1σ, light: 2σ). **Lower**: source counts for the radio sources with and without radio excess (pink and purple, respectively). The source counts from the Bonaldi et al. (2019) simulations are shown by the solid lines. We omit these from the upper plot, as their simulations do not model the MLAGN and HLAGN populations separately.

hence reflect two effects: at low flux densities the effective field of view of our observations is small, such that the uncertainties resulting from cosmic variance are large. At high flux densities, the effect of cosmic variance is similarly large as bright sources are relatively rare, and this outweighs the increased effective field of view.

As the simulations by Bonaldi et al. (2019) do not explicitly model the population of AGN without radio-excess, we combine our observed number counts with their results to obtain an estimate of the effect of cosmic variance for this sub-population of AGN. We extrapolate our measured number counts for clean SFGs, HLAGN and MLAGN to fainter flux densities by fitting a quadratic function in log-space to the measured number counts of SFGs, and a linear function to the MLAGN and HLAGN. We then draw sources from the Bonaldi et al. (2019) simulations based on the expected ratios of these three radio populations, and repeat the cosmic variance calculation as for the star-forming and radio-excess samples. We caution that our extrapolations are not based on any physical model, but we judge the cosmic variance results to be robust in the range of flux densities we probe ($\sim 2 - 100\,\mu$Jy) based on the good correspondence between the fits, our data and the shape of the number counts as obtained from the Bonaldi et al. (2019) simulations. The typical 1σ uncertainties as result of cosmic variance are ~ 0.1 dex for SFGs, and ~ 0.3 dex for AGN – substantial compared to the formal uncertainties on the derived Euclidean number counts. The additional uncertainty due to cosmic variance must therefore be taken into account when comparing our results to different radio surveys.

2.5.3 Optically dark Sources

In total, our radio sample comprises 70 sources that were not matched to a counterpart in any of the three catalogs used for cross-matching. As we expect only ~ 20 spurious detections, most of the unmatched sources are likely to be real. About half of these radio-only detected sources have Super-deblended counterparts within $2\farcs0$, which is beyond our adopted cross-matching radius of $0\farcs9$. However, visual inspection of these sources at shorter wavelengths shows that the nearby Super-deblended entries are potentially associated to the same source, but exhibit spatial offsets between the infrared (K_s and IRAC 3.6μm) and radio emission, similar to what has been observed at mm-wavelengths (e.g. Hodge et al. 2012). Nevertheless, a substantial number of detections have SNR $\gtrsim 6$ yet have no counterpart within $\gtrsim 5''$, making it likely that these are indeed optically-dark radio sources.

For an additional 53 S-band detected sources we obtained a counterpart in the Super-deblended catalog, but no counterpart at shorter wavelengths. A subset of 23 of these sources was previously catalogued in the K_s-band selected catalog by Muzzin et al. (2013), but was excluded from the COSMOS2015 catalog as they are located close to saturated optical stars. As this might affect their optical and near-IR photometry and consequently any derived physical quantities such as their photometric redshifts, we have not further analyzed this sample. The remainder of the sources we solely identify with a counterpart from the Super-deblended catalog are however based on a single detection at 3 GHz in the VLA-COSMOS survey, which we verify in this work through our deeper radio observations. These 30 sources have no existing photometric detections below MIPS $24\,\mu$m, which is a potential sign of obscured AGN at $z \gtrsim 6$ (e.g. Rujopakarn et al. 2018) or highly dusty SFGs (e.g. Simpson et al. 2014; Dudzevičiūtė et al. 2020), both of which evade detection at short wavelengths. Whereas no robust photometric redshifts for these sources exist due to the lack of optical/near-IR photometry, Jin et al. (2018) have employed photometric redshift fitting based on the FIR data available for these sources. While these redshifts are rather uncertain as a result of a degeneracy between redshift and dust temperature (Jin et al. 2018 quote a relative uncertainty of up to $\sim 0.1\times(1+z_{\rm IR})$ on the derived values), 13 sources are placed beyond $z \geqslant 3$, including 8 sources at $z \geqslant 4$. Additional data are needed to robustly ascertain whether these sources are indeed at such high redshift, but we verified that the sample of $z \geqslant 4$ sources are all roughly consistent with the radio-FIR correlation as obtained in Section 2.4.2, extrapolated to the FIR-derived redshifts. This indicates that – if these photometric redshifts are correct – the majority of this subsample is likely to have radio emission of a star-forming origin. This is in agreement with our results from Section 2.5.1, as we expect ~ 3 out of 30 sources (10%) to be radio-excess AGN based on their 3 GHz flux densities.

We compile a sub-sample of optically dark detections, consisting of sources detected either only at 3 GHz, or cross-matched to a Super-deblended counterpart which in turn was based on a prior position from the VLA COSMOS survey. For the former set, we further ensure that there is no COSMOS2015 counterpart within $2\farcs0$ around any of the detections. This requirement ensures that the remaining sources are indeed 'optically dark', as entries in the COSMOS2015 catalog are – by construction – detected at short (NIR) wavelengths. The separation of $2\farcs0$ is motivated by the fact

that beyond this distance, the distribution of separations between S-band sources and COSMOS2015 counterparts is consistent with being solely the result of chance associations. We further remove all sources with a peak signal-to-noise at 3 GHz below six, to ensure the optically dark sample is robust against spurious detections. We additionally remove any objects flagged due to being located near a bright radio source, leaving us with a sample of 46 sources that we inspect visually in the Subaru/Suprime-cam $i+$, VISTA/Vircam K_s and *Spitzer*/IRAC 3.6μm bands. From this subset, we then discard radio sources that largely overlap with bright or saturated objects in the optical/near-IR bands, as source blending at these wavelengths is likely to have affected the source detection. The remaining 29 optically dark sources are compiled in Table 2.3.

We investigate the multi-wavelength properties of these sources by stacking on their radio positions in optical/near-IR bands, as well as at 1.4 GHz. We do not attempt to stack in any of the *Herschel* bands, due to the large PSF at these wavelengths. All bands used for stacking, the corresponding photometry and the limiting magnitudes of the stacks are listed in Table 2.4. We perform aperture photometry on the optical/near-IR stacks using a $1\farcs5$ diameter aperture for all bands up to VISTA/Vircam K_s, and adopt a $3\farcs0$ diameter aperture for the *Spitzer*/IRAC channels owing to the larger point spread function at these wavelengths. We compute uncertainties on the fluxes by placing the apertures on random locations in the 100×100 pixel^2 stack, away from the central region and computing the flux within these apertures. The median and standard deviation of these measured aperture fluxes are then taken to be the background and typical flux uncertainty in the stack, respectively.

We determine the photometric redshift of the stacked SED through EAzY (Brammer et al. 2008), using the standard set of templates provided with the code. The stack is assigned a best-fitting redshift of $z_{\rm stack} = 4.65$, with a $16^{\rm th} - 84^{\rm th}$ confidence interval of $z = (3.22 - 5.63)$. This interval was computed via a bootstrap analysis, whereby we sampled, with replacement, from the 29 optically dark sources, generating a total of 200 bootstrap samples. We then stacked all of these samples, and for each performed aperture photometry and photometric redshift fitting in the same way as for the original stack. The given confidence interval on the best-fitting photometric redshift as such represents the $16^{\rm th} - 84^{\rm th}$ percentile of the bootstrapped redshift distribution. To further verify the robustness of SED-fitting our stacked sample, we additionally stack an identical number of sources that do have optical/NIR photometry, and have a robustly mea-

Table 2.3: Optically dark sources detected at 3 GHz.

RA	DEC	Flux[a]	Error[a]	SNR	S17[b]
		(μJy)	(μJy)		
$10^h00^m12.05^s$	$02°36'48.95''$	33.73	0.76	44.5	1
$10^h00^m00.40^s$	$02°36'12.40''$	32.66	1.72	28.3	1
$10^h00^m03.82^s$	$02°26'31.33''$	36.81	1.39	26.5	1
$10^h00^m38.06^s$	$02°28'06.06''$	20.27	0.83	24.5	1
$09^h59^m58.46^s$	$02°30'34.58''$	26.06	1.07	24.3	1
$10^h00^m03.28^s$	$02°34'48.64''$	20.06	0.84	24.0	1
$10^h00^m26.66^s$	$02°31'26.71''$	16.93	1.38	21.5	1
$10^h00^m54.48^s$	$02°34'35.86''$	28.08	1.90	17.7	1
$10^h00^m03.27^s$	$02°29'42.80''$	23.03	1.65	16.9	1
$09^h59^m58.79^s$	$02°34'57.61''$	15.41	1.02	15.2	1
$10^h00^m19.89^s$	$02°33'31.45''$	8.56	0.57	15.1	0
$09^h59^m59.81^s$	$02°34'54.66''$	17.69	1.55	12.0	1
$10^h00^m07.39^s$	$02°42'03.22''$	59.45	3.69	12.0	0
$10^h00^m20.11^s$	$02°39'39.99''$	12.01	1.02	11.8	1
$10^h00^m24.44^s$	$02°37'49.34''$	6.77	0.74	9.1	0
$10^h00^m29.93^s$	$02°29'18.17''$	5.86	0.65	9.1	0
$10^h00^m09.52^s$	$02°26'48.42''$	10.07	1.13	8.9	0
$10^h01^m03.04^s$	$02°29'11.96''$	29.77	3.52	8.4	1
$10^h00^m39.20^s$	$02°40'52.58''$	27.73	2.20	7.7	0
$10^h00^m25.08^s$	$02°26'07.27''$	7.62	1.00	7.6	1
$10^h00^m35.34^s$	$02°28'27.00''$	5.83	0.77	7.6	0
$10^h00^m15.11^s$	$02°38'17.58''$	6.50	0.88	7.4	0
$10^h00^m04.85^s$	$02°35'59.51''$	6.21	0.85	7.3	0
$10^h00^m08.64^s$	$02°32'50.79''$	4.50	0.68	6.6	0
$10^h00^m24.56^s$	$02°39'11.57''$	6.34	0.97	6.5	0
$10^h00^m41.82^s$	$02°25'47.13''$	8.80	1.35	6.5	1
$10^h00^m48.46^s$	$02°36'41.25''$	6.54	1.01	6.4	0
$10^h00^m11.73^s$	$02°34'25.69''$	4.27	0.66	6.4	0
$10^h00^m34.83^s$	$02°28'35.83''$	4.41	0.73	6.1	0

[a]Peak or integrated flux density and its corresponding uncertainty, based on the analysis in Paper I.

[b]Boolean flag indicating whether the source is also present in Smolčić et al. (2017a).

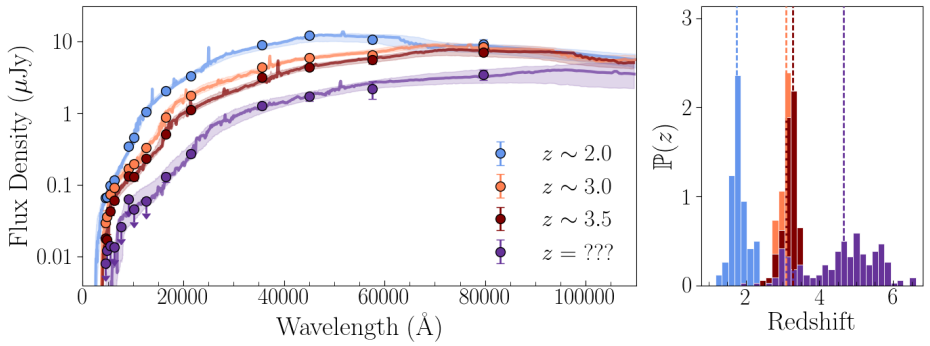

Figure 2.16: Left: Best fitting SED for a stack of 29 high-redshift radio detections, with a median redshift of $z = 1.99$ (blue), $z = 2.93$ (orange) and $z = 3.42$ (red), as well as the stack for our optically dark sample (purple). The shaded regions indicate the $16^{\text{th}} - 84^{\text{th}}$ confidence limits around the stacked SED, as obtained from bootstrap re-sampling. **Right**: The redshift distributions of the bootstrapped optically dark and control samples. The vertical dashed lines indicate the best-fitting redshift for the original stacks. The median redshift of the control samples are fairly well recovered, strengthening the conclusion that the 'optically dark' sample consists predominantly of high-redshift ($z \gtrsim 4$) sources.

sured photometric or spectroscopic redshift, to see if the average redshift is indeed correctly recovered. For this, we draw 29 sources from our radio sample at random, within three different redshift ranges, requiring only that the sources have no additional COSMOS2015 counterpart within $2\farcs0$ to minimize source blending. Three sets of radio sources were drawn within a redshift of $1.5 \leqslant z \leqslant 3.0$ (median redshift $z = 1.99$), $2.5 \leqslant z \leqslant 4.0$ (median redshift $z = 2.93$) and $z \geqslant 3$ (median redshift $z = 3.42$). Our radio sample does not contain sufficiently many sources to further probe higher redshift ranges. The SEDs of both the optically dark and the control samples are shown in Figure 2.16. The recovered photometric redshifts and bootstrapped uncertainties are $z = 1.76^{+0.28}_{-0.14}$, $z = 3.10^{+0.17}_{-0.21}$ and $z = 3.28^{+0.10}_{-0.28}$ for these three stacked samples, respectively, and hence recover the median redshift of the control sample relatively well. As the redshift probability distribution of the true optically dark sample is substantially broader than that of the control samples, it is likely that it consists of sources across a wider range of redshifts, with a typical value of $z \sim 4 - 5$. Nevertheless, if we make the assumption that all sources in the stack lie at the best-fitting photometric redshift, this would imply $\sim$ 90% of our sample at $z \sim 5$ is undetected in optical and near-IR photometry. As a sanity check, we com-

pare with the infrared-derived photometric redshifts for the 15 optically dark sources detected only in the Super-deblended catalog from Jin et al. (2018), corresponding to roughly half of the total optically dark sample. This subset has a mean redshift of $z_{\rm IR} = 3.3$ (with a scatter of $\sigma_z = 1.9$), substantiating the typical high-redshift nature of these detections. We note, however, that these IR-derived redshifts are highly uncertain and therefore mostly indicative, and as such we do not use them in this work. This is further illustrated by the recent work from Jin et al. (2019), who, upon spectroscopic confirmation, find significant differences ($\Delta z \gtrsim 1$) between the true and infrared-derived redshifts for a sample of four dusty galaxies in the COSMOS field. We further note that, at sub-millimeter wavelengths, the typical redshift of the optically dark population is indeed also higher than that of the typical population of sub-millimeter galaxies (e.g. Simpson et al. 2014; Dudzevičiūtė et al. 2020), similar to what we observe here in the radio.

In addition to stacking in optical/NIR data, the optically dark sources are also detected in the 1.4 GHz stack. The spectral index between the 1.4 and 3 GHz data is found to be $\alpha_3^{1.4} = -0.65^{+0.26}_{-0.22}$, consistent with a typical radio spectrum of $\alpha \sim -0.70$. Based on the observed 3 GHz peak flux density of $S_{3\,\rm GHz} = 10.7 \pm 0.20$ μJy, we expect $\lesssim 1$ radio-excess AGN to be present in our sample, based on the results in Section 2.5, which in turn implies radio surveys may miss a large fraction of the high-redshift star-forming population when optically dark sources are simply discarded. The consequences of this on the COSMOS-XS-derived cosmic star-formation history will be addressed in a forthcoming paper (Van der Vlugt et al. in prep). If we assume the radio emission from the optically dark sample to be fully powered by star formation, we expect their average star-formation rates to be SFR $\sim 500 - 1500\ M_\odot\ {\rm yr}^{-1}$ when assuming the local value of $q_{\rm TIR}$ derived by Bell (2003), and placing the sources at a redshift between $z \sim 3.5 - 6$. Adopting the redshift-dependent conversion from Delhaize et al. (2017) instead results in more modest star-formation rates between $150 - 350\ M_\odot\ {\rm yr}^{-1}$, though we stress that both the large spread in the redshift range of the optically dark sample, as well as the unknown value of $q_{\rm TIR}$ for typical SFGs above $z \gtrsim 3$, are large factors of uncertainty in the derived SFRs. The range of radio luminosities and SFRs spanned by this optically dark sample is shown via the shaded purple region on the COSMOS-XS sensitivity curve in Figure 2.5.

We lastly investigate the average X-ray properties of the optically dark

sample through an X-ray stacking analysis using C-STACK[13], and find that the radio sample is not detected in the X-ray stack, with the count rate in both the soft ($[0.5-2]$ keV) and hard ($[2-10]$ keV) bands being consistent with zero at the 1σ level. This corresponds to an upper limit of $L_{[0.5-8]\,\mathrm{keV}} \lesssim 2 \times 10^{43}$ erg/s, assuming a redshift of $z = 5.0$ for the stack. Based on this fairly shallow upper limit, we cannot place any constraints on whether the typical source in the stack exhibits X-ray emission suggestive of AGN activity. Nevertheless, the upper limit is consistent with the typical radio-derived SFR for the stack, assuming the FIRC from Delhaize et al. (2017) and the X-ray−SFR-relations from Symeonidis et al. (2014), further substantiating the notion that the optically dark sample is dominated by high-redshift star-forming galaxies.

2.5.4 Implications for Next-Generation Radio Surveys

The two largest upcoming radio telescopes are the next-generation VLA (ngVLA) and the Square Kilometer Array (SKA). Both are expected to revolutionize the radio view on galaxy evolution owing to their greatly improved sensitivity and resolution compared to present-day radio interferometers. For example, the ngVLA will be able to reach the COSMOS-XS 3 GHz RMS-sensitivity of $\sim 0.53\,\mu$Jy/beam at a similar frequency within an hour of observing time (Selina et al. 2018).

Additionally, assuming a spectral index of $\alpha = -0.7$ and an observing frequency of ~ 1 GHz, the SKA will reach a similar sensitivity as our 3 GHz observations as part of the SKA Wide survey, which is expected to cover an immense area of $\sim 10^3$ deg^2 (Prandoni & Seymour 2015). This is a factor $\sim 10^4$ larger than our surveyed area, such that a zeroth order scaling of our number counts predicts that the SKA Wide Survey will detect upwards of $\gtrsim 10^7$ faint radio sources.

Both our results for the faint radio source counts and predictions from simulations (Wilman et al. 2008; Bonaldi et al. 2019) are consistent with a continuous increase in the fraction of sources without radio-excess towards lower flux densities. This is in further agreement with the recent work from Novak et al. (2018), who extrapolate the VLA-COSMOS luminosity functions to predict the relative contributions of SFGs and AGN. Based on a simple power-law extrapolation of our radio number counts below $30\,\mu$Jy, we find that at $\sim 1\,\mu$Jy, the fractional contribution of radio-excess sources

[13] C-STACK is an online X-ray stacking tool developed by Takamitsu Mijayi, and can be accessed via `http://cstack.ucsd.edu/` or `http://lambic.astrosen.unam.mx/cstack/`.

Table 2.4: Data used for stacking of optically dark sample.

Band[a]	Wavelength (μm)	Depth[b]	Flux Density (μJy)[c]	Error (μJy)	SNR
Subaru/Suprime-cam B	0.4458	28.6	0.003	0.003	1.2
Subaru/Suprime-cam $g+$	0.4777	28.1	0.004	0.004	1.0
Subaru/Suprime-cam V	0.5478	28.0	0.005	0.005	1.0
Subaru/Suprime-cam $r+$	0.6288	28.0	0.013	0.005	2.8
Subaru/Suprime-cam $i+$	0.7683	27.3	0.022	0.009	2.5
Subaru/Suprime-cam $z+$	0.9037	26.4	0.063	0.020	3.2
VISTA/Vircam Y	1.0214	26.7	0.046	0.015	3.0
VISTA/Vircam J	1.2534	26.5	0.060	0.019	3.2
VISTA/Vircam H	1.6454	26.4	0.13	0.020	6.6
VISTA/Vircam K_s	2.1540	26.0	0.27	0.030	9.1
Spitzer/IRAC CH1	3.5634	24.2	1.29	0.15	8.9
Spitzer/IRAC CH2	4.5110	23.8	1.72	0.22	7.7
Spitzer/IRAC CH3	5.7593	22.7	2.20	0.60	3.7
Spitzer/IRAC CH4	7.9595	22.8	3.47	0.57	6.1
VLA/S-band	3.0 GHz (10 cm)	-	10.7	0.20	53.5
VLA/L-band	1.4 GHz (21 cm)	-	17.6	3.1	5.7

[a]References: Subaru/Suprime-cam images from Capak et al. (2007); VISTA/Vircam data are UltraVISTA DR3 (McCracken et al. 2012); *Spitzer*/IRAC images are from S-COSMOS (Sanders et al. 2007); the VLA L-band mosaic is from Schinnerer et al. (2007).

[b]For the optical/near-IR bands, this corresponds to the 5σ limiting magnitude in $1\farcs5$ apertures ($3\farcs0$ for *Spitzer*/IRAC). For the radio data, see the error on the flux density as measure of the depth of the stack.

[c]For the two radio bands, these are the peak flux densities in μJy beam^{-1}.

is $\lesssim 1\%$, such that the next-generation radio surveys will be highly sensitive to the faint, star-forming population. In fact, simple flux cuts on the radio-detected sample are likely to be sufficient for obtaining a highly pure sample of star-forming sources.

2.6 Summary & Future

We have presented a multi-wavelength analysis of the faint radio population identified in the COSMOS-XS survey, which is the deepest multi-frequency radio survey to date, reaching a 5σ flux limit of $\sim 2.7\,\mu$Jy beam^{-1} within the centre of the 3 GHz image (RMS of $0.53\,\mu$Jy beam^{-1}). This image, which covers a total area of ~ 350 arcmin^2, is a factor ~ 5 deeper than the previously deepest radio data over COSMOS at this frequency, and enables the direct detection of the typical star-forming population (SFR $\lesssim 100\,M_{\odot}\,\mathrm{yr}^{-1}$) out to $z \lesssim 3$ (Figures 2.1 and 2.5). To characterize the observed faint radio population, we associated multi-wavelength counterparts to our radio sample by drawing from the several photometric catalogs available over the well-studied COSMOS field. In total, we associated such counterparts to 96.6% of our radio sources. We restrict ourselves to the cross-matches with robustly determined photometric (59%) or spectroscopic (41%) redshifts available, accounting for a total of 1437 sources (93.3% of the total radio sample). The median redshift of the population is $\langle z \rangle = 0.97 \pm 0.03$, and the sample further includes 51 high-redshift sources with $3.0 \leqslant z \leqslant 5.3$.

We separate this faint radio population into star-forming sources and AGN, where the latter are again divided into different subclasses, either based on their radiative luminosities or on an excess in radio emission based on what is predicted from star-formation related emission alone. Sources with moderate-to-high radiative luminosities (HLAGN) exhibit AGN-related emission throughout their multi-wavelength spectral energy distribution, and are identified through strong X-ray emission, AGN-specific mid-IR colors or based on clear AGN-like components from SED-fitting. On the other hand, low-to-moderate luminosity AGN (MLAGN) are identified through an observed lack of star formation, based on red rest-frame UV/optical colors, or an excess in radio emission compared to their full $8 - 1000\,\mu$m FIR luminosity.

The full catalog of sources detected at 3 GHz, including their multi-wavelength source identifications, and the results from our AGN identification is available with this Paper in standard FITS format. We show a sample of the catalog in Table 2.6, and elaborate on its contents in Appendix 2.D.

Overall, these multi-wavelength diagnostics identify 23.2 ± 1.3% of the COSMOS-XS sample as AGN, with only 8.8 ± 0.8% of the radio-detected sources exhibiting AGN-related emission at the observed radio frequencies. Radio emission from the remainder of the sample therefore appears consistent with originating from star formation (Figure 2.9). The incidence of the various types of AGN is a strong function of flux density (Figures 2.12 and 2.13); the relative contributions of clean SFGs, MLAGN and HLAGN are similar for $S_{3\,\mathrm{GHz}} \gtrsim 50\,\mu$Jy, but towards lower flux densities the fraction of clean star-forming sources rises rapidly, reaching $\gtrsim 80$% at $S_{3\,\mathrm{GHz}} \lesssim 20\,\mu$Jy. Moreover, sources without a radio-excess form the overwhelming majority of our radio sample for $S_{3\,\mathrm{GHz}} \lesssim 50\mu$Jy and reach a fraction of $\gtrsim 90 - 95$% below $S_{3\,\mathrm{GHz}} \lesssim 30\,\mu$Jy. Our radio sample is therefore strongly dominated by the star-forming population. Next-generation radio surveys, capable of reaching sensitivities similar to COSMOS-XS in an hour, are therefore ideally suited to probe this faint population and constrain the dust-insensitive star formation history of the universe accordingly.

We additionally observe an interesting subset of radio-detected sources with multi-wavelength counterparts solely at far-infrared wavelengths, or no such counterparts at all. A stacking analysis at optical, near-infrared and radio wavelengths indicates these sources are likely to be high-redshift in nature ($z \sim 5$, Figure 2.16). If powered entirely through star-formation, this implies radio-based star-formation rates of hundreds of solar masses per year. As such, these 'optically dark' sources may contribute appreciably to cosmic star-formation at high-redshift.

We further present the completeness-corrected Euclidean-normalized 3 GHz radio number counts within the faint regime ($2\,\mu\mathrm{Jy} \lesssim S_{3\,\mathrm{GHz}} \lesssim 100\,\mu$Jy) for the various radio population in Figure 2.15, and show that the COSMOS-XS sample forms a natural extension of the previous literature towards fainter flux densities. Additionally our number counts are in good agreement with recent simulations of the radio sky within the expected scatter of cosmic variance.

Overall, COSMOS-XS provides the deepest multi-frequency radio survey to date, and probes a new, faint parameter space in the radio. In this work – the second paper in the COSMOS-XS series – we have presented the decomposition of the faint radio population into star-forming galaxies and AGN. It will be followed by additional works studying the radio-derived star formation history and AGN accretion history, and additionally, we will leverage the multi-frequency data over COSMOS to further study the radio properties of the COSMOS-XS sample, including the evolution of the

far-infrared-radio correlation, and the intrinsic radio spectra of the faint, star-forming population.

Acknowledgements

We wish to thank the anonymous referee for their comments and suggestions which greatly improved this work. The authors wish to thank Chris Carilli for the useful discussions while preparing the proposal and for his help planning the observations, and Mara Salvato for providing us with the COSMOS spectroscopic master catalog. The National Radio Astronomy Observatory is a facility of the National Science Foundation operated under cooperative agreement by Associated Universities, Inc. H.A., D.vdV. and J.H. acknowledge support of the VIDI research programme with project number 639.042.611, which is (partly) financed by the Netherlands Organization for Scientific Research (NWO). I.S. acknowledges support from STFC (ST/P000541/1). D.R. acknowledges support from the National Science Foundation under grant number AST-1614213. D.R. also acknowledges support from the Alexander von Humboldt Foundation through a Humboldt Research Fellowship for Experienced Researchers.

Appendix

2.A AGN Diagnostics from SED Fitting

We utilize Bayesian Markov Chain Monte Carlo (MCMC) SED-fitting code AGNfitter (Calistro Rivera et al. 2016, 2017) to identify AGN based on a comparison between the integrated luminosities in two sets of components: the direct stellar light and the accretion disk in the wavelength range $0.1 - 1\,\mu$m, and the MIR-continuum emission from a warm, dusty torus and the stellar-heated dust in the wavelength range $1-30\,\mu$m. As AGNfitter returns realistic uncertainties on these luminosities through an MCMC-approach, we compare the resulting probability distributions instead of simply comparing the luminosities from the best fit. We write $L_{\mathrm{C,p}}$ to be the p^{th} percentile of the integrated luminosity in component C. A source is then identified as an AGN if

$$\left(L_{\mathrm{disk,97.5}} \geqslant L_{\mathrm{stellar,2.5}}\right) \vee \left(L_{\mathrm{torus,97.5}} \geqslant L_{\mathrm{cold\ dust,2.5}}\right) \ .$$

Here $\vee$ denotes the logical or operator, and the 2.5^{th} and 97.5^{th} percentiles are equivalent to Gaussian confidence intervals 2σ below and above the mean, respectively. We slightly modify this procedure for sources without any FIR-photometry, as for this subset of our radio sample the MIR to FIR-SED is nearly fully unconstrained as AGNfitter does not impose energy balance. As a result, the MIR-continuum of such sources is potentially fully fitted by a torus component, whereas the FIR-luminosity is artificially low, as illustrated in the upper panel of Figure 2.17. To avoid identifying such sources as AGN, we define parameter $f_{\text{bolo}} = L_{\text{torus,2.5}} / \left(L_{\text{torus,2.5}} + L_{8-1000\,\mu\text{m}}\right)$, which measures the fractional contribution of the torus to the total FIR-luminosity. Here the luminosity $L_{8-1000\,\mu\text{m}}$ is – by definition – not well-constrained, and therefore we utilize the upper limit on this value as determined empirically in Section 2.4.2, Figure 2.9 (lower panel), where we fit the sensitivity curve of our *Herschel* observations, and hence find a redshift-dependent upper limit on the FIR-luminosity that a source without any FIR-detections can have. Based on visual inspection of the SEDs, as well as the distribution of f_{bolo} for sources that do have accurately constrained FIR-luminosities, we then require that sources without FIR-photometry have $f_{\text{bolo}} \geqslant 0.20$ in order to be considered an AGN. This, in turn, identifies sources such as the example shown in the lower panel of Figure 2.17 as an AGN based on a strong torus component and stringent upper limits on the FIR-photometry. Through this procedure, we can then accurately assess whether sources without robust FIR-detections are likely to be AGN based on a substantial torus component, without having to invoke the uncertainties associated with energy balance. Additionally, the separation between SFGs and AGN is done based on physically motivated properties, instead of the comparison of goodness-of-fit.

2.B Comparison to 3 GHz VLA-COSMOS

The 3 GHz VLA-COSMOS project (Smolčić et al. 2017a,b; Delvecchio et al. 2017) covers the full 2 square degree COSMOS field at an identical frequency, allowing us to compare the multi-wavelength AGN identification for the bright end of our radio sample. Overall, we have 471 radio sources in common (based on cross-matching within $1\farcs0$), subject to two independent analyses. While our overall AGN diagnostics are similar, there are a few differences in the overall analysis. Primarily, we are using improved FIR-photometry taken from the recent Super-deblended catalog (Jin et al. 2018), which includes photometry up to 1.2mm, whereas the COSMOS2015

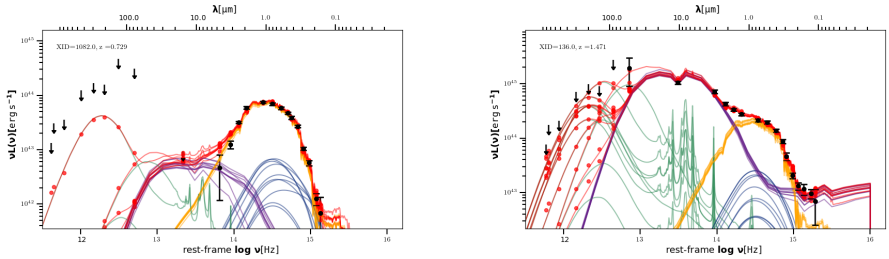

Figure 2.17: Example SEDs from AGNfitter. The photometric data are shown through the black points, and upper limits are indicated by downward arrows. The fitted direct stellar contribution is shown in yellow, the accretion disk in blue, the dusty torus in purple and the stellar-heated dust in green. The overall fit is shown in red. A total of 10 random MCMC-realizations are plotted. **Left:** SED of a source without FIR-photometry, which shows a substantial torus component in the $1-30\mu$m range, and has negligible cold dust component despite having very unconstraining upper limits. Sources such as these are not classified as AGN. **Right:** SED of a source without reliable ($\geqslant 3\sigma$) FIR-photometry which shows a large torus component and additionally has stringent upper limits on the total FIR-component. Sources such as these are classified as AGN.

catalog (Laigle et al. 2016) used in the 3 GHz VLA-COSMOS project contains photometry only up to $500\ \mu$m (*Herschel*/SPIRE). In addition, the deblending procedure employed by Jin et al. (2018) is more detailed than previous techniques, and is optimized for highly confused images. Nevertheless, based on the sample both surveys have in common, the overall number of AGN identified is highly similar: we identify 176 out of these 471 sources as AGN, compared to 193 AGN in VLA-COSMOS. The overlap between these two AGN samples is substantial, with 147 of these AGN ($\sim 84\%$) being identified in both surveys. The small remaining differences can be explained by the slightly different criteria and multi-wavelength datasets employed in the AGN identification process. We expand upon all of these in the next sections, and summarize the results in Table 2.5.

2.B.1 Radio-excess AGN

In the 3 GHz VLA-COSMOS project, radio-excess AGN are identified through a redshift-dependent threshold in $\log_{10}\left(L_{1.4\,\mathrm{GHz}}/\mathrm{SFR_{IR}}\right)$. This quantity is equal to minus q_{TIR}, up to a constant. The threshold for radio-excess AGN was then determined by considering the scatter towards values below the median in the distribution of $\log_{10}\left(L_{1.4\,\mathrm{GHz}}/\mathrm{SFR_{IR}}\right)$, as this regime should predominantly be populated by star-forming galaxies, and will hence trace

the intrinsic scatter in the far-infrared radio correlation. Radio AGN should instead only scatter towards larger values. However, since only the observed radio sources are used to determine the spread in the distribution, any upper limits or non-detections will affect the observed scatter. Radio-faint star-forming galaxies in particular are potentially missed, such that the observed spread about the correlation is lower than the intrinsic scatter. As a result, the adopted threshold for classifying AGN is likely to be somewhat conservative, whereby some star-formation powered sources with low $q_{\rm TIR}$ will be classified as AGN. In a subsequent paper as part of the 3 GHz VLA COSMOS survey, Delhaize et al. (2017) re-calculated the distribution of $q_{\rm TIR}$ for star-forming galaxies, now including detection limits in both the far-infrared and radio. We adopted their best-fitting trend for star-forming sources, and classified radio-excess AGN as the sources that are $> 2.5\sigma$ offset from the correlation. In addition, we take into account sources without FIR-photometry by comparing the expected infrared luminosity, assuming the radio emission is powered by star formation only, with the *Herschel* sensitivity curves (see the lower panel of Figure 2.9). Nevertheless, the difference in the total number of radio-excess AGN identified in both surveys is small: we find 94 such AGN in COSMOS-XS, whereas there are 102 identified in VLA-COSMOS, among the 471 radio sources in common. This small difference likely reflects the slightly different thresholds adopted.

2.B.2 SED-fitted AGN

In our analysis, we adopted the AGNfitter SED-fitting code to decompose the full SED of our radio-detected sample into star-forming and AGN components. This code is fundamentally different from sed3fit used in the 3 GHz VLA-COSMOS project, as it does not adopt energy balance and is based on an MCMC method. As a result, AGNfitter is designed to distinguish between AGN and star-forming sources not based on a goodness-of-fit test, but instead on physical properties, taking into account the robust uncertainties obtained from MCMC-fitting (see the discussion in Appendix 2.A).

Overall, we recover a similar number of AGN through SED-fitting, namely 59 in COSMOS-XS versus 65 in VLA-COSMOS, though only 26 of these are in common between the two radio samples. This difference may most likely be explained by the different fitting codes adopted, in particular whether or not the assumption of energy balance is made, and by the different criteria used for establishing whether a source is AGN. In addition, the slight differences between the two surveys further highlights that there is no clear

Table 2.5: Comparison of the COSMOS-XS AGN sample with the 3 GHz VLA-COSMOS survey, based on 471 sources in common

Diagnostic	COSMOS-XS	VLA-COSMOS	Overlap
X-ray	61	61	56
IRAC	20	26	20
SED-fitting	59	65	26
Radio-excess	116	102	71
$[\mathrm{NUV} - r^{+}]$	33	52	28
Overall[a]	190	193	154

[a]Represents the total number of AGN identified across all five diagnostics in the two surveys.

distinction between AGN and SFGs, and instead indicates that a large fraction of sources is composite in nature.

2.B.3 Red, quiescent AGN

In this paper we follow the method of Ilbert et al. (2010), where galaxies are classified as star-forming or quiescent based on their $[\mathrm{NUV}-r^{+}]$-colors. In particular, both in this work and in Smolčić et al. (2017a), sources are identified as quiescent AGN when $[\mathrm{NUV} - r^{+}] > 3.5$, where the colors are corrected for dust attenuation. Despite these identical criteria, there is some variation in the AGN identified through this method as in the VLA-COSMOS survey the number of AGN found through red rest-frame UV/optical colors is $\sim 58\%$ larger than found in this work (33 in COSMOS-XS versus 52 in VLA-COSMOS, with 28 sources in common). This cannot be explained by our requirement that sources identified through red colors lie below $z \leqslant 2$, as this does not discard any additional red objects from the sample. Nevertheless, in both our and the VLA-COSMOS survey the red, quiescent AGN are also identified through radio-excess in the majority of the cases (56% in COSMOS-XS versus 64% in VLA-COSMOS), which indicates that sources identified solely through red rest-frame optical/NUV-colors are only a small fraction of the overall AGN population.

2.C Incompleteness in the Multi-wavelength Photometry

As we utilize multi-wavelength photometry spanning X-ray to radio wavelengths in order to identify AGN, this identification may be affected by incompleteness in the various datasets we employ. We here study the effect this has on our sample of AGN.

2.C.1 X-ray AGN

We identify moderate-to-high luminosity AGN (HLAGN) through a combination of X-ray, mid-IR and SED-fitting techniques. Our X-ray data in particular are relatively shallow – we are already incomplete to X-ray sources with a luminosity of $L_{[0.5\text{ - }8]\,\mathrm{keV}} \sim 10^{42}$ erg s^{-1} beyond $z \sim 0.5$ (see also Figure 7 in Marchesi et al. 2016a). While we hence cannot place any direct constraints on the X-ray luminosities of sources beyond this redshift, we employ X-ray stacking to investigate the typical X-ray properties of our clean, star-forming galaxy sample, making use of X-ray stacking tool C-STACK. By stacking in four redshift bins between $0.5 \lesssim z \lesssim 2.5$, we find that the average X-ray luminosities of this clean SFG sample are fully consistent with the star formation – X-ray luminosity relations from Symeonidis et al. (2014). We will further address this, as well as the stacked X-ray properties for the different classes of AGN, in a forthcoming paper. Overall, this implies that our sample of clean SFGs is likely minimally contaminated by X-ray AGN.

2.C.2 MIR AGN

In our analysis, we identify 28 sources as mid-IR AGN based on their *Spitzer*/IRAC colors, following the criteria from Donley et al. (2012) for sources with $z \leqslant 2.7$. However, we only have IRAC photometry in all four channels for $\sim 60\%$ of our radio sample, which will cause us to miss some MIR-AGN simply based on lack of photometry. In Figure 2.18 we show the fraction of radio sources with with IRAC photometry as a function of 3 GHz flux density, which decreases to $\sim 30\%$ for our lowest flux density bin ($\sim 4\,\mu$Jy).[14] The total number of MIR-AGN expected in a given radio flux density bin is then the observed number divided by the fraction of sources with full IRAC photometry. The corrected fraction of MIR AGN is shown with the

[14] We limit this analysis to the 1390 radio sources (96.7%) with $S_{3\,\mathrm{GHz}} \leqslant 100\,\mu$Jy due to poor statistics at the brighter end. This includes 25 of the in total 28 MIR-AGN.

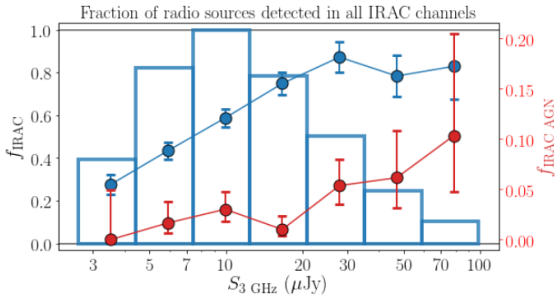

Figure 2.18: The fraction of sources with measured IRAC flux densities in all four channels as a function of 3 GHz flux density (blue line and points). The background histogram shows the overall distribution of radio flux densities, and the red line - corresponding to the right ordinate axis - denotes the fraction of MIR-AGN we expect when correcting for the incompleteness in IRAC photometry. Similar to our overall results for HLAGN, the fraction of MIR-AGN decreases towards fainter flux densities, even after correcting for the incompleteness.

red datapoints in Figure 2.18. After applying this completeness correction, the fraction of MIR-AGN is still decreasing towards lower radio flux densities, which is a trend we observe for HLAGN in general. Overall, we expect to find 53 ± 14 MIR-AGN in our sample of radio sources, after correcting for the IRAC incompleteness, which implies we are missing 28 ± 8 additional MIR-AGN. However, as the majority ($\sim 80\%$) of IRAC AGN are also identified through either our X-ray or SED-fitting criteria, we expect to miss only 6 ± 2 AGN based on our incomplete IRAC photometry, accounting for only $\sim 3\%$ of the total number of HLAGN. We are therefore not limited by incompleteness in the MIR-photometry in our identification of (HL)AGN.

2.C.3 Radio-excess AGN

Radio-excess AGN are identified through an excess in radio emission compared to what is expected based on their total FIR-luminosity, with this additional radio emission being ascribed to AGN activity. While our full sample is – by definition – detected at 3 GHz, we only have FIR-photometry for $\sim 50\%$ of our radio sources, which complicates the determination of accurate total ($8 - 1000\,\mu$m) infrared luminosities. In order to identify radio-excess AGN, we therefore assume energy balance between the UV to near-IR data and the longer wavelength emission, as the photometry at short wavelengths is typically better constrained. We test the reliability of the FIR-luminosities derived in this way by artificially removing the

FIR-photometry of sources that do have detections at such wavelengths and subsequently re-fitting their SEDs with magphys. For this, we limit ourselves to the 1371 radio sources that we cross-matched with both COSMOS2015 and the Super-deblended catalog. Among these sources, we identified 118 radio-excess AGN (103 and 61 via the normal and 'inverse' radio excess criteria, respectively, with substantial overlap; see Figure 2.13).

After removing all FIR-detections, we recover a total of 143 radio-excess AGN instead (118 and 71 sources through the regular and inverse criteria, respectively – note that we use the empirical detection limit in Figure 2.9 for the latter, as before), $\sim$ 20% larger than the number of AGN we find when we do include available FIR-photometry. This indicates that the energy balance magphys employs works well for the majority of sources, as even without far-infrared information accurate FIR-luminosities, and hence $q_{\rm TIR}$, are predicted. We further note that the 'inverse' radio-excess criterion we apply requires a priori information on the far-infrared properties of a subset of our radio sample, as these are used to determine an appropriate sensitivity limit for the various *Herschel* photometric bands. When removing all FIR-information, we can no longer directly apply this criterion. Using only the standard radio-excess diagnostic, we recover a total of 118 AGN – equal to the number identified through the combined radio-excess and 'inverse' radio-excess criteria when far-infrared data are included. Overall, we therefore conclude that the lack of far-infrared photometry for half of our radio sample does not substantially impede our classification of radio-excess AGN.

2.C.4 Summary

In the previous subsections, we have established that incompleteness issues are not expected to have a substantial effect on the AGN classification in this work. What remains is then to show that any of the trends we see for the SFGs and various types of AGN with either flux density (Figures 2.12, 2.13 and 2.15) or redshift (Figure 2.14) are not caused by any of the AGN diagnostics being more efficient in identifying sources within a given flux density or redshift interval. In Figure 2.19, we therefore plot the fractional contribution of each of these diagnostics to the total AGN counts versus redshift (left panel) and flux density (right panel). No strong trends are visible in either of the panels, which indicates that we are not biased towards finding a specific subset of AGN in a given bin of our redshift- and

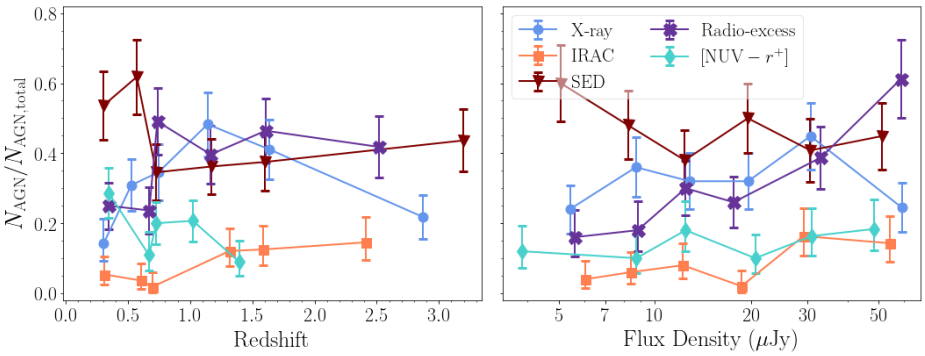

Figure 2.19: Left: the fractional contribution of the different AGN diagnostics (X-ray emission, *Spitzer*/IRAC colors, SED-fitting, radio-excess and red rest-frame NUV/optical colors) to the overall sample of AGN as a function of redshift. The data were binned into six fixed redshift ranges, containing an approximately equal number of AGN in total. The redshift value of each datapoint marks the median value per bin, and the errorbars represent Poissonian uncertainties. Note that the fractional contribution sums to a number greater than unity, as a single AGN may be identified through multiple diagnostics. The lack of strong trends with redshift indicate that we do not suffer from substantial biases as function of redshift (e.g. luminosity incompleteness) in our identification of AGN. **Right:** the fractional contribution of the different AGN diagnostics to the overall sample of AGN as a function of flux density. The data follow a similar binning as used in the left panel. With exception of the radio-excess AGN, which we established show a real and significant trend with flux density in the main text, no trends of the other AGN diagnostics are seen to correlate with radio flux density. This indicates that our various methods of AGN identification are reliable across the full range of fluxes probed in the COSMOS-XS survey.

flux density space.[15] In particular, the fractional contribution of the various types of AGN is a near-constant function of flux density, which substantiates our results in Section 2.5 that AGN make up a comparatively smaller fraction of the faint radio population.

2.D Final Counterpart Catalog

The catalog of sources detected at 3 GHz, including their multi-wavelength source identifications, is available with this Paper in standard FITS format.

[15]We, however, caution that one cannot robustly disentangle whether a trend with redshift is a physical effect or the result of a selection bias. Nevertheless, a lack of any given trend substantiates that no such bias is present.

We show a sample of the catalog in Table 2.6, and elaborate here on its contents.

1. *Column 1.* Source ID, equal to the ID assigned in Paper I.
2. *Columns 2-3.* Radio coordinates of the source as determined by `PyBDSF`.
3. *Columns 4-5.* Optimal redshift of the radio source, including a boolean indicating whether it is spectroscopic or photometric.
4. *Columns 6-11.* Flux densities and errors of the source at, respectively, 1.4, 3 and 10 GHz, in μJy. In the absence of a radio counterpart at 1.4 or 10 GHz, both the flux and error are set to -99.
5. *Columns 12-14.* ID of the source in, respectively, the Super-Deblended catalog, COSMOS2015 and the $i-$band selected catalog. If no counterpart was found, this value is set to -99.
6. *Column 15.* Boolean indicating whether the source is flagged as 'potentially spurious' based on the discussion in Section 2.2.1, in which case it is set to True.
7. *Columns 16-18.* The rest-frame 1.4 GHz luminosity of the source and its 16^{th} and 84^{th} percentiles (equivalent to 1σ confidence intervals), using the measured spectral index if available, or a fixed value of $\alpha = -0.7$ otherwise. The luminosity is given in W Hz^{-1}.
8. *Columns 19-21.* The value of the radio-FIR correlation parameter q_{TIR} as defined in equation 2.1, and its 16^{th} and 84^{th} percentiles.
9. *Column 22.* Boolean indicating whether the source is identified as an X-ray AGN, in which case it is set to True.
10. *Column 23.* Boolean indicating whether the source is identified as an AGN through its mid-IR colors, by means of the Donley et al. (2012) wedge.
11. *Column 24.* Boolean indicating whether the source is identified as an AGN based on SED fitting.
12. *Column 25.* Boolean indicating whether the source is identified as an SED-AGN based on a MIR torus component.
13. *Column 26.* Boolean indicating whether the source is identified as an SED-AGN based on a UV/optical accretion disk component.
14. *Column 27.* Boolean indicating whether the source is identified as an AGN based on red rest-frame near-UV and optical colors.
15. *Column 28.* Boolean indicating whether the source is identified as an AGN based on an excess in radio emission from what is expected

from the radio-FIR correlation, with FIR luminosities calculated using magphys.

16. *Column 29.* Boolean indicating whether the source is identified as an AGN based on an excess in radio emission from what is expected from the radio-FIR correlation, in the absence of *Herschel* FIR-photometry, through comparison with the detection limit of *Herschel*.
17. *Column 30.* Boolean indicating whether the source is identified as an HLAGN, which is True when either of columns $22 - 26$ are True.
18. *Column 31.* Boolean indicating whether the source is identified as an MLAGN, which is True when all of columns $22 - 26$ are False and either of columns $27 - 29$ are True.
19. *Column 32.* Boolean indicating whether the source is a radio-excess AGN, which is True when either of columns $28 - 29$ is True.
20. *Column 33.* Boolean indicating whether the source is an AGN without radio excess, which is True when either of columns $22 - 27$ are True and both columns $28 - 29$ are False.

Table 2.6: Sample of the COSMOS-XS Multi-wavelength and AGN catalog

ID	RA	DEC	Redshift	Spec$-z$		$S_{3\,GHz}$	$\sigma_{3,GHz}$		No-qE AGN
	[deg]	[deg]				[μJy]	[μJy]		
CXS J100016.55+023309.17	150.06894	2.55255	4.36	0	...	4.95	0.59	...	1
CXS J095952.41+023148.56	149.96837	2.53016	1.60	0	...	8.26	1.39	...	0
CXS J100034.78+022849.87	150.14493	2.48052	1.56	0	...	10.56	0.71	...	0
CXS J100036.03+023937.91	150.15012	2.66053	1.22	0	...	507.22	1.16	...	0
CXS J100019.40+022936.63	150.08083	2.49351	0.21	0	...	5.22	0.62	...	0
CXS J100057.22+023644.73	150.23842	2.61243	1.77	0	...	10.11	1.56	...	0
CXS J100028.30+024008.46	150.11790	2.66902	0.35	1	...	13.27	1.38	...	0
CXS J100000.45+022739.28	150.00188	2.46091	0.73	0	...	12.79	1.37	...	1
CXS J100016.38+023620.36	150.06823	2.60565	2.26	0	...	3.90	0.69	...	0
CXS J100015.53+023742.11	150.06469	2.62836	0.69	0	...	11.87	1.31	...	0

Note. — The contents of the COSMOS-XS multi-wavelength catalog, including a description of the various columns, are elaborated in the text.

3 The Far-infrared/Radio Correlation for Dusty Star-forming Galaxies

Abstract

We study the radio properties of 706 sub-millimeter galaxies (SMGs) selected at $870\,\mu$m with the Atacama Large Millimeter Array from the SCUBA-2 Cosmology Legacy Survey map of the Ultra Deep Survey field. We detect 273 SMGs at $> 4\sigma$ in deep *Karl G. Jansky* Very Large Array 1.4 GHz observations, of which a subset of 45 SMGs are additionally detected in 610 MHz Giant Metre-Wave Radio Telescope imaging. We quantify the far-infrared/radio correlation through parameter $q_{\rm IR}$, defined as the logarithmic ratio of the far-infrared and radio luminosity, and include the radio-undetected SMGs through a stacking analysis. We determine a median $q_{\rm IR} = 2.20 \pm 0.03$ for the full sample, independent of redshift, which places these $z \sim 2.5$ dusty star-forming galaxies 0.44 ± 0.04 dex below the local correlation for both normal star-forming galaxies and local ultra-luminous infrared galaxies (ULIRGs). Both the lack of redshift-evolution and the offset from the local correlation are likely the result of the different physical conditions in high-redshift starburst galaxies, compared to local star-forming sources. We explain the offset through a combination of strong magnetic fields ($B \gtrsim 0.2$ mG), high interstellar medium (ISM) densities and additional radio emission generated by secondary cosmic rays. While local ULIRGs are likely to have similar magnetic field strengths, we find that their compactness, in combination with a higher ISM density compared to SMGs, naturally explains why local and high-redshift dusty star-forming galaxies follow a different far-infrared/radio correlation. Overall, our findings paint SMGs as a homogeneous population of galaxies, as illustrated by their tight and non-evolving far-infrared/radio correlation.

H. S. B. Algera, I. R. Smail, U. Dudzevičiūtė *et al.*
The Astrophysical Journal 903, 138 (2020)

3.1 Introduction

The most vigorously star-forming galaxies in the Universe are known to be highly dust-enshrouded, and as such reprocess the bulk of the ultra-violet radiation associated with massive star formation to emission at rest-frame far-infrared (FIR) wavelengths. While in the local Universe these galaxies contribute little to cosmic star formation (e.g., Blain et al. 2002), early sub-millimeter surveys discovered they were orders of magnitude more numerous at high-redshift (Smail et al. 1997; Hughes et al. 1998; Barger et al. 1998). Accordingly, these distant, dust-enshrouded galaxies were dubbed sub-millimeter galaxies (SMGs, Blain et al. 2002). The sub-millimeter surveys leading to their discovery were limited in angular resolution, complicating the identification of counterparts to SMGs at other wavelengths. An effective way around this difficulty was provided by follow-up radio observations with high enough resolution allowing for a less ambiguous determination of the origin of the far-infrared emission (Ivison et al. 1998; Smail et al. 2000; Lindner et al. 2011; Barger et al. 2012). This approach relies on the close connection between the total infrared output and radio luminosity of star-forming galaxies that has been known to exist for decades (Van der Kruit 1971, 1973; De Jong et al. 1985; Helou et al. 1985; Condon 1992; Yun et al. 2001; Bell 2003). The existence of this far-infrared/radio correlation (FIRRC) is a natural outcome if galaxies are 'calorimeters', as proposed initially by Völk (1989) and Lisenfeld et al. (1996). In this model, galaxies are fully internally opaque to the ultra-violet (UV) radiation arising from massive star formation, such that these UV-photons are reprocessed by dust in the galaxy's interstellar medium, and subsequently re-radiated in the far-infrared. For this reason, far-infrared emission is a robust tracer of recent ($\lesssim 100\,\mathrm{Myr}$, e.g., Kennicutt 1998) star formation, provided the galaxy is optically thick to UV-photons. Since these very same massive stars ($M_\star \sim 8 - 40\,\mathrm{M}_\odot$, Heger et al. 2003) end their lives in Type-II supernovae, the resulting energetic cosmic rays traverse through the galaxy's magnetic field and lose energy via synchrotron emission. Provided only a small fraction of cosmic rays escape the galaxy before cooling, a correlation between the far-infrared and radio emission of a star-forming galaxy naturally arises (Völk 1989).

The ubiquity and apparent tightness of this correlation across a wide range of galaxy luminosities allows for the use of radio emission as an indirect indicator of dust-obscured star formation, and as such it has been widely utilized to study the history of cosmic star formation (e.g., Haarsma

et al. 2000; Smolčić et al. 2009; Karim et al. 2011; Novak et al. 2017). This application of the far-infrared/radio correlation at high redshift, however, requires a clear understanding of whether it evolves across cosmic time. From a theoretical point of view, such evolution is indeed expected. For example, the increased energy density of the cosmic microwave background (CMB) at high redshift is expected to suppress radio emission in star-forming galaxies, as cosmic rays will experience additional cooling from inverse Compton scattering off the CMB (e.g., Murphy 2009b; Lacki & Thompson 2010). The exact magnitude of this process, however, will depend on the magnetic field strengths of the individual galaxies, which – especially at high redshift – are poorly understood. From an observational perspective, significant effort has been undertaken to assess whether the far-infrared/radio correlation evolves throughout cosmic time. While a number of studies find no evidence for such evolution (e.g., Ivison et al. 2010b; Sargent et al. 2010; Mao et al. 2011; Duncan et al. 2020), some studies suggest redshift-evolution in the far-infrared/radio correlation in the opposite sense to what is expected theoretically (Ivison et al. 2010a; Thomson et al. 2014; Magnelli et al. 2015; Delhaize et al. 2017; Calistro Rivera et al. 2017; Ocran et al. 2020), seemingly implying that high-redshift ($z \gtrsim 1$) star-forming galaxies have increased radio emission (or, alternatively, decreased far-infrared emission) compared to their local counterparts.

The most obvious explanation of this apparent evolution is contamination of the observed radio luminosity by emission from an active galactic nucleus (AGN) in the galaxy (e.g., Murphy et al. 2009). While such emission is straightforward to identify for radio-loud AGN – precisely because it drives a galaxy away from the FIRRC – composite sources may exhibit only low-level AGN activity, making them difficult to distinguish from typical star-forming galaxies (e.g., Beswick et al. 2008; Padovani et al. 2009; Bonzini et al. 2013). A major uncertainty of the applicability of the FIRRC is therefore one's ability to identify radio-AGN, which is generally more challenging at high redshift. An additional potential driver of apparent redshift-evolution of the FIRRC involves sample selection (e.g., Sargent et al. 2010). Differences in the relative depths of the radio and far-infrared observations, if not properly taken into account, will result in a biased sample. Additionally, the sensitivity of radio- and FIR-surveys to galaxies at high redshift are typically substantially different. While (sub-)mm surveys are nearly uniformly sensitive to dust-obscured star-formation across a wide range of redshifts ($1 \lesssim z \lesssim 10$, Blain et al. 2002) and predominantly select galaxies at $z \approx 2 - 3$ (e.g., Chapman et al. 2005; Dudzevičiūtė et al.

2020) owing to the strong, negative K-correction, radio surveys instead suffer from a positive K-correction (Condon 1992), and therefore predominantly select sources around $z \sim 1$ (Condon 1989). Evidently, such selection biases must be addressed in order to assess the evolution of the far-infrared/radio correlation in the early Universe.

The cleanest way of studying any evolution in the FIRRC is therefore to start from a sample where the selection is well understood, and where radio AGN are less of a complicating factor. For this purpose, we employ the ALMA[1] SCUBA-2 UDS survey (AS2UDS), which constitutes the largest, homogeneously selected, sample of SMGs currently available (Stach et al. 2019; Dudzevičiūtė et al. 2020). While the far-infrared/radio correlation has been studied using FIR-selected samples before (e.g., Ivison et al. 2010a,b; Thomson et al. 2014), the extent to which it evolves with cosmic time has remained unclear, due to either the limited resolution of the far-infrared data, the modest available sample sizes, or biases in these samples. The more than 700 ALMA-detected SMGs from the AS2UDS survey improve upon these shortcomings, and hence allow for a detailed investigation of the far-infrared/radio correlation for strongly star-forming sources at high redshift.

The structure of this paper is as follows. In Section 3.2 we outline the sub-millimeter and radio observations of the AS2UDS sample. In Section 3.3, we separate radio-AGN from our sample, and investigate the redshift evolution of the star-forming SMGs. In Section 3.4 we discuss our results in terms of the physical properties of SMGs. Finally, we present our conclusions in Section 3.5. Throughout this paper, we adopt a flat Λ-Cold Dark Matter cosmology, with $\Omega_{\rm m} = 0.30$, $\Omega_{\Lambda} = 0.70$ and $H_0 = 70\,{\rm km\,s^{-1}\,Mpc^{-1}}$. We further assume a Chabrier (2003) Initial Mass Function, quote magnitudes in the AB system, and define the radio spectral index α such that $S_\nu \propto \nu^\alpha$, where S_ν represents the flux density at frequency ν.

3.2 Observations & Methods

3.2.1 Submillimeter Observations

The AS2UDS survey (Stach et al. 2019) constitutes a high-resolution follow-up with ALMA of SCUBA-2 $850\,\mu$m sources originally detected over the UKIDSS Ultra Deep Survey (UDS) field as part of the SCUBA-2 Cosmology Legacy Survey (S2CLS, Geach et al. 2017). The parent single-dish sub-

[1]Atacama Large Millimeter/sub-millimeter Array

millimeter survey spans an area of $0.96\,\mathrm{deg}^2$, to a median depth of $\sigma_{850} = 0.88\,\mathrm{mJy\,beam}^{-1}$. All sources detected at a significance of $> 4\sigma$ ($S_{850} \geqslant 3.6\,\mathrm{mJy}$) were targeted with ALMA observations in Band 7 ($344\,\mathrm{GHz}$ or $870\,\mu\mathrm{m}$) across four different Cycles (1, 3, 4, 5). As a result, the beam size of the data varies between $0\farcs15 - 0\farcs5$, though for source detection all images were homogenized to $0\farcs5$ FWHM. Further details of the survey strategy and data reduction are presented in Stach et al. (2019). The final submillimeter catalog contains 708 SMGs detected at $\geqslant 4.3\sigma$ ($S_{870} > 0.9\,\mathrm{mJy}$), with an estimated false-positive rate of 2%.

3.2.2 Radio Observations

The UDS field has been observed at 1.4 GHz by the *Karl G. Jansky* Very Large Array (VLA). These observations will be fully described in Arumugam et al. (in prep.) and are additionally briefly summarized in Thomson et al. (2019) and Dudzevičiūtė et al. (2020). In short, the 1.4-GHz image consists of a 14-pointing mosaic, for a total integration time of $\sim 160\,\mathrm{hr}$, across multiple VLA configurations. The bulk of the data ($\sim 110\,\mathrm{hr}$) were taken in A-configuration, augmented by $\sim 50\,\mathrm{hr}$ of observations in VLA B-array and $\sim 1.5\,\mathrm{hr}$ in the DnC configuration. The final root-mean-square (RMS) noise in the map is nearly uniform, reaching $7\,\mu\mathrm{Jy\,beam}^{-1}$ in the image centre, up to $10\,\mu\mathrm{Jy\,beam}^{-1}$ near the mosaic edges. The resulting synthesized beam is well-described by an elliptical Gaussian with major and minor axes of, respectively, $1\farcs8$ and $1\farcs6$. The final flux densities have been corrected for bandwidth-smearing, to be described in detail in Arumugam et al. (in prep.), and are provided for the AS2UDS sources by Dudzevičiūtė et al. (2020). Overall, 706/708 SMGs fall within the 1.4-GHz radio footprint covering the UDS field. These sources form the focus of this work.

The UDS field has further been targeted at 610 MHz by the Giant Metre-Wave Telescope (GMRT) during 2006 February 3-6 and December 5-10. Details of the data reduction and imaging are provided in Ibar et al. (2009). In summary, the GMRT image comprises a three-pointing mosaic, with each pointing accounting for 12 hr of observing time. The final RMS noise of the 610-MHz mosaic is $45\,\mu\mathrm{Jy\,beam}^{-1}$ in the image centre, and reaches up to $80\,\mu\mathrm{Jy\,beam}^{-1}$ near the edges, for a typical value of $65\,\mu\mathrm{Jy\,beam}^{-1}$. The synthesized beam of the image is well described by a slightly elliptical Gaussian of size $6\farcs1 \times 5\farcs1$. A total of 689 SMGs fall within the footprint of the 610 MHz observations. Source detection was performed using PyBDSF (Mohan & Rafferty 2015), down to a peak threshold of 4.0σ, leading to the identification of a total of 853 radio sources, though only a small

fraction of those are associated with AS2UDS sub-millimeter galaxies (Section 3.3). Due to the large beam size, the counterparts of AS2UDS SMGs are unresolved at 610 MHz, and as such we adopt peak flux densities for all of them. We further verified that source blending is not an issue, as only 2% of AS2UDS SMGs have more than one radio-detected source at 1.4 GHz in their vicinity within a GMRT beam full-width half maximum. In addition, for a source to be detected at 610 MHz, but not at 1.4 GHz, requires an unphysically steep spectral index of $\alpha \approx -2.7$, very different from the typical radio spectral index of $\alpha \sim -0.80$ (Condon 1992; Ibar et al. 2010, see also Section 3.3). As a result, the VLA map is sufficiently deep that further confusion or flux boosting at 610 MHz can also be ruled out when no radio counterpart is detected at 1.4 GHz.

3.2.3 Additional Multi-wavelength Data

In order to investigate the physical properties of our SMG sample, it is crucial to obtain panchromatic coverage of their spectral energy distributions (SEDs). At UV, optical and near-infrared wavelengths, these SEDs are dominated by (dust-attenuated) stellar emission, which includes spectral features that are critical for obtaining accurate photometric redshifts. As SMGs are typically high-redshift in nature ($z \approx 2-3$, e.g., Chapman et al. 2005; Danielson et al. 2017), these rest-frame wavelengths can be probed with near- and mid-infrared observations. The multi-wavelength coverage of the UDS field, as well as the association of counterparts to the SMG sample, is described in detail in Dudzevičiūtė et al. (2020), and further summarized in their Table 1, although we briefly repeat the key points here.

Dudzevičiūtė et al. (2020) collated optical/near-infrared photometry for the AS2UDS SMGs from the 11$^{\rm th}$ UDS data release (UKIDSS DR11, Almaini et al. in prep.). DR11 constitutes a K-band-selected photometric catalog covering an area of $0.8\,\mathrm{deg}^2$. The K-band image reaches a 3σ depth of 25.7 mag, in $2''$ diameter apertures, and the resulting photometric catalog contains nearly 300,000 sources. This catalog further contains photometry in the J- and H-bands from the UKIRT WFCAM, as well as Y-band observations from VISTA/VIDEO, $BVRi'z'$-band photometry from Subaru/Suprimecam and U-band observations from the CFHT/Megacam survey.

In total, 634 SMGs lie within the area covered by deep K-band imaging. The ALMA and K-band selected catalogs have been cross-matched using a radius of $0\farcs6$, resulting in 526/634 associations with an expected false-

match rate of 3.5%. A significant number of SMGs, 17%, are hence undetected even in deep K-band imaging (see Smail et al., in prep.). Further imaging in the infrared is provided by *Spitzer*, in the four IRAC channels, as well as MIPS $24\,\mu$m, as part of the *Spitzer* Legacy Program (SPUDS, PI: J. Dunlop). Upon adopting a conservative blending criterion where SMGs with nearby K-band detections are treated as upper limits (see Dudzevičiūtė et al. 2020 for details), 73% of the SMGs covered by the IRAC maps are detected at $3.6\,\mu$m. In total, 48% of SMGs are further detected at $24\,\mu$m.

While the AS2UDS sample is, by construction, detected in the sub-millimeter at $870\,\mu$m, additional sampling of the long-wavelength dust continuum is crucial in order to obtain accurate far-infared luminosities, as well constraints on SMG dust properties, such as dust masses and temperatures. For this purpose, we employ observations taken with the PACS and SPIRE instruments aboard the *Herschel* Space Observatory. To compensate for the coarse point spread function at these wavelengths and the resulting source blending, Dudzevičiūtė et al. (2020) deblended the data following Swinbank et al. (2014), adopting ALMA, *Spitzer*/MIPS $24\,\mu$m and 1.4 GHz observations as positional priors. Overall, 68% of ALMA SMGs have a measured (potentially deblended) flux density in at least one of the PACS or SPIRE bands.

3.2.4 SMG Redshifts and Physical Properties

The redshift distributions, as well as numerous other physical properties of the AS2UDS SMGs, have been investigated by Dudzevičiūtė et al. (2020). For this, they employ the SED-fitting code magphys (da Cunha et al. 2008, 2015; Battisti et al. 2019), which is designed to fit the full UV-to-radio SED of star-forming galaxies. In order to self-consistently constrain the spectral energy distribution, magphys employs an energy balance procedure, whereby emission in the UV, optical, and near-infrared is physically coupled to the emission at longer wavelengths by accounting for absorption and scattering by dust within the galaxy. The star-formation histories of individual galaxies are modeled as a delayed exponential function, following Lee et al. (2010), which corresponds to an initial linearly increasing star-formation rate, followed by an exponential decline. In addition, it allows for bursts to be superimposed on top this continuous star-formation history, during which stars are formed at a constant rate for up to 300 Myr. We note, however, that constraining the star-formation history and assigning ages by fitting to the broadband photometry of strongly dust-obscured galaxies is notoriously challenging (e.g, Hainline et al. 2011; Michałowski

et al. 2012; Simpson et al. 2014). Further details of the magphys analysis, including an extensive description of calibration and testing, are provided in Dudzevičiūtė et al. (2020).

The latest extension of magphys, presented in Battisti et al. (2019), further incorporates fitting for the photometric redshifts of galaxies. Accurate redshift information is crucial for a complete characterization of the SMG population, as any uncertainties on a galaxy's redshift will propagate into the error on derived physical quantities. Incorporating far-infrared data in the fitting can further alleviate degeneracies between optical colours and redshift, potentially allowing for a more robust determination of photometric redshifts (Battisti et al. 2019). This is especially relevant for submillimeter galaxies, as these typically constitute an optically faint population.

In total, 44 AS2UDS SMGs have a measured spectroscopic redshift. Dudzevičiūtė et al. (2020) compared the photometric redshifts (derived for both this SMG sub-sample, as well as for around 7000 field galaxies in the UDS field with spectroscopic redshifts) to the existing spectroscopic ones, and find a photometric accuracy of $\Delta z/(1+z_{\rm spec}) = -0.005 \pm 0.003$. Hence, the photometric redshifts provided by magphys are in excellent agreement with the spectroscopic values. The typical uncertainty on the photometric redshift for the AS2UDS SMGs is $\Delta z \approx 0.25$.

Finally, various physical quantities are determined for the SMG sample via magphys, including star-formation rates, mass-weighted ages, stellar and dust masses, as well as far-infrared luminosities. The accuracy of these values has been assessed by Dudzevičiūtė et al. (2020) through comparing with simulated galaxies from EAGLE (Schaye et al. 2015; Crain et al. 2015; McAlpine et al. 2019), where these properties are known a priori. The simulated and magphys-derived values for the various physical parameters are typically in good agreement.

We caution that magphys does not allow for any contribution from an AGN to the overall SED. In particular, emission from a mid-infrared power-law component, indicative of an AGN torus, may therefore result in slightly boosted FIR-emission. Such a mid-infrared power law is however not expected to contaminate the observed $870\,\mu$m (rest-frame $\sim 250\,\mu$m) flux density (e.g., Lyu & Rieke 2017; Xu et al. 2020), and as such does not affect our sample selection. Therefore, we can quantify the typical contribution of the mid-infrared power-law to the total infrared luminosity for the AS2UDS SMGs. For this, we limit ourselves to the 442 SMGs at $z \leqslant 3.0$,

following Stach et al. (2019), since above this redshift the criteria are prone to misclassifying dusty star-forming galaxies. This constitutes a total of 82 sources (12% of the full AS2UDS sample). We find the median $8-1000\,\mu$m luminosity to be $\log_{10} L_{\rm FIR} = 12.54^{+0.07}_{-0.04}\,L_\odot$ and $\log_{10} L_{\rm FIR} = 12.33^{+0.02}_{-0.03}\,L_\odot$ for sources with and without a mid-infrared power-law, respectively. We therefore conclude that the typical AGN contribution to the total infrared luminosity is at most $\lesssim 0.2$ dex.

An additional diagnostic of an AGN is luminous X-ray emission. However, only one-third of the AS2UDS SMGs lie within the footprint of the available *Chandra* X-ray imaging as part of the X-UDS survey (Kocevski et al. 2018; see also Stach et al. 2019). In particular, out of the 23 SMGs associated with strong X-ray emitters, 18 are additionally identified as AGN through their mid-infrared power-law emission. Therefore, when discussing AGN in the SMG population, we focus on the 82 mid-infrared-selected sources, which make up the bulk of the AGN in the AS2UDS sample.

Studies of radio-selected samples have shown that AGN activity at radio wavelengths is often disjoint from AGN-related emission at X-ray and mid-infrared wavelengths (e.g., Delvecchio et al. 2017; Algera et al. 2020b). In particular, Algera et al. (2020b) show that radio sources with X-ray and/or mid-infrared power-law emission fall onto the same far-infrared/radio correlation as "clean" star-forming sources. For this reason, we have decided to retain sources with non-radio AGN signatures in our sample (Section 3.3.2). In all relevant figures in this work, we however distinguish between "clean SMGs" and sources with a mid-infrared power-law signature via different plotting symbols. We additionally emphasize that our results are unaffected if these AGN are removed from the analysis entirely.

3.2.5 Radio Stacking

A comprehensive analysis of the far-infrared/radio correlation requires addressing any biases in the sample selection. In particular, the majority of AS2UDS sources are not detected in the 1.4-GHz VLA map (about 60%; Section 3.3.1), yet their – a priori unknown – radio properties must still be included in the analysis. In this work, we employ a stacking technique in order to obtain a census of the typical radio properties of the AS2UDS sample.

For the stacking, we create cutouts of 51×51 pixels ($18'' \times 18''$) from the 1.4 GHz radio map, centered on the precise ALMA positions of the AS2UDS sources. We average these cutouts together by taking the median value across each pixel. In order to properly account for the full SMG popu-

lation, we stack both the radio-detected and -undetected SMGs together. Additionally, we stack empty regions within the image, away from radio sources, to create an "empty" stack indicative of the background and typical RMS-value (following e.g., Decarli et al. 2014). We have verified that the RMS is reduced following a typical $1/\sqrt{N}$-behaviour, where N is the number of sources being stacked. This indicates we are not significantly affected by confusion noise. We pass both the real and empty stacks to PyBDSF (Mohan & Rafferty 2015) to obtain peak, integrated, and aperture flux densities. We have run extensive simulations, using mock sources inserted into the image plane, to ascertain which flux density is the correct one to use. We elaborate on these simulations in Appendix 3.A, and will describe them in further detail in a future work (Algera et al. in prep.). The simulations show that integrated fluxes provide the most robust flux measurement for our data at moderate signal-to-noise (SNR $\gtrsim 10$). In this work, we therefore use integrated fluxes obtained from PyBDSF. The only exceptions are the GMRT 610-MHz stacks described in Section 3.3.3, since due to the large beam size (about $5''$) all stacks are unresolved, and peak and integrated flux densities are consistent. For the GMRT stacks, we therefore adopt peak flux densities.

In order to determine realistic uncertainties on the stacked flux densities, we perform a bootstrap analysis, whereby we repeat the procedure described above 100 times. This involves sampling SMGs from each bin with replacement, such that duplicate cutouts are allowed. In this way, the uncertainties on the final flux density reflect both the uncertainties on the photometry, as well as the intrinsic variation in the radio flux densities among the AS2UDS SMGs.

3.3 Results

3.3.1 Radio Properties of AS2UDS

In total, 273 out of the 706 SMGs in the 1.4-GHz coverage of AS2UDS (39%) can be cross-matched to a radio counterpart detected at $\geqslant 4\sigma$ at 1.4 GHz, within a matching radius of $1\farcs6$ (chosen such that the fraction of false positives is 1%; Dudzevičiūtė et al. 2020). This detection fraction is typical for high-redshift SMGs (e.g., Biggs et al. 2011; Hodge et al. 2013). We additionally detect 45 SMGs down to a 4σ threshold in the shallower 610 MHz observations. All of the sources detected in the 610 MHz map have a counterpart at 1.4 GHz, based on a cross-matching radius of $2\farcs0$. This is slightly

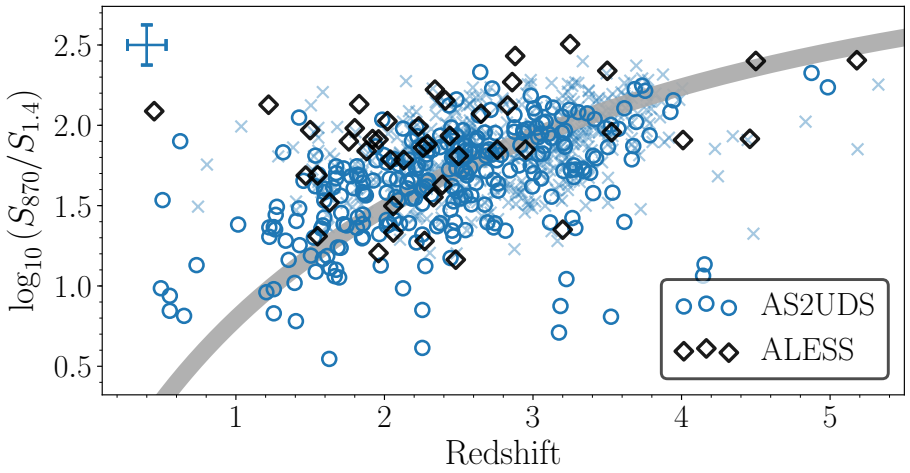

Figure 3.1: Ratio of the sub-millimeter to radio flux density as a function of redshift, for both the AS2UDS and ALESS samples. This ratio provides a crude proxy for redshift (Carilli & Yun 1999), as a result of the different typical K-corrections at $870\,\mu$m and 1.4 GHz. The expected trend with redshift is overlaid in gray, assuming a fixed far-infrared luminosity, dust emissivity and temperature, and FIRRC-parameter $q_{\rm IR}$ (see text for details). In total, 273 (433 undetected) AS2UDS SMGs are detected at $\geqslant 4\sigma$ (lower limits are shown as crosses) at 1.4 GHz, compared to 44 (32 undetected; not shown) for ALESS. The increase in sample size in comparison to ALESS constitutes nearly a factor of ten.

larger than matching radius adopted for the VLA radio data to account for the coarser GMRT 610 MHz resolution, but still ensures a small false positive fraction of $\lesssim 0.1\%$.

We present the far-infrared and radio properties of the AS2UDS sample in Figure 3.1, which shows the ratio of sub-millimeter to radio flux density for the AS2UDS SMGs as a function of redshift. As result of the different K-corrections in the far-infrared and radio, this ratio provides a crude proxy for redshift (e.g., Carilli & Yun 1999). The AS2UDS detections are consistent with the expected trend, plotted for a galaxy with a far-infrared luminosity of $10^{12.5} L_{\odot}$, which is typical for AS2UDS (Dudzevičiūtė et al. 2020). This further assumes a fixed dust emissivity and temperature of $\beta = 1.8$ and $T_{\rm dust} = 35\,$K, respectively, as well as a fixed radio spectral index of $\alpha = -0.8$ and a redshift-independent FIRRC, equal to the median value for AS2UDS (Section 3.3.3). There is, however, substantial scatter around this trend, as may be expected from intrinsic variations in the dust

and radio properties of our SMG sample.

Figure 3.1 further emphasizes the substantial increase in sample size that AS2UDS provides compared to the ALESS survey (Hodge et al. 2013; Karim et al. 2013). The latter constitutes an ALMA follow-up of SMGs originally identified in the Extended *Chandra* Deep Field South as part of the LESS survey using the LABOCA bolometer (Weiß et al. 2009). ALESS is similar to AS2UDS in terms of sample selection, and therefore provides the best means of comparison for this work. Additionally, the depth of both its far-infrared and radio observations closely match that of AS2UDS. In total, the ALESS survey covers 76 SMGs within its radio footprint (Thomson et al. 2014). AS2UDS, therefore, constitutes a sample nearly ten times larger than ALESS. We compare the combined far-infrared and radio properties of the AS2UDS and ALESS samples in Section 3.4.1.

We show the redshift distribution of the AS2UDS sources with radio detections in Figure 3.2 (left panel). As expected, the radio sources lie at a slightly lower redshift than the overall AS2UDS population, owing to the different K-corrections for typical radio and submillimeter detected sources. The median redshift of the 1.4-GHz detected subsample is $\langle z \rangle = 2.44^{+0.04}_{-0.15}$, while that of the 45 GMRT-detected sources is $\langle z \rangle = 1.85^{+0.24}_{-0.21}$, compared to $\langle z \rangle = 2.62^{+0.06}_{-0.04}$ for the full sample of AS2UDS SMGs (Dudzevičiūtė et al. 2020).

We find a typical spectral index between 610 and 1400 MHz of $\alpha = -0.77^{+0.05}_{-0.03}$, consistent with the typical radio spectrum of star-forming galaxies of $\alpha \approx -0.80$ (e.g., Condon 1992; Ibar et al. 2010). Nevertheless, there is substantial variation in the spectra among the 45 sources detected at the two radio frequencies, with the 16^{th}-84^{th} percentile range spanning $\alpha \in [-1.19, -0.48]$. This range is wider than the variation expected based on the typical uncertainty on the spectral index of ~ 0.24 dex, indicating that at least some of this scatter is intrinsic variation in the radio spectral indices. The full distribution of spectral indices, including lower limits for sources detected solely at 1.4 GHz, is shown in the middle and right panels of Figure 3.2. These limits were calculated by adopting four times the local RMS noise at the position of the radio source as an upper limit on the GMRT flux density. It is evident that most of the resulting lower limits on the spectral index are not very constraining, due to the limited depth of the 610 MHz data. In order to assign a spectral index to the entire radio-detected population, we median stack all AS2UDS SMGs detected solely at 1.4 GHz in both radio maps (225 sources within both the VLA and GMRT

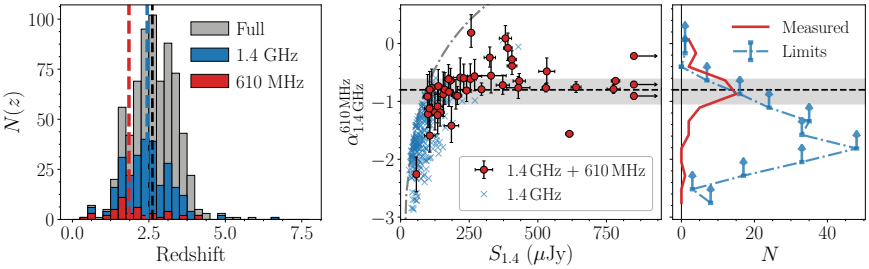

Figure 3.2: Left: Distribution of the radio-detected AS2UDS population as a function of redshift. The full AS2UDS sample is shown, as are the subset detected at 1.4 GHz, and those sources detected at both 610 MHz and 1.4 GHz. The vertical, dashed lines show the median redshift of these three populations. The radio-detected subset lies at a slightly lower redshift than the full AS2UDS sample, as a result of the different K-corrections for the typical FIR- and radio-detected populations. **Middle:** Radio spectral index as a function of the 1.4-GHz flux density. Sources with a 610 MHz detection, and hence with a measured spectral index, are highlighted. As expected, a large fraction of the lower limits on the spectral index corresponds to faint radio sources. The dash-dotted line indicates the shallowest spectral index these sources can have in order to be detected at both 610 and 1400 MHz, assuming the central RMS of $45\,\mu$Jy beam^{-1} at 610 MHz. For the limits, we adopt a fixed spectral index of $\alpha = -0.80$ (dashed horizontal line). This value lies well within the 1σ uncertainty on the stacked spectral index we find for AS2UDS subset detected at 1.4 GHz but not at 610 MHz (gray shaded region). Three sources with $S_{1.4} > 1$ mJy lie outside the plotting limits, and are shown as the arrows placed on the right. **Right:** Distribution of spectral indices for the radio-detected AS2UDS sample, including direct measurements and lower limits. In this work, we mostly rely on a single radio detection at 1.4 GHz, and hence adopt a fixed spectral index for the majority of the radio-detected SMG sample.

footprints). The typical stacked $610-1400$ MHz spectral index is then found to be $\alpha = -0.81^{+0.20}_{-0.23}$. This value is consistent with the median spectral index obtained for the AS2UDS subsample having two radio detections, as well as with the typically assumed value of $\alpha = -0.80$ for SMGs. For ease of comparison to the literature, we will therefore adopt a fixed $\alpha = -0.80$ for all AS2UDS SMGs detected only in the 1.4-GHz map. We note that, while the beam size of our GMRT observations is significantly larger than that of the VLA data, the typical low-frequency radio sizes of SMGs are $\sim 0.5-1.5''$ (Miettinen et al. 2017; Jiménez-Andrade et al. 2019; Thomson et al. 2019), similar to the synthesized beam at 1.4 GHz. As such, this is much smaller than the largest angular scale to which we are sensitive with our data of $\sim 120''$ based on the ~ 50 h of data taken in the VLA B-array configura-

tion.[2] Thomson et al. (2019) have further empirically verified the robustness of the theoretical largest angular scale, and as such, we do not expect to miss any diffuse emission at 1.4 GHz. Our spectral index measurements are therefore unaffected by the differing resolutions of our radio observations (see also Gim et al. 2019). We further discuss the spectral indices of the AS2UDS sample in Section 3.3.3.

Given these spectral indices for the radio-detected SMG subsample, we calculate the luminosity at a rest-frame frequency of $\nu = 1.4\,\mathrm{GHz}$ as

$$L_{1.4} = \frac{4\pi D_L^2}{(1+z)^{1+\alpha}} S_{1.4}\,. \tag{3.1}$$

Here D_L is the luminosity distance to a source at redshift z, and $S_{1.4}$ is its flux density at the observer-frame frequency of 1.4 GHz. Note that our 1.4-GHz radio observations probe a typical rest-frame frequency of $\nu \sim 5$ GHz, for a source at the median AS2UDS redshift. Adopting the 16^{th} or 84^{th} percentile of our spectral index distribution for the K-correction (instead of $\alpha = -0.80$) leads to a typical difference of a factor of $1.5\times$ in the rest-frame 1.4-GHz radio luminosity. For SMGs without a radio counterpart, we adopt $4\times$ the local RMS-noise in the 1.4 GHz map and a fixed spectral index of $\alpha = -0.80$ in order to calculate the corresponding upper limit on the radio luminosity. The far-infrared luminosities for the AS2UDS sample, obtained via magphys, are determined in the wavelength range $8 - 1000\,\mu$m, and allow us to define the parameter q_{IR} characterizing the far-infrared/radio correlation. Following e.g., Condon et al. (1991b); Bell (2003); Magnelli et al. (2015); Calistro Rivera et al. (2017), we define it as:

$$q_{\mathrm{IR}} = \log_{10}\left(\frac{L_{\mathrm{FIR}}}{3.75\times10^{12}\,\mathrm{W}}\right) - \log_{10}\left(\frac{L_{1.4}}{\mathrm{W\,Hz^{-1}}}\right)\,. \tag{3.2}$$

Here, the FIR-luminosity L_{FIR} is normalized such that q_{IR} is dimensionless. For the full radio-detected subsample, we find a median $q_{\mathrm{IR}} = 2.10 \pm 0.02$. Had we neglected the 610-MHz data and instead assumed a fixed spectral index of $\alpha = -0.80$, we would obtain a similar value of $q_{\mathrm{IR}} = 2.11 \pm 0.02$. This value is lower than what is found for local, typically less strongly star-forming galaxies of $q_{\mathrm{IR}} = 2.64 \pm 0.02$ (Bell 2003). However, it is similar to the values found by Kovács et al. (2006) and Magnelli

[2] The largest angular scale in A-array, accounting for two-thirds of the observation time, equals $36''$, still significantly ($\sim 40\times$) larger than the typical radio sizes of SMGs.

et al. (2010) of respectively $q_{\rm IR} = 2.07 \pm 0.09$ and $q_{\rm IR} = 2.17 \pm 0.19$ for $z \approx 2$ radio-detected dusty star-forming galaxies, although other studies of SMGs find typical values for $q_{\rm IR}$ that are more similar to the local correlation (e.g., Sargent et al. 2010; Ivison et al. 2010a). We emphasize, however, that the average value of $q_{\rm IR}$ for any given sample is highly dependent on its selection, and the relative depths of the far-infrared and radio observations. Therefore, we compare with the results from the ALESS survey by Thomson et al. (2014) in more detail in Section 3.4.1, as both its submillimeter selection and radio coverage at 1.4 GHz are similar to that of AS2UDS.

In the following sections, we will study the far-infrared/radio correlation for two samples. First of all, we utilize all SMGs within the redshift range $1.5 \leqslant z \leqslant 4.0$, totalling 659 sources (93% of the entire AS2UDS sample). We limit ourselves to this redshift range to provide a more uniform selection of SMGs (Dudzevičiūtė et al. 2020), and will refer to this sample as the "full AS2UDS sample". Secondly, we follow Dudzevičiūtė et al. (2020) and focus on the 133 SMGs at $1.5 \leqslant z \leqslant 4.0$ within the luminosity range $L_{\rm FIR} = 4 - 7 \times 10^{12}\ L_{\odot}$ with at least one *Herschel*/SPIRE detection. By restricting ourselves to this luminosity range, we ensure the sample is complete with respect to the SPIRE detection limits. As such, we retain a subsample complete in far-infrared luminosity, but with better constraints on its dust properties, due to the additional sampling of the far-infrared SEDs. Following Dudzevičiūtė et al. (2020), we will refer to this sample as the "luminosity-limited sample".

3.3.2 AGN in AS2UDS

A subset of our SMG sample exhibits strong radio emission causing them to be substantially offset from the far-infrared/radio correlation for purely star-forming galaxies (Figure 3.3). This excess in radio power is attributed to additional emission from an active galactic nucleus in the centre of the galaxy, and hence forms a contaminant for studies of the far-infrared/radio correlation. As a result, such radio-excess AGN must be discarded from our sample, as it is not possible to disentangle the radio emission emanating from star formation or from the central AGN without resolving the radio emission, via e.g., very long baseline interferometry (e.g., Muxlow et al. 2005, 2020; Middelberg et al. 2013). Typically, radio-excess AGN are seen to be hosted in red, passive galaxies (Smolčić 2009). Nevertheless, about 1% of local Ultra-Luminous Infra-Red Galaxies (ULIRGs) are also known

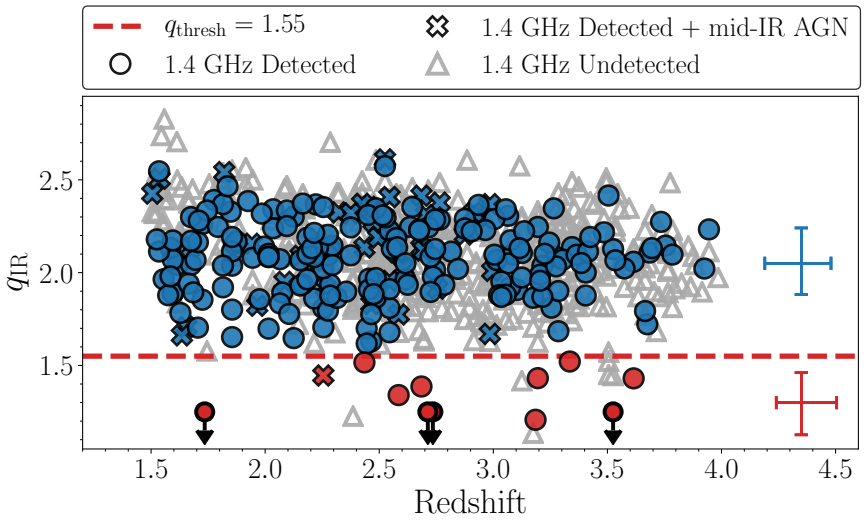

Figure 3.3: Distribution of $q_{\rm IR}$ as a function of redshift for the AS2UDS SMGs within $1.5 \leqslant z \leqslant 4.0$. Galaxies with radio emission consistent with originating from star formation, defined as $q_{\rm IR} > 1.55$ (red dashed line) are shown in blue, whereas radio-excess AGN are shown in red. The plotting limits are chosen to focus on the cloud of star-forming sources around $q_{\rm IR} \sim 2.1$, which cuts off four radio-excess AGN within the range $q_{\rm IR} = 0.35 - 0.95$. These are shown as red circles with downward pointing arrows. We additionally show two representative errorbars for the radio-detected star-forming and AGN populations. Lower limits on $q_{\rm IR}$ are calculated using the corresponding upper limits on the SMG radio luminosity. Overall, AGN make up only 1.8 ± 0.5% of the SMG population, and hence the radio emission of the majority of SMGs is consistent with originating from star formation.

to host such AGN (Condon & Broderick 1986, 1991; Yun et al. 1999). Because our selection of SMGs does not involve their radio properties, it allows for an unbiased census of radio-excess AGN in high-redshift, strongly star-forming galaxies, as compared to previous radio-selected studies.

We identify AGN based on a fixed threshold of $q_{\rm IR} \leqslant 1.55$, with sources below this threshold being defined as a radio-excess AGN (following e.g., Del Moro et al. 2013). This value is chosen such that sources that are $\gtrsim 5\times$ radio-brighter compared to the median (stacked) FIRRC for the AS2UDS sample, as derived in Section 3.3.3, are identified as radio-excess AGN. Our threshold is similar to the value of $q_{\rm IR} = 1.70$ adopted by Thomson et al. (2014), but takes into account that our typical $q_{\rm IR}$ is slightly lower than that of their sample.

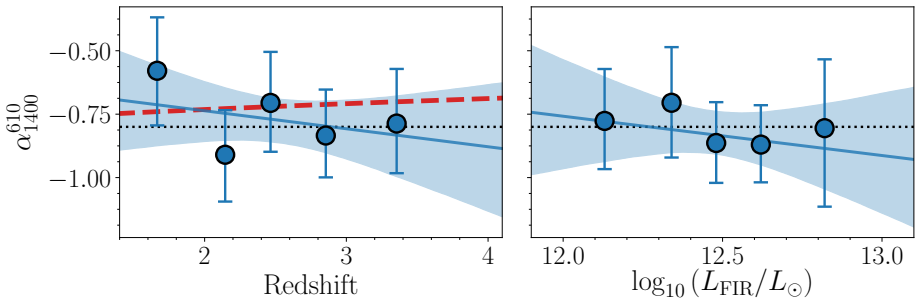

Figure 3.4: The spectral index between 610 MHz and 1.4 GHz for the full AS2UDS sample within $1.5 \leqslant z \leqslant 4.0$ (629 sources in total), computed for stacks in five bins in redshift (left) and FIR-luminosity (right). The expected redshift-evolution of the spectral index for an assumed synchrotron (free-free) spectral index of $\alpha = -0.85$ ($\alpha = -0.10$) and a thermal contribution of 10% at rest-frame 1.4 GHz is shown via the red dashed line in the left panel (e.g., Condon 1992). In both panels a linear fit is shown via the blue line, with the uncertainty shown through the shaded region. The fits are consistent with no gradient in both redshift and far-infrared luminosity, and hence adopting a fixed $\alpha = -0.80$ (black dotted line) does not affect our calculation of the far-infrared/radio correlation.

Upon adopting $q_{\rm IR} = 1.55$ as our threshold, we find 12 radio-excess AGN within the full AS2UDS sample (Figure 3.3), corresponding to a surface density of $\sim 12.5 \pm 3.6\,{\rm deg}^{-2}$ at $S_{870} \gtrsim 4$ mJy and $S_{1.4} \gtrsim 30\,\mu$Jy beam^{-1}. Overall, 1.8 ± 0.5% of SMGs therefore hosts a radio-excess AGN, similar to what is observed in local ULIRGs (Condon & Broderick 1986, 1991; Yun et al. 1999). We have further investigated adopting other possible thresholds for identifying radio-excess sources, including using different cuts in $q_{\rm IR}$, or adopting a redshift-dependent threshold in $q_{\rm IR}$. The latter is commonly used for identifying AGN in radio-selected samples (Delhaize et al. 2017; Calistro Rivera et al. 2017). However, we find that the far-infrared/radio correlation for AS2UDS is insensitive to the particular threshold we adopt, as the fraction of radio-excess AGN we identify among our sample is small regardless. As such, we proceed with a threshold of $q_{\rm IR} = 1.55$.

3.3.3 (A lack of) Redshift Evolution in the FIRRC

In this section, we set out to constrain whether there is any redshift-evolution in the far-infrared/radio correlation for the AS2UDS sub-millimeter galaxies. In recent years, several studies have hinted at a decreasing value of

$q_{\rm IR}$ at increasing redshift. However, these studies have mainly been based on radio-selected samples (e.g., Delhaize et al. 2017; Calistro Rivera et al. 2017) or optically selected samples (e.g., Magnelli et al. 2015). Thomson et al. (2014) carried out a study of the FIRRC based on a sub-millimeter selected sample from the ALESS survey. However, with a modest sample of ~ 70 sources, Thomson et al. (2014) were unable to distinguish between a redshift-independent far-infrared/radio correlation, or one where $q_{\rm IR}$ decreases with redshift, as seen in radio-selected studies. With its tenfold increase in sample size, AS2UDS now provides a set of SMGs numerous enough to distinguish between these possible scenarios.

Before we proceed, we address one potential limitation of our analysis, which is the lack of available spectral indices for the majority of our radio sample. It has recently been suggested that a simple power-law approximation for the radio spectrum of highly star-forming galaxies may be insufficient, and that in fact radio spectra may exhibit a spectral break around a rest-frame frequency of ~ 5 GHz (Tisanić et al. 2019; Thomson et al. 2019). For the full AS2UDS sample, where we probe rest-frame frequencies between $\nu_{\rm rest} = 3.5 - 7$ GHz, any spectral steepening at high frequencies will affect the radio luminosities we calculate at rest-frame 1.4 GHz, which in turn will affect $q_{\rm IR}$. A source at redshift z with a true spectral index α, for which a fixed value of $\alpha = -0.80$ was assumed, will have a calculated value of $q_{\rm IR}$ which is off by $\Delta q_{\rm IR} = -\left(0.80 + \alpha\right) \times \log_{10}\left(1 + z\right)$, which amounts to approximately 0.2 dex at $z = 3$ for a spectral index equal to the $16^{\rm th}$ or $84^{\rm th}$ percentiles of our α_{1400}^{610}−distribution. Any systematic variations in the radio spectral index with redshift will therefore induce – or potentially mask – evolution in the FIRRC.

To assess the extent to which such variations might affect the far-infrared/radio correlation for AS2UDS, we stack the full SMG sample – excluding radio AGN, but including sources undetected at 1.4 GHz – in five distinct redshift bins, in both the 610-MHz and 1.4-GHz maps. We additionally stack in $L_{\rm FIR}$ and show the results in Figure 3.4. A linear fit through the data shows no evidence of spectral index evolution with either redshift or far-infrared luminosity, with a linear slope of -0.07 ± 0.16 and -0.15 ± 0.42 for the two parameters, respectively. The mean spectral indices are $\langle\alpha\rangle_z = -0.76 \pm 0.07$ for the redshift bins, and $\langle\alpha\rangle_{L_{\rm FIR}} = -0.80 \pm 0.04$ for the stacks in far-infrared luminosity. Both values are consistent with a typical spectral slope of $\alpha = -0.80$, as well as with each other, within the uncertainties. We further compare our values with the evolution expected in the spectral index when assuming an increasing contribution of free-free emission at

high redshift, as a result of probing higher rest-frame frequencies for these galaxies. For this, we assume the simple model for star-forming galaxies from Condon (1992), with a spectral index for synchrotron and free-free emission of, respectively, $\alpha_{\text{synch}} = -0.85$ and $\alpha_{\text{FF}} = -0.10$ (consistent with the values found by Niklas et al. 1997; Murphy et al. 2011). The expected flattening of the 610-1400 MHz spectral index between $1.5 \leqslant z \leqslant 4.0$ is $\Delta\alpha \lesssim 0.1$, and we find no evidence for such modest evolution. This is fully consistent with Thomson et al. (2019), who in fact find a deficit in free-free emission for high-redshift SMGs. Overall, we find no significant variation in the $610 - 1400$ MHz spectral index with either redshift or L_{FIR}, and we therefore conclude that the adopted radio spectral index is unlikely to be a driver of any trends in the AS2UDS far-infrared/radio correlation.

We now proceed by investigating any potential redshift evolution in the far-infrared/radio correlation for sub-millimeter galaxies. In Figure 3.5 we show q_{IR} as a function of redshift for the full AS2UDS sample and the luminosity-limited sample. In both cases, we fit a function of the form $q_{\text{IR}}(z) \propto (1+z)^{\gamma}$ to *only* the SMGs detected at 1.4 GHz. As such, this sample is by construction biased towards radio-bright sources at higher redshift. For the full radio-detected AS2UDS sample, we find a lack of redshift-evolution, with a best fit solution of $\gamma_{\text{full}} = -0.01 \pm 0.03$. For the luminosity-limited sample, we do find an apparent evolution, and measure $\gamma_{\text{lum}} = -0.26 \pm 0.06$. However, this evolution is heavily driven by selection effects. While this sample is complete in far-infrared luminosity, the radio observations suffer from a positive K-correction, limiting the detection rate at high redshift. As a result, we are biased towards only the brightest radio sources at $z \gtrsim 3$. For a fixed range in L_{FIR} – which the luminosity-limited sample is by construction – radio-bright sources will have a low value of q_{IR}, and hence drive the average q_{IR} down at higher redshift.

While the lack of redshift evolution for the full radio-detected AS2UDS sample – which *still* is biased – is already interesting by itself, we need to address the radio-undetected population to get a proper census of any potential evolution of q_{IR} across redshift. We do this by stacking the full and luminosity-limited samples in distinct redshift bins, having removed any radio AGN. We show q_{IR} as a function of redshift for the stacked full and luminosity-limited samples in the bottom panels of Figure 3.5. Neither sample shows any evidence of variation with redshift, with the full sample following a trend given by $\gamma_{\text{full}} = 0.02 \pm 0.06$, and the luminosity-limited sample having a best fit of $\gamma_{\text{lum}} = -0.02 \pm 0.16$. For reference, we addition-

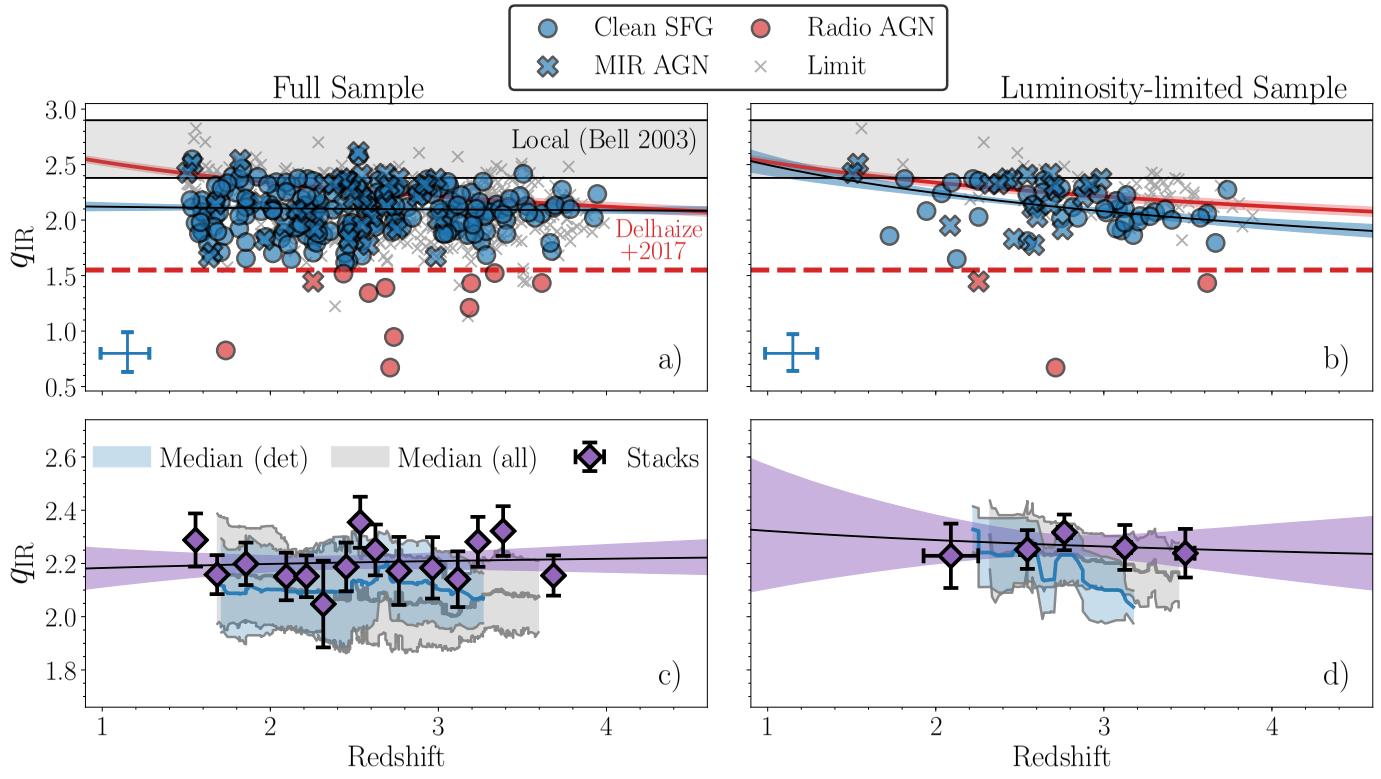

Figure 3.5: The far-infrared/radio correlation for AS2UDS as a function of redshift. **a)** the FIRRC for the full AS2UDS sample. The radio-detected star-forming sources are fitted by a power law of the form $q_{\rm IR} \propto (1+z)^{\gamma}$. This fit and corresponding 1σ uncertainty are indicated via the black line and the blue, shaded region. The FIRRC for the full radio-detected AS2UDS sample shows no hint of redshift-evolution. For comparison, the local FIRRC and 1σ scatter from Bell (2003) is shown via the gray shaded band, and the evolving $q_{\rm IR}$ from Delhaize et al. (2017) is shown in red. A representative errorbar on $q_{\rm IR}$ is shown in the bottom left corner, and star-forming sources and AGN are separated adopting a threshold of $q_{\rm IR} = 1.55$ (dashed red line). **b)** the FIRRC for the radio-detected luminosity-limited AS2UDS sample. In contrast to the full sample, this subset *does* show (artificial) evolution with redshift, as we select sources within a narrow range of $L_{\rm FIR}$, but are only sensitive to the brightest radio sources at the high-redshift tail of AS2UDS. **c)** the FIRRC for the full AS2UDS sample, based on stacking in the 1.4-GHz radio map in 15 distinct redshift bins. The black line and purple shaded region show a power-law fit through these points, and its corresponding confidence interval. The blue (gray) shaded region shows the running median through the radio detections (detections + non-detections), where the spread indicates the median absolute deviation. The stacked full AS2UDS sample shows no hint of redshift-evolution. **d)** the stacked FIRRC for the luminosity-limited AS2UDS sample. In contrast to the radio-detections only, the stacked luminosity-limited sample shows no redshift-evolution in its far-infrared/radio correlation.

ally show the fifteen stacks and corresponding residuals of the full sample in Appendix 3.A (Figure 3.10). We ensure the stacks are all of sufficient signal-to-noise (SNR $\gtrsim 10$), such that reliable integrated flux measurements can be made, and any effects of noise boosting are minimal. As a result, the higher redshift bins contain a larger number of sources than the low-redshift ones, to compensate for the negative radio K-correction. We verified however, that the results are not affected by the method of binning, and simply adopting bins with an equal number of sources gives consistent results in all cases.

From the stacked results we further obtain an average value of $q_{\rm IR}$ that, given our observed lack of redshift-evolution, is representative for submillimeter galaxies. For the full AS2UDS sample, we find a mean $q_{\rm IR,full} = 2.20 \pm 0.03$, where the error represents the bootstrapped variation among the stacks. For the luminosity-limited sample, we find a similar value of $q_{\rm IR,lum} = 2.26 \pm 0.02$, although across only five redshift bins. We further verify in Appendix 3.A that the expected systematic uncertainty on these values, as a result of our reliance on a stacking analysis, is small, and amounts to $\Delta q_{\rm IR} \lesssim 0.05$. As the typical values of $q_{\rm IR}$ for the full and luminosity-limited samples are consistent with one another, we will in the following investigate any possible trends between $q_{\rm IR}$ and other physical parameters for the full AS2UDS sample, as its radio and far-infrared properties match those of the luminosity-limited subsample. Interestingly, this typical $q_{\rm IR}$ for both samples is ~ 0.4 dex lower than the far-infrared/radio correlation observed locally (Bell 2003). We discuss this offset further in Section 3.4.2.

3.3.4 Correlations with Physical Properties

AS2UDS provides a large sample of SMGs for which Dudzevičiūtė et al. (2020) have derived various physical properties via magphys, such as stellar and dust masses, and star-formation rates. In this section, we investigate if there is any variation in $q_{\rm IR}$ as a function of these parameters. In Figure 3.6 we show $q_{\rm IR}$ as a function of, respectively, $L_{\rm FIR}$, SFR, $M_\star$, $M_{\rm dust}$, $T_{\rm dust}$ and effective observed-frame $870\,\mu$m-radius $R_{\rm eff}$, the latter of which was calculated for a subset of submm-bright AS2UDS sources by Gullberg et al. (2019). In total, we have robust size measurements for 153 SMGs (70 are detected at 1.4 GHz). In order to assess the variation in $q_{\rm IR}$ in an unbiased way, we perform a stacking analysis by dividing our SMG sample into distinct bins for the aforementioned physical parameters, after the removal of radio AGN.

The first panel shows $q_{\rm IR}$ as a function of infrared luminosity. While

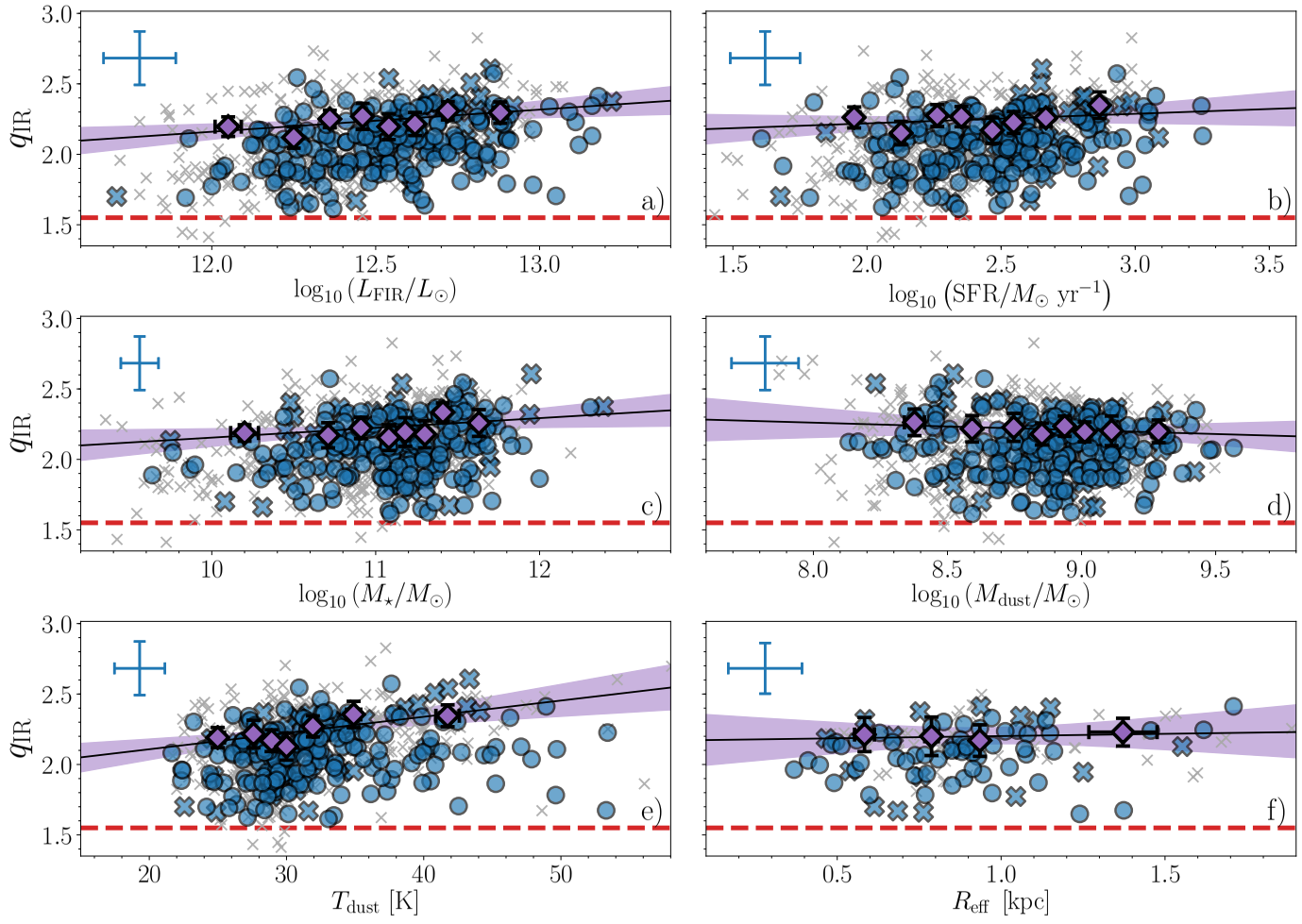

Figure 3.6: FIRRC parameter $q_{\rm IR}$ as a function of several physical parameters for the full AS2UDS sample, after removal of radio-excess AGN. In all panels, we show radio-detected SMGs as blue circles (or blue crosses, when they show a mid-infrared AGN signature). A representative uncertainty for these is shown in the upper left corner of each panel. Lower limits on $q_{\rm IR}$ are shown as gray crosses. The stacks are plotted as purple diamonds, with a linear fit to the stacks shown via the black line. The purple shaded region indicates the corresponding $16^{\rm th}$-$84^{\rm th}$ percentile confidence region on the fit. **a)** $q_{\rm IR}$ as a function of far-infrared luminosity. **b)** $q_{\rm IR}$ as a function of star-formation rate. **c)** $q_{\rm IR}$ as a function of stellar mass. **d)** $q_{\rm IR}$ as a function of dust mass. **e)** $q_{\rm IR}$ as a function of dust temperature. **f)** $q_{\rm IR}$ as a function of effective radius for sources with a robust submillimeter size measurement from Gullberg et al. (2019). None of the panels show any significant trends between $q_{\rm IR}$ and the various physical parameters at a $\geqslant 2\sigma$ level.

the radio-detected subset of AS2UDS follows a weak positive trend, any correlation disappears when stacking. A linear fit through the stacked datapoints indicates a slope of $\beta = 0.16 \pm 0.10$, consistent with no evolution. Similarly, no correlation between $q_{\rm IR}$ and star-formation rate exists (slope of $\beta = 0.07 \pm 0.10$), which is expected since $L_{\rm FIR}$ should be a good proxy for the star-formation rate of SMGs.

Similarly, there does not appear to be any strong trend between $q_{\rm IR}$ and stellar mass, with a linear fit through the stacks being consistent with a slope of zero ($\beta = 0.07 \pm 0.06$). Likewise, there is no evidence for any trends between $q_{\rm IR}$ and either dust mass or temperature, with a slope of $\beta = -0.06 \pm 0.11$ and $\beta = (11 \pm 6) \times 10^{-3}$, respectively. Since no trend with dust luminosity exists, which is a combination of $M_{\rm dust}$ and $T_{\rm dust}$, it is unsurprising that neither of these two parameters show any trend with $q_{\rm IR}$ either. Finally, we show $q_{\rm IR}$ as a function of $870\,\mu$m effective radius. As only a quarter of the full AS2UDS sample has measured submillimeter radii, we employ a smaller number of bins to obtain sufficient signal-to-noise in each stack. Nevertheless, we see no hint of a trend between $q_{\rm IR}$ and $R_{\rm eff}$, with a best-fitting linear slope of $\beta = 0.03 \pm 0.19$.

Overall, the AS2UDS SMGs do not appear to show any strong variation in $q_{\rm IR}$ as a function of their physical properties. None of the six parameters explored show any hint of a correlation with $q_{\rm IR}$ at a 2σ or greater level. This may be the result of the relatively small dynamic range spanned by the sample, or may in fact imply that the FIRRC constitutes an especially robust correlation, even at high star-formation rates and high redshift. We further discuss this in Section 3.4.2.

3.4 Discussion

3.4.1 Previous Studies of the FIRRC

Neither the full AS2UDS sample, nor its radio-detected subset, show any evidence for evolution in their far-infrared/radio correlations. In this Section, we compare this lack of evolution with previous studies, including radio-based ones, which typically have large sample sizes, and SMG-based ones, having selection criteria that are more similar to ours.

Recently, the FIRRC has been studied by Delhaize et al. (2017) for the 3 GHz selected VLA-COSMOS sample (Smolčić et al. 2017b,a). They utilize a sample of nearly 10,000 star-forming galaxies at a median redshift of $z \sim 1.0$, and employ a survival analysis to attempt to account for non-

detections at either radio or far-infrared wavelengths. They find statistically significant redshift-evolution of the FIRRC, with a slope of $\gamma_{\rm D17} = -0.19 \pm 0.01$, out to $z \sim 3$. Molnár et al. (2018) extend this study by further tying in rest-frame ultraviolet morphological information for a subset of ~ 4700 sources out to $z \sim 1.5$. They split their sample into disk- and spheroid-dominated galaxies, and find that while the FIRRC for the latter shows significant redshift-evolution, similar to the study by Delhaize et al. (2017), the disk-dominated galaxies show minimal evolution, with a slope of $\gamma_{\rm M18} = -0.037 \pm 0.012$. As radio AGN are typically found in red, bulge-dominated galaxies (e.g., Smolčić 2009), this difference between the two samples is interpreted by Molnár et al. (2018) as residual AGN contamination in spheroidal galaxies, and they argue the 'true' FIRRC shows no evolution out to $z \sim 1.5$.

The FIRRC was additionally studied at 1.4 GHz for a different radio sample by Calistro Rivera et al. (2017), using Westerbork Synthesis Radio Telescope observations over the Boötes field. They include upper limits at both FIR- and radio wavelengths by using forced photometry, for a total of ~ 800 sources. They too find siginificant redshift-evolution in the FIRRC at 1.4 GHz, out to $z \lesssim 2.5$, with a slope of $\gamma_{\rm CR17} = -0.15 \pm 0.03$, consistent with the aforementioned results from Delhaize et al. (2017).

Radio-selected samples, however, are by definition sensitive to radio-bright sources, and hence by construction select based on the combined radio luminosity from star-formation and AGN activity. Far-infrared-based surveys, in this regard, are mostly sensitive to emission solely from star-formation activity, as emission from a warm AGN torus is typically confined to mid-infrared wavelengths (e.g., Lyu & Rieke 2017; Xu et al. 2020). To substantiate this, we show in Appendix 3.B that radio AGN are a factor of ~ 5 more prevalent in radio-selected samples than in AS2UDS, at matched flux densities. As such, FIR-selected samples are expected to be substantially less contaminated by AGN.

For this reason, we now turn to two infrared-based studies of the far-infrared/radio correlation. We stress, however, that these typically have smaller sample sizes compared to radio-based surveys, but are less likely to suffer AGN contamination. Ivison et al. (2010b) investigated the FIRRC out to $z \sim 2$ using a *Herschel* 250 μm selected sample over the GOODS-North field. They find modest evolution of $\gamma_{\rm I10} = -0.26 \pm 0.07$ for a FIR-detected sample with $L_{\rm FIR} = 10^{11} - 10^{12}\,L_{\odot}$, though their study is potentially affected by the large *Herschel* point spread function and lack of

high-resolution $250\,\mu$m identifications, complicating the association of radio counterparts to FIR-detections, and additionally complicating any stacking analyses.

These problems were overcome by Thomson et al. (2014), who investigated the FIRRC for the ALESS $870\,\mu$m sample. Their sample selection is similar to that of AS2UDS, constituting an ALMA interferometic follow-up of submillimeter sources initially detected at the same wavelength in a single-dish survey (Karim et al. 2013; Hodge et al. 2013). The depth of both the ALESS and AS2UDS parent surveys and follow-up ALMA observations are roughly similar, as are the noise levels of the 1.4-GHz radio maps over the ECDFS and UDS fields, with the main difference being survey area and hence sample size. Therefore, ALESS forms the natural comparison sample to AS2UDS, and as such we compare the two surveys in additional detail.

Thomson et al. (2014) individually detect 52 SMGs at 1.4 GHz, out of a parent SMG sample of 76 galaxies. We note that this parent sample excludes 21 SMGs that are optically faint, and hence had no reliable photometric redshift available (see also Simpson et al. 2014). For the radio-detected subsample, Thomson et al. (2014) find no evidence of redshift-evolution in the FIRRC, with a fitted slope of $\gamma_{\rm T14} = -0.15 \pm 0.17$. Upon further including radio-undetected sources via a stacking analysis, they find a typical $q_{\rm IR}$ across the full ALESS sample of $q_{\rm IR} = 2.35 \pm 0.04$.[3] When limiting ourselves to the SMGs at $z \geqslant 1.5$ that do not exhibit a radio-excess signature, similar to our approach for AS2UDS, the ALESS sample shows a typical value of $q_{\rm IR} = 2.33 \pm 0.04$. This is roughly similar to the typical value for AS2UDS of $q_{\rm IR} = 2.20 \pm 0.03$. The small remaining difference of ~ 0.1 dex is likely the result of the slightly deeper SCUBA-2 map (typical RMS of $\sigma = 0.9\,\mu$Jy beam^{-1}, Geach et al. 2017; Stach et al. 2019) compared to the LESS parent survey for ALESS ($\sigma = 1.2\,\mu$Jy beam^{-1}, Hodge et al. 2013). Similarly, the AS2UDS ALMA observations are deeper than their ALESS counterparts. As a result, AS2UDS will identify somewhat infrared-fainter galaxies, which will decrease the typical $q_{\rm IR}$ of the sample. We further note that Thomson et al. (2019) study the far-infrared/radio correlation for a subset of 38 AS2UDS sources detected at both 1.4 and 6 GHz, for which they find a typical $q_{\rm IR,T19} = 2.20 \pm 0.06$, consistent with the typical $q_{\rm IR}$ we derive for the full AS2UDS sample.

Overall, while redshift-evolution of the far-infrared/radio correlation

[3] This is ~ 0.2 dex lower than was quoted in Thomson et al. 2014 (A. Thomson priv. comm.).

is near-unanimously found in radio surveys, evidence for such evolution when starting from infrared-selected samples is only weak. Both this observation and the aforementioned results from Molnár et al. (2018) point towards unidentified radio AGN being the root cause of artificial evolution in the far-infrared/radio correlation in radio-selected surveys. However, we show in Appendix 3.C, based on a combination of low-resolution radio and Very Large Baseline Interferometry (VLBI) observations in the COSMOS field, that this bias is insufficient. Summarizing, the VLBI data are predominantly sensitive to radio AGN – however, the total radio emission in these high-resolution observations is not sufficient to explain the AGN contamination required in order to generate an evolving far-infrared/radio correlation, when compared to the total radio emission observed in the lower resolution Very Large Array radio observations.

3.4.2 The FIRRC for SMGs

Observations of SMGs at high redshift have suggested that these systems are typically radio-bright compared to the local far-infrared/radio correlation (e.g., Kovács et al. 2006; Murphy et al. 2009; Magnelli et al. 2010), though a clear demonstration of this offset has until now been complicated by the mostly small sample sizes employed, and their reliance on incomplete, radio-detected subsamples. For just the radio-detected AS2UDS SMGs, we find a typical $q_{\rm IR} = 2.10 \pm 0.02$ (scatter $\sigma_q = 0.21$ dex[4]), which is indeed substantially offset from the local correlation ($q_{\rm IR} = 2.64$ with a scatter of 0.26 dex, Bell 2003). However, this median value for AS2UDS is biased towards radio-bright sources as a result of selection. A truly representative value of $q_{\rm IR}$ is obtained through our stacking analysis, which indicates a typical $q_{\rm IR} = 2.20 \pm 0.03$. This implies that, even after correcting for selection effects, the FIRRC for our AS2UDS SMGs is offset from the local correlation for star-forming galaxies by 0.44 ± 0.04 dex (a factor of 2.8 ± 0.2), while not showing any evidence for redshift-evolution between $1.5 \leqslant z \leqslant 4.0$ (a 3σ upper limit of $\leqslant 0.08$ dex across this ~ 3 Gyr period). Consequently, this substantiates the finding of SMGs being radio-brighter relative to their FIR-luminosity compared to normal, star-forming galaxies found locally.

The most straightforward explanation for this offset would be the contribution from an AGN to the observed radio emission. Based on the 0.4 dex

[4]This scatter is likely predominantly driven by the propagated measurement error on $q_{\rm IR}$, which averages 0.18 dex.

offset from the local FIRRC, this requires the AGN to contribute $\sim 70\%$ of the total radio luminosity. However, the small amount of scatter we observe around the correlation, as well as the low fraction of radio-excess AGN, requires substantial fine-tuning of AGN luminosities. VLBI observations further indicate a modest incidence of radio-AGN, with 3 out of 11 SMGs in the literature showing evidence for a compact core, indicative of an AGN (based on the combined samples of Biggs et al. 2010; Momjian et al. 2010; Chen et al. 2020). These samples, in turn, explicitly target radio-bright SMGs, and the bright radio population is known to be dominated by radio-excess AGN (e.g., Condon 1989). As such, the incidence of dominant radio AGN in SMGs is likely to be a lot smaller than the $\sim 30\%$ indicated by these VLBI studies.

Instead, both the offset in the FIRRC, as well as the lack of redshift-evolution for SMGs, are likely to be indicative of the different physics at play in normal, low-luminosity star-forming galaxies observed locally, and the much more active systems being studied at high redshift.

The calorimetric models of the far-infrared/radio correlation indeed make predictions for variations in the FIRRC as a function of star-formation surface density (Lacki et al. 2010), which may explain the difference between SMGs and the normal star-forming population. In addition, Lacki & Thompson (2010) model the behaviour of the FIRRC at high redshift, for galaxies with a variety of star-formation surface densities. With our large, homogeneous sample of SMGs, we can investigate the predictions of these models in detail. In the next section, we compare the far-infrared/radio correlation of the AS2UDS SMGs with that of normal star-forming galaxies. In Section 3.4.2, we focus on the comparison with ULIRGs, thought to be the closest local analogs of $z \sim 2$ dusty, star-forming galaxies.

SMGs Compared to Normal Star-forming Galaxies

Given that our low-frequency radio observations predominantly probe non-thermal synchrotron emission originating from relativistic electrons, we first discuss the far-infrared/radio correlation in terms of the various physical processes that compete for these electrons. In theory, the correlation is expected to break down at high redshift due to the increased inverse Compton losses of cosmic rays on the CMB (e.g., Murphy 2009b; Lacki & Thompson 2010; Schleicher & Beck 2013). Under the assumption that synchrotron and inverse Compton are the dominant processes of energy loss, a star-forming galaxy with a magnetic field of $B = 10\,\mu$G, as is typical for local, normal star-forming galaxies (Beck & Wielebinski 2013; Tabatabaei

et al. 2017), is expected to show an increased $q_{\rm IR}$ at $z = 4$ compared to the local value of $\Delta q_{\rm IR} \simeq 1.0$ dex, as a result of the warmer CMB at high-redshift. Highly star-forming galaxies, however, are the most resilient to this, as their star-formation powered radiation fields are substantially stronger than the cosmic microwave background, even at moderate redshift. Under the assumption that our SMGs represent central starbursts with typical radius of 1 kpc (e.g., Gullberg et al. 2019), the energy density $U_{\rm rad}$ of their star-formation powered radiation field is still an order of magnitude higher than that of the CMB at $z = 3$. The two energy densities are only expected to coincide at $z \sim 6$, and due to the steep redshift-dependency of inverse Compton losses on the CMB ($U_{\rm CMB} \propto (1+z)^4$, e.g., Murphy 2009b), such losses are negligible for the typical redshift range covered by sub-millimeter galaxies. As such, no evolution in the far-infrared/radio correlation is expected for the AS2UDS sample as a result of the warmer CMB at high redshift.

As we find the FIRRC for SMGs to constitute a particularly tight correlation, the relative radiative losses to synchrotron, inverse Compton and other potential sources of energy loss, such as ionization losses and bremsstrahlung (see e.g., Thompson et al. 2006; Murphy 2009b; Lacki et al. 2010), have to be relatively constant across our sample (and hence, across redshift). This, too, is not surprising. We find no significant variation in $q_{\rm IR}$ with a variety of physical parameters (Section 3.3.4), neither for the individually radio-detected sources, nor for the stacks. Dudzevičiūtė et al. (2020) further investigated any redshift-evolution for a variety of physical properties of the AS2UDS SMGs, and find only a strong increase in typical star-formation rates with increasing redshift. Further evolution in e.g., dust masses or gas fractions is only modest, and typically less than the differential evolution observed for the UDS field population. Overall, this paints the picture of SMGs as a fairly homogeneous galaxy population across redshift. Using a simple analytic model, Dudzevičiūtė et al. (2020) explain the redshift distribution of SMGs as the combination of systems growing through a characteristic halo mass ($M_h \sim 4 \times 10^{12}\,M_\odot$) and acquiring a certain minimal gas fraction. If this threshold is associated with starburst activity, the SMG population might consist of physically similar galaxies, simply observed at different cosmic epochs. As radiative losses on the CMB remain negligible for our SMGs, as a result of the high star-formation powered radiation fields, the lack of redshift-evolution in the far-infrared/radio correlation of SMGs may simply be a consequence of their homogeneity.

This lack of evolution does however not explain the intrinsic offset of SMGs with respect to the local far-infrared/radio correlation. Lacki et al. (2010) argue that this offset is likely the result of the enhanced magnetic fields in SMGs, compared to those of the normal star-forming population. Neglecting, for now, other potential sources of cosmic ray energy loss besides inverse Compton, the fact that SMGs obey the far-infrared/radio correlation implies that $U_{\mathrm{B}}/U_{\mathrm{rad}} \gtrsim 1$ (Murphy 2009b), where $U_{\mathrm{B}} = B^2/8\pi$. In other words, synchrotron emission must dominate the energy loss of cosmic rays, and the ratio of synchrotron to inverse Compton losses has to be relatively constant in general to explain the small scatter about the FIRRC. This, in turn, implies a minimum magnetic field strength for SMGs of $B_{\mathrm{min}} \gtrsim 0.1-0.2\,\mathrm{mG}$. Such magnetic fields are indeed expected for SMGs (Thompson et al. 2006; Murphy 2009b), and are additionally in agreement with the $B-$SFR-relation deduced for local, normal star-forming galaxies by Tabatabaei et al. (2017), though we caution this requires an extrapolation across nearly two orders of magnitude in star-formation rate.

If ionization losses and bremsstrahlung are additionally expected to become important in highly star-forming galaxies, synchrotron emission has to be even stronger to maintain the far-infrared/radio correlation. In particular, enhanced synchrotron emission in SMGs is expected, as a result of their strong magnetic fields and what Lacki et al. (2010) call the 'ν_{c}-effect': a cosmic ray electron with an energy E will predominantly emit synchrotron radiation at a frequency ν_{c}, which is given by (e.g., Murphy 2009b)

$$\left(\frac{\nu_c}{\mathrm{GHz}}\right) = 1.3 \times \left(\frac{B}{0.1\,\mathrm{mG}}\right)\left(\frac{E}{\mathrm{GeV}}\right)^2 . \tag{3.3}$$

Hence, at a greater magnetic field strength, observations at a fixed frequency will probe lower-energy electrons. The distribution of injected electrons typically follows a power-law distribution in energy, $N(E) \propto E^{-p}$, where p relates to the observed radio spectral index via $p = -(2\alpha - 1)$, in the absence of cooling. Typical values are $p > 2$, and in particular with $\alpha \approx -0.80$ we obtain $p \approx 2.6$. This, in turn, implies that the lower typical energy of the electrons we probe is more than compensated for by them being substantially more numerous than their high-energy counterparts. This will, then, enhance the radio emission seen in SMGs. In particular, Lacki et al. (2010) propose that $q_{\mathrm{IR}} \propto \left(1 - \frac{1}{2}p\right)\log_{10} B$. If we as-

sume the offset of SMGs with respect to the local FIRRC is solely the effect of stronger magnetic fields in SMGs and the resulting ν_c-effect, our observed $p = 2.6$ implies SMGs have magnetic field strengths about 20 times larger than for typical local galaxies. As these generally have magnetic fields of $B \sim 10\,\mu$G (e.g., Tabatabaei et al. 2017), this implies that SMGs likely have magnetic fields of $B \sim 0.2\,$mG, consistent with our previous minimum requirement on the field strength to maintain a linear far-infrared/radio correlation. While such magnetic fields are indeed strong compared to local, normal star-forming sources, they are smaller than the typical $\sim 1\,$mG fields observed in local ULIRGs (Robishaw et al. 2008; McBride et al. 2014). Arp220, in particular, has an estimated magnetic field strength of $B \approx 2\,$mG (McBride et al. 2015; Yoast-Hull et al. 2016). This difference is potentially due to ULIRGs being substantially more compact than SMGs, having similar levels of star formation in volumes of a few $100\,$pc (Solomon et al. 1997; Downes & Solomon 1998), instead of the $\sim$kpc scales that is typical for sub-millimeter galaxies (Simpson et al. 2015; Hodge et al. 2016; Gullberg et al. 2019). We compare the far-infrared/radio correlation for SMGs and ULIRGs in more detail in Section 3.4.2.

While seemingly satisfactory, simply enhancing the magnetic field of SMGs with respect to normal star-forming galaxies raises another issue, as was already noted by Thompson et al. (2006). The synchrotron cooling time is proportional to $B^{-3/2}$ (Murphy 2009b), and hence large magnetic field strengths imply very short synchrotron cooling times. This spectral ageing should in principle be observable in the synchrotron spectrum, manifesting itself as a spectral break. Such spectral features have indeed been claimed in the radio spectra of SMGs (e.g., Thomson et al. 2019), at frequencies $\nu_\mathrm{b} \gtrsim 5\,$GHz. For a single injection event of cosmic rays, subject to a magnetic field B, a spectral break arises at frequency ν_b after a time τ_b, which is given by (Carilli & Barthel 1996)

$$\tau_\mathrm{b} = 1.6 \times \left(\frac{B}{0.1\,\mathrm{mG}}\right)^{-3/2} \left(\frac{\nu_\mathrm{b}}{\mathrm{GHz}}\right)^{-1/2} \mathrm{Myr}\,. \tag{3.4}$$

For a single, short burst of star formation, a spectral break at $5\,$GHz implies the synchrotron emission must have arisen within the last Myr, assuming $B = 0.2\,$mG.[5] Additionally, for a top-hat star-formation history, modelled as a succession of single injection events following Thomson

[5]Given that we observe no deviations from a fixed spectral index of $\alpha = -0.80$ – typical

et al. (2019), the $610 - 1400$ MHz spectral index should have steepened to $\alpha \approx -1.2$ after only 20 Myr, with only minor differences when either a linearly rising, or exponentially declining star-formation history is assumed instead. Even accounting for the fact that synchrotron emission will lag the onset of the starburst by ~ 30 Myr (Bressan et al. 2002), this is still inconsistent with the expected typical age of our SMGs of ~ 150 Myr, based on an analysis of depletion timescales (Dudzevičiūtė et al. 2020).

At more realistic starburst timescales, the spectral break should manifest at much lower frequencies, and hence the $610 - 1400$ MHz spectral index should be considerably steeper than the observed $\alpha \approx -0.8$. Thompson et al. (2006) argue that, in the dense starburst environments, bremsstrahlung and ionization form additional sources of energy loss of cosmic ray electrons. Ionization losses, in particular, are most effective for low-energy cosmic rays, and hence will flatten the observed radio spectrum. For the cooling times for inverse Compton emission and ionization losses (respectively equations 4 and 10 in Murphy 2009b) to be equal, given a magnetic field of 0.1 mG (1 mG), requires an ISM density of $n_{\rm ISM} \sim 10^3\,{\rm cm}^{-3}$ ($n_{\rm ISM} \sim 10^2\,{\rm cm}^{-3}$). That is, for larger densities, ionization losses will dominate over inverse Compton cooling. Such densities are typical for the central regions of SMGs (e.g., Bothwell et al. 2013; Rybak et al. 2019), and hence the spectral steepening can be counteracted via ionization losses. In the models of Thompson et al. (2006) and Lacki & Thompson (2010), this indeed results in an expected $\alpha \approx -0.80$ at the rest-frame frequencies we probe for the AS2UDS SMGs, which is consistent with our observations.

However, if ionization cooling is additionally important in sub-millimeter galaxies, it will compete with synchrotron emission for the available cosmic rays. In particular, increased ionization losses should work to reduce the observed synchrotron emission by a factor of ~ 2 ($\Delta q_{\rm IR} \approx +0.3$ dex, Thompson et al. 2006), which in turn partially compensates for the offset in the FIRRC as a result of the stronger magnetic fields in SMGs. To alleviate this tension, Lacki et al. (2010) suggest that the production of secondary cosmic ray electrons and positrons, resulting from proton-proton collisions in the high-density environment of a starburst galaxy, are generating additional synchrotron emission. Indeed, their models including the creation of secondary cosmic rays show a decrease of $\Delta q_{\rm IR} \approx -0.4$ dex at SMG-like gas surface densities, compared to models with only primary

for uncooled synchrotron emission – out to $z \approx 4.0$, if a break exists, it is likely to lie at $\nu_{\rm b} > 5$ GHz, which will further decrease $\tau_{\rm b}$.

cosmic rays, which offsets the additional energy loss from bremsstrahlung and ionization losses. In particular, the creation of secondary cosmic rays should counteract strong spectral index gradients in galaxies hosting a central starburst, as these can be generated also outside the star-forming regions. While testing this at high-redshift is currently only possible in strongly gravitationally lensed galaxies (e.g., Thomson et al. 2015), resolved multi-frequency observations of Arp220 between 150 MHz and 33 GHz indicate that cosmic ray electrons are required to be accelerated far outside the central regions in order to explain the spectral index maps (Varenius et al. 2016), providing support to the importance of secondary cosmic rays (see also the discussion of multi-frequency source sizes in Thomson et al. 2019).

Overall, our favored explanation for the lack of evolution in the far-infrared/radio correlation for SMGs, as well as its offset from the local value for normal star-forming galaxies, involves a fair amount of fine-tuning. Summarizing, it requires (i) strong magnetic fields ($B \gtrsim 0.1 - 0.2\,\mathrm{mG}$) to explain the offset in the FIRRC; (ii) significant ionization losses to counteract spectral ageing and flatten the observed radio spectra, and; (iii) secondary cosmic rays to compensate for this additional energy loss through ionization. This 'conspiracy' indeed forms the basis for the models by Lacki et al. (2010); Lacki & Thompson (2010) in order to maintain a linear FIRRC across a wide range of far-infrared and radio luminosities. To test this scenario in more detail, ideally resolved radio- and far-infrared observations of a sizeable sample of SMGs are required. However, unresolved observations may be able to shed some light on the physical processes as well. The magnetic field strength of a galaxy likely depends on its star-formation activity, either through the gas surface or volume density and the Kennicutt-Schmidt relation (Lacki et al. 2010; Lacki & Thompson 2010), or directly via the observed star-formation rate (Tabatabaei et al. 2017). If this correlation is continuous, one expects to see a negative correlation between q_{IR} and star-formation rate, across a wide range from normal star-forming galaxies down to SMGs.

If such a trend indeed exists, this will have a significant effect on studies of the far-infrared/radio correlation that are not uniformly sensitive to star formation across redshift. In particular, we argued in Section 3.4.1 and Appendix 3.C that radio AGN alone cannot explain the observed redshift-evolution in radio-selected studies of the FIRRC. As such, it is probable that this evolution is instead the result of probing different galaxy populations locally and at high redshift. Unlike in the case of our far-infrared selected

sample, selection at radio wavelengths is subject to a positive K-correction, such that at high redshift one is only sensitive to strongly star-forming galaxies (e.g., Condon 1992). In addition, the average high-redshift galaxy is more rapidly forming stars than a typical local star-forming galaxy (e.g., Speagle et al. 2014). As such, radio-based studies will probe more 'SMG-like' galaxies at high redshift, which implies that the average $q_{\rm IR}$ probed should reflect the lower normalization for the far-infrared/radio correlation of SMGs. In turn, this should induce redshift-evolution in the far-infrared/radio correlation, similar to what is observed (Delhaize et al. 2017; Calistro Rivera et al. 2017). The evolving $q_{\rm IR}$ adopted in recent radio-based studies of the cosmic star-formation rate density (e.g., Novak et al. 2017; Ocran et al. 2020) should therefore be appropriate, as this quantity encompasses the modified conversion from radio emission to star-formation rate when considering different galaxy populations.

Testing this scenario, however, will require a star-forming sample with a fixed range of SFRs across redshift, where the star-formation rate is measured using a preferably dust-unbiased tracer independent of far-infrared and synchrotron emission. The most obvious candidates for this will be radio free-free emission and [C ii] $158\,\mu$m emission, both of which suffer little from dust attenuation, and may provide an effective means of studying the far-infrared/radio correlation without requiring expensive, resolved far-infrared and radio observations.

SMGs Compared to Local ULIRGs

The discussion in the previous section focused primarily on the difference in the far-infrared/radio correlation between SMGs and local, normal star-forming galaxies. However, ULIRGs potentially constitute the closest local analogues of $z \sim 2.5$ sub-millimeter galaxies. They show far-infrared luminosities in excess of $10^{12}\,L_{\odot}$, and their typical magnetic field reaches mG strengths (Robishaw et al. 2008; McBride et al. 2014, 2015; Yoast-Hull et al. 2016), substantially larger than that of normal galaxies. However, ULIRGs *do* fall onto the local far-infrared/radio correlation (Yun et al. 2001; Farrah et al. 2003; Jarvis et al. 2010; Galvin et al. 2018). If ULIRGs are indeed close analogs of SMGs, and magnetic fields are the primary driver of their different far-infrared/radio correlation, this raises the question why these seemingly similar galaxy populations are offset in $q_{\rm IR}$ by ~ 0.4 dex.

While a detailed investigation of this offset is beyond the scope of this paper, we can afford to be more quantitative in a comparison between ULIRGs

and SMGs. In the following, we will assume that all star formation is dust-obscured in both populations, and that the same physical processes for cosmic ray energy loss dominate. In particular, the strong magnetic fields and high densities present in both ULIRGs and SMGs indicate that the dominant processes are synchrotron, inverse Compton, ionization and bremsstrahlung. Their cooling times are given in Murphy (2009b), and are reproduced here:

$$\begin{aligned}
\left(\frac{\tau_{\rm syn}}{\rm yr}\right) &\approx 4.4\times10^{4}\left(\frac{\nu}{\rm GHz}\right)^{-1/2}\left(\frac{B}{\rm mG}\right)^{-3/2}\\
\left(\frac{\tau_{\rm IC}}{\rm yr}\right) &\approx 1.6\times10^{6}\left(\frac{\nu}{\rm GHz}\right)^{-1/2}\left(\frac{B}{\rm mG}\right)^{1/2}\\
&\quad\times\left(\frac{L_{\rm bol}}{10^{12}\,L_{\odot}}\right)^{-1}\left(\frac{R}{\rm kpc}\right)^{2}\\
\left(\frac{\tau_{\rm ion}}{\rm yr}\right) &\approx 1.1\times10^{9}\left(\frac{\nu}{\rm GHz}\right)^{1/2}\left(\frac{B}{\rm mG}\right)^{-1/2}\left(\frac{n_{\rm ISM}}{\rm cm^{-3}}\right)^{-1}\\
&\quad\times\left(\frac{3}{2}\left[\ln\left(\frac{\nu}{\rm GHz}\right)-\ln\left(\frac{B}{\rm mG}\right)\right]+39\right)^{-1}\\
\left(\frac{\tau_{\rm brem}}{\rm yr}\right) &\approx 8.7\times10^{7}\left(\frac{n_{\rm ISM}}{\rm cm^{-3}}\right)^{-1}\,.
\end{aligned} \tag{3.5}$$

Here $L_{\rm bol}$ is the bolometric luminosity of the galaxy, assumed to equal the $8-1000\,\mu$m luminosity, and $n_{\rm ISM}$ is the particle number density of the interstellar medium. The fraction of cosmic ray energy that is emitted via synchrotron radiation can then be written as

$$f_{\rm syn}=\frac{1/\tau_{\rm syn}}{\sum_{{\rm proc},i}1/\tau_i}\,, \tag{3.6}$$

where the sum iterates over all cooling timescales in Equation 3.5. Crucially, $f_{\rm syn}$ will depend on the frequency probed, as the various cooling timescales in Equation 3.5, with the exception of bremsstrahlung, all contain a frequency-dependence. Synchrotron and inverse Compton losses are stronger at higher frequencies, as these probe more energetic particles (as per Equation 3.3). Ionization losses, on the other hand, are enhanced for less energetic particles, and will hence be weaker when probing higher rest-frame frequencies. Since we observe the AS2UDS SMGs at a fixed frequency of $\nu_{\rm obs}=1.4\,$GHz, the rest-frame frequency probed will

be $\nu_{\rm rest} = 1.4 \times (1+z)$ GHz. As was noted in Lacki & Thompson (2010), this implies that the observed radio luminosity $L_{\nu_{\rm rest}}$ will be proportional to $f_{\rm syn}(\nu_{\rm rest})$. An observer will then K-correct $L_{\nu_{\rm rest}}$ to rest-frame 1.4 GHz with a given spectral index. However, since our SMG sample spans a range of redshifts, yet is observed at a fixed frequency, a range of $f_{\rm syn}(\nu_{\rm rest})$ is probed, and as such $f_{\rm syn}$ will be a function of redshift. Crucially, this implies that $q_{\rm IR}$ too will vary with redshift as

$$q_{\rm IR} = q_0 - \log_{10}\left(f_{\rm syn}(z)\right) \ , \tag{3.7}$$

for some a priori unknown normalization q_0, under the assumption that the SMG population itself does not evolve significantly with redshift. If the same physical processes are at play in shaping the far-infrared/radio correlation for SMGs and ULIRGs, we can use the observed normalization of the local FIRRC for the latter to model the expected evolution in the correlation for SMGs. In particular, we may write

$$q_{\rm IR}(z) = 2.64 + \log_{10}\left(\frac{f_{\rm syn}^{\rm ULIRG}}{f_{\rm syn}^{\rm SMG}(z)}\right) \ , \tag{3.8}$$

where the normalization of $q_0 = 2.64$ from Bell (2003) was adopted for ULIRGs. We note this is consistent with $q_{\rm IR} = 2.70 \pm 0.06$ from Farrah et al. (2003) and $q_{\rm IR} = 2.64 \pm 0.01$ measured by Yun et al. (2001).[6]

Parameter $f_{\rm syn}$ is fully determined, under our simplifying assumptions, by the magnetic field strength, ISM density, physical size, far-infrared luminosity and redshift of any given source. As such, we adopt a set of standard values for these parameters for both ULIRGs and SMGs, as tabulated in Table 3.1. We note that the magnetic field strength and particle densities are not particularly well-constrained in either, and as such this 'benchmark' model comes with inherent uncertainties. Nevertheless, for simplicity we adopt equal magnetic field strengths of $B = 1.0$ mG for SMGs and ULIRGs, which is consistent with the lower limit of $B \gtrsim 0.2$ mG we determined for SMGs in order to maintain a linear far-infrared/radio correlation in the previous Section. We further adopt far-infrared luminosities typical for the Farrah et al. (2003) and AS2UDS samples for ULIRGs and SMGs,

[6] For Yun et al. (2001), we convert FIR-luminosities from $42.5 - 122.5\,\mu$m to the $8 - 1000\,\mu$m range used in this work by adding 0.30 dex, following Bell (2003); Delhaize et al. (2017).

Table 3.1: Benchmark Models for ULIRGs and SMGs

Parameter	**Unit**	**ULIRG**	**SMG**
$\log_{10} L_{\rm IR}$	$L_\odot$	12.0	12.5
$R_{\rm eff}$	kpc	0.25	1.0
B	mG	1.0	1.0
$n_{\rm ISM}$	$\rm cm^{-3}$	2×10^3	1×10^3

respectively. In addition, we adopt a typical effective radius for the dust emission in SMGs of $1.0\,$kpc (e.g., Gullberg et al. 2019), and adopt $250\,$pc for ULIRGs (e.g., Solomon et al. 1997; Downes & Solomon 1998). The far-infrared/radio correlation of SMGs, however, is not particularly sensitive to the adopted physical size, since it only affects inverse Compton losses, as per Equation 3.5. Cosmic rays in the more compact ULIRGs, however, lose a substantially larger fraction of their energy via inverse Compton cooling, as ULIRGs have far-infrared luminosities comparable to those of SMGs, yet condensed into a smaller volume. Given their increased compactness, we additionally adopt a larger typical ISM density in ULIRGs than in SMGs, although we stress both are inherently uncertain. Given these limitations, we do not aim to make strong predictions on the physical conditions in either ULIRGs or SMGs, but instead use this simplified model to explain global trends in their far-infrared/radio correlation.

We plot the expected $q_{\rm IR}(z)$ for SMGs, normalized to the local far-infrared/radio correlation for ULIRGs, in Figure 3.7. In addition, we indicate how this trend is affected by an increase/decrease in B or $n_{\rm ISM}$ by a factor of five. It is clear that our benchmark model recovers the correct normalization of the FIRRC for SMGs. In addition, the frequency-dependence of the cooling times induces a slight redshift-dependency, which, if fitted by $q_{\rm IR} \propto (1+z)^\gamma$, implies that $\gamma \approx -0.05$, which is marginally consistent with our results. Note that an extrapolation of this model to $z = 0$ results in a typical $q_{\rm IR} \approx 2.4$, which is below the local far-infrared/radio correlation. This should however not be interpreted as the predicted normalization for local ULIRGs. Instead, this is the typical $q_{\rm IR}$ an SMG would have when a rest-frame frequency of 1.4 GHz is probed directly.

The variations on the benchmark model in Figure 3.7 indicate that $q_{\rm IR}$ is substantially affected by changes in the density or magnetic field strength. Increasing the latter naturally increases the relative contribution of syn-

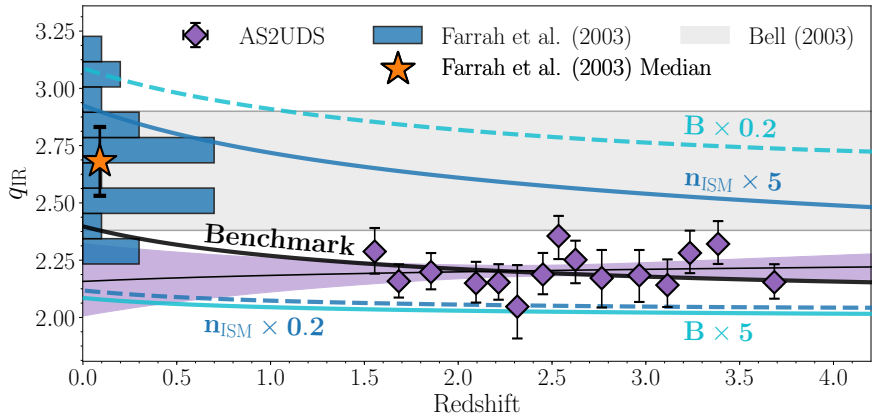

Figure 3.7: A comparison of the far-infrared/radio correlation for the AS2UDS SMGs with a heterogeneous mix of local, star-forming galaxies (Bell 2003) and local ULIRGs (Farrah et al. 2003). The AS2UDS points and fit from Figure 3.5c are shown in purple. In addition, five evolutionary toy models for the FIRRC are overlaid. The benchmark model adopts the same magnetic field strength in SMGs and ULIRGs, but assumes the latter are both more compact, and more dense. Four variations are also shown, adopting different magnetic field strengths and densities for SMGs relative to the benchmark model. The increased compactness of ULIRGs compared to $z \sim 2.5$ dusty star-forming galaxies results in higher ionization and inverse Compton losses, and hence in a subdominant contribution from synchrotron emission. This, in turn gives rise to an increased $q_{\rm IR}$.

chrotron emission to the overall cosmic ray energy loss, and as such decreases $q_{\rm IR}$ (Equation 3.7). Decreasing the density has an analogous effect, as the relative contribution of ionization losses is diminished, and hence $f_{\rm syn}$ is enhanced. We emphasize that our benchmark model is simply one of a family of models with the correct behaviour, reproducing the normalization and lack of strong redshift-evolution in the FIRRC for SMGs. However, all such models require that synchrotron emission is dominant in SMGs, with a subdominant contribution from ionization losses. A large value of $f_{\rm syn} \gtrsim 0.6$ is additionally required to obtain a relatively flat slope in the $q_{\rm IR}$-redshift plane. In ULIRGs, however, synchrotron emission is subdominant ($f_{\rm syn} < 0.5$), and instead substantial contributions from ionization and inverse Compton losses ensure that their far-infrared/radio correlation is offset from that of SMGs, and is consistent with that of typical star-forming galaxies observed locally.

The interpretation that synchrotron emission is subdominant in ULIRGs

implies that these should have flatter radio spectral indices compared to SMGs due to the increased importance of ionization losses, at comparable rest-frame frequencies. This is in agreement with results in the literature, which indicate that ULIRGs typically show a $1.4 - 5\,\mathrm{GHz}$ spectral index of $\alpha \approx -0.50$ to -0.60 (Clemens et al. 2008; Leroy et al. 2011; Galvin et al. 2016; Klein et al. 2018). Our $610\,\mathrm{MHz}-1.4\,\mathrm{GHz}$ observations of $z \sim 2-3$ SMGs probe identical rest-frame frequencies as the higher frequency data for local ULIRGs, but these instead show a steeper $\alpha \approx -0.80$. While Clemens et al. (2008) interpret this flattening in ULIRGs as the result of increased free-free absorption, they note that ionization losses will have a similar effect on the spectral index. Since no such flattening is observed in SMGs at identical rest-frame frequencies, we prefer the latter interpretation. While we rely mostly on stacked spectral indices in this work, the combination of matched-depth 610 MHz and 1.4 GHz observations of SMGs will provide a suitable means to investigate this in additional detail.

The fact that synchrotron emission is subdominant in ULIRGs further implies that the intrinsic scatter about their far-infrared/radio correlation is likely to be enhanced, as small deviations in e.g., the magnetic field strength or density will have a relatively large impact on the observed f_{syn}, and in turn on the q_{IR} of individual sources. Such an increase in the scatter about the FIRRC at high far-infrared luminosities has been widely observed (Helou et al. 1985; Condon et al. 1991a; Yun et al. 2001; Bressan et al. 2002; Bell 2003), and may hence be related to the subdominance of synchrotron emission in ULIRGs. However, Bressan et al. (2002) instead interpret this increased scatter as being due to a timescale effect, as far-infrared emission arises on a shorter timescale than radio emission after the onset of star formation. If ULIRGs constitute strong yet relatively short-lived starbursts, the scatter about their far-infrared/radio correlation will be enhanced compared to that of more continuously star-forming systems. In order to test these interpretations, an indicator of the starburst age is required. Multi-frequency radio observations may provide a way forward here too, as spectral indices form a proxy for starburst age. In combination with other age-indicators, such as star-formation rate tracers that probe different timescales, it is possible to begin reconstructing the recent star-formation history observationally. In addition, with multi-frequency radio observations one can eliminate the inherent uncertainties arising from the intrinsic scatter expected about the far-infrared/radio correlation when a fixed spectral index is assumed.

3.5 Conclusions

We have presented a study of the far-infrared/radio correlation for AS2UDS (Stach et al. 2019; Dudzevičiūtė et al. 2020) – a homogeneously selected sample of 706 sub-millimeter galaxies identified through ALMA band 7 follow-up of SCUBA-2 $850\,\mu$m observations of the UKIDSS/UDS field. Through combining these sub-millimeter data with deep ($\sigma_{\rm RMS} \sim 7\,\mu{\rm Jy\,beam^{-1}}$) Very Large Array radio observations at 1.4 GHz and available 610 MHz coverage from the GMRT, we study their joint far-infrared and radio properties within the redshift range $1.5 \leqslant z \leqslant 4.0$, where our selection is uniform in terms of dust mass or far-infrared luminosity.

We address the incompleteness in the radio observations through a stacking analysis, and find a typical far-infrared/radio correlation parameter $q_{\rm IR} = 2.20 \pm 0.03$ for sub-millimeter galaxies, which is ~ 0.4 dex lower than the local value for a heterogeneous mix of star-forming galaxies (Bell 2003) and ULIRGs (Yun et al. 2001; Farrah et al. 2003). This value of $q_{\rm IR}$ further shows no evidence of evolution between $1.5 \leqslant z \leqslant 4.0$, which likely illustrates that SMGs are a physically homogeneous population of galaxies across redshift, for which no strong redshift-evolution is expected.

This offset for SMGs with respect to the local far-infrared/radio correlation is unlikely to be the result of residual contamination by radio AGN, which is more likely to affect radio-selected samples. Instead, we interpret the offset with respect to the far-infrared/radio correlation of normal galaxies through strong magnetic fields in SMGs ($B \gtrsim 0.2\,$mG), combined with the production of secondary cosmic rays, both of which serve to increase the radio output of a galaxy for a given star-formation rate (Lacki et al. 2010; Lacki & Thompson 2010). Combined high-resolution radio and far-infrared observations of a large sample of sub-millimeter galaxies will provide a robust way to test this interpretation in the future. We additionally model the offset in the FIRRC between SMGs and local ULIRGs, under the assumption that the same physical processes are at play in either. In particular, a model wherein ULIRGs are denser and more compact than SMGs can fully explain the observed offset, as well as the lack of evolution in the far-infrared/radio correlation of SMGs. A prediction of this interpretation is that SMGs have steeper GHz radio spectral indices than ULIRGs, and a reduced scatter about their far-infrared/radio correlation. We argue that matched-depth, multi-frequency radio observations of SMGs are crucial in order to test both of these predictions.

Acknowledgements

We wish to thank the anonymous referee for their comments and suggestions which have improved this work. HSBA, JAH and DvdV acknowledge support of the VIDI research programme with project number 639.042.611, which is (partly) financed by the Netherlands Organization for Scientific Research (NWO). IS, UD, AMS and SS acknowledge support from STFC (ST/T000244/1). EdC gratefully acknowledges the Australian Research Council as the recipient of a Future Fellowship (project FT150100079). CCC acknowledges support from the Ministry of Science and Technology of Taiwan (MOST 109-2112-M-001-016-MY3). JLW acknowledges support from an STFC Ernest Rutherford Fellowship (ST/P004784/1 and ST/P004784/2). The National Radio Astronomy Observatory is a facility of the National Science Foundation operated under cooperative agreement by Associated Universities, Inc. The ALMA data used in this paper were obtained under programs ADS/JAO.ALMA#2012.1.00090.S, #2015.1.01528.S and #2016.1.00434.S. ALMA is a partnership of ESO (representing its member states), NSF (USA) and NINS (Japan), together with NRC (Canada) and NSC and ASIAA (Taiwan), in cooperation with the Republic of Chile. The Joint ALMA Observatory is operated by ESO, AUI/NRAO, and NAOJ.

Appendix

3.A Stacking

Throughout this work, we employ a stacking technique in order to incorporate the radio-undetected population. While in principle a straightforward procedure, in practice stacking involves a variety of choices. In particular, the first choice one must make, is whether to adopt either the mean or median when stacking. In this work, we adopt the latter, as the median is considerably less affected by outliers in the underlying distribution of flux densities (e.g., White et al. 2007). In addition, Condon et al. (2013) show that the mean is likely to be significantly affected by sources close to the survey detection limit, and as such may be less representative of the full underlying population. We have verified, however, that our results are unchanged when adopting a clipped-mean stacking procedure, whereby SMGs with nearby bright radio sources are omitted from the stacking. While this agreement is encouraging, we still prefer the me-

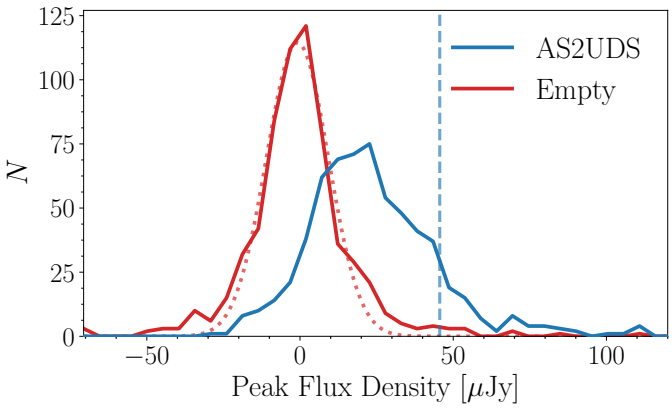

Figure 3.8: Distribution of peak-pixel flux densities for the AS2UDS SMGs, and empty background regions. The red, dotted line shows a Gaussian fit to the latter, with a mean of approximately zero, and the vertical dashed line indicates the detection limit (4σ) at 1.4 GHz. The peak-pixel values for AS2UDS show a clear positive excess, indicative of a large number of sources below the detection limit.

dian as it does not require a (somewhat arbitrary) rejection of sources when stacking, in addition to the reasons elaborated above.

A second choice one must make is how to measure stacked flux densities. In radio astronomy, typically the peak flux density is adopted for a source that is unresolved, while the integrated flux density is utilized for extended sources. Ideally, for a set of unresolved radio sources, one would simply take the pixel value at the location of the sub-millimeter galaxy, which is equivalent to adopting the peak flux density when all sources are perfectly aligned, in the absence of noise. We show the distribution of peak pixel values in the 1.4 GHz map for the AS2UDS SMGs in Figure 3.8, and further verify that the fluxes in the off-source stacks used for determining the background and RMS-noise level are Gaussian and centered around zero. The distribution of fluxes at the AS2UDS source positions are consistent with a power-law at high flux densities, and are dominated by the local Gaussian noise in the mosaic at flux densities near the typical RMS in the map.

However, these peak-pixel flux densities are likely to underestimate the true flux density of our stacks, as there might be spatial offsets between the radio and far-infrared emission – either real or as a result of the local noise in the maps. In addition, the sources are not expected to be per-

fectly unresolved – for instance, at a resolution of $1\farcs8 \times 1\farcs6$ at 1.4 GHz, nearly half of the radio-detected AS2UDS SMGs are (marginally) resolved at the 3σ level, based on their deconvolved source sizes (following Thomson et al. 2019). As such, integrated flux densities are likely to be more appropriate for the AS2UDS stacks at 1.4 GHz. This is further substantiated by the fact that the integrated flux densities for the stacks of the full AS2UDS sample in Figure 3.5 exceed the peak flux density by a typical factor of $S_{\rm int}/S_{\rm peak} = 1.64 \pm 0.08$. However, in order to determine integrated flux densities, one typically fits Gaussians to the stacked detections, which in turn may be biased when the stacks are at low signal-to-noise. We investigate this via a mock-stacking procedure, whereby we insert faint (i.e., including flux densities well below the detection limit) mock sources into the UDS 1.4 GHz map, stack them, and compare both the inserted and recovered flux densities, as well as the recovered peak and integrated values. We adopt a power-law distribution in inserted mock source flux densities with a slope of -2, which is typical for radio number counts for star-forming sources in the sub-mJy regime (e.g., Prandoni et al. 2018), and is additionally consistent with the distribution of peak pixel fluxes shown in Figure 3.8. The number of sources sampled from this distribution was further varied between $N = 30 - 100$ in order to match the typical number of sources stacked in this work. We then compare the results of two runs: in the first, mock sources are inserted as unresolved, while in the second 40% of mock sources are slightly resolved, randomly being assigned a Gaussian size between $1.2 - 1.6\times$ the beam size. In addition, in order to mimic a true survey, the catalogued mock source positions – those which are used for stacking – are slightly different from the true mock source positions, as we randomly draw an offset in both right ascension and declination from a Gaussian distribution with zero mean and standard deviation of $\sigma = 0.30''$. This positional offset is consistent with the observed distribution of separations between the far-infrared and radio positions of the AS2UDS sources with radio counterparts at 1.4 GHz.

We compare the two mock-stacking runs in Figure 3.9, where we quantify the difference between recovered integrated and peak flux densities, as well as the level of "flux boosting", that is, the ratio of the recovered and inserted flux density. For unresolved mock sources, the integrated-to-peak ratio is typically slightly larger than unity, indicating that at a modest SNR $\lesssim 10$, integrated flux densities may be slightly overestimated. However, at the typical SNR $\sim 8.5 - 15$ we obtain for the AS2UDS stacks, $S_{\rm int}/S_{\rm peak} = 1.18 \pm 0.02$ for the unresolved mock sources, while the real

data indicate a much higher value of $S_{\rm int}/S_{\rm peak} = 1.64 \pm 0.08$. This implies that the peak flux density does not constitute an accurate measurement of the true stacked flux density. Instead, if we allow for resolved sources and random positional offsets, we find that the typical $S_{\rm int}/S_{\rm peak}$ we obtain for the AS2UDS sample is accurately recovered by the simulated stacks. In this case, peak flux densities underestimate the true radio flux density by a factor of 0.74 ± 0.11, which in turn leads to $q_{\rm IR}$ being overestimated by a typical $\Delta q_{\rm IR} = 0.13 \pm 0.06$, where the uncertainty represents the standard deviation across the stacked mock sources. However, in the SNR-range achieved for AS2UDS, we find $\Delta q_{\rm IR} = -0.05 \pm 0.08$ for the integrated flux density. As such, total fluxes from Gaussian fits constitute a better measurement of the true radio flux of the AS2UDS SMGs than peak flux densities. Conversely, the measured AS2UDS stacks in the GMRT 610 MHz map shown in Figure 3.4 have an average ratio of their integrated-to-peak flux density of $S_{\rm int}/S_{\rm peak} = 1.07 \pm 0.05$. This value is consistent with a value of unity, and hence with the stacks being unresolved – as may be expected given the large beam size of the GMRT observations. We therefore adopt the peak flux density for the GMRT stacks in this work. We have additionally verified through stacking of simulated sources that these peak flux densities are reliable for the GMRT data.

Figure 3.9 further indicates that at low signal-to-noise, the integrated flux density becomes increasingly biased, and tends to overestimate the true flux density, similar to what was observed by Leslie et al. (2020). While we investigate this in more detail in a forthcoming paper, in this work we ensure the stacks are all of high signal-to-noise (SNR $\gtrsim 10$) in order for reliable integrated flux density measurements to be made. As a representative example, we show in Figure 3.10 the stacks and residuals corresponding to the stacked data for the full AS2UDS sample in Figure 3.5. The featureless residuals show the integrated flux density measurements to be accurate.

3.B Radio AGN in submm and radio-selected Samples

By construction, radio-selected studies are sensitive to the combined emission from star-formation and AGN activity, whereas sub-millimeter surveys are restricted solely to dust-obscured star formation. As such, a higher incidence of radio-excess AGN may naturally be expected in radio-selected samples.

We show in the left panel of Figure 3.11 the fraction of radio-excess AGN in both AS2UDS and two 3 GHz-selected radio samples (Smolčić et al.

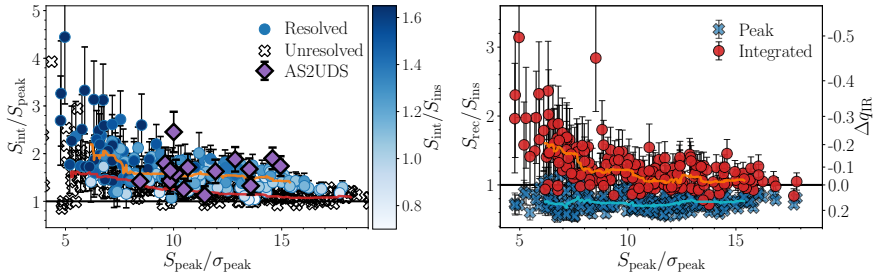

Figure 3.9: Left: The ratio of the recovered integrated and peak flux densities of the stacked mock sources, as a function of peak SNR. The data are colored by the magnitude of flux boosting. Black crosses correspond to stacking of unresolved mock sources only, while the circles include resolved sources, as well as small, random positional offsets between the true and catalogued source centers. The running median through the circles (crosses) is shown via the orange (red) line. The stacked AS2UDS SMGs (purple diamonds) show a substantially larger typical integrated-to-peak flux density ratio than the unresolved mock sources. **Right:** The ratio of recovered/inserted flux density versus recovered peak SNR. The orange (blue) line indicates the running median through the points representing integrated (peak) flux density measurements, and the right ordinate axis shows the propagated offset in $q_{\rm IR}$ based on the difference in the true and recovered flux densities. Overall, the integrated value constitutes a better estimate of the true flux density of the stacks at SNR $\gtrsim 10$.

2017a; Algera et al. 2020b) as a function of radio flux density. In the latter two studies, AGN were similarly identified via a radio-excess criterion, though by adopting a redshift-dependent radio-excess threshold instead of the fixed value we adopt in this work. For the radio studies, we scale flux densities from 3 to 1.4 GHz assuming a spectral index of $\alpha = -0.70$ (following e.g., Smolčić et al. 2017b).

At the faint end of AS2UDS, $S_{1.4} \sim 50\,\mu$Jy, Algera et al. (2020b) find that radio-excess AGN still make up $\sim 10\%$ of the radio population, while the AGN fraction in the SMGs in this regime is consistent with zero. At higher flux densities $S_{1.4} \sim 300\,\mu$Jy, Smolčić et al. (2017a) determine AGN fractions of $\sim 50\%$, compared to the $\sim 10\%$ for the radio-detected AS2UDS sample. This emphasizes that, while both radio and far-infrared emission are tracers of star formation, the former suffers significant contamination. The increased incidence of radio-excess AGN in radio surveys is not surprising – after all, these constitute some of the brightest radio sources observed. However, it may suggest that studies of the FIRRC based on radio-selected samples will be biased by contamination from active galactic nuclei. In particular, such surveys will be more sensitive to composite

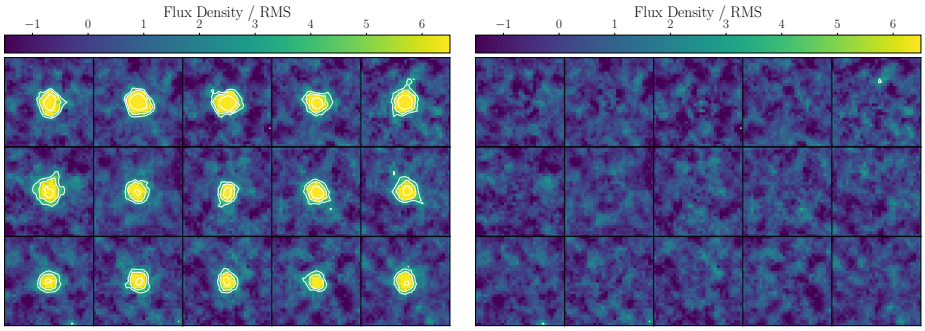

Figure 3.10: Left: Stacked detections for the 15 bins shown in Figure 3.5c, combining 222 and 418 radio-detected and -undetected sources, respectively. Only the central 31×31 pixels ($11'' \times 11''$) are shown, for clarity. The color scheme runs from -1.5 to 6.5σ, where σ is the RMS-noise in the stack. Contours are shown at levels of -3 (dashed) and $3, 5, 9\sigma$ (solid). **Right:** The residuals, after fitting the stacked detections with an elliptical Gaussian via PyBDSF (Mohan & Rafferty 2015). All stacks show a detection at a high signal-to-noise (median SNR of 11σ), and are well-fit by the Gaussian model as demonstrated by the featureless residuals.

sources, where radio emission from both AGN activity and star formation contributes to the overall radio luminosity, compared to a submm-selected sample. This is further demonstrated in the right panel of Figure 3.11, where we show the radio-AGN fraction as a function of $870\,\mu$m flux density. We find no evidence for any correlation, and a linear fit through the data returns a slope of $(2.2 \pm 2.3) \times 10^{-3}$, consistent with no gradient at the 1σ level. This substantiates that a FIR-based selection renders the sample insensitive to radio AGN.

3.C The FIRRC in Radio-selected Samples

As outlined in Section 3.4.1, radio-selected samples typically observe a declining $q_{\rm IR}$ with redshift, whereas we observe no such evolution in our sample of SMGs. A likely explanation is that this evolution towards lower values of $q_{\rm IR}$ is the result of (low-level) AGN emission (Murphy 2009b). However, obtaining conclusive evidence for this is complicated by the fact that, by definition, these AGN are very difficult to identify in radio surveys. One clear way to distinguish AGN from purely star-forming sources in the radio, however, is through Very Large Baseline Interferometry (VLBI) observa-

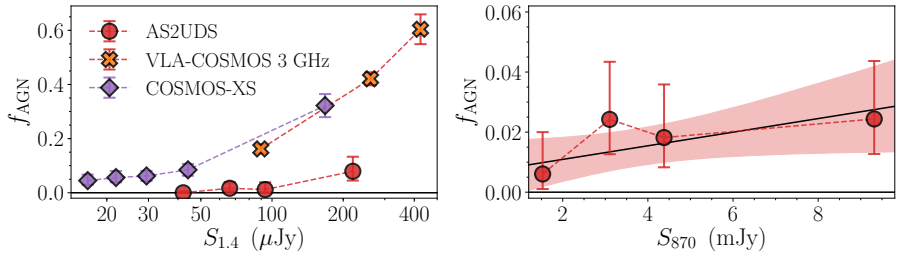

Figure 3.11: Left: The distribution of radio-excess AGN as a function of 1.4 GHz flux density. The full radio-detected AS2UDS sample is subdivided into four different bins, from which AGN are identified as having $q_{\rm IR} \leqslant 1.55$. The uncertainty on the points represents the counting error from Gehrels (1986). At flux densities $S_{1.4} \lesssim 100\,\mu$Jy, the AGN fraction is only $f_{\rm AGN} = 1^{+2}_{-1}\%$. For comparison, we overplot fractions of radio-excess AGN from two deep radio surveys at 3 GHz (scaled to 1.4 GHz using $\alpha = -0.70$): COSMOS-XS (Van der Vlugt et al. 2020, Algera et al. 2020) in purple and VLA-COSMOS (Smolčić et al. 2017b,a) in orange. The incidence of radio-excess AGN in such radio-selected samples is an order of magnitude larger than in the AS2UDS SMG sample. **Right:** The distribution of radio-excess AGN as a function of $870\,\mu$m flux density, for the full AS2UDS sample, including the radio undetected population. The red, shaded region represents a linear fit through the data, and shows no evidence of a trend between between the incidence of radio AGN and sub-millimeter flux.

tions, which are sensitive only to strong and compact sources of radio emission. If we assume the evolution in the far-infrared/radio correlation seen in recent radio surveys is solely due to low-level radio AGN, we can calculate the redshift-dependent fraction of radio emission that originates from star formation. This further requires the assumption that FIR-emission is a perfect tracer of star-formation rate across all redshifts. Given a local 'correct' value of $q_{\rm IR}$ equal to q_0, as well as redshift-evolution with slope γ, as defined in Section 3.3.3, the average redshift-dependent fraction of radio emission that originates from star formation, $f_{\rm SFR}$, is equal to

$$f_{\rm SFR}(z) = 10^{q_0[(1+z)^{\gamma}-1]}\,. \tag{3.9}$$

Herrera Ruiz et al. (2017) observed the 2-square degree COSMOS field with VLBI observations at 1.4 GHz, reaching a sensitivity of $\sigma \sim 10-15\,\mu$Jy, similar to that of the original 1.4 GHz VLA COSMOS survey (Schinnerer et al. 2007, 2010). They identify 438 radio sources at $\geqslant 5.5\sigma$ significance, with a typical VLBI flux density of $\sim 0.6-0.7$ times the total flux density, ob-

tained from the lower resolution VLA observations. This constitutes a typical detection fraction of $f_{\rm det} \simeq 0.20$ in the VLBI data. Additionally, they find that the sub-mJy radio population is more likely to host a dominant radio AGN, i.e. contributing a larger fraction of the total radio luminosity, though this is likely to (at least partially) be a selection effect, as faint sources require a strong AGN contribution to be detectable in the VLBI observations in the first place. In the following, we define $f_{\rm AGN} = 1 - f_{\rm SFR} = S_{\rm VLBI}/S_{\rm VLA}$, following Herrera Ruiz et al. (2017), and we adopt a value of $f_{\rm AGN} = 0.70$, which is typical for their sample at $S_{\rm VLA} \lesssim 1$mJy. Due to the aforementioned selection effects, this likely constitutes an upper limit to the actual contribution from a typical AGN within this flux density range. Additionally, we do not explicitly remove radio-excess AGN from this sample, which are typically discarded prior to calculating the FIRRC, and as a result, the calculated $f_{\rm AGN}$ in this way will constitute a rather strict upper limit.

We show in Figure 3.12 the expected $f_{\rm SFR}$ as a function of redshift, assuming the evolution in the FIRRC found by Delhaize et al. (2017) is solely the result of unidentified AGN contamination. We overplot the expected contribution from AGN based on the Herrera Ruiz et al. (2017) VLBI sample, as well as the $f_{\rm SFR}$ expected when *all* sources from the 1.4 GHz VLA COSMOS survey that are undetected in the VLBI observations have the maximal possible AGN contribution to render them just below the detection limit, i.e. $f_{\rm AGN}^{\rm max} = 5.5 \times \sigma_{\rm RMS}/S_{\rm VLA}$. This, evidently, constitutes a highly unrealistic scenario. The VLBI sample from Herrera Ruiz et al. (2017) implies an upper limit on the fraction of AGN contamination on the order of 20%. Additionally, this fraction is not a strong function of redshift, as the fraction of known radio sources they detect in the VLBI observations does not vary much across cosmic time. While the "maximally AGN" scenario coincides with the expected $f_{\rm SFR}$ at $z \sim 1$, the lack of a redshift-dependency ensures that at higher redshifts even this worst-case scenario underestimates how much AGN are required to contribute in order to obtain the observed redshift-evolution in the FIRRC in radio-selected samples.

Overall, an enhanced AGN contribution at high-redshift alone is therefore unlikely to fully account for the observed evolution in the FIRRC seen in radio surveys, and even by requiring all VLBI-undetected sources to be radio AGN, we cannot explain the observed $f_{\rm SFR}$. As a result, it is likely that the difference between the far-infrared/radio correlations for radio-selected and submm-selected samples is due to the different galaxy populations such studies probe.

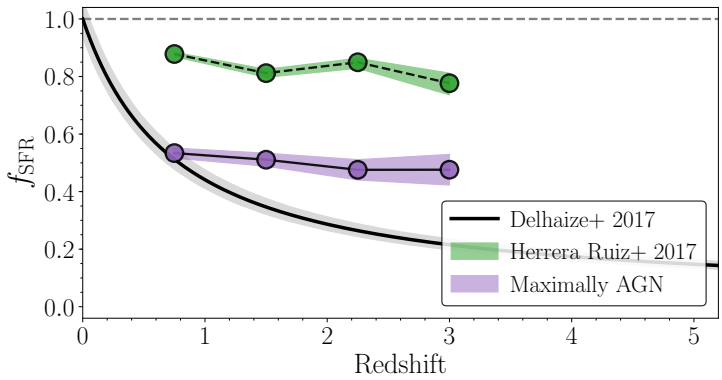

Figure 3.12: Fractional contribution of star-formation to the total radio emission as a function of redshift, under the assumption that the FIRRC is non-evolving, and any observed variation in the correlation is the result of emission from unidentified AGN. The black line shows the evolution measured by Delhaize et al. (2017), using data from the 3 GHz VLA-COSMOS project. The green, shaded region shows the expected fraction of star-formation-powered radio emission based on the VLBI observations from Herrera Ruiz et al. (2017), given their detection rate as a function of redshift, and a fixed fraction of $f_{\rm AGN} = S_{\rm VLBI}/S_{\rm VLA} = 0.70$. This region still constitutes a lower limit on $f_{\rm SFR}$ as radio-excess AGN were not removed from the VLBI sample. The purple shaded region constitutes the expected $f_{\rm SFR}$ when all VLBI-undetected sources in the 1.4 GHz VLA COSMOS project (Schinnerer et al. 2007, 2010) have the maximum possible AGN contribution to render them just below the VLBI detection limit. Even this unrealistic scenario cannot explain the measured redshift-dependency of the FIRRC in radio studies beyond $z \gtrsim 1.5$, and hence an enhanced AGN contribution at high-redshift alone is unlikely to be enough to fully account for the observed evolution in the FIRRC seen in radio-based samples.

4 Free-free Emission in High-redshift Star-forming Galaxies

The high-frequency radio sky has historically remained largely unexplored due to the typical faintness of sources in this regime, and the modest survey speed compared to observations at lower frequencies. However, high-frequency radio surveys offer an invaluable tracer of high-redshift star-formation, as they directly target the faint radio free-free emission. We present deep continuum observations at 34 GHz in the COSMOS and GOODS-North fields from the *Karl G. Jansky* Very Large Array (VLA), as part of the COLDz survey. The deep COSMOS mosaic spans $\sim 10\,\mathrm{arcmin}^2$ down to $\sigma = 1.3\,\mu\mathrm{Jy\,beam}^{-1}$, while the wider GOODS-N observations cover $\sim 50\,\mathrm{arcmin}^2$ to $\sigma = 5.3\,\mu\mathrm{Jy\,beam}^{-1}$. We detect a total of 18 galaxies at 34 GHz, of which nine show radio emission consistent with being powered by star-formation, although for two sources this is likely due to thermal emission from dust. Utilizing deep ancillary radio data at 1.4, 3, 5 and 10 GHz, we decompose the spectra of the remaining seven star-forming galaxies into their synchrotron and thermal free-free components, and find typical thermal fractions and synchrotron spectral indices comparable to those observed in local star-forming galaxies. We further determine free-free star-formation rates (SFRs), and show that these are in agreement with SFRs from SED-fitting and the far-infrared/radio correlation. Our observations place strong constraints on the high-frequency radio emission in typical galaxies at high-redshift, and provide some of the first insight in what is set to become a key area of study with future radio facilities as the Square Kilometer Array Phase 1 and next-generation VLA.

H. S. B. Algera, J. A. Hodge, D. A. Riechers *et al.*
The Astrophysical Journal 912, 73 (2021)

4.1 Introduction

Deep radio observations offer an invaluable view on star-formation in the high-redshift Universe. With current facilities, such as the upgraded NSF's *Karl G. Jansky* Very Large Array (VLA), both star-forming galaxies and faint active galactic nuclei (AGN) can now be studied down to microjansky flux densities at GHz frequencies. However, a regime that remains substantially understudied is the faint radio population at high frequencies ($\nu \gtrsim 10$ GHz), which is for a large part the result of the comparative inefficiency at which high-frequency radio surveys can be executed. Firstly, for a fixed telescope size, the field of view of a single pointing decreases steeply with frequency as ν^{-2}. Secondly, radio sources are generally intrinsically fainter at high radio frequencies, $S_\nu \propto \nu^\alpha$, where $\alpha \sim -0.7$ (Condon 1992), and thirdly, typically only a modest fraction of telescope observing time is suitable for high-frequency observations due to more stringent requirements on the observing conditions. As a result, the survey speed at 34 GHz is $\gtrsim 5000$ times smaller compared to observations at the more commonly utilized frequency of 1.4 GHz.

Despite these observational difficulties, high-frequency radio observations provide complementary insight into both star-forming galaxies and AGN. Historically, low-frequency radio observations have been used as a tracer of star-formation activity through the far-infrared/radio correlation (FIRRC; Van der Kruit 1971, 1973; De Jong et al. 1985; Helou et al. 1985). This correlation, which has been shown to hold over several orders of magnitude in terms of luminosity (Yun et al. 2001; Bell 2003), as well as to high redshift ($z \sim 5$, Delhaize et al. 2017; Calistro Rivera et al. 2017; Algera et al. 2020a; Delvecchio et al. 2021), relates the predominantly non-thermal synchrotron emission of a star-forming galaxy to its far-infrared (FIR) luminosity. The latter has been well-calibrated as a tracer of star-formation, as at FIR-wavelengths dust re-emits the light absorbed from young, massive stars (e.g., Kennicutt 1998). The synchrotron emission, instead, emanates from cosmic rays accelerated by supernova-induced shocks, and as such constitutes a tracer of the end product of massive-star formation (Condon 1992; Bressan et al. 2002). However, a second process is expected to dominate the radio spectral energy distribution (SED) at high frequencies ($\nu \gtrsim 30$ GHz): radio free-free emission (FFE). Unlike radio synchrotron radiation, free-free emission is a much more direct star-formation rate tracer, as it originates from the HII regions in which massive stars have recently formed. In addition, unlike other commonly used probes of star-formation

such as UV continuum emission or the hydrogen Balmer lines, free-free emission constitutes a tracer of star-formation that is largely unbiased by dust extinction. These characteristics establish free-free emission as one of the most reliable tracers of star formation, both in the local and the high-redshift Universe.

Locally, the radio spectra of both individual star-forming regions and star-forming galaxies have been well-characterized, and have established free-free emission as a means of calibrating other tracers of star-formation (Murphy et al. 2011). In addition, in nearby galaxies free-free emission can typically be separated spatially from non-thermal synchrotron emission, as individual extragalactic star-forming regions can be resolved (Tabatabaei et al. 2013; Querejeta et al. 2019; Linden et al. 2020). However, in the high-redshift Universe, free-free emission has remained elusive, despite the observational advantage that high-frequency continuum emission redshifts into radio bands that are more easily accessible from Earth, facilitating the sampling of the free-free-dominated regime of the radio spectrum. The comparative faintness of high-redshift galaxies, however, complicates the usage of free-free emission as a tracer of star formation at early cosmic epochs. Indeed, current detections of high-frequency continuum emission in distant galaxies remain limited to bright or gravitationally lensed starbursts (Thomson et al. 2012; Aravena et al. 2013; Riechers et al. 2013; Wagg et al. 2014; Huynh et al. 2017; Penney et al. 2020). In addition, most of these studies lacked the ancillary low-frequency data required to robustly disentangle free-free emission from the overall radio continuum, which requires observations at a minimum of three frequencies (e.g., Tabatabaei et al. 2017; Klein et al. 2018), or probed rest-frame frequencies dominated by thermal emission from dust ($\nu \gtrsim 200\,\mathrm{GHz}$; Condon 1992). Despite this observational complexity, one of the key science goals for upcoming radio facilities such as the next-generation VLA is to systematically use free-free emission as a probe of star-formation in the high-redshift galaxy population (Barger et al. 2018). As such, it is of considerable interest to already explore this high-frequency parameter space with current radio facilities.

While radio continuum observations are invaluable in characterizing high-redshift star-formation in a dust-unbiased manner, radio surveys are additionally capable of detecting what fuels this process, namely molecular gas. For a clear census of the molecular gas reservoir of the Universe, blind surveys are crucial, as they do not suffer from any biases arising from follow-up radio observations of known high-redshift sources. The first such blind surveys have recently been completed, such as ASPECS (Walter et al.

2016; Decarli et al. 2016), and the CO Luminosity Density at High Redshift survey (COLDz; Pavesi et al. 2018; Riechers et al. 2019, 2020), which targets low-J CO observations at 34 GHz using the VLA. Due to the large bandwidth of its high-frequency receivers, deep VLA surveys of molecular gas result in sensitive continuum images essentially 'for free'. In this work, we describe the deep continuum observations of the COLDz survey. Our main goal is to constrain the radio spectra of typical sources in a frequency range that has not been widely explored, and extend our analysis to a new parameter space of faint AGN and star-forming galaxies, down to the μJy level. The COLDz survey covers a region of two well-studied extragalactic fields, COSMOS (Scoville et al. 2007) and GOODS-North (Giavalisco et al. 2004), and hence allows for a multi-wavelength perspective on this faint population.

The outline of this paper is as follows. In Section 4.2 we describe our 34 GHz VLA observations and the creation of deep continuum images, as well as the existing ancillary multi-wavelength data. We outline the detection and source extraction of sources at 34 GHz in Section 4.3, and assign the radio sample multi-wavelength counterparts and redshifts in Section 4.4. We present our deep radio number counts at 34 GHz in Section 4.5, and separate the sample into radio AGN and star-forming galaxies in Section 4.6. In this Section, we additionally decompose the spectra of the star-forming galaxies into radio synchrotron and free-free emission, and compare the latter as a tracer of star-formation with more commonly adopted tracers at high-redshift. Section 4.7 provides an outlook for the future, and discusses how upcoming radio facilities will revolutionize high-redshift studies of radio star-formation. Finally, we summarize our findings in Section 4.8. Where necessary, we assume a standard Λ-Cold Dark Matter cosmology, with $H_0 = 70\,\mathrm{km\,s^{-1}\,Mpc^{-1}}$, $\Omega_m = 0.30$ and $\Omega_\Lambda = 0.70$. Magnitudes are quoted in the AB-system and a Chabrier (2003) initial mass function is assumed.

4.2 Observations & Data Reduction

4.2.1 COLDz

The COLDz survey (Pavesi et al. 2018; Riechers et al. 2019, 2020) was designed to blindly probe the low$-J$ CO-lines in high-redshift galaxies, which requires high-frequency observations spanning a large bandwidth. Both are provided by the Ka-band of the upgraded VLA, which allows for a total

of 8 GHz of contiguous frequency coverage, tuneable to be within the range of $26.5 - 40.0$ GHz. The COLDz observing strategy is presented in Pavesi et al. (2018), to which we refer the reader for additional details.

For the optimal constraints on the CO luminosity function, COLDz combines a deep yet small mosaic in the COSMOS field with wider but shallower observations in the GOODS-N field. The COSMOS observations constitute a 7-pointing mosaic, and account for a total on-source time of 93 hr. The data were taken in the VLA D (82 hr) and DnC (11 hr) configurations, and span a total frequency range of $30.969 - 39.033$ GHz, using dual polarization. The observations of the GOODS-N field comprise a total of 122 hr of on-source time, and make up a 57-pointing mosaic. The data were predominantly taken in the D-configuration (83.5 hr), with additional observations taking place in the D→DnC (4.4 hr), DnC (30.8 hr) and DnC→C (3 hr) configurations. The observations cover a frequency range between $29.981 - 38.001$ GHz, and in what follows we will refer to both the COSMOS and GOODS-N observations by their typical central frequency of 34 GHz.

Calibration of the observations was done in CASA version 4.1.0, with extensive use being made of a modified version of the VLA pipeline, the details of which can be found in Pavesi et al. (2018). As one of the main goals of COLDz is to detect spectral lines, both Hanning smoothing and RFLAG, used to remove radio frequency interference (RFI), were switched off. Instead, some persistent RFI at 31.5 GHz was flagged manually, and some occasions of narrow noise spikes were flagged via the methods detailed in Pavesi et al. (2018). The data were then concatenated, and, for the continuum observations presented here, subsequently averaged in time (9 s) and frequency (16 channels), in order to reduce the size of the dataset prior to imaging. The imaging of the calibrated 34 GHz observations was carried out in CASA version 4.3.1, using the 'mosaic' mode of CASA task clean. For both the COSMOS and the GOODS-N mosaics, a multi-frequency synthesis algorithm was employed to take into account the large bandwidth of the observations. A natural weighting was further adopted, in order to maximize the sensitivity of the data. The data were imaged iteratively, by cleaning all sources at $> 6\sigma$ down to the 2σ level.

We present the 34 GHz continuum maps across the COSMOS and GOODS-N fields, as well as the corresponding root mean square (RMS) noise maps, in Figures 4.1 and 4.2. The COSMOS mosaic covers a field-of-view of 9.6 arcmin^2 out to 20% of the peak primary beam sensitivity. The central RMS-noise in the image equals $1.3\,\mu$Jy beam^{-1}, with the typical RMS increasing to

$1.5\,\mu$Jy beam^{-1} and $1.9\,\mu$Jy beam^{-1}, within 50 and 20 per cent of the peak primary beam sensitivity, respectively. The synthesized beam of the COSMOS observations is well-described by an elliptical Gaussian of $2\farcs70 \times 2\farcs41$ with a position angle of $-0.7°$.

The GOODS-N mosaic spans an area of 51 arcmin^2 out to 20% of the peak primary beam sensitivity, covering roughly a third of the 'traditional' GOODS-N survey (Giavalisco et al. 2004). The typical noise level varies slightly across the mosaic, with a single, deep 34 GHz pointing in the field reaching a central noise level of $3.2\,\mu$Jy beam^{-1}. Across the entire GOODS-N field, within 50 and 20 per cent of the peak primary beam sensitivity, respectively, the typical RMS-noise equals $5.3\,\mu$Jy beam^{-1} and $5.5\,\mu$Jy beam^{-1}. The synthesized beam is well-described by an elliptical Gaussian of $2\farcs19 \times 1\farcs84$, with a position angle of $75.3°$, after smoothing the different pointings to a common beam. Pavesi et al. (2018) also provide a version of the GOODS-N radio map where all pointings have been imaged at their native resolution. While the resulting mosaic cannot be described by a single beam, it allows for the search for unresolved sources at slightly higher signal-to-noise (S/N), as no smoothing or tapering was required. We use this "unsmoothed" map for source detection in Section 4.3, in addition to the regular mosaic with a homogenized beam.

4.2.2 Ancillary Radio Observations

The COLDz observations in the COSMOS field overlap in their entirety with deep 3 and 10 GHz VLA pointings from the COSMOS-XS survey (van der Vlugt et al. 2021; Algera et al. 2020b). These images have a resolution similar to COLDz, with a synthesized beam of $2\farcs14 \times 1\farcs81$ and $2\farcs33 \times 2\farcs01$ at 3 and 10 GHz, respectively. At 3 GHz, the observations reach a central RMS of $0.53\,\mu$Jy beam^{-1}, with a typical primary beam sensitivity of 90% of the maximum across the COLDz mosaic. The 10 GHz data reach a central RMS-sensitivity of $0.41\,\mu$Jy beam^{-1} (typical primary beam sensitivity of 80%), and were centered on the COLDz observations by design. In total, 70 sources detected at 3 GHz at $\geqslant 5\sigma$ fall within the ~ 10 arcmin^2 COLDz field-of-view. A subset of 40 are additionally detected at 10 GHz. In addition, the central region of the COSMOS field, spanning ≈ 1 deg^2, is covered by VLA observations at 1.4 GHz (Schinnerer et al. 2007, 2010). These observations reach a typical RMS sensitivity of $12\,\mu$Jy beam^{-1} across the COLDz field-of-view, at a resolution of $1\farcs5 \times 1\farcs4$. In total, two sources within the COLDz field-of-view are detected at 1.4 GHz. Adopting a typical spectral index of $\alpha = -0.70$, the COLDz and 1.4 GHz COSMOS observa-

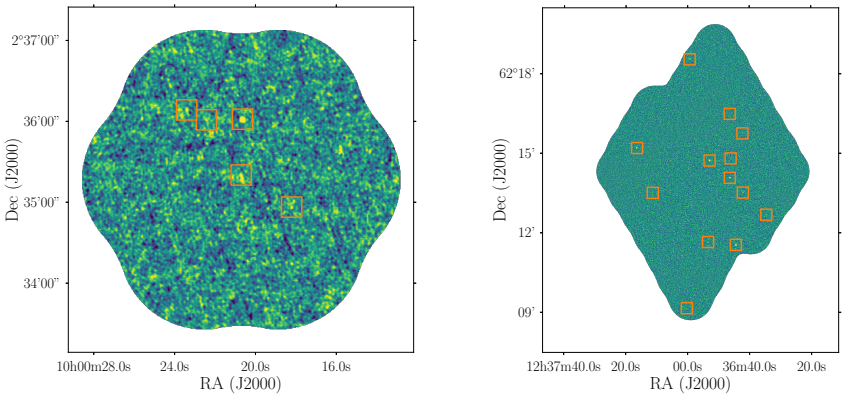

Figure 4.1: Left: The 7-pointing COSMOS 34 GHz continuum mosaic of $\sim 10\,\mathrm{arcmin}^2$. The five robust detections (Section 4.3) are highlighted via orange squares. **Right:** The $\sim 50\,\mathrm{arcmin}^2$ GOODS-North 34 GHz mosaic (pointings $1-56$), with the thirteen robust detections highlighted. Both mosaics are uncorrected for primary beam attenuation, and the colorscale runs from -3σ to 3σ, where σ represents the (uncorrected) RMS-noise in the image. It is clear that many 34-GHz detections lie close to the 3σ detection threshold, and would not have been identified without deep, ancillary radio data across the fields.

tions are approximately of equal relative depth.[1]

The GOODS-N field is similarly well-covered by radio observations from the VLA. At 1.4 GHz, the entire field has been imaged in a single pointing by Owen (2018), down to a central RMS of $2.2\,\mu\mathrm{Jy\,beam}^{-1}$ with little variation across the field-of-view of the COLDz mosaic. The resolution of the radio data equals $1\farcs6$, and a total of 186 sources detected at 1.4 GHz by Owen (2018) fall within the 20 percent power point of the GOODS-N COLDz image. The field has additionally been mapped at 5 GHz by Gim et al. (2019). They detect 52 sources down to an RMS of $3.5\,\mu\mathrm{Jy\,beam}^{-1}$ across two VLA pointings covering a total area of $109\,\mathrm{arcmin}^2$, which fully overlaps with the COLDz footprint. Their angular resolution of $1\farcs47 \times 1\farcs42$ is similar to that of the deeper 1.4 GHz observations, and Gim et al. (2019) find that all 5 GHz detections have a counterpart in this lower frequency map. Finally, Murphy et al. (2017) present a single pointing at 10 GHz in the GOODS-N field (primary beam FWHM of $4\farcm25$) at a native resolution of

[1]However, we note that we adopt a 3σ detection threshold for the COLDz data in Section 4.3, whereas a 5σ threshold was adopted by Schinnerer et al. (2007) for the 1.4 GHz observations. As such, sources detected at 3σ in the COLDz survey require a spectral index of $\alpha \lesssim -0.85$ to additionally be detected at 1.4 GHz.

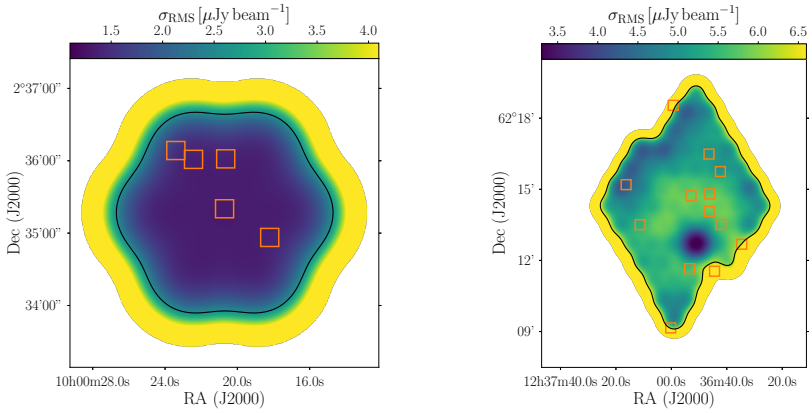

Figure 4.2: Left: The COLDz COSMOS RMS-map, after correction for primary beam attenuation. The uncorrected RMS-map is highly uniform, and any structure in the map is solely the result of the beam correction. **Right:** The RMS-map of the 34-GHz observations across the GOODS-N field. The map uncorrected for the beam is highly uniform in its noise properties, and the structure in the map indicates the differences in observing time across the mosaic, with a single deep pointing centered on R.A. = 12:36:51.06, Dec. = +62:12:43.8, designed to overlap with the PdBI observations from Decarli et al. (2014), highlighted as the region with the lowest RMS. The black lines outlining the mosaics indicate the region where the e primary beam reaches 50% of its maximum sensitivity, and the robust detections in both fields are highlighted via the orange boxes as in Figure 4.1.

$0\farcs22$. At this high angular resolution, their observations reach a sensitivity of $0.57\,\mu$Jy beam^{-1} in the center of the pointing. Murphy et al. (2017) further provide two tapered images with a resolution of $1''$ and $2''$, similar to the ancillary radio data in the field. These images reach an RMS-noise of 1.1 and $1.5\,\mu$Jy beam^{-1}, respectively. In total, Murphy et al. (2017) recover 38 sources across the combined high-resolution and tapered images. Approximately 75% of the COLDz GOODS-N data overlap with the smaller pointing at 10 GHz, when imaged out to 5% of the primary beam FWHM (Murphy et al. 2017).

We summarize the detection limits of the various radio observations across both COSMOS and GOODS-N in Figure 4.3, and compare these with the typical radio spectrum of a star-forming galaxy (SFR $= 100\,M_\odot\,{\rm yr}^{-1}$ at $z = 1$). This assumes the Kennicutt (1998) conversion between SFR and infrared luminosity, adapted for a Chabrier IMF, as well as a simple optically thin dust spectral energy distribution with $\beta = 1.8$ and $T_{\rm dust} = 35$ K. We further adopt the Condon (1992) model for the radio spectrum of

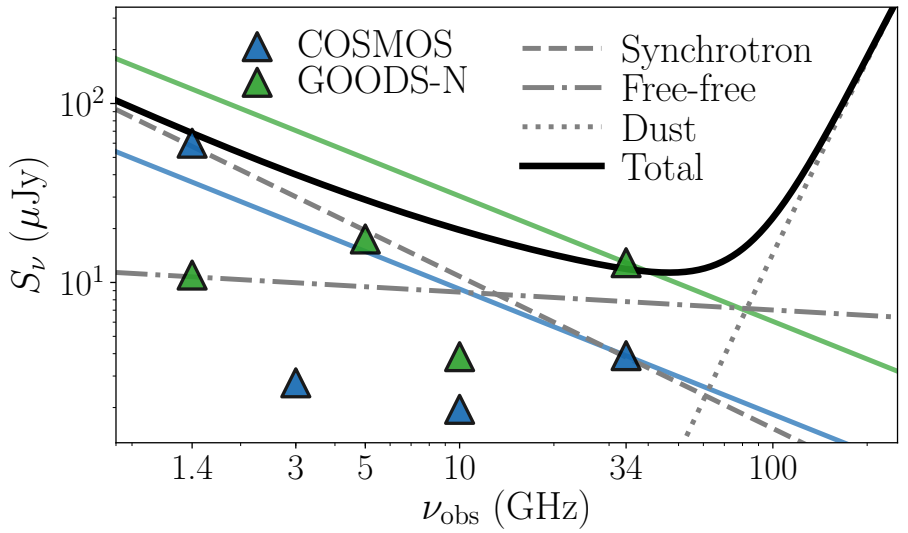

Figure 4.3: The detection limits of the various radio observations across COSMOS and GOODS-N, superimposed on the radio spectrum of a star-forming galaxy (SFR $= 100\,M_\odot\,{\rm yr}^{-1}$ at $z = 1$; see text for details). The blue (green) lines indicate the detection limit of the COLDz 34 GHz continuum data, scaled with a typical $\alpha = -0.70$. The different constituents of the radio spectrum are shown, including free-free emission which is expected to become dominant at rest-frame $\nu \gtrsim 30$ GHz. As such, the COLDz observations directly target the strongly free-free-dominated regime.

star-forming galaxies, and assume the far-infrared/radio correlation from Delhaize et al. (2017). Under these assumptions, a galaxy with SFR $= 100\,M_\odot\,{\rm yr}^{-1}$ can be directly detected at 34 GHz out to $z = 2$ ($z = 1$) in the COSMOS (GOODS-N) field.

4.2.3 Ultra-violet to Submillimeter Observations

Both the COSMOS and GOODS-North fields have been targeted by a wealth of multi-wavelength observations, spanning the full X-ray to radio regime. For the COSMOS field, we adopt the multi-wavelength matching procedure for the COSMOS-XS survey (Algera et al. 2020b), as all 34 GHz continuum detections have radio counterparts in this survey (Section 4.3). This cross-matching procedure invokes the recent "Super-deblended" catalog from Jin et al. (2018), who adopt a novel deblending technique to address con-

fused mid-infrared to submillimeter observations. The Super-deblended catalog provides photometry from *Spitzer*/IRAC $3.6\,\mu$m to MAMBO 1.2 mm (for a full list of references see Jin et al. 2018), as well as radio data at 1.4 and 3 GHz from Schinnerer et al. (2010) and Smolčić et al. (2017b), respectively. However, we directly adopt the radio fluxes from the 1.4 GHz catalog from Schinnerer et al. (2007, 2010), and use the deeper COSMOS-XS 3 GHz data in favor of the observations from Smolčić et al. (2017b). In addition, Algera et al. (2020b) cross-match with the $z^{++}YJHK_s$-selected COSMOS2015 catalog from Laigle et al. (2016) containing far-ultraviolet to near-infrared photometry, in order to complete the coverage of the spectral energy distribution. Finally, we search for Atacama Large Millimeter/submillimeter Array (ALMA) counterparts as part of the AS2COSMOS (Simpson et al. 2020) and A3COSMOS surveys (Liu et al. 2019), which constitute a collection of individual pointings across the COSMOS field.

A wealth of multi-wavelength data similarly exist across the GOODS-N field. In order to obtain optical/near-infrared photometry for the 34 GHz continuum detections, we adopt the 3D-HST photometric catalog from Skelton et al. (2014). Source detection was performed in a deep combined F125W+F140W+F160W image, and further photometry is carried out in the wavelength range of $0.3 - 8\,\mu$m, including *Spitzer*/IRAC observations from Dickinson et al. (2003) and Ashby et al. (2013). For further details, we refer the reader to Skelton et al. (2014). We obtain additional mid- and far-infrared photometry from the Super-deblended catalog across the GOODS-N field by Liu et al. (2018). They adopt combined priors from *Spitzer*/IRAC, *Spitzer*/MIPS $24\,\mu$m and VLA 1.4 GHz observations, and utilize these to deblend the photometry at more strongly confused wavelengths. The Super-deblended catalog provides additional photometry from *Spitzer*/IRS, *Herschel*/PACS (Magnelli et al. 2013) and *Herschel*/SPIRE (Elbaz et al. 2011), as well as data from JCMT/SCUBA-2 $850\,\mu$m (Geach et al. 2017) and AzTEC+MAMBO 1.2 mm (Penner et al. 2011).

4.2.4 X-ray Observations

While a radio-based selection renders one sensitive to AGN activity at radio wavelengths, $\sim 20 - 25\%$ of the faint radio population ($S_{1.4} \lesssim 1$ mJy; equivalent to $S_{34} \lesssim 100\,\mu$Jy given $\alpha = -0.70$) is thought to consist of radio-quiet AGN (Bonzini et al. 2013; Smolčić et al. 2017a). These sources show no substantial AGN-related emission at radio wavelengths, but are instead classified as AGN based on signatures at other wavelengths. Strong X-ray emission, in particular, forms an unmistakable manifestation of AGN ac-

tivity. As such, we make use of the deep X-ray coverage over both the COSMOS and GOODS-N fields to characterize the nature of the 34 GHz continuum detections.

The COSMOS field is covered in its entirety by the 4.6 Ms *Chandra* COSMOS Legacy survey (Civano et al. 2016), with the individual *Chandra* pointings accounting for a typical ≈ 160 ks of exposure time. The area covered by the COLDz survey contains 3 X-ray detections, at a typical detection limit of the survey of $\sim 2 \times 10^{-15}$ erg cm^{-2}s^{-1} in the full range of $2-10$ keV. The catalog provided by Marchesi et al. (2016a) further includes X-ray luminosities for X-ray detections with robust optical and infrared counterparts.

The GOODS-North field is similarly covered by deep 2 MS *Chandra* observations as part of the *Chandra* Deep Field North Survey (Xue et al. 2016). Across the COLDz field-of-view, the survey identifies 189 X-ray sources, and attains a flux limit of $\sim 3.5 \times 10^{-17}$ erg cm^{-2} s^{-1} in the $0.5-7$ keV energy range – nearly a factor of 50 deeper than the COSMOS data, when converted to the same energy range adopting $\Gamma = 1.8$. The catalog provided by Xue et al. (2016) further includes X-ray luminosities for the entries with reliable redshift information.

4.3 Continuum Sources

We run source detection on our 34 GHz radio maps using PyBDSF (Mohan & Rafferty 2015), prior to correcting the images for the primary beam. This has the benefit that the noise properties are uniform across the mosaics, which facilitates source detection, and additionally ensures that fewer spurious sources arise around the noisy edges of the maps.[2] In our source detection procedure we can afford to set a liberal detection threshold, as both the COSMOS and GOODS-N fields contain additional low-frequency radio data of greater depth relative to the COLDz observations, and as such we expect any 34 GHz detections to have radio counterparts. In this work, we therefore adopt a 3σ peak detection threshold for both images.

In the COSMOS field, we compare to the deep S- and X-band observations from van der Vlugt et al. (2021). For a source to be undetected in this 10 GHz map, yet detected at 34 GHz, requires a highly inverted spectral index of $\alpha_{34}^{10} \gtrsim 0.55$. In the GOODS-N field, we compare with the

[2]We have verified that, after applying the primary beam correction, the flux densities are consistent with those obtained from running source detection on the primary-beam-corrected map, with a typical ratio of $S_{\rm uncorr}/S_{\rm corr} = 1.05 \pm 0.07$.

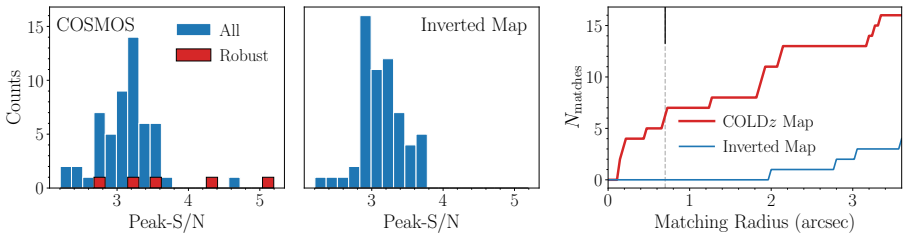

Figure 4.4: Left: distribution of S/N ratios for all the peaks identified in the COSMOS 34 GHz image. Sources with lower-frequency radio counterparts within $0\farcs7$ are highlighted in red. The most significant detection at a 34 GHz S/N $= 17$ is not shown for clarity. **Middle:** same as the left panel, now showing "sources" detected in the inverted image. No matches within $0\farcs7$ are found with lower-frequency radio counterparts, and no spurious detection above S/N $= 3.7$ exists. **Right:** number of cross-matches between the 34 GHz continuum detections and the detections in the deeper 3 GHz COSMOS-XS map, as a function of matching radius. The radius adopted in this work is indicated via the black vertical line. No spurious matches are found in the inverted map out to $\sim 2''$, indicating the sources recovered in the 34 GHz map are likely to be real.

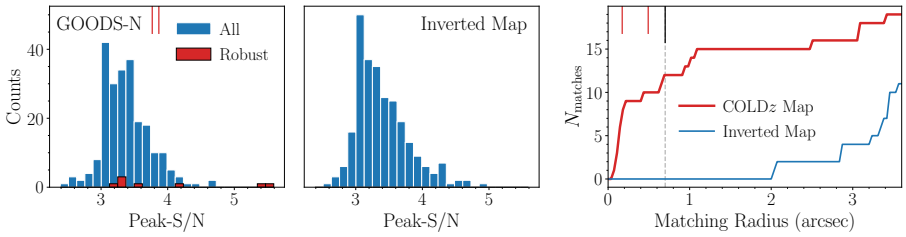

Figure 4.5: Same as Figure 4.4, now showing peaks identified in the GOODS-N radio map. Four high-S/N detections in the real map are not shown for clarity, and the two red, vertical dashes indicate the two additional sources we recover when performing source detection in the unsmoothed radio map (see text for details). In total, 13 sources are robustly detected at 34 GHz in GOODS-N.

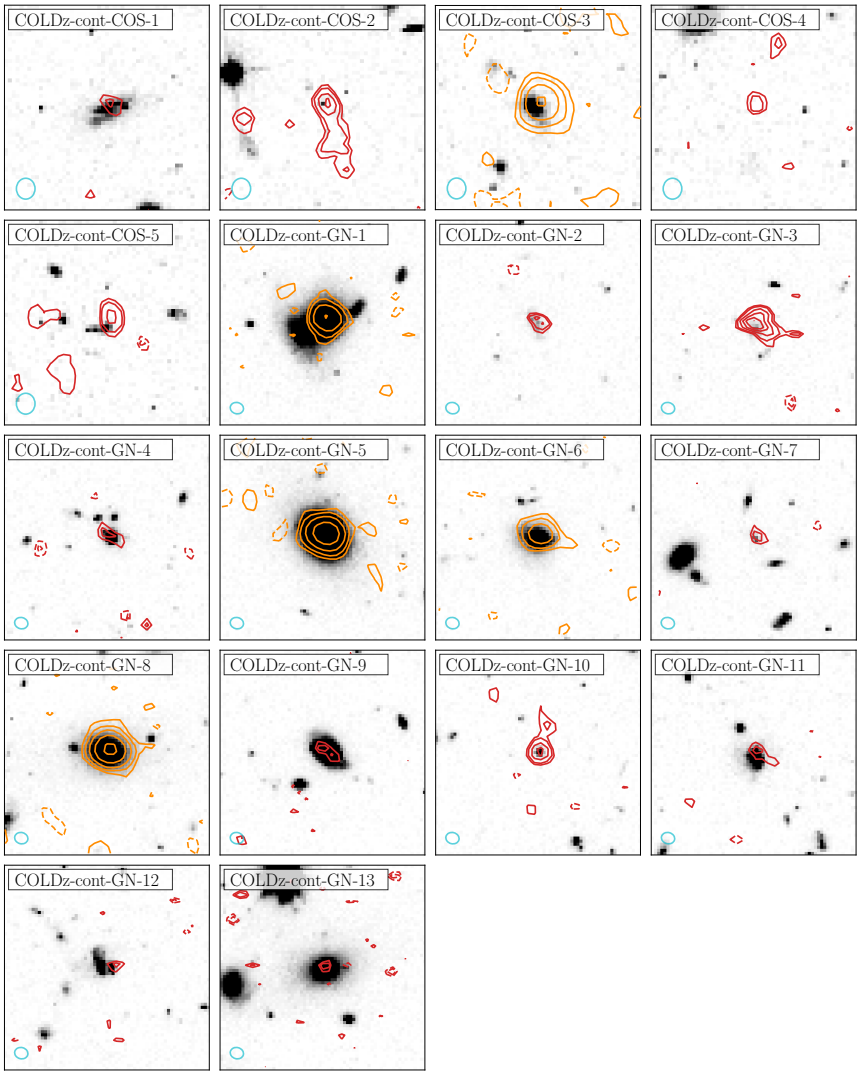

Figure 4.6: Postage stamps ($16'' \times 16''$) of the 18 robust COLDz detections, overlaid on *HST* F814W (COSMOS) or F160W (GOODS-N) images. For faint sources (S/N $\leqslant 10$ at 34 GHz), 34 GHz contours are shown in red, and represent $\pm 2.5\sigma$, followed by $\pm 3\sigma, \pm 4\sigma \ldots$ in steps of 1σ, where σ represents the local RMS in the radio map. Bright sources – typically radio AGN, as will be quantified in Section 4.6.1 – are shown via orange contours, in steps of $\pm 2^N \sigma$, where $N = 1, 2, \ldots$. Negative contours are shown via dashed lines, and the beam size is indicated in the lower left corner via the cyan ellipse. While half of the sample is detected at relatively low S/N ($3 - 5\sigma$), most of these are star-forming galaxies, likely dominated at these frequencies by radio free-free emission (Section 4.6.2), and form the focus of this work.

1.4 GHz observations from Owen (2018), and find that 34 GHz sources require an inverted spectral index of $\alpha_{34}^{1.4} \gtrsim 0.15$ to remain undetected in the lower-frequency map. We note that, as we perform source detection at low S/N, the source sizes calculated via PyBDSF may be affected by the local noise properties within the images. In particular, sources with fitted radio sizes smaller than the synthesized beam will have an integrated flux density smaller than the peak value, and will have an uncertainty on the latter that is smaller than the local RMS-noise in the map (Condon 1997). We show in Appendix 4.A.2 that all but one source are likely to be unresolved at $\sim 2\farcs5$ resolution. For all unresolved sources, we adopt the peak brightness, while the integrated flux density is used otherwise. Following the discussion above, we redefine the uncertainty on the peak brightness and conservatively adopt the maximum of the calculated uncertainty from PyBDSF and the local RMS at the source position.

In the COSMOS map we detect 57 peaks at $\geqslant 3\sigma$ within 20% of the peak primary beam sensitivity (Figure 4.4). We can match six to COSMOS-XS counterparts within $0\farcs7$, where we expect to have $N_{\rm false} = 0.2$ false matches based on randomly shifting the coordinates of all $\geqslant 3\sigma$ peaks in the mosaic, and repeating the matching a large number of times. This radius was chosen to include all close associations to COSMOS-XS sources, while minimizing the number of expected false matches ($N_{\rm false} \ll 1$). To further verify the robustness of the six close counterparts, we run our source detection procedure on the inverted radio map (i.e., multiplied by $\times -1$), and find a total of 60 negative "sources", all of which are by definition spurious. None of these can be matched to COSMOS-XS counterparts within $0\farcs7$, indicating the real matches are likely to be robust. However, out of the six associations to COSMOS-XS galaxies within $0\farcs7$, we find that one candidate source (S/N $= 3.3$ at 34 GHz) is detected solely at 3 GHz while a 10 GHz counterpart is also expected, implying it is likely to be spurious. As such, we discard it from our sample and retain 5 sources which form the robust COSMOS continuum sample. Three of these have a signal-to-noise ratio larger than the highest peak-S/N in the inverted radio map of 3.7σ. The remaining two have a relatively low S/N of ~ 3.5, but are deemed robust due to their multi-wavelength associations.

We adopt an identical source detection procedure for the GOODS-N 34 GHz map. In total, PyBDSF identifies 236 peaks above 3σ in the map, of which we match 12 with low-frequency radio counterparts in the catalog

from Owen (2018) at $0\farcs7$, where we expect $N_{\rm false} = 0.3$ incorrect identifications. We find 263 sources in the inverted radio map, none of which are matched to lower-frequency radio counterparts within $0\farcs7$. However, upon cross-matching our 12 robust sources with the 5 GHz catalog from Gim et al. (2019), we find only 11 matches within $0\farcs7$. The single unmatched source (S/N $= 3.3$ at 34 GHz) also falls within field-of-view of the single deep X-band pointing from Murphy et al. (2017), but is additionally undetected at 10 GHz. As such, this source is likely to be spurious, and we discard it from further analysis. The signal-to-noise distributions of all peaks identified by PyBDSF in the GOODS-N image and its inverted counterpart are shown in Figure 4.5. The maximum S/N in the inverted map is S/N ≈ 5.0, which implies that 5/11 robust 34 GHz detections lie below the most significant spurious source. This emphasizes the added value of the deep, low-frequency data, which allow us to identify faint sources that would not have been recovered in a blind source detection procedure. We further perform source detection via PyBDSF on the unsmoothed mosaic (Section 4.2), using the same detection threshold as adopted for the regular GOODS-N mosaic, in order to maximize the number of recovered sources. We find two additional matches with low-frequency counterparts at both 1.4 and 5 GHz, resulting in a total of 13 sources identified in GOODS-N. We adopt the peak brightness for these two sources, given the lack of a common beam in the unsmoothed mosaic, and use the local RMS in the map as the appropriate uncertainty.

Given that we require any identifications at 34 GHz to have robust low-frequency radio counterparts, we may be missing any sources with highly unusual inverted spectra. To investigate this possibility, we median-stack in the low-frequency radio maps on the positions of the highest signal-to-noise peaks at 34 GHz for which no radio counterpart was found (3 and 10 GHz in COSMOS, 1.4 GHz in GOODS-N, using the publicly available radio map from Morrison et al. 2010). In neither the COSMOS nor the GOODS-N fields do we see any evidence for positive signal in the stacks, indicating that most – and likely all – of these S/N $\approx 3-5$ peaks at 34 GHz are spurious. In addition, we cross-match the peaks in the 34 GHz map that do not have radio counterparts with optical/NIR-selected sources from the COSMOS2015 and 3D-HST catalogs in COSMOS and GOODS-N, respectively, within $0\farcs7$. We find two matches with the COSMOS2015 catalog, at $\sim 0\farcs4$. However, based on a visual inspection, there is no hint of emission at either 3 or 10 GHz for these sources, indicating they are likely to be spurious. We find 37 matches within $0\farcs7$ between $\geqslant 3\sigma$ peaks in the 34 GHz

GOODS-N radio map without radio counterparts and the 3D-HST catalog. In addition to a visual inspection, we stack these sources at 1.4 GHz, but find no detection in the stack, and place a 3σ upper limit on the average 1.4 GHz emission of $S_{1.4} \leqslant 2.7\,\mu$Jy beam^{-1}, which corresponds to a highly inverted $\alpha_{34}^{1.4} \gtrsim 0.6$. This further substantiates that the majority of the low-S/N peaks identified at 34 GHz are likely to be spurious.

We summarize the radio properties of the eighteen sources detected at 34 GHz in Table 4.1, and show postage stamps on top of *Hubble Space Telescope* images in Figure 4.6. The tabulated flux densities are further corrected for flux boosting, as outlined in Appendix 4.A.3. For a source detected at 3σ (4σ), the typical correction factor is 20% (10%), whereas at S/N $\gtrsim 5$, the effects of flux boosting are found to be negligible.

4.4 Multi-Wavelength Properties

4.4.1 Multi-wavelength Counterparts and Redshifts

Across the combined COSMOS and GOODS-N 34 GHz mosaics, we identify a total of 18 robust high-frequency continuum detections. In this section, we detail the association of multi-wavelength counterparts to this radio-selected sample. For the five COSMOS sources, we follow the cross-matching procedure from Algera et al. (2020b). We first match the 34 GHz continuum detections to the Super-deblended catalog containing far-infrared photometry, exploring matching radii up to $0\farcs9$. However, we find all five sources can be matched to Super-deblended counterparts within $0\farcs3$, where we expect a negligible number of false associations. We further find that the five sources can be additionally cross-matched to galaxies in the COSMOS2015 catalog, similarly within $0\farcs3$. We subsequently cross-match with the AS2COSMOS and A3COSMOS ALMA catalogs, finding a single match at $0\farcs1$ that appears in both catalogs, and adopt the photometry from the former. We additionally match with the robust and tentative catalog of COLDz CO-emitters from Pavesi et al. (2018) and recover two matches within $0\farcs3$ within the robust set of blind CO-detections.[3]

We then extract the optimal photometric or spectroscopic redshift from these catalogs. We prioritize redshifts in the following order: 1) a spectroscopic value based on a COLDz CO-line, 2) a spectroscopic redshift within

[3] As such, the observed 34 GHz continuum emission may be in part due to these bright CO-lines. We investigate this in Section 4.6.3.

Table 4.1: Radio Properties of the 34 GHz-selected COLDz sample

ID	RA	Dec	z[a]	$S_{1.4}$[b]	S_3	S_5	S_{10}	S_{34}[c]
	[deg]	[deg]		[μJy]	[μJy]	[μJy]	[μJy]	[μJy]
COLDz-cont-COS-1	150.093436	2.600324	0.89	< 60.0	8.8 ± 0.6	-	5.4 ± 0.5	3.2 ± 1.4
COLDz-cont-COS-2[d]	150.086281	2.588947	5.30	< 60.0	21.9 ± 0.6	-	9.1 ± 0.4	6.8 ± 1.3
COLDz-cont-COS-3	150.086022	2.600442	0.98 ± 0.01	272.0 ± 13.0	159.1 ± 0.6	-	78.2 ± 0.5	23.6 ± 1.4
COLDz-cont-COS-4[e]	150.075874	2.582339	2.48	< 60.0	17.8 ± 0.6	-	7.6 ± 0.5	4.3 ± 1.4
COLDz-cont-COS-5	150.097512	2.602361	1.00	< 60.0	27.4 ± 0.6	-	11.3 ± 0.5	6.3 ± 1.5
COLDz-cont-GN-1	189.318274	62.253407	0.56	175.4 ± 5.9	-	153.0 ± 3.7	133.0 ± 12.9	72.3 ± 4.3
COLDz-cont-GN-2[f]	189.251020	62.152715	$1.61^{+0.27}_{-0.01}$	297.4 ± 10.1	-	114.2 ± 5.3	-	25.4 ± 6.4
COLDz-cont-GN-3	189.247233	62.309206	$2.00^{+0.02}_{-0.01}$	4600.8 ± 78.0	-	1106.0 ± 6.0	-	42.7 ± 7.6
COLDz-cont-GN-4	189.222491	62.194332	1.27	74.4 ± 7.6	-	19.7 ± 3.5	17.4 ± 2.1	15.3 ± 5.7
COLDz-cont-GN-5	189.220371	62.245561	0.32	214.0 ± 7.8	-	188.1 ± 3.5	191.5 ± 3.5	185.7 ± 11.4
COLDz-cont-GN-6	189.193081	62.234673	0.96	278.2 ± 9.4	-	177.7 ± 3.5	138.9 ± 2.9	79.4 ± 5.8
COLDz-cont-GN-7[g]	189.191979	62.246903	$2.95^{+0.06}_{-0.02}$	103.9 ± 3.7	-	42.6 ± 8.3	35.1 ± 2.9	15.4 ± 5.8
COLDz-cont-GN-8	189.184957	62.192532	1.01	1792.0 ± 76.2	-	963.0 ± 6.3	449.8 ± 5.8	317.8 ± 8.2
COLDz-cont-GN-9	189.176004	62.262621	0.86	185.0 ± 7.2	-	46.3 ± 4.3	39.0 ± 2.8	15.6 ± 5.1
COLDz-cont-GN-10	189.175494	62.225399	2.02	461.3 ± 6.9	-	137.8 ± 3.5	67.0 ± 2.2	30.6 ± 5.7
COLDz-cont-GN-11[h]	189.143948	62.211490	1.22	188.5 ± 7.7	-	59.8 ± 3.4	31.5 ± 2.4	17.6 ± 6.5
COLDz-cont-GN-12	189.297011	62.225238	2.00	126.0 ± 6.3	-	46.6 ± 8.1	16.3 ± 2.6	18.1 ± 5.4
COLDz-cont-GN-13	189.193158	62.274894	0.50	403.0 ± 14.2	-	95.9 ± 12.4	26.0 ± 4.8	18.0 ± 5.1

[a]Uncertainties are quoted on the photometric redshifts only.

[b]Where applicable, 5σ upper limits are quoted for the COSMOS field, based on the typical RMS in the 1.4 GHz map (Schinnerer et al. 2007, 2010).

[c]Flux densities are corrected for flux boosting (Appendix 4.A.3). The flux densities listed for COLDz-cont-COS-2 and COLDz-cont-COS-4 are predominantly due to the combination of a bright CO-line and dust continuum emission (Section 4.6.3).

[d]Detected in CO(2-1) emission in the COLDz survey as COLDz.COS.0 (Pavesi et al. 2018); also known as AzTEC-3.

[e]Detected in CO(1-0) emission in the COLDz survey as COLDz.COS.2 (Pavesi et al. 2018).

[f]Identified as GN-16 in the submillimeter observations by Pope et al. (2005)

[g]Identified as GN-12 by Pope et al. (2005).

[h]Identified as GN-26 by Pope et al. (2005); has a CO(2-1)-based redshift from Frayer et al. (2008).

the Super-deblended catalog and 3) a photometric redshift within the COSMOS2015 catalog. In total, we find that 4 out of 5 COLDz COSMOS detections have a spectroscopically confirmed redshift, while the remaining source has a well-constrained photometric redshift measurement (COLDz-cont-COS-3 at $z = 0.98 \pm 0.01$). We note that one of our 34 GHz continuum detections (COLDz-cont-COS-2) is the well-studied submillimeter galaxy AzTEC.3 at $z = 5.3$, which is additionally detected in CO-emission in the COLDz survey. For AzTEC.3, we further compile additional available ALMA continuum photometry at 230 and 300 GHz from Pavesi et al. (2016).

For the GOODS-N field, we follow a similar procedure. We first cross-match the COLDz continuum detections with the 3D-HST survey (Brammer et al. 2012; Skelton et al. 2014; Momcheva et al. 2016), adopting the radio positions at 1.4 GHz from Owen (2018), as these are of higher signal-to-noise than the 34 GHz data, and as such are less susceptible to the local noise properties. We find that all 13 radio sources have counterparts in the 3D-HST survey within $0\farcs3$, where no spurious matches are expected. We subsequently cross-match with the Super-deblended catalog, and find that all but one of the 34 GHz continuum sources have a counterpart at far-infrared wavelengths. All 12 cross-matches have a Super-deblended counterpart within $0\farcs3$, while there are no further matches within $3\farcs0$ of the single unmatched entry. We further find 3 cross-matches within $0\farcs1$ with the catalog of submillimeter-selected galaxies from Pope et al. (2005), which we identify with GN12, GN16 and GN26, the latter of which has a spectroscopically measured redshift of $z = 1.22$ based on a CO(2-1) detection from Frayer et al. (2008). Additional matching with the COLDz catalog of line emitters in the GOODS-N field does not result in further matches. As such, the $z = 5.3$ submillimeter galaxy GN10 (Daddi et al. 2009; Riechers et al. 2020), detected in COLDz as the brightest CO-emitter (Pavesi et al. 2018), remains undetected in deep 34 GHz imaging. Upon performing photometry at the known position of GN10, we determine a peak brightness of $S_{34} = 11.0 \pm 5.6\,\mu$Jy beam^{-1} ($\approx 2\sigma$), placing it well below our survey detection limit.

We compile the optimal redshifts for the 13 GOODS-N 34 GHz continuum sources in a similar manner as for the COSMOS field. In order of priority, we adopt a spectroscopic redshift from the Super-deblended catalog, or the best redshift from 3D-HST (Momcheva et al. 2016), the latter being either a spectroscopic redshift from *HST*/GRISM, or a photometric

redshift from Skelton et al. (2014). We further overwrite a single spectroscopic value for COLDz-cont-GN-10 at $z = 4.424$ with the updated value of $z = 2.018$, based on the discussion in Murphy et al. (2017). Overall, 10/13 sources have a spectroscopically confirmed redshift, while the remaining 3 sources have a well-constrained photometric redshift.

4.4.2 Spectral Energy Distributions

We use spectral energy distribution fitting code magphys (da Cunha et al. 2008, 2015) to determine the physical properties of the 34 GHz continuum detections. magphys adopts an energy balance technique to couple the stellar emission at ultra-violet to near-infrared wavelengths to thermal dust emission at longer wavelengths, and as such models the ultra-violet to far-infrared SED in a self-consistent way. This is additionally useful for sources lacking far-infrared photometry, as in this case shorter wavelengths will still provide constraints on the total dust emission. While magphys is also capable of modelling the radio spectrum of star-forming galaxies, we do not utilize any observations at wavelengths beyond 1.3 mm in our SED-fitting procedure, as any emission from an active galactic nucleus at radio wavelengths is not incorporated in the fitting. We additionally add a 10% uncertainty in quadrature to the catalogued flux density uncertainties bluewards of *Spitzer*/MIPS 24μm, following e.g., Battisti et al. (2019). This accounts for uncertainties in the photometric zeropoints, and further serves to guide the fitting into better constraining the far-infrared part of the spectral energy distribution. Via magphys, we obtain several physical properties for our galaxies, including far-infrared luminosities, star-formation rates and stellar masses. We show the fitted spectral energy distributions for all eighteen COLDz continuum detections in Figure 4.17 in Appendix 4.B, and tabulate their physical parameters in Table 4.4.

4.4.3 X-ray and Mid-infrared AGN Signatures

Given that the COLDz continuum detections in the COSMOS field are all identified in the COSMOS-XS survey, we adopt the results from Algera et al. (2020b), who match the COSMOS-XS 3 GHz continuum sources with the X-ray catalog from Marchesi et al. (2016a). None of the five COLDz COSMOS continuum sources, however, have counterparts in X-ray emission within a separation of $1\farcs4$, and as such we calculate upper limits on their X-ray luminosity adopting $\Gamma = 1.8$. However, as the resulting limits are of modest depth, we cannot state definitively whether the COLDz COS-

MOS sources are X-ray AGN. We note, however, that all of them fall below the typical X-ray emission seen in submillimeter galaxies (Alexander et al. 2005), which in turn are thought to predominantly be star-formation dominated. We additionally adopt the criteria from Donley et al. (2012) in order to identify AGN at $z \leqslant 2.7$ through the mid-infrared signature ascribed to a dusty torus surrounding the accreting black hole, and similarly find no signature of AGN-related emission at mid-infrared wavelengths. We limit ourselves to this redshift range, as at higher redshifts the Donley et al. (2012) criteria are susceptible to false positives in the form of dusty star-forming galaxies (e.g., Stach et al. 2019).

For the GOODS-N field, we find 11/13 matches with the X-ray catalog from Xue et al. (2016), within a separation of $1\farcs0$. At this matching radius, no false identifications are expected. We compare the X-ray luminosities with the emission expected from star-formation, adopting the relations from Symeonidis et al. (2014). This comparison classifies nine sources as AGN based on their X-ray emission, despite two of these sources having [0.5-8] keV X-ray luminosities below the typical threshold for AGN of $L_X = 10^{42}\,\mathrm{erg\,s^{-1}}$. We additionally find that only a single X-ray detected source exhibits mid-infrared colors that place it within the Donley et al. (2012) wedge. Overall, we conclude that the majority of 34 GHz continuum detections in the GOODS-N field are X-ray AGN. Due to the COSMOS X-ray data being comparatively shallower, we cannot assess definitely whether the five 34 GHz continuum sources in the COSMOS field are similarly AGN based on their X-ray emission. However, a lower AGN fraction in COSMOS is expected, as its radio observations are significantly deeper than in GOODS-N, and the incidence rate of AGN is a strong function of radio flux density (Smolčić et al. 2017a; Algera et al. 2020b). Regardless, if X-ray AGN are present in the COLDz/COSMOS detections, they are unlikely to be dominating the spectral energy distribution.

4.5 34 GHz Source Counts

Radio number counts, while historically used as a probe for the cosmology of the Universe, remain a useful tool for comparing surveys, in addition to visualizing the onset of different radio populations. At the bright end ($S_{1.4} \gg 1\,\mathrm{mJy}$), the Euclidean number counts decline smoothly towards lower flux densities, and are dominated by luminous radio AGN (e.g., Condon & Mitchell 1984). At 1.4 GHz, the number counts show a flattening at $S_{1.4} \approx 1\,\mathrm{mJy}$, believed to be the advent of star-forming galaxies and radio-

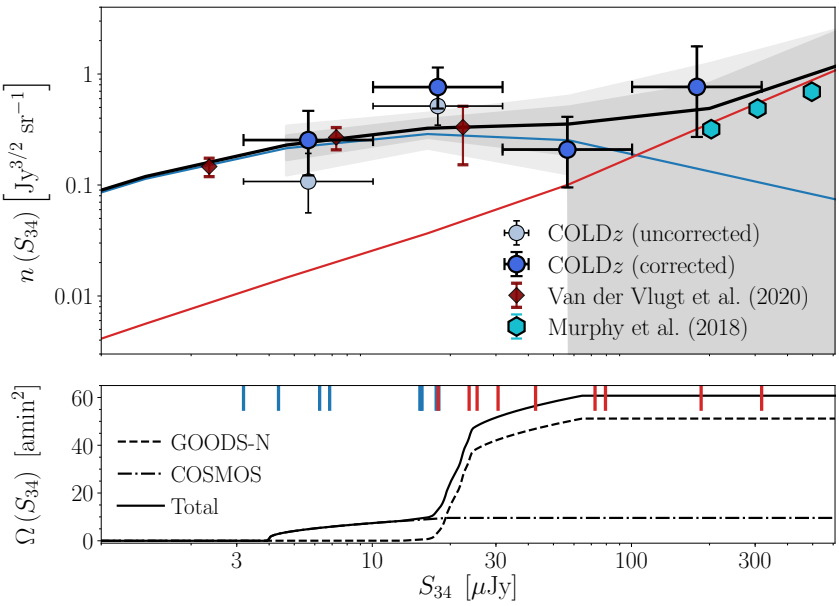

Figure 4.7: Upper: Completeness-corrected Euclidean-normalized radio source counts at 34 GHz across the combined COSMOS and GOODS-N mosaics. The purple diamonds show the 10 GHz counts from van der Vlugt et al. (2021), and the cyan hexagons represent the 28.5 GHz counts from Murphy & Chary (2018), both rescaled to 34 GHz assuming $\alpha = -0.70$. The blue and red lines indicate the scaled source counts for star-forming galaxies and AGN from the Bonaldi et al. (2019) simulations at 20 GHz, respectively. The dark (light) grey regions indicate the expected 1σ (2σ) level of cosmic variance, which drops to zero at low flux densities when our effective area is zero. **Lower:** The effective area of the COLDz observations as a function of flux density. For $S_{34} \lesssim 20\,\mu$Jy, we are restricted to the relatively small field-of-view of the COLDz COSMOS observations. The blue (red) vertical bars indicate the (deboosted) 34 GHz flux density at which a star-forming galaxy (radio AGN) is detected (Section 4.6). Despite the relatively large uncertainties, our 34 GHz number counts are in good agreement with (rescaled) measurements and predictions in the literature.

quiet AGN as the dominant radio populations (e.g., Rowan-Robinson et al. 1993; Seymour et al. 2004; Padovani et al. 2009; Smolčić et al. 2017a). For a typical spectral index of $\alpha = -0.70$, this flattening should arise around $S_{34} \approx 100\,\mu$Jy, and hence is covered in the range of flux densities probed in this work. We note that these flux densities may be "contaminated" by

Table 4.2: Euclidean Number Counts at 34 GHz

$S_{\rm centre}$	$S_{\rm low}$	$S_{\rm high}$	$n_{\rm uncorr}(S)$	$n_{\rm corr}(S)$
[μJy]	[μJy]	[μJy]	[Jy$^{3/2}$ sr^{-1}]	[Jy$^{3/2}$ sr^{-1}]
5.7	3.2	10.1	$0.108^{+0.085}_{-0.051}$	$0.254^{+0.212}_{-0.132}$
17.9	10.1	31.8	$0.514^{+0.235}_{-0.168}$	$0.763^{+0.382}_{-0.274}$
56.6	31.8	100.6	$0.209^{+0.203}_{-0.114}$	$0.209^{+0.203}_{-0.114}$
178.8	100.6	317.8	$0.765^{+1.010}_{-0.494}$	$0.765^{+1.010}_{-0.494}$

Note. — (1) Central flux density of the bin, (2), (3) Lower and upper flux density of the bin, (4) Number counts uncorrected for incompleteness, (5) Number counts corrected for incompleteness.

thermal emission from dust, or in the case of two COSMOS sources, by bright CO-emission, which are typically not an issue in low-frequency radio source counts. However, while we correct for this when examining the radio spectra of the star-forming COLDz continuum detections in detail (Section 4.6.2), here we compute the number counts based on the raw observed flux densities.

As we adopt deep radio observations as prior positions for possible 34-GHz continuum sources, we expect our sample to be fully reliable, i.e., not to contain any spurious detections. However, our sample may still be incomplete, in particular as a result of the RMS of our radio maps increasing rapidly towards the image edges due to the enhanced primary beam attenuation (c.f., Figure 4.2). In turn, in these regions we may miss faint 34 GHz continuum sources that would have been observed had the RMS been constant across our field-of-view. As such, we adopt the fractional incompleteness as a function of radio flux density as determined from inserting mock sources into our radio maps (Appendix 4.A.1). Denoting the completeness at flux density S_ν for field i as $f_i(S_\nu)$, the correction factor per field is simply $C_i = f_i^{-1}(S_\nu)$. For multiple fields, we then adopt the full completeness to be

$$C(S_\nu) = \frac{\sum_i f_i^{-1}(S_\nu)\Omega_i(S_\nu)}{\sum_i \Omega_i(S_\nu)} \,, \tag{4.1}$$

where $\Omega_i(S_\nu)$ denotes the area in arcmin^2 across which a source of flux density S_ν can be detected in field i at $\geqslant 3\sigma$ significance. As such, the overall completeness is the area-weighted average of the completeness in the COSMOS and GOODS-N fields.

We present the completeness-corrected Euclidean-normalized number counts at 34 GHz in Figure 4.7, and tabulate the results in Table 4.2. The number counts combine the continuum detections across both the COSMOS and GOODS-N fields, using the same area-weighting that is adopted for the completeness calculation (Equation 4.1). The uncertainties on the individual points constitute the combination of the error on the counting statistics from Gehrels (1986) – which are more appropriate than simple Poissonian errors for bins with few sources – and the error on the completeness. Cosmic variance is not included in the uncertainties, but its magnitude is discussed below.

While the high-frequency ($\nu \gtrsim 30$ GHz) radio sky has been explored at the millijansky level (e.g., Mason et al. 2009), the COLDz survey provides the first constraints on the 34 GHz number counts in the regime where star-forming galaxies are expected to emerge as the dominant population, complicating any direct comparisons to the literature. At the bright end of our 34 GHz observations, we compare with Murphy & Chary (2018), who perform a stacking analysis in *Planck* observations at 28.5 GHz, based on priors at 1.4 GHz from NVSS (Condon et al. 1998). We rescale the number counts from 28.5 GHz to 34 GHz adopting $\alpha = -0.70$, and find them to be in agreement with the COLDz observations at $S_{34} \gtrsim 200\,\mu$Jy.

As no 34 GHz observations with a similar sensitivity to COLDz exist in the literature, the next best solution is to compare to the highest-frequency number counts available, and scale the counts to 34 GHz. For this, we adopt the recent 10 GHz number counts from van der Vlugt et al. (2021), as part of the COSMOS-XS survey, which we scale to 34 GHz via $\alpha = -0.70$. As the parent survey constitutes a very deep single pointing ($\sim 0.40\,\mu$Jy across ~ 30 arcmin^2), these data probe down to slightly fainter flux densities than those probed in this work. However, within the flux density range in common, we find that the number counts are in good agreement, despite the inherent uncertainties associated with the required frequency scaling.

While observationally little is known about the faint high-frequency radio sky, this is no less true for simulations. Modelling of the radio sky

has predominantly been performed at low frequencies, with simulations by Wilman et al. (2008) and more recently by Bonaldi et al. (2019) only extending to 18 and 20 GHz, respectively. As such, we again invoke a frequency scaling to 34 GHz, adopting as before a spectral index of $\alpha = -0.70$. We focus on the recent 20 GHz simulations by Bonaldi et al. (2019), who model the radio population for two distinct classes of sources: star-forming galaxies that follow the far-infrared/radio correlation, and radio AGN that show a strong excess in radio power compared to this correlation. We show both the individual and combined contributions of the two populations in Figure 4.7, and find that the simulations predict that below $S_{34} \lesssim 100\,\mu$Jy star-forming galaxies should make up the bulk of the radio population. Our measurements are in good agreement with the simulated number counts, indicating that a scaling from 20 to 34 GHz with a fixed spectral index is likely to be appropriate. We caution, however, that the uncertainties on our number counts are large as a result of the small number of sources detected in the 34 GHz continuum maps.

Furthermore, cosmic variance constitutes an additional uncertainty on our number counts, as our radio observations probe a relatively small field-of-view. We show the area probed as a function of flux density in the bottom panel of Figure 4.7. Out to $S_{34} \lesssim 15\,\mu$Jy, the total area is dominated by the deeper COSMOS mosaic, and accounts for approximately $10\,\mathrm{arcmin}^2$. At flux densities above $S_{34} \gtrsim 30\,\mu$Jy, our field-of-view increases to approximately $60\,\mathrm{arcmin}^2$, as now sources can be detected across the full GOODS-N mosaic as well. We quantify the magnitude of cosmic variance via the Bonaldi et al. (2019) simulations, following Algera et al. (2020b). Briefly, for each of the flux density bins adopted in our computation of the 34 GHz number counts, we determine the effective area of the COLDz survey in which sources in the given bin can be detected. We then sample 200 independent circular regions of equivalent area from the 20 GHz Bonaldi et al. (2019) simulations, accounting for the flux density scaling with $\alpha = -0.70$. We determine the number counts for all independent areas, and compute the 16-84$^{\mathrm{th}}$ and 5-95$^{\mathrm{th}}$ percentiles, which we adopt to be the 1 and 2σ uncertainties due to cosmic variance, shown as the dark and light grey regions in Figure 4.7, respectively. We note that such a calculation of the cosmic variance encapsulates two effects: at low flux densities we have a relatively small field-of-view, which naturally increases the magnitude of cosmic variance. At large flux densities, our field of view constitutes the full $\sim 60\,\mathrm{arcmin}^2$, but due to the relative paucity of bright radio sources, cosmic variance similarly constitutes an appreciable uncertainty. The typ-

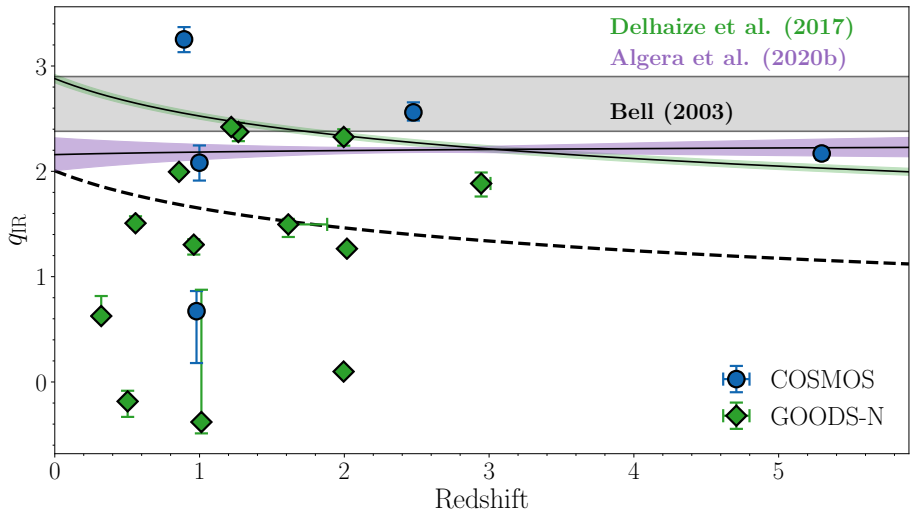

Figure 4.8: The far-infrared/radio correlation for the COLDz 34 GHz continuum detections. Three literature results for the correlation are shown: the local value from Bell (2003), the correlation for 3 GHz-selected galaxies from Delhaize et al. (2017) and the correlation for submillimeter galaxies from Algera et al. (2020a). The threshold for identifying radio-excess AGN is shown via the dashed curve, which is the FIRRC from Delhaize et al. (2017) minus $2.5\times$ the intrinsic scatter. We identify half of the 34 GHz continuum sample (9/18 sources) as radio AGN.

ical magnitude of cosmic variance between $5 \lesssim S_{34} \lesssim 60\,\mu$Jy induces an additional uncertainty on the number counts of $\sim 0.1 - 0.2$ dex – comparable to the Poissonian uncertainties – although this value rapidly increases for higher flux densities. Overall, we therefore conclude that our number counts are in good agreement with both observed and simulated counts from the literature at lower-frequencies.

4.6 34 GHz Continuum Source Properties

4.6.1 Radio AGN

In the local Universe, the existence of a linear correlation between the total far-infrared and radio emission of star-forming galaxies has been well-established (Yun et al. 2001; Bell 2003). This far-infrared/radio correlation has been shown to hold over a wide range of luminosities, from dwarf

galaxies to dust-obscured starbursts (Bell 2003). The correlation is commonly expressed via parameter $q_{\rm IR}$, first introduced by Helou et al. (1985), and defined as

$$q_{\rm IR} = \log_{10}\left(\frac{L_{\rm IR}}{3.75\times10^{12}\,{\rm W}}\right) - \log_{10}\left(\frac{L_{1.4}}{{\rm W\,Hz^{-1}}}\right)\,. \tag{4.2}$$

Here $L_{\rm IR}$ represents the $8-1000\,\mu$m luminosity, and $L_{1.4}$ is the K-corrected radio-luminosity at rest-frame 1.4 GHz, computed via the closest observed-frame flux density and the measured radio spectral index. A number of recent, radio-selected studies of the far-infrared/radio correlation have found it to evolve with cosmic time (e.g., Delhaize et al. 2017; Calistro Rivera et al. 2017; Read et al. 2018; Ocran et al. 2020). While the origin of this evolution is debated, and may be the result of residual AGN contamination (Molnár et al. 2018), or due to the different physical conditions in massive star-forming galaxies at high-redshift compared to local sources (Algera et al. 2020a; Delvecchio et al. 2021), we adopt an evolving far-infrared/radio correlation to identify radio-AGN among the eighteen 34 GHz detections. In particular, we adopt the correlation determined for a 3 GHz selected sample by Delhaize et al. (2017), and follow Algera et al. (2020b) by identifying galaxies as radio AGN if they fall below the correlation at the 2.5σ level.

We show the far-infrared/radio correlation for the eighteen 34 GHz continuum detections as a function of redshift in Figure 4.8. In total, half of the COLDz sample are identified as radio AGN, comprising eight AGN in GOODS-N, and one in COSMOS (Table 4.4). The fact that radio AGN make up a large fraction of the bright radio population is evidenced by the relatively large contribution of AGN in the wider but shallower GOODS-N observations. Among the galaxies classified as star-forming, Figure 4.6 suggests the existence of an extended tail at 34 GHz in COS-2, at face value indicative of an AGN jet. However, such extended features are absent in the deeper 3 and 10 GHz observations of this source, and at these frequencies the galaxy is consistent with being a point source at $2''$ resolution. As the spectrum of jetted AGN tends to steepen towards higher frequencies (e.g., Mahatma et al. 2018), and should therefore be detectable in the lower frequency ancillary radio data, we interpret the extended tail at 34 GHz as simply being due to noise. As we adopt the peak brightness for COS-2, its flux density measurement is unlikely to be substantially affected by this noisy region in the radio map.

In total, 6/8 radio-AGN in the GOODS-N field are additionally classified as AGN through their strong X-ray emission. While constituting only a small number of sources, this is a relatively large fraction, as the overlap between radio AGN selected at lower frequencies and X-ray AGN is typically found to be small ($\lesssim 30\%$, e.g., Smolčić et al. 2017a; Delvecchio et al. 2017; Algera et al. 2020b). This difference, however, may in part be due to the deeper X-ray data available in GOODS-N, compared to the COSMOS field where these studies were undertaken.

We further show the long-wavelength spectra of the nine radio AGN in Figure 4.9. The median $1.4 - 34$ GHz spectral index of the sample equals $\alpha = -0.77 \pm 0.13$, which is consistent with the commonly assumed synchrotron slope of $\alpha = -0.70$. However, the modest sample still spans a wide range of spectral slopes between 1.4 and 34 GHz, ranging from nearly flat ($\alpha = -0.04 \pm 0.02$) to steep ($\alpha = -1.47 \pm 0.06$). In addition, the AGN exhibit relatively smooth spectra, with the median spectral index between $1.4 - 3$ (or 5) GHz of $\alpha_{3/5}^{1.4} = -0.70 \pm 0.12$ being consistent with the typical high-frequency slope of $\alpha_{34}^{3/5} = -0.79 \pm 0.15$. Only two AGN exhibit strong evidence for steepening of their radio spectra towards higher frequencies, although sources with strongly steepening spectra are more likely to be missed in a selection at high radio frequencies. Such spectral steepening is expected to occur due to synchrotron ageing losses increasing towards higher frequencies, and in turn relates to the age of the AGN (e.g., Carilli et al. 1991).

4.6.2 Radio Spectral Decomposition for Star-forming Galaxies

Detecting radio free-free emission in high-redshift star-forming galaxies is challenging due to its expected faintness, and the presence of a radio AGN only further hinders the detection of this already elusive component in the radio spectrum. As such, we now turn our attention to the star-formation-powered sources detected in the COLDz survey. The radio spectrum of star-forming galaxies is frequently assumed to be the superposition of two power laws arising from non-thermal synchrotron and thermal free-free emission (Condon 1992; Murphy et al. 2017; Tabatabaei et al. 2017). Denoting their spectral indices as $\alpha_{\rm NT}$ and $\alpha_{\rm FF}$, respectively, the radio flux density at a given frequency ν may be written as

$$S_\nu = S_{\nu_0}^{\rm NT} \left(\frac{\nu}{\nu_0}\right)^{\alpha_{\rm NT}} + S_{\nu_0}^{\rm FF} \left(\frac{\nu}{\nu_0}\right)^{\alpha_{\rm FF}} , \tag{4.3}$$

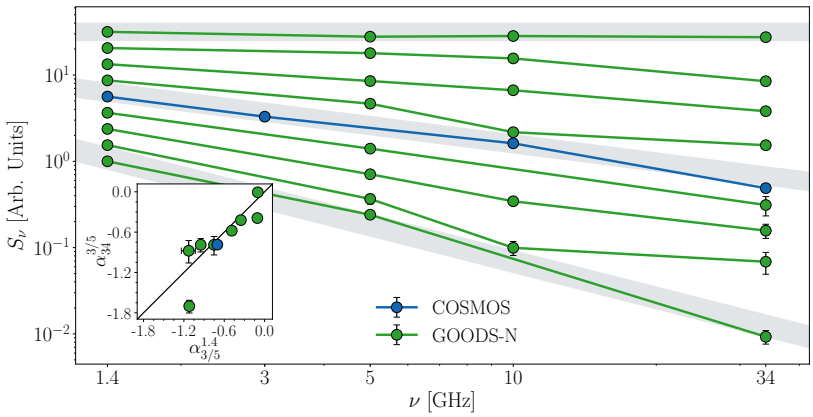

Figure 4.9: The radio spectra of the nine radio AGN identified in COSMOS (1) and GOODS-North (8). The sources have been arbitrarily normalized, and are arranged from the flattest to steepest $1.4 - 34\,\mathrm{GHz}$ spectral index. Note that the errorbars are typically smaller than the chosen plotting symbols. The grey bands indicate slopes of $\alpha = 0.0, -0.70, -1.40$ (from top to bottom), comparable to the flattest, median and steepest $1.4 - 34\,\mathrm{GHz}$ spectral slopes we observe for the COLDz AGN, and are shown for reference. The inset shows the $5 - 34\,\mathrm{GHz}$ spectral index versus the $1.4 - 5\,\mathrm{GHz}$ slope ($3 - 34\,\mathrm{GHz}$ and $1.4 - 3\,\mathrm{GHz}$ for COSMOS). The radio AGN show a variety of spectral slopes, with a median spectral index of $\alpha_{34}^{1.4} = -0.77 \pm 0.13$. However, the AGN exhibit relatively smooth radio spectra, with only two sources showing strong evidence for spectral curvature.

given a reference frequency ν_0, as well as the thermal and non-thermal flux densities $S_{\nu_0}^{\mathrm{FF}}$ and $S_{\nu_0}^{\mathrm{NT}}$, respectively, evaluated at this frequency. We rewrite this equation by introducing the thermal fraction, defined through $f_{\nu_0}^{\mathrm{th}} = S_{\nu_0}^{\mathrm{FF}}/(S_{\nu_0}^{\mathrm{FF}} + S_{\nu_0}^{\mathrm{NT}})$, as is common in the literature (e.g., Condon 1992; Tabatabaei et al. 2017). As such, we rewrite the radio spectrum as

$$S_\nu = \left(1 - f_{\nu_0}^{\mathrm{th}}\right) S_{\nu_0} \left(\frac{\nu}{\nu_0}\right)^{\alpha_{\mathrm{NT}}} + f_{\nu_0}^{\mathrm{th}} S_{\nu_0} \left(\frac{\nu}{\nu_0}\right)^{-0.1} . \tag{4.4}$$

This further assumes the spectral index for thermal free-free emission is fixed at $\alpha_{\mathrm{FF}} = -0.10$ (Condon 1992; Murphy et al. 2011). We then determine the remaining free parameters, $f_{\nu_0}^{\mathrm{th}}$, α_{NT} and S_{ν_0}, using a Monte Carlo Markov Chain (MCMC) based fitting routine. In addition, we adopt an observer-frame frequency of 1.4 GHz as the reference frequency ν_0, which defines the frequency where the thermal fraction is normalized. Where

necessary, we convert the thermal fraction from observed-frame frequency ν to a rest-frame frequency ν' via

$$f_{\nu'}^{\rm th} = \frac{f_{\nu(1+z)}^{\rm th}\left(\frac{\nu'}{\nu(1+z)}\right)^{-0.10}}{f_{\nu(1+z)}^{\rm th}\left(\frac{\nu'}{\nu(1+z)}\right)^{-0.10} + (1-f_{\nu(1+z)}^{\rm th})\left(\frac{\nu'}{\nu(1+z)}\right)^{\alpha_{\rm NT}}} \,. \tag{4.5}$$

We adopt flat priors in our fitting routine for the normalization S_{ν_0} and thermal fraction $f_{\rm th}$, while we adopt Gaussian priors for the non-thermal spectral index (following, e.g., Linden et al. 2020). For the former two parameters, we require that $-1\,{\rm Jy} < S_{\nu_0} < 1\,{\rm Jy}$ and $-0.5 < f_{\rm th} < 1.5$, that is, we allow both the normalization and the thermal fraction to take on unphysical, negative values, as artificially bounding both to be greater than zero will not fully capture the uncertainties in the MCMC-sampling. In addition, allowing negative values in the thermal fraction will demonstrate the necessity for the thermal component, as well as limitations inherent to the simple model we adopt for the radio spectrum (see also Tabatabaei et al. 2017).

The Gaussian priors adopted on the non-thermal spectral index are motivated by a degeneracy that manifests between the synchrotron slope and thermal fraction at low signal-to-noise. This degeneracy occurs because it is impossible to accurately distinguish between an overall flat spectrum as being due to dominant free-free emission, or an intrinsically shallow synchrotron slope. To partially alleviate this degeneracy, we adopt prior knowledge from the local Universe that the synchrotron spectral indices are typically distributed around $\alpha_{\rm NT} \approx -0.85$ (Niklas et al. 1997; Murphy et al. 2011). In large radio-selected samples, the scatter around the typical low-frequency spectral index equals $0.3-0.5$ dex (Smolčić et al. 2017b; Calistro Rivera et al. 2017; Gim et al. 2019), and is approximately Gaussian. While these spectral index measurements include both the synchrotron and free-free components, the low-frequency nature of these data ensure the radio fluxes are likely dominated by non-thermal emission, and as such, the overall variation in the spectral index constitutes a proxy for the scatter in the typical synchrotron spectral index. To encompass the full observed scatter in the synchrotron slopes, we therefore adopt a Gaussian prior on $\alpha_{\rm NT}$ centered on a mean value of -0.85, with a scatter of 0.50.

4.6.3 Line and Dust Continuum Subtraction

Prior to fitting the radio spectra of the star-forming COLDz continuum detections, we need to ensure the 34 GHz flux density is not contaminated by thermal emission from dust, or by strong line emission. In particular, the 34 GHz flux density of the two COLDz COSMOS sources detected in CO-emission (COS-2, a.k.a. AzTEC.3, and COS-4), may be boosted by their respective CO-lines. We re-extract the peak brightness of these two sources after removing the channels contaminated by the CO-emission, and, as a sanity check, repeat this for the three COSMOS sources that do not show any evidence for strong line emission. While for the latter the flux densities are unaffected by this procedure, we find line-uncontaminated flux densities for COS-2 and COS-4 of $S_{34} = 5.2 \pm 1.3\,\mu$Jy and $S_{34} = 3.0 \pm 1.4\,\mu$Jy, respectively, which are lower than the original catalogued flux densities by $\sim 25\%$ and $\sim 40\%$ (Table 4.1). In turn, this correction brings the 34 GHz flux density from COS-4 below the formal detection limit (S/N ≈ 2).

The 34 GHz continuum flux densities may further contain a contribution from thermal emission by dust, which, at least for local normal star-forming galaxies, is thought to dominate the radio spectrum beyond rest-frame $\nu \gtrsim 100 - 200$ GHz (Condon 1992). To determine the extent of this contribution, we fit – where available – the far-infrared observations of our galaxy sample with both optically thin and thick modified blackbody spectra, and extrapolate the resulting dust SED to observed-frame 34 GHz. We note that this methodology is rather sensitive to how well the global dust properties (e.g., temperature and emissivity) can be constrained, and as a result the predicted flux densities are quite uncertain. Nevertheless, we find that the 34 GHz emission of COS-2 and COS-4 is likely to be dominated by emission from dust, with predicted dust contributions of $4.9^{+6.1}_{-3.6}\,\mu$Jy and $3.3^{+7.2}_{-1.5}\,\mu$Jy, respectively. As a result, the full 34 GHz flux densities of these two sources are consistent with being powered by the combination of CO-emission and dust. As we probe rest-frame frequencies of $\nu' \approx 210$ GHz and $\nu' \approx 120$ GHz for COS-2 and COS-4, respectively, this finding is consistent with the typical model for the long-wavelength SED of star-forming galaxies (Condon 1992).

In what follows, we will discard COS-2 and COS-4 from our sample, as any remaining contribution from free-free or synchrotron emission to the measured 34 GHz flux density is not statistically significant, such that no robust spectral decomposition for these two sources can be performed. One source in GOODS-N, GN-7 at $z = 2.95$ ($\nu' \approx 130$ GHz), may have $\sim 25\%$

of its continuum flux density contaminated by dust emission. However, due to the aforementioned uncertainties in the fitting of the dust SED, we do not correct for this potential contribution. This analysis indicates that, even at low flux densities ($S_{34} \lesssim 25\,\mu$Jy), a 34-GHz-selected sample does not automatically yield a free-free-dominated population.

4.6.4 The Radio Spectra of High-redshift Star-forming Galaxies

We show the radio spectra of the seven remaining star-forming sources across the COSMOS and GOODS-N fields in Figure 4.10. All sources can be well-described by the combination of a synchrotron and free-free component, although for three sources (COS-3, GN-7, GN-11) – while some contribution from free-free emission is preferred – the fitted thermal fractions are consistent with zero within 1σ. In turn, for these sources a single power-law representing synchrotron emission is sufficient to match the observed flux densities. We additionally emphasize that there is considerable covariance between the thermal fraction and synchrotron slope, and as such any quoted one-dimensional uncertainties are not fully representative of the multi-dimensional posterior distribution (Figure 4.11). We therefore utilize these full posterior distributions in order to propagate the uncertainties into physical quantities such as free-free star-formation rates (Section 4.6.5).

The fitted spectral parameters are presented in Figure 4.11 and Table 4.3. Our bootstrapped median thermal fraction, scaled to 1.4 GHz rest-frame as is common in the literature, equals $f_{\rm th} = 0.06 \pm 0.03$, with a standard deviation of $\sigma = 0.05$. None of the seven star-forming galaxies exhibit thermal fractions of $f_{\rm th} \gtrsim 0.20$, indicating a fairly narrow distribution of $f_{\rm th}$ at rest-frame 1.4 GHz, even among a sample showing substantial variation in star-formation rates. Our average thermal fraction is slightly lower than the average value observed by Tabatabaei et al. (2017) of $f_{\rm th} = 0.10$ for star-forming galaxies in the local Universe, though they report a large scatter of $\sigma = 0.09$. Additionally, the typical thermal fraction is similar to what was observed by Niklas et al. (1997), who determined $f_{\rm th} = 0.08 \pm 0.01$ at 1 GHz, with a scatter of $\sigma = 0.04$ across 74 local galaxies.

We further determine an average thermal fraction at observed-frame 34 GHz (i.e., probing $34 \times (1+z)$ GHz rest-frame) of $f_{\rm th} = 0.78 \pm 0.07$, with a range of $f_{\rm th} = 0.45 - 0.95$, and a scatter of $\sigma = 0.20$ (Figure 4.12). As such, we find that, even at rest-frame frequencies $\nu \gtrsim 60$ GHz, the radio spectrum is not fully dominated by thermal free-free emission, though we caution the uncertainties on the individual thermal fractions are large. We first com-

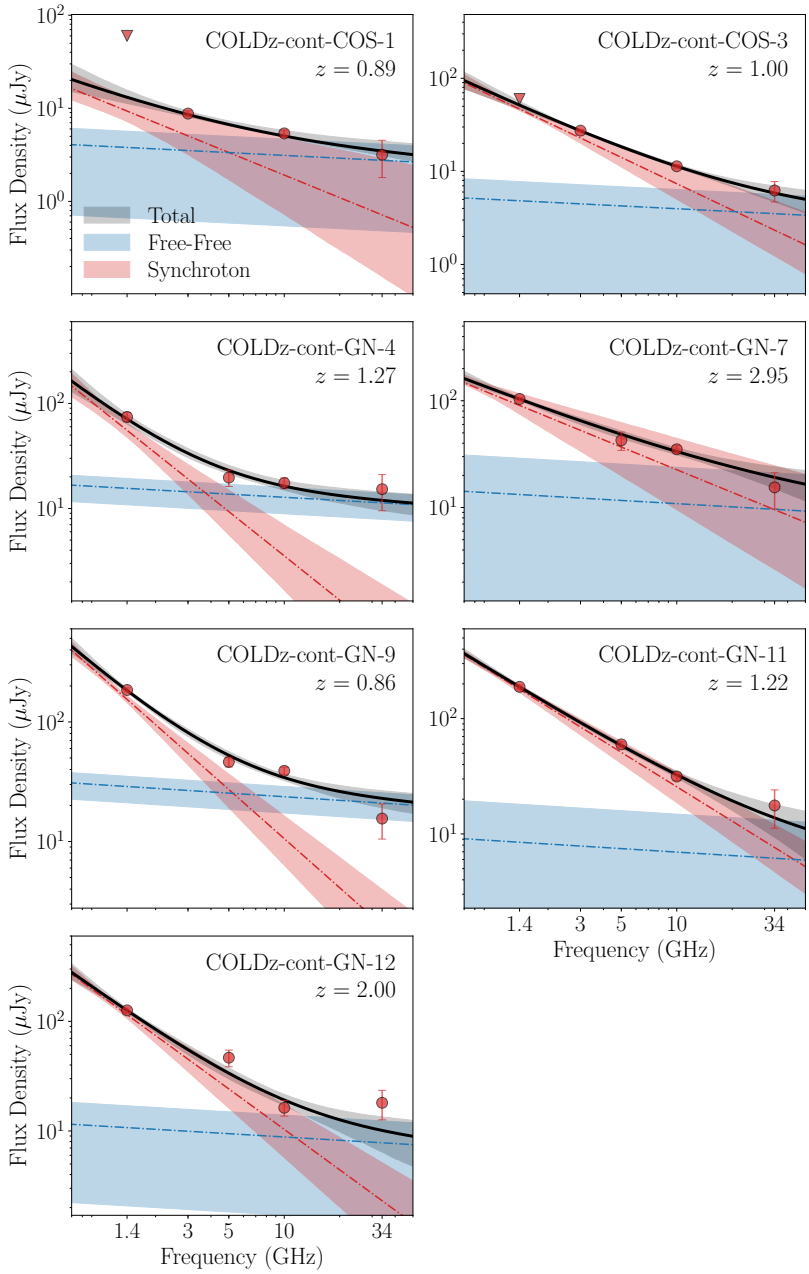

Figure 4.10: The radio spectra of the seven star-forming galaxies in the COSMOS (first 2 panels) and GOODS-North (last 5) fields. We show the decomposition of the spectra into their synchrotron and free-free components, with the shaded regions indicating the 1σ confidence region on the fits. We find the radio emission for four out of seven galaxies (COS-1, GN-4, GN-9 and GN-12) to be dominated by free-free emission at observed-frame 34 GHz, whereas for the remainder only a relatively minor thermal contribution is preferred.

Table 4.3: Spectral parameters of the star-forming COLDz sample

ID	ν'[a]	$f_{\rm th}(1.4\,{\rm GHz})$[b]	$f_{\rm th}(\nu')$[c]	$\alpha_{\rm NT}$	$\rm SFR_{FF}$[d]	$\rm SFR_{1.4}$
	[GHz]				[$\log M_\odot\,{\rm yr}^{-1}$]	[$\log M_\odot\,{\rm yr}^{-1}$]
COLDz-cont-COS-1	64	$0.18^{+0.11}_{-0.15}$	$0.82^{+0.14}_{-0.71}$	$-0.81^{+0.38}_{-0.49}$	28^{+19}_{-23}	12^{+2}_{-2}
COLDz-cont-COS-3	68	$0.05^{+0.02}_{-0.05}$	$0.60^{+0.22}_{-0.61}$	$-0.94^{+0.22}_{-0.21}$	53^{+20}_{-54}	69^{+5}_{-5}
COLDz-cont-GN-4	77	$0.08^{+0.03}_{-0.02}$	$0.95^{+0.04}_{-0.14}$	$-1.40^{+0.33}_{-0.36}$	289^{+123}_{-94}	213^{+47}_{-40}
COLDz-cont-GN-7	134	$0.06^{+0.04}_{-0.13}$	$0.50^{+0.38}_{-1.20}$	$-0.71^{+0.23}_{-0.34}$	1440^{+1181}_{-3530}	857^{+239}_{-161}
COLDz-cont-GN-9	63	$0.08^{+0.01}_{-0.02}$	$0.91^{+0.05}_{-0.12}$	$-1.36^{+0.21}_{-0.25}$	254^{+45}_{-52}	254^{+19}_{-18}
COLDz-cont-GN-11	75	$0.02^{+0.02}_{-0.03}$	$0.45^{+0.30}_{-0.74}$	$-0.99^{+0.13}_{-0.15}$	162^{+166}_{-243}	444^{+34}_{-32}
COLDz-cont-GN-12	102	$0.02^{+0.01}_{-0.02}$	$0.78^{+0.16}_{-0.53}$	$-1.22^{+0.24}_{-0.28}$	342^{+174}_{-260}	622^{+127}_{-96}

[a]The rest-frame frequency probed by the COLDz 34 GHz observations.

[b]The thermal fraction at rest-frame 1.4 GHz.

[c]The thermal fraction at rest-frame frequency ν'.

[d]The uncertainties on the free-free SFRs are propagated from those on the thermal fraction and radio luminosity. The sources where these SFRs are consistent with zero within 1σ are plotted as upper limits in Figure 4.13.

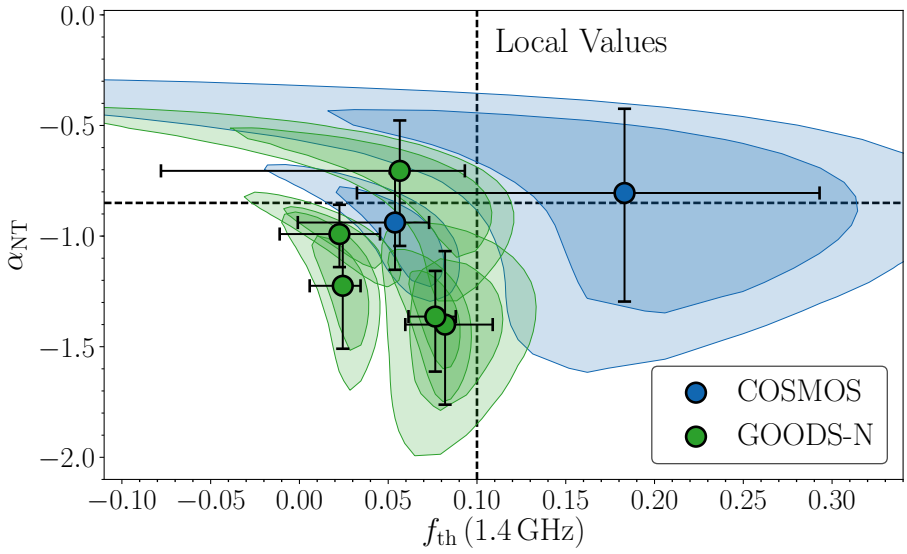

Figure 4.11: The fitted synchrotron spectral index versus the rest-frame 1.4 GHz thermal fraction for the seven star-forming COLDz continuum detections. The blue and green shaded regions indicate the covariance between the parameters, with the darker (lighter) shading indicating the 1σ (2σ) confidence regions. The datapoints show the corresponding one-dimensional uncertainties, and the typical local values are indicated through the dashed lines. The COLDz galaxies are predominantly located in the lower left quadrant, indicating slightly steeper synchrotron spectral indices, and lower thermal fractions than what is typically observed locally.

pare these results with two local studies, both of which map free-free emission on sub-kpc scales. At a typical resolution of ≈ 0.9 kpc, Murphy et al. (2012) find an average thermal fraction across 103 star-forming regions of $f_{\rm th} = 0.76$ at rest-frame 33 GHz, with a scatter of $\sigma = 0.24$. Extrapolating this value via the simple model from Condon (1992), the typical thermal fraction at ~ 60 GHz is expected to be $\sim 0.85-0.90$, which is slightly higher than the thermal fraction we find for high-redshift star-forming galaxies. In addition, Linden et al. (2020) recently measured a typical thermal fraction at 33 GHz of $f_{\rm th} = 93 \pm 0.8\%$ across 118 star-forming complexes in local galaxies, at a resolution of ≈ 0.2 kpc. Their typical thermal fraction is both higher than was determined by Murphy et al. (2012), and the values measured in this work. This, however, is not surprising, given that the thermal fractions presented in this work are integrated over the entire galaxy.

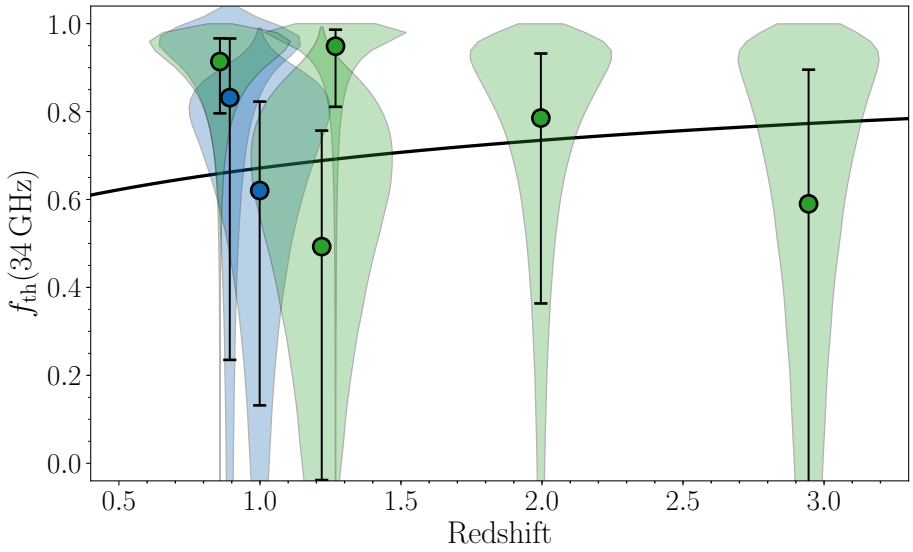

Figure 4.12: Violin diagrams of the thermal fraction at 34 GHz (observed-frame, hence probing rest-frame $34 \times (1+z)$ GHz) as a function of redshift. The width of the shaded regions represents the probability distribution of the thermal fraction, while the datapoints indicate the median and 16-84$^{\rm th}$ percentiles. The probability distributions of the thermal fractions are characterized by a typically high probability of having a large thermal fraction $f_{\rm th} \gtrsim 0.7 - 0.8$, with a long tail extending towards lower values. The model from Condon (1992), adopting $\alpha_{\rm NT} = -0.85$ and $f_{\rm th} = 0.10$ at 1.4 GHz, is shown as the solid black line, and predicts similar high-frequency thermal fractions as observed across the star-forming galaxies.

As free-free emission is predominantly produced in star-forming regions, spatial variations in the thermal fraction across a galaxy are naturally expected, with the thermal fraction peaking in star-forming complexes.

At high-redshift, no previous studies have directly targeted the free-free-dominated regime ($\nu \gtrsim 30$ GHz) in blindly selected galaxy samples, at a depth where star-forming galaxies are expected to dominate the radio population. However, particularly in bright dusty star-forming galaxies, some works have serendipitously detected high-frequency radio continuum emission, typically as a byproduct when targeting the CO(1-0) line. Thomson et al. (2012) detect free-free emission in two $z \sim 2.9$ lensed submillimeter galaxies, and determine thermal fractions of $f_{\rm th} \sim 0.3 - 0.4$ at 34 GHz. Other studies of highly star-forming galaxies (Aravena et al. 2013; Huynh et al. 2017) have additionally detected radio continuum emission

at observed-frame $\sim 30 - 35$ GHz, but had to assume fixed synchrotron spectral indices due to a lack of ancillary data. Nevertheless, they estimate thermal fractions between $f_{\rm th} \sim 40 - 70\%$. Overall, these studies find thermal fractions that are broadly consistent with, albeit typically slightly lower than, what we determine for the star-forming sample detected in our non-targeted 34 GHz observations.

Finally, we compare our results with the 10 GHz pointing from Murphy et al. (2017) in GOODS-N. They determine thermal fractions from $1.4 - 10$ GHz spectral indices for ~ 25 galaxies, under the assumption of a fixed synchrotron slope of $\alpha_{\rm NT} = -0.85$. At a typical rest-frame frequency of $\nu \sim 20$ GHz, they find a median thermal fraction of $f_{\rm th} \approx 50\%$. Extrapolating this value to rest-frame 60 GHz, this would imply a thermal fraction of $f_{\rm th} \sim 0.7$, similar to what we observe among the COLDz star-forming sample.

We further determine a median non-thermal spectral index for the star-forming COLDz sample of $\alpha_{\rm NT} = -0.99^{+0.19}_{-0.37}$, with a standard deviation of $\sigma = 0.25$. This typical value is consistent with the value observed by Tabatabaei et al. (2017) for local star-forming galaxies of $\alpha_{\rm NT} = -0.97 \pm 0.16$, but is slightly steeper than that of individual star-forming regions in NGC 6946, where Murphy et al. (2011) find a typical value of $\alpha_{\rm NT} = -0.81 \pm 0.02$. This is not surprising, as these observations directly target the acceleration sites of cosmic rays, where the spectrum should be flatter. However, our median synchrotron slope is additionally slightly steeper than the value obtained by Niklas et al. (1997), who determine an average $\alpha_{\rm NT} = -0.83 \pm 0.02$ ($\sigma = 0.13$) across 74 local galaxies. The slightly steeper non-thermal spectral index we find for the COLDz sample may be the result of the higher rest-frame frequencies probed in this work, compared to the aforementioned local studies. Synchrotron cooling losses increase towards high rest-frame frequencies, and result in the steepening of the non-thermal spectral index (e.g., Thomson et al. 2019). While our data do not have the constraining power to determine whether such spectral ageing occurs, as this requires additional sampling of the radio spectrum, such increased high-frequency losses would be fitted by a relatively steep synchrotron slope in our two-component model, and may plausibly contribute to our moderately lower value for $\alpha_{\rm NT}$ compared to local studies.

Based on the spectral parameters we determine for the COLDz sample, we calculate the rest-frame frequency ν'_{50} where the thermal fraction reaches 50% via

$$\nu'_{50} = \nu' \left(\frac{1 - f_{\rm th}(\nu')}{f_{\rm th}(\nu')} \right)^{-1/(\alpha_{\rm NT}+0.10)} . \quad (4.6)$$

While the uncertainties on this value are substantial for the individual star-forming galaxies due to its dependence on both the thermal fraction and synchrotron slope, we determine a median value of $\nu'_{50} = 11.5^{+20.0}_{-7.4}$ GHz, with a standard deviation of $\sigma = 5.9$ GHz. This is slightly lower than, albeit still consistent with, the canonically assumed value of $\nu'_{50} \approx 25 - 30$ GHz (e.g., Condon 1992), which is likely due to the relatively steep synchrotron slopes we are finding for the COLDz star-forming galaxies.

While the differences between the spectral parameters determined for COLDz and those observed in local star-forming galaxies are of minor statistical significance, a high-frequency selection of star-forming galaxies is likely to bias the sample towards having overall shallow radio spectra. Combining the $10 - 34$ GHz spectral indices for the star-forming galaxies across COSMOS and GOODS-N, we find an average slope of $\alpha^{10}_{34} = -0.47 \pm 0.10$ ($\sigma = 0.28$), which is substantially shallower than the canonical $\alpha = -0.70$ assumed at lower frequencies. Shallow spectra are naturally expected in the free-free dominated regime, in particular for young starburst galaxies. Such sources should exhibit large thermal fractions, as synchrotron emission lags the onset of a starburst by $\gtrsim 30$ Myr (e.g., Bressan et al. 2002), and the galaxies should hence be dominated by free-free emission across the entire radio spectrum. However, our sample is fully comprised of sources with typical or low thermal fractions ($f_{\rm th} \lesssim 0.20$ at 1.4 GHz), and rather steep synchrotron spectra ($\alpha_{\rm NT} \lesssim -0.85$). This, in turn, indicates we are likely detecting relatively mature starbursts, as opposed to young star-forming galaxies. In particular, galaxies with a declining star-formation history are expected to exhibit only modest levels of free-free emission at low radio frequencies, and may show steepening of their synchrotron spectra towards higher frequencies. This scenario is qualitatively consistent with the spectral parameters we are finding for the COLDz star-forming galaxies, and may therefore be typical for a high-frequency-selected sample.

Alternatively, the relatively low thermal fractions observed for our star-forming sample at low frequencies may be the result of residual AGN contamination. An AGN will contribute additional synchrotron emission in excess of that arising from star-formation, while the overall contribution from free-free emission is mostly unaffected. In this case, one may expect typi-

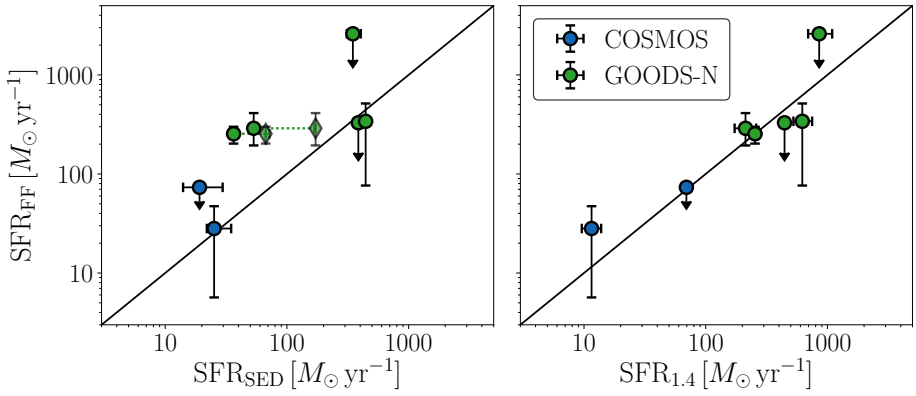

Figure 4.13: Left: A comparison of the star-formation rates obtained from free-free emission, versus those from magphys. The one-to-one relation is shown through the solid black line, and the vertical errorbars represent the propagated uncertainties on the radio luminosity and thermal fraction. For three sources, we can only place upper limits on their free-free SFRs. The diamonds show the SFRs that we infer from SED-fitting when we instead convert the far-infrared luminosity into a star-formation rate, for the two sources where these values are discrepant (see text for details). **Right:** Free-free star-formation rates versus those obtained from radio synchrotron emission, adopting the FIRRC from Delhaize et al. (2017). Despite the uncertainties on $\mathrm{SFR_{FF}}$ being large as a result of the low signal-to-noise at 34 GHz, and the limited available sample size, we find that the free-free star-formation rates are in reasonable agreement with the values derived from SED-fitting and low-frequency radio emission.

cal synchrotron spectra, in combination with low thermal fractions. However, we find no strong evidence for systematic residual radio AGN activity based on the values of q_{IR} of our star-forming galaxies, as we find that half of our sample falls onto or above the far-infrared/radio correlation for star-forming galaxies (Delhaize et al. 2017; Algera et al. 2020a).

4.6.5 Free-Free Star-Formation Rates

Free-free emission is one of the most robust tracers of star-formation, as it constitutes a direct probe of the ionizing photons emitted by recently formed ($\lesssim 10\,\mathrm{Myr}$) massive stars. As such, it does not rely on reprocessed starlight, or emission produced by stellar remnants, such as, respectively, far-infrared and radio synchrotron emission. However, some caveats still apply, as carefully summarized in Querejeta et al. (2019). In particular, any ionizing photons absorbed by dust within the HII-region will not contribute

to the ionization of hydrogen atoms, and as such will reduce the free-free luminosity at a fixed star-formation rate (e.g., Inoue et al. 2001; Dopita et al. 2003). Alternatively, if there is substantial leakage of ionizing photons, free-free emission will similarly be suppressed. Finally, since free-free emission is only sensitive to the massive end of the initial mass function, any variations in the IMF may substantially affect the calculated star-formation rates. We note that these caveats also apply to star-formation rates estimated using the Balmer lines (e.g., Hα, Hβ), with the clear advantage of free-free emission being that it is fully dust-insensitive on scales beyond the HII-region wherein the star-formation occurs.

With these caveats in mind, we now set out to calculate free-free star-formation rates for the seven star-forming galaxies detected at 34 GHz. The calibration from Murphy et al. (2012), adapted to a Chabrier IMF, is given by

$$\left(\frac{\mathrm{SFR_{FF}}}{M_\odot\,\mathrm{yr}^{-1}}\right) = 4.3\times10^{-28}\left(\frac{T_e}{10^4\,\mathrm{K}}\right)^{-0.45}\left(\frac{\nu}{\mathrm{GHz}}\right)^{0.10} \times\left(\frac{f_{\mathrm{th}}(\nu)L_\nu}{\mathrm{erg\,s^{-1}\,Hz^{-1}}}\right)\,. \tag{4.7}$$

Here T_e is the electron temperature, which we assume to equal $T_e = 10^4$ K. However, we note that our results are somewhat insensitive to the precise value adopted, given the modest exponent of $T_e^{-0.45}$. The star-formation rate is further directly proportional to the product of the thermal fraction and the radio luminosity, which we evaluate at a rest-frame frequency of $\nu = 1.4$ GHz.

We derive typical free-free star-formation rates between SFR $\approx 30 - 350\,M_\odot\,\mathrm{yr}^{-1}$ for the 4/7 sources for which we have robustly constrained thermal fractions. The remaining sources instead have a thermal fraction that is consistent with zero within 1σ, such that we can only provide upper limits on their free-free star-formation rates. We compare the free-free star-formation rates with those derived from magphys, as well as from low-frequency radio synchrotron emission in Figure 4.13. For the latter, we adopt the far-infrared/radio correlation from Delhaize et al. (2017), which is suitable for the radio-detected star-forming population. While we have derived individual q_{IR}-values for the star-forming COLDz sample in Section 4.4, we adopt a fixed far-infrared/radio correlation from the literature to ensure the synchrotron-derived star-formation rates are independent of those from far-infrared emission.

Overall, we observe a reasonable agreement between the star-formation rates from free-free emission, and those from the more commonly adopted tracers we use for comparison. This likely implies that the various aforementioned caveats do not greatly affect our calculated SFRs. However, the correlation between the two radio-based tracers appears tighter than the one between the SFRs from free-free emission and SED-fitting, which is surprising as the timescale for far-infrared emission should more closely resemble that of FFE than synchrotron emission. Two sources in particular, GN-4 ($z = 1.27$) and GN-9 ($z = 0.87$) appear to have well-constrained free-free SFRs which exceed the ones from SED-fitting by a factor of 5.6 ± 0.1 and 7.0 ± 0.3, respectively. If dust extinction within the HII-region, or leakage of ionizing photons were a concern, the free-free SFRs should be suppressed, in contrast to what we observe for these two sources. Instead, for GN-4 this offset is likely related to the SFR determined from SED-fitting. While the infrared SED of this galaxy is well-constrained (Figure 4.17), magphys predicts that a substantial fraction of the infrared emission from GN-4 originates from an older stellar population, with the ratio between its infrared-based star-formation rate – assuming the conversion from Kennicutt (1998) adjusted for a Chabrier IMF – and the fitted SFR equaling 3.2 ± 0.1. Given that the SFRs from free-free emission and the 1.4 GHz luminosity are in good agreement for GN-4, it is likely that the contribution from old stars to the FIR-luminosity is overestimated in the SED-fitting.

A similar discrepancy can be seen between the free-free and infrared star-formation rates derived for GN-9. While this source too has a modest contribution to its dust luminosity from older stars, upon accounting for this, its ratio between the free-free and SED-fitted star-formation rates remains a factor of $3.8^{+0.1}_{-0.3}$. Instead, the radio flux densities of this source are likely to be boosted by the emission from an AGN. We find a far-infrared/radio correlation parameter of $q_{\rm IR} = 1.99 \pm 0.04$ for GN-9 (Section 4.6.1), which implies it lies ~ 0.5 dex below the median value for radio-selected star-forming galaxies at its redshift of $z = 0.87$ (Delhaize et al. 2017), though still above the threshold we adopt for identifying radio AGN. Nevertheless, GN-9 is $\sim 3.5\times$ radio-bright with respect to the median far-infrared/radio correlation, which fully accounts for the difference between its radio and SED-fitted star-formation rates.

Interestingly, we can only place upper limits on the free-free star formation rates for two of the brightest star-forming galaxies in GOODS-N ($\rm SFR_{SED} \sim 400\,M_\odot\,yr^{-1}$), GN-7 and GN-11. While naively these galax-

ies might be expected to exhibit strong free-free emission, recent studies of starburst galaxies have found that their radio spectra might steepen towards higher frequencies (Tisanić et al. 2019; Thomson et al. 2019). This may be related either to a deficit in free-free emission, or to the steepening of their synchrotron spectra. However, these studies were limited to rest-frame frequencies $\nu \lesssim 20$ GHz, and hence did not probe the regime where free-free emission is expected to dominate. While our study does directly target this high-frequency regime, with the current sampling of the radio spectrum we are unable to distinguish between a deficit in free-free emission, or more complex behavior in the synchrotron emission. Nevertheless, our lack of a robust detection of free-free emission in these strongly star-forming sources provides support for the existence of more complex radio spectra, which may be constrained by probing their radio emission at intermediate frequencies, using, for example, the VLA K-band (22 GHz).

Taking the aforementioned caveats into account, our derived free-free star-formation rates are in good agreement with those from SED-fitting and the low-frequency far-infrared/radio correlation. While the uncertainties on the free-free SFRs remain large as a result of the typical faintness of star-forming galaxies at high rest-frame frequencies, our analysis indicates that a deep, 34-GHz selected sample, supplemented by deep ancillary radio observations, can be used to accurately constrain star-formation at high-redshift. This, in turn, will be possible for significantly larger galaxy samples in the future, with the increased sensitivity of next-generation radio facilities.

4.7 Free-free Emission with the SKA and ngVLA

The next large radio telescope to come online is the Square-Kilometer Array Phase 1 (SKA1), with SKA1-Mid set to cover a frequency range of $0.35 - 15$ GHz. As such, observations with the highest-frequency band of the SKA1-Mid (at a central frequency of $\nu_c = 12.5$ GHz) will start probing the regime where free-free emission dominates in star-forming galaxies at $z \gtrsim 1$. A galaxy with SFR $= 10\,M_\odot\,\mathrm{yr}^{-1}$ at $z = 1$ will have a flux density of approximately $S_{12.5} \approx 1.5\,\mu$Jy in this band, assuming the FIRRC from Delhaize et al. (2017), and the calibration between star-formation and free-free emission from Murphy et al. (2012). This, in turn, requires $\sim 15 - 20$ hr of telescope time for a 5σ detection, based on the SKA1 sensitivity estimates from Braun et al. (2019). In order to robustly probe the free-free emission in such a modestly star-forming galaxy, additional sampling of its low-

frequency radio spectrum is crucial. In particular, for a similar 5σ detection at 1.4 and 6.7 GHz, a further $\sim 10-15$ hr of total telescope time is required. Given the $\sim 4\times$ larger field-of-view at 6.7 GHz compared to at 12.5 GHz, a possible observing strategy for the detection of free-free emission in faint star-forming galaxies is to combine two single SKA1-Mid pointings at 1.4 and 6.7 GHz with a five pointing mosaic at 12.5 GHz, covering the entire 6.7 GHz field-of-view. With a total telescope time of ~ 100 hr, this allows for the mapping of free-free emission in all $z \gtrsim 1$ star-forming galaxies at $S_{12.5} \gtrsim 1.5\,\mu$Jy across an area of ~ 120 arcmin^2. Adopting the Bonaldi et al. (2019) simulations of the radio sky, developed specifically for the SKA1, a typical $\sim 1100-1200$ galaxies are expected at $S_{12.5} \gtrsim 1.5\,\mu$Jy within this field-of-view. In particular, approximately $\sim 68 \pm 2\%$ ($\sim 12 \pm 1\%$) of this sample is expected to lie at a redshift $z \geqslant 1$ ($z \geqslant 3$), allowing for the robust sampling of the free-free dominated regime. For comparison, the 200 hr VLA COSMOS-XS survey (van der Vlugt et al. 2021), reaches a similar depth to these template SKA1-Mid observations at 3 and 10 GHz, but covers a smaller area of ~ 30 arcmin^2. The increased survey speed of SKA1-Mid, therefore, allows for a $\gtrsim 8\times$ quicker mapping of free-free emission up to ~ 15 GHz, compared to the VLA. However, as the frequency coverage of SKA1-Mid is not fully optimized to directly probe the high-frequency radio emission in star-forming galaxies, significant synergy with the VLA remains, as it allows for the extension of the spectral coverage from the SKA1 to higher frequencies.

The ngVLA (Murphy et al. 2018; McKinnon et al. 2019), however, is set to truly transform our understanding of the high-frequency radio spectrum in distant galaxies, and will allow for the usage of free-free emission as a high-redshift SFR-tracer on an unprecedented scale. The current sensitivity estimates (Butler et al. 2019) indicate that the ngVLA will attain a typical RMS of $\sigma \approx 0.3\,\mu$Jy beam^{-1} in one hour of Band four ($\nu = 20.5-34.0$ GHz) observations. This, in turn, translates to a 5σ detection of a galaxy forming stars at $100\,M_\odot$ yr^{-1} at $z = 2.5$, probing rest-frame 80 GHz, similar to the frequency range probed in this work for $z \approx 2$ star-forming galaxies. However, with the expected improvement in sensitivity the ngVLA provides over the current VLA, high-redshift sources may more easily be targeted at relatively low observing frequencies, enabling wider surveys while still allowing for the free-free dominated regime to be probed. For example, Barger et al. (2018) propose a survey at 8 GHz (ngVLA Band two) to $0.2\,\mu$Jy beam^{-1} across a large area of 1 deg^2, which requires just an hour per pointing. By adopting a typical wedding cake strategy, deeper observa-

tions across a smaller area can further be used to target fainter star-forming galaxies. As an example, a star-forming galaxy of SFR $= 25\,M_{\odot}\,\mathrm{yr}^{-1}$ at $z = 3$ ($z = 5$) can in principle be detected at 8 GHz in only ~ 3 hr (~ 15 hr), modulo, of course, the large uncertainties on the typical thermal fraction in faint, star-forming sources, and the nature of the far-infrared/radio correlation in this population.

4.8 Conclusions

We have presented a deep continuum survey of the high-frequency radio sky with the Very Large Array, which probes the microjansky galaxy population at 34 GHz. This regime has historically remained largely unexplored due to the relatively low survey speed of radio telescopes at these frequencies, as well as the expected faintness of sources. However, the high radio frequencies hold one of the most reliable tracers of star-formation, radio free-free emission, and as such are set to become a key area of study with next-generation radio facilities.

We employ deep observations at 34 GHz from the COLDz project (Pavesi et al. 2018; Riechers et al. 2019, 2020) which cover the well-studied COSMOS ($10\,\mathrm{arcmin}^2$) and GOODS-North ($50\,\mathrm{arcmin}^2$) fields to a typical depth of $\sim 1.5\,\mu\mathrm{Jy\,beam}^{-1}$ and $\sim 5.3\,\mu\mathrm{Jy\,beam}^{-1}$, respectively. We perform source detection on the images down to a liberal 3σ detection threshold, aided by deep ancillary radio data across both fields, resulting in the detection of high-frequency continuum emission in eighteen galaxies. We cross-match these detections with additional deep radio observations at 1.4, 3 and 10 GHz in the COSMOS field, as well as data at 1.4, 5 and 10 GHz in GOODS-N. In addition, we leverage the wealth of multi-wavelength data across both fields to fully sample the SEDs of the galaxies from the X-ray to radio regime. The COLDz continuum sample spans a redshift range of $z = 0.50 - 5.30$, and lies at a median (mean) redshift of $z = 1.12^{+0.52}_{-0.15}$ ($z = 1.55^{+0.41}_{-0.35}$). The sample contains six sources at $z \geqslant 2$, and includes the well-studied submillimeter galaxy AzTEC.3 at $z = 5.3$. Our main findings are the following:

- We present the first constraints on the radio number counts at 34 GHz in the regime where star-forming galaxies dominate the radio population (Figure 4.7), and find that these are in good agreement with lower-frequency number counts in the literature, both from observations (van der Vlugt et al. 2021) and simulations (Bonaldi et al. 2019).

- We use the far-infrared/radio correlation to divide the 34 GHz continuum sample into star-forming galaxies and active galactic nuclei (Figure 4.8). In total, half of the sample (9 sources) shows AGN activity at radio wavelengths (Figure 4.9), while the radio emission of the remainder is consistent with being powered predominantly through star-formation. All but one of the faintest galaxies in our sample ($S_{34} \lesssim 20\,\mu$Jy) show radio emission of a star-forming origin, which is qualitatively consistent with the small fraction of radio AGN found in deep observations at lower frequencies (e.g., Algera et al. 2020b). Two sources, including AzTEC.3 at $z = 5.3$, likely have their continuum emission at 34 GHz dominated by thermal emission from dust, leaving 7/18 sources ($\sim 40\%$) of the sample with high-frequency radio continuum emission dominated by the combination of synchrotron and free-free emission.

- We use the wealth of ancillary radio data across the COSMOS and GOODS-N fields to construct radio spectra of the star-forming galaxies, covering four frequencies in the range $1.4 - 34$ GHz (Figure 4.10). We fit the radio spectra with a combination of free-free and synchrotron emission, and determine thermal fractions and non-thermal spectral indices for our sample (Figures 4.11 and 4.12), which are consistent with the values observed in local galaxies. We further determine free-free star-formation rates for seven star-forming galaxies, and find good agreement with those obtained from SED-fitting and the far-infrared/radio correlation (Figure 4.13).

With the 34 GHz continuum data from the COLDz survey, we have directly targeted free-free emission in faint star-forming sources at high redshift. While currently limited to a modest sample, next-generation radio facilities are set to significantly increase the number of galaxies for which the full radio spectrum is constrained, and will transform our understanding of high-frequency radio continuum emission in star-forming galaxies. However, combined with the wealth of ancillary data in the COSMOS and GOODS-N fields, the COLDz observations already allow for a census of free-free emission in the typical star-forming population via a multi-frequency radio stacking analysis, which will be presented in a forthcoming publication (Algera et al. 2021, in preparation).

Acknowledgements

The authors would like to thank the anonymous referee for their comments on the manuscript. H.S.B. Algera would like to thank A. de Graaff and D. Blanco for useful and constructive discussions. The authors thank Chris Carilli and Ian Smail for providing comments on the manuscript, and Fabian Walter for his help in the early stages of this project. The National Radio Astronomy Observatory is a facility of the National Science Foundation operated under cooperative agreement by Associated Universities, Inc. H.S.B.A. and J.A.H. acknowledge support of the VIDI research programme with project number 639.042.611, which is (partly) financed by the Netherlands Organization for Scientific Research (NWO). D.R. acknowledges support from the National Science Foundation under grant numbers AST-1614213 and AST-1910107. D.R. also acknowledges support from the Alexander von Humboldt Foundation through a Humboldt Research Fellowship for Experienced Researchers. M.A. and this work have been supported by grants "CONICYT+PCI+REDES 19019" and "CONICYT + PCI + INSTITUTO MAX PLANCK DE ASTRONOMIA MPG190030".

Appendix

4.A Image Properties

We discuss some of the properties of the COSMOS and GOODS-N 34 GHz images below, including the completeness, and the level of flux boosting. In addition, we detail how we assign flux densities to the 34 GHz continuum detections.

4.A.1 Completeness

We determine the completeness of the COSMOS and GOODS-N mosaics by inserting mock sources into the image, and extracting them via our regular source detection procedure (Section 4.3). The fraction of resolved sources at a resolution of $\sim 2''$ at 10 GHz – similar to the resolution of our 34 GHz observations – is just $\sim 10\%$ (van der Vlugt et al. 2021), and is expected to be smaller at even higher frequencies, where sources are more compact (Murphy et al. 2017; Thomson et al. 2019). As such, we only include unresolved mock sources in our completeness analysis. Sources are inserted in the maps uncorrected for the primary beam (PB), as in this case it is

straightforward to incorporate the incompleteness due to the decreased PB-sensitivity by inserting sources with a true flux density S_ν as $A(r) \times S_\nu$, where $A(r)$ represents the primary beam sensitivity at position r within the mosaic.

We randomize source positions within both mosaics, above $A(r) \geqslant 0.20$, and draw flux densities from a powerlaw distribution to ensure low flux densities – where incompleteness will be the largest – are amply sampled. For COSMOS, we insert 50 mock sources each run, for a total of 200 runs. As the GOODS-N mosaic is substantially larger, we instead insert 100 mock sources per run, for 100 runs total. In both cases, mock sources are required to be 2.5 beam sizes away from both real sources and other mock sources. We then repeat the source detection procedure described in Section 4.3, and cross-match the recovered sources to the inserted ones, using a matching radius of $0\farcs7$. We record their inserted flux density, as well as their recovered peak and integrated flux densities. We define the completeness in a given flux density bin i as $C_i = N_{\mathrm{rec},i}/N_{\mathrm{ins},i}$, that is, as the ratio of the number of inserted and recovered mock sources with a flux density that falls within the i-th bin. We determine the corresponding uncertainty via a bootstrap analysis, whereby we resample from the inserted flux densities, with replacement, and determine for each flux density bin the fraction of this sample that was recovered in our source detection procedure. The uncertainty then represents the $16^{\mathrm{th}} - 84^{\mathrm{th}}$ percentile of the bootstrapped completeness analyses. We show the completeness in both the COSMOS and GOODS-N mosaics in Figure 4.14.

In the COSMOS field, we reach 50 and 80 per cent completeness at flux densities of $S_{34} = 7.3\,\mu\mathrm{Jy\,beam}^{-1}$ ($\approx 6\sigma$, where σ represents the typical RMS in the map) and $S_{34} = 13.3\,\mu\mathrm{Jy\,beam}^{-1}$ ($\approx 10\sigma$), respectively. In GOODS-North, we reach completeness fractions of 50 and 80 per cent at $S_{34} = 19.6\,\mu\mathrm{Jy\,beam}^{-1}$ ($\approx 4\sigma$) and $S_{34} = 29.3\,\mu\mathrm{Jy\,beam}^{-1}$ ($\approx 6\sigma$), respectively. These differences may be explained by the non-uniform exposure map of the GOODS-N mosaic, allowing for faint sources to still be detected in a small portion of the mosaic.

4.A.2 Peak versus Integrated Fluxes

In order to assign a flux density to the detected radio sources, we need to establish if they are resolved. Our observations have a typical beam-size of $\sim 2\farcs5$, and as such, we expect most sources to be unresolved, based on the typical (sub-)arcsecond radio sizes of star-forming galaxies at low-frequencies (Cotton et al. 2018; Jiménez-Andrade et al. 2019), and the find-

ing that these sources are more compact at higher frequencies (Murphy et al. 2017; Thomson et al. 2019). To verify this, we use our runs of inserted mock sources, which by construction are unresolved, and compare their peak and integrated flux densities as a function of signal-to-noise. We show the results in Figure 4.15, for both the COSMOS and GOODS-N fields. We divide the results into logarithmically spaced bins in S/N, and determine the integrated/peak ratio encompassing 95 percent of sources per bin (following, e.g., Bondi et al. 2008; van der Vlugt et al. 2021). These percentiles are fitted with a power-law, with the region below the best fit defining the limiting integrated/peak flux density where sources are taken to be unresolved. It is clear that at modest signal-to-noise, S/N $\lesssim 5$, sources can have $S_{\rm int}/S_{\rm peak} \gtrsim 2$, despite being unresolved. This is a result of nearby noise peaks elongating the source, or throwing off the fitting, which mostly affects the integrated flux density. We find that all sources, with the exception of one bright (S/N ~ 25) detection in GOODS-N, show an integrated/peak ratio which is consistent with the source being unresolved. As such, we adopt the integrated flux density for this single source, and the peak brightness for the rest.

4.A.3 Flux Boosting

At low signal-to-noise, the peak brightness may be 'boosted' as a result of noise properties in the image. To establish whether this is affecting the flux densities of our 34 GHz detections, we compare the recovered and inserted flux densities of our mock source analysis. The results are shown in Figure 4.16, for both COSMOS and GOODS-N. At S/N $\gtrsim 5$, the median ratio of recovered to inserted flux density is consistent with unity, with a spread of less than $\lesssim 20\%$. At S/N $\lesssim 5$, which is the typical signal-to-noise at which the faintest 34 GHz sources are detected, the level of flux boosting steadily increases, with a typical correction of $\sim 20\%$ at S/N ≈ 3 in either field. In this low-S/N regime, the typical spread on the ratio of recovered and inserted flux densities similarly increases strongly. Following, e.g., Stach et al. (2019), we correct the flux densities of the sources detected at 34 GHz by the median level of flux boosting at their observed S/N. The uncertainty on the corrected flux density includes the propagated bootstrapped error on the median.

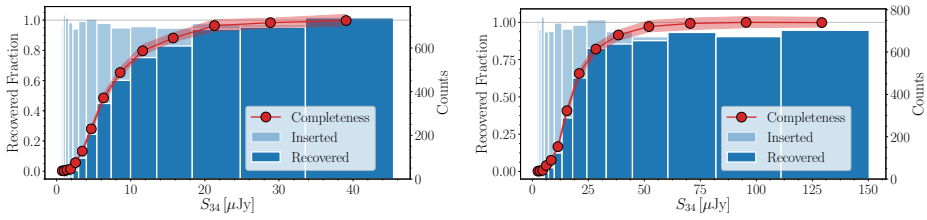

Figure 4.14: Left: Completeness analysis for the COSMOS field, showing the fraction of inserted mock sources we recover as a function of their flux density. The red datapoints and shaded region indicate the measured completeness and confidence region, respectively. **Right:** Completeness analysis for GOODS-North. Both panels take into account the variation in the primary beam sensitivity across the mosaic, and as such the total completeness correction constitutes the combination of missing sources due to a decreased primary beam sensitivity, and local noise properties within the mosaics.

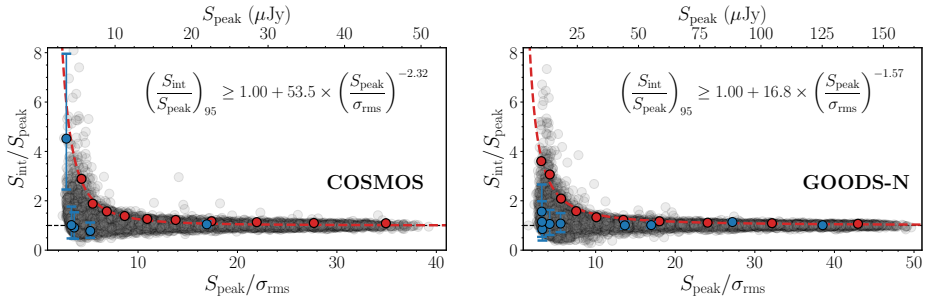

Figure 4.15: The ratio of integrated to peak flux density as a function of the peak S/N for unresolved mock sources inserted into the COSMOS and GOODS-N fields. Both panels show a power-law fit to the upper 95th percentile of each bin in S/N (red points) via the red, dashed line. Sources below this line are taken to be unresolved, and for these the peak brightness is adopted. The robust sources detected in both fields are shown in blue. A single source in GOODS-N is consistent with being resolved, whereas the remaining continuum detections are unresolved. Since the mock sources are inserted into the mosaic uncorrected for the primary beam, the RMS is highly uniform, and hence the S/N can be mapped into a peak brightness (upper horizontal axis).

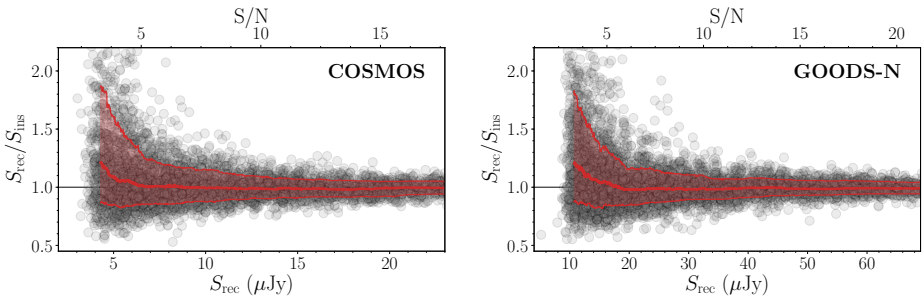

Figure 4.16: The ratio of recovered and inserted peak flux density as a function of recovered flux density, for unresolved mock sources inserted into the COSMOS and GOODS-N 34 GHz maps. A running median and the corresponding $16 - 84^{\rm th}$ percentile spread are indicated through the red line and shaded area. While for both fields the median level of flux boosting is negligible at S/N $\gtrsim 5$, the correction reaches $\sim 20\%$ at S/N ≈ 3.

4.B Spectral Energy Distributions

We show the full spectral energy distributions for the eighteen COLDz continuum detections, fitted with magphys, in Figure 4.17, and present their physical parameters in Table 4.4.

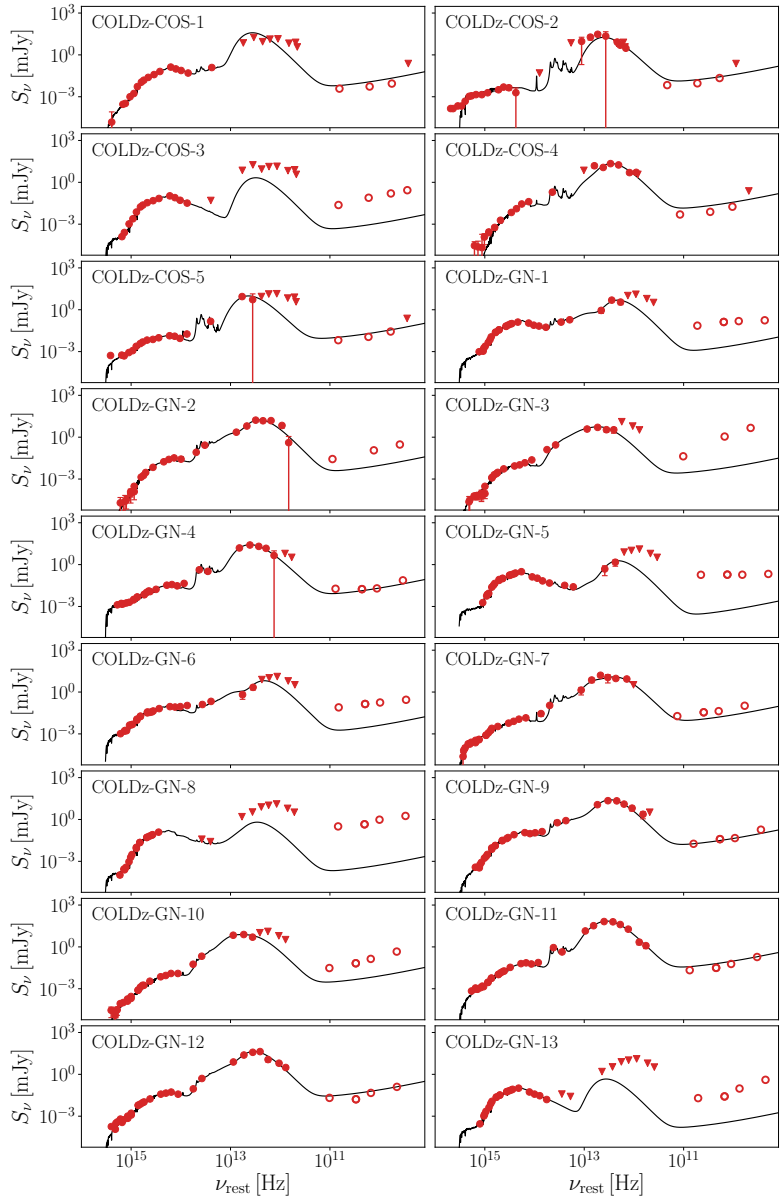

Figure 4.17: The spectral energy distributions of the 18 COLDz continuum detections. All datapoints are shown in red, with triangles indicating upper limits and open symbols indicating the radio observations, which are not fitted. In half of the sources, the measured radio flux densities lie well above the extrapolated value from magphys, indicative of additional emission from a radio AGN.

Table 4.4: Physical Properties of the 34 GHz-selected COLDz sample

ID	$L_{\rm IR}$	SFR[a]	M_*	$L_{1.4}$[b]	$q_{\rm IR}$	AGN[c]
	[$\log L_\odot$]	[$\log M_\odot\,{\rm yr}^{-1}$]	[$\log M_\odot$]	[$\log {\rm W\,Hz}^{-1}$]		
COLDz-cont-COS-1	$11.75^{+0.09}_{-0.09}$	$1.40^{+0.14}_{-0.06}$	$11.39^{+0.09}_{-0.06}$	$22.51^{+0.08}_{-0.08}$	$3.25^{+0.12}_{-0.12}$	0
COLDz-cont-COS-2	$13.00^{+0.01}_{-0.03}$	$2.80^{+0.01}_{-0.03}$	$10.78^{+0.02}_{-0.03}$	$24.83^{+0.06}_{-0.06}$	$2.17^{+0.06}_{-0.06}$	0
COLDz-cont-COS-3	$10.70^{+0.19}_{-0.51}$	$0.01^{+0.17}_{-0.34}$	$11.16^{+0.09}_{-0.01}$	$24.04^{+0.04}_{-0.04}$	$0.67^{+0.20}_{-0.49}$	1
COLDz-cont-COS-4	$12.54^{+0.10}_{-0.03}$	$2.21^{+0.21}_{-0.40}$	$11.93^{+0.03}_{-0.19}$	$24.01^{+0.06}_{-0.06}$	$2.56^{+0.10}_{-0.08}$	0
COLDz-cont-COS-5	$11.38^{+0.17}_{-0.16}$	$1.28^{+0.19}_{-0.14}$	$10.23^{+0.05}_{-0.08}$	$23.32^{+0.03}_{-0.03}$	$2.08^{+0.17}_{-0.17}$	0
COLDz-cont-GN-1	$10.66^{+0.07}_{-0.03}$	$0.31^{+0.08}_{-0.11}$	$11.04^{+0.05}_{-0.03}$	$23.17^{+0.02}_{-0.02}$	$1.51^{+0.06}_{-0.04}$	1
COLDz-cont-GN-2	$12.12^{+0.02}_{-0.02}$	$1.84^{+0.07}_{-0.12}$	$11.47^{+0.11}_{-0.09}$	$24.63^{+0.13}_{-0.05}$	$1.49^{+0.05}_{-0.13}$	1
COLDz-cont-GN-3	$12.27^{+0.01}_{-0.01}$	$1.92^{+0.01}_{-0.01}$	$11.01^{+0.01}_{-0.01}$	$26.18^{+0.02}_{-0.02}$	$0.10^{+0.02}_{-0.02}$	1
COLDz-cont-GN-4	$12.23^{+0.01}_{-0.01}$	$1.73^{+0.01}_{-0.01}$	$10.64^{+0.01}_{-0.01}$	$23.86^{+0.09}_{-0.09}$	$2.37^{+0.09}_{-0.09}$	0
COLDz-cont-GN-5	$9.34^{+0.21}_{-0.01}$	$-0.88^{+0.17}_{-0.10}$	$10.83^{+0.09}_{-0.06}$	$22.75^{+0.02}_{-0.02}$	$0.62^{+0.18}_{-0.04}$	1
COLDz-cont-GN-6	$11.23^{+0.04}_{-0.10}$	$1.11^{+0.01}_{-0.11}$	$11.06^{+0.05}_{-0.02}$	$23.93^{+0.02}_{-0.02}$	$1.30^{+0.05}_{-0.10}$	1
COLDz-cont-GN-7	$12.60^{+0.04}_{-0.07}$	$2.54^{+0.07}_{-0.05}$	$10.81^{+0.03}_{-0.07}$	$24.72^{+0.10}_{-0.09}$	$1.88^{+0.11}_{-0.12}$	0
COLDz-cont-GN-8	$10.38^{+1.31}_{-0.04}$	$-0.15^{+1.01}_{-0.13}$	$11.56^{+0.01}_{-0.12}$	$24.83^{+0.03}_{-0.03}$	$-0.40^{+1.25}_{-0.09}$	1
COLDz-cont-GN-9	$11.82^{+0.03}_{-0.01}$	$1.56^{+0.02}_{-0.01}$	$11.23^{+0.14}_{-0.01}$	$23.85^{+0.03}_{-0.03}$	$1.99^{+0.04}_{-0.03}$	0
COLDz-cont-GN-10	$12.37^{+0.01}_{-0.01}$	$2.34^{+0.01}_{-0.01}$	$10.59^{+0.06}_{-0.01}$	$25.11^{+0.02}_{-0.02}$	$1.26^{+0.02}_{-0.02}$	1
COLDz-cont-GN-11	$12.58^{+0.01}_{-0.01}$	$2.59^{+0.01}_{-0.01}$	$11.01^{+0.01}_{-0.01}$	$24.17^{+0.03}_{-0.03}$	$2.42^{+0.03}_{-0.03}$	0
COLDz-cont-GN-12	$12.78^{+0.01}_{-0.02}$	$2.65^{+0.02}_{-0.01}$	$11.59^{+0.01}_{-0.12}$	$24.46^{+0.08}_{-0.07}$	$2.32^{+0.07}_{-0.08}$	0
COLDz-cont-GN-13	$9.43^{+0.10}_{-0.15}$	$-1.00^{+0.11}_{-0.08}$	$10.77^{+0.02}_{-0.03}$	$23.62^{+0.03}_{-0.03}$	$-0.19^{+0.10}_{-0.15}$	1

[a]The star-formation rate as determined via magphys.

[b]The radio luminosity at rest-frame 1.4 GHz is computed using the closest observed-frame flux density (1.4 or 3 GHz) and the measured radio spectral index.

[c]Sources are identified as radio AGN based on their offset from the far-infrared/radio correlation (Section 4.6.1).

5 Probing Cosmic Star Formation With Radio Free-free Emission

Radio free-free emission is considered one of the most reliable tracers of star formation in galaxies. However, as it constitutes the faintest part of the radio spectrum – being roughly an order of magnitude less luminous than radio synchrotron emission at the GHz frequencies typically targeted in radio surveys – the usage of free-free emission as a star formation rate tracer has mostly remained limited to the local Universe. We here perform a multi-frequency radio stacking analysis using deep *Karl G. Jansky* Very Large Array observations at 1.4, 3, 5, 10 and 34 GHz in the COSMOS and GOODS-North fields to probe free-free emission in the typical galaxy population at the peak of cosmic star-formation. We find that $z \sim 0.5 - 2.5$ star-forming galaxies exhibit radio emission at rest-frame frequencies of $\sim 60 - 80$ GHz that is $\sim 1.5 - 2\times$ fainter than would be expected from a simple combination of free-free and synchrotron emission, as in the prototypical starburst galaxy M82. We interpret this as a deficit in high-frequency synchrotron emission, while the typical level of free-free emission is as expected from M82. We additionally provide the first constraints on the cosmic star-formation history using free-free emission at $0.5 \lesssim z \lesssim 2.5$, and find a good agreement with more established tracers at high redshift. In the future, deep multi-frequency radio surveys will be crucial in order to accurately determine the shape of the radio spectrum of faint star-forming galaxies, and to further establish radio free-free emission as a tracer of high-redshift star formation.

H. S. B. Algera, J. A. Hodge, D. A. Riechers *et al.*
The Astrophysical Journal, submitted (2021)

5.1 Introduction

One of the major goals in extragalactic astronomy is to constrain the cosmic star-formation rate density (SFRD). The SFRD is known to peak between $z \sim 1-3$, and then declines rapidly towards the present (e.g., Madau & Dickinson 2014; Bouwens et al. 2020; Leslie et al. 2020; Zavala et al. 2021). However, beyond $z \gtrsim 3$ star-formation rates have predominantly been measured using rest-frame ultra-violet observations (Bouwens et al. 2020). Whilst a powerful tracer of star formation, UV-emission is easily attenuated by dust, and may therefore miss an appreciable fraction of the total star formation taking place in the early Universe (Casey et al. 2018). In turn, uncertain dust corrections are typically adopted in order to constrain the earliest epochs of cosmic star formation (Bouwens et al. 2009, 2014; Burgarella et al. 2013; Oesch et al. 2013). Such complications may be circumvented by instead using infrared observations, which probe dust-reprocessed starlight, and as such constrain the fraction of star formation that is dust-obscured (e.g., Kennicutt 1998). However, with most current infrared facilities it is notoriously difficult to probe beyond the peak of cosmic star formation, due to the limited depth and resolution provided by both ground- and space-based facilities (Hodge & da Cunha 2020). In recent years, the highly sensitive Atacama Large Millimeter/submillimeter Array (ALMA) has enabled progress out to higher redshift (Bouwens et al. 2020; Dudzevičiūtė et al. 2020; Gruppioni et al. 2020; Zavala et al. 2021), although its limited field of view makes wide-area far-infrared surveys of star-formation highly expensive.

At longer wavelengths, radio emission has provided a powerful tracer of cosmic star-formation out to $z \sim 5$ (Novak et al. 2017; Leslie et al. 2020). This relies on the tight correlation between the radio and far-infrared luminosities of star-forming galaxies, which has been established to hold across a wide range of galaxy types in the local Universe (Helou et al. 1985; Condon 1992; Yun et al. 2001; Bell 2003). Low-frequency radio synchrotron emission in star-forming galaxies originates predominantly from the shocks produced by supernovae, and as such forms a delayed tracer of star formation activity ($\sim 30-100$ Myr; Bressan et al. 2002). However, both at low and high redshift, the far-infrared/radio correlation remains an area of active investigation, with various studies finding that it may be non-linear, change with cosmic time, or depend on galaxy type or physical parameters such as stellar mass (Ivison et al. 2010b; Sargent et al. 2010; Thomson et al. 2014; Basu et al. 2015; Magnelli et al. 2015; Delhaize et al. 2017;

Read et al. 2018; Algera et al. 2020a; Delvecchio et al. 2021; Molnár et al. 2021). In addition, active galactic nuclei (AGN) may similarly emit at radio wavelengths, and can therefore further bias studies of radio star formation (e.g., Molnár et al. 2018; Algera et al. 2020a). Combined with the presently incomplete theoretical underpinning of the far-infrared/radio correlation, the appropriate conversion between radio luminosity and star-formation rate in the high-redshift Universe remains not fully understood.

However, the radio regime offers an additional tracer of star formation: at high-frequencies ($\nu \gtrsim 30\,\mathrm{GHz}$), free-free emission is thought to overtake synchrotron radiation as the dominant mechanism generating radio emission (Condon 1992; Murphy et al. 2011; Tabatabaei et al. 2017; Querejeta et al. 2019). Free-free emission originates directly from sites of massive star formation ($M \gtrsim 5M_{\odot}$) on short timescales ($\lesssim 10\,\mathrm{Myr}$), and its long wavelength nature ensures it is mostly insensitive to obscuration by dust. Therefore, free-free emission provides a direct and dust-unbiased tracer of star formation that has been used to calibrate various local tracers (Murphy et al. 2011, 2012). The clear next step, then, is to investigate this powerful tracer in the early Universe.

Targeting free-free emission at high redshift, however, remains challenging with current radio facilities. Algera et al. (2021) recently presented a blind survey of free-free emission in high-redshift galaxies, using a 34 GHz-selected sample identified in deep observations from the *Karl G. Jansky* Very Large Array (VLA) CO Luminosity Density at High redshift survey (COLDz; Pavesi et al. 2018; Riechers et al. 2019, 2020), in combination with multi-frequency ancillary data. Algera et al. (2021) identified seven star-forming galaxies in these observations with 34 GHz flux densities dominated by a combination of free-free and synchrotron emission, and as such provided the first blind constraints on free-free emission at high redshift. While limited to a modest sample, they found a good agreement between star-formation rates determined from free-free emission and those from canonical tracers such as spectral energy distribution (SED) fitting and the far-infrared/radio correlation.

With present facilities, it remains prohibitively expensive to expand the study of free-free emission at high redshift to significantly larger galaxy samples, and push beyond the bright star-forming population. As an example, a galaxy with a star-formation rate of just $10\,\mathrm{M}_{\odot}\,\mathrm{yr}^{-1}$ at $z = 1$ ($z = 2$) is expected to have a 34 GHz flux density of $S_{34} \approx 1.0\,\mu$Jy ($S_{34} \approx 0.3\,\mu$Jy), which will remain out of reach for radio telescopes until the advent of the next-generation VLA. However, through a multi-frequency stacking analy-

sis, it is possible to already study the nature of high-frequency radio emission in normal star-forming galaxies. In this work, we adopt such stacking techniques in combination with the deep radio observations available across the Cosmic Evolution Survey (COSMOS; Scoville et al. 2007) and the Great Observatories Origins Deep Survey North (GOODS-N; Giavalisco et al. 2004) in order to provide the first constraints on the nature of free-free emission in representative high-redshift galaxies.

In addition, a multi-frequency stacking analysis simultaneously allows for constraints on the shape of the radio spectra of typical star-forming galaxies. In recent years, a growing amount of evidence has suggested that the radio spectrum of star-forming galaxies may be more complex than the widely adopted combination of just power-law free-free and synchrotron emission. Local Ultra-Luminous Infrared Galaxies (ULIRGs), for example, typically show radio spectra that steepen towards higher frequencies (Clemens et al. 2008; Leroy et al. 2011; Galvin et al. 2018). At high redshift, the radio spectra of the radio-bright population have similarly been studied in detail, revealing relatively typical synchrotron-dominated spectra at low frequencies (rest-frame $\lesssim 5$ GHz; Ibar et al. 2010; Thomson et al. 2014; Calistro Rivera et al. 2017; Algera et al. 2020a). However, subsequent follow-up probing higher rest-frame frequencies in starburst galaxies (SFR $\gtrsim 100\,M_{\odot}\,\mathrm{yr}^{-1}$) indicate their radio spectra might show spectral steepening similar to local ULIRGs (Thomson et al. 2019; Tisanić et al. 2019), which is most readily interpreted as a deficit of free-free emission, or spectral ageing of the synchrotron component. Finally, a puzzling component dubbed anomalous microwave emission has been observed in local star-forming regions and galaxies (Murphy et al. 2015, 2020), occupying a similar frequency range as free-free emission. Deep radio observations, capable of probing rest-frame frequencies $\nu \gtrsim 10$ GHz are crucial in order to better understand what powers the high-frequency emission in galaxies.

The structure of this paper is as follows. In Section 5.2, we introduce the radio and ancillary data utilized in this work. In Section 5.3, we detail the stacking analysis and our modelling of the radio spectrum. We present stacked radio spectra of the high-redshift galaxy population in Section 5.4 and interpret our results in Section 5.5. Finally, we summarize our findings in Section 5.6. Throughout this work, we assume a standard ΛCDM cosmology, with $H_0 = 70\,\mathrm{km\,s^{-1}\,Mpc^{-1}}$, $\Omega_m = 0.30$ and $\Omega_\Lambda = 0.70$ and adopt a Chabrier (2003) initial mass function. The radio spectral index α is further defined as $S_\nu \propto \nu^\alpha$, where S_ν represents the flux density at frequency ν.

5.2 Data

5.2.1 Radio Data

In this work, we combine various sensitive multi-frequency VLA observations across the COSMOS and GOODS-North fields. At the core of our analysis lie the COLDz 34 GHz continuum observations, which are described in detail in Pavesi et al. (2018) and Algera et al. (2021). These observations combine a deep but small mosaic in the COSMOS field, and a shallower but wider radio map in GOODS-N, following the traditional "wedding-cake" design. Briefly, the data in the COSMOS field consist of a 7-pointing mosaic accounting for a total of 93 hr of on-source time across the VLA D and DnC configurations. The central root-mean-square (RMS) noise in the map is $1.3\,\mu$Jy beam^{-1}, and the mosaic covers a field of view of 9.6 arcmin^2. The GOODS-N field was observed for 122 hr on-source across the VLA D, D$\rightarrow$DnC, DnC and DnC$\rightarrow$C configurations. The resulting 57-pointing mosaic spans an area of 51 arcmin^2, with a typical RMS of $5.3\,\mu$Jy beam^{-1}. In addition, a single deep pointing within the mosaic, designed to overlap with the NOEMA observations in Decarli et al. (2014), probes down to $3.2\,\mu$Jy beam^{-1}. Both mosaics reach a typical resolution of $2''$ - $2\farcs5$, which is large enough that most continuum detections remain unresolved (Algera et al. 2021), allowing for the cleanest measurement of their flux densities.

Deep ancillary radio data are crucial in order to accurately constrain the shape of the radio spectrum in star-forming galaxies. A full description of the available radio data across the COSMOS and GOODS-N fields is given in Algera et al. (2021), which we summarize here. In the COSMOS field, we employ sensitive observations at 3 and 10 GHz from the COSMOS-XS survey (Algera et al. 2020b; van der Vlugt et al. 2021), which fully cover the COLDz footprint. These data reach a typical RMS sensitivity of $0.53\,\mu$Jy beam^{-1} and $0.41\,\mu$Jy beam^{-1} at 3 and 10 GHz, respectively, and as such are a factor of $\sim 10\times$ more sensitive toward radio synchrotron emission from star-forming galaxies than the COLDz observations, after a spectral scaling with a typical $\alpha = -0.70$ (Condon 1992). At both frequencies, the COSMOS-XS observations attain a typical resolution of $\sim 2\farcs0$, similar to that of the 34 GHz data.

To constrain the low-frequency radio emission of the sources individually detected in the 34 GHz data across COSMOS, Algera et al. (2021) adopted the 1.4 GHz observations from Schinnerer et al. (2007, 2010) which reach a typical RMS of $12\,\mu$Jy beam^{-1}. However, in this work we utilize

new, more sensitive VLA observations at 1.4 GHz covering the COSMOS-XS and COLDz footprints as part of the COSMOS-XL survey (PI: Algera). These observations will be fully described in a forthcoming publication (Algera et al., in preparation), but we briefly summarize their key properties here. The COSMOS field was observed in a single 1.4 GHz pointing for a total of 26.5 hr in the VLA A-configuration, centered on R.A. $10^{\rm h}00^{\rm m}20.7^{\rm s}$, Decl. $+02^\circ32'52\farcs6$. These observations were taken between 20 Oct 2019 and 24 Feb 2021 as part of VLA programs 19A-370 and 20A-370. The data were calibrated using the standard VLA pipeline, and imaging was performed in CASA 5.7.1 via tclean. We adopted a multi-frequency synthesis algorithm with *nterms* = 2 to account for the large fractional bandwidth, and used w-projection to account for the non-coplanarity of baselines. The data were Briggs-weighted with a robust parameter of 0.5. Prior to the primary beam correction, the median RMS within 20% of the primary beam sensitivity equals $1.8\,\mu$Jy beam^{-1}. As a result, these 1.4 GHz observations are roughly 7 times deeper than the existing VLA observations at 1.4 GHz across the COLDz footprint. In addition, they are also roughly 7 times deeper than the 34 GHz data across COSMOS, assuming a standard spectral index of $\alpha = -0.70$ (Condon 1992).

The GOODS-N field similarly benefits from a wealth of ancillary radio observations. We make use of the 1.4 GHz map from Owen (2018), which reaches a typical RMS-noise of $2.2\,\mu$Jy beam^{-1} in the pointing center, at a resolution of $1\farcs6$. In addition, Gim et al. (2019) covered the GOODS-N field with two VLA pointings at 5 GHz. Their data reach an RMS-noise of $3.5\,\mu$Jy beam^{-1}, and attain a resolution of $1\farcs5$. Furthermore, Murphy et al. (2017) imaged the GOODS-N field at 10 GHz in a single VLA pointing, covering approximately 75% of the COLDz footprint. At their native resolution of $0\farcs22$, the 10 GHz observations reach an RMS-sensitivity of $0.57\,\mu$Jy beam^{-1}. However, in this work we make use of the tapered maps provided by Murphy et al. (2017), in order to better match the resolution of the other radio observations, and ensure that we accurately capture all the flux of the (stacked) radio sources. The 10 GHz map tapered to $1''$ ($2''$) reaches a central RMS of $1.1\,\mu$Jy beam^{-1} ($1.5\,\mu$Jy beam^{-1}). For our analysis, we adopt the 10 GHz map with a $2''$ taper to better match the resolution of the ancillary radio maps.

The archival radio data in GOODS-N are of a higher relative sensitivity than the 34 GHz map, when scaled with a fixed spectral index of $\alpha = -0.70$. At 1.4 GHz, the Owen (2018) radio map is roughly $20\times$ deeper, while at 5

and 10 GHz, the radio images from Gim et al. (2019) and Murphy et al. (2017) are, respectively $6\times$ and $8\times$ more sensitive. As such, we expect to be limited by the signal-to-noise at 34 GHz in our analysis. Nevertheless, the COLDz continuum data provide crucial high-frequency constraints on the radio spectra of star-forming galaxies, and form the foundation of this work.

At the typical resolution of our radio data of $1\farcs5 - 2\farcs0$, we do not expect to resolve (stacks of) star-forming galaxies, which are typically subarcsecond in size in the μJy regime (Murphy et al. 2017; Bondi et al. 2018; Cotton et al. 2018; Jiménez-Andrade et al. 2019, 2021). In addition, galaxies are expected to become increasingly compact towards higher radio frequencies, which form the focus of this work (Murphy et al. 2017; Thomson et al. 2019). In turn, we do not expect to resolve out any emission when measuring radio flux densities, allowing for unbiased spectral index measurements. However, the resolution of our radio data is additionally high enough that any effects of source blending are negligible.

5.2.2 Optical/FIR Data

We employ deep optical and infrared observations across the COSMOS and GOODS-N fields, to serve as prior positional information for our stacking analysis. In the COSMOS field, we make use of the $z^{++}YJHK_s$-selected COSMOS2015 catalog from Laigle et al. (2016), which compiles data spanning ultra-violet to far-infrared wavelengths. Laigle et al. (2016) additionally use the SED-fitting code LePhare (Ilbert et al. 2009) to determine photometric redshifts, stellar masses and star-formation rates for all entries in the catalog. In total, 1158 galaxies from COSMOS2015 fall within 20% of the COLDz/COSMOS primary beam sensitivity.

In order to derive useful and unbiased constraints on the radio properties of star-forming galaxies via a stacking analysis, it is necessary to assess the completeness of the input sample. The mass-completeness of the COSMOS2015 catalog is assessed by Laigle et al. (2016), who estimate the catalog to be 90% complete above stellar masses of $10^9, 10^{9.5}$ and $10^{10}\,M_\odot$ out to $z \lesssim 1.3, z \lesssim 2.3$ and $z \lesssim 4.0$, respectively.[1]

Across the GOODS-North field, we employ the photometry compiled in the 3D-HST catalog (Brammer et al. 2012; Skelton et al. 2014). Source detection for 3D-HST was performed in a combined F125+F140W+F160W

[1]These completeness limits were determined for the UltraVISTA "ultra-deep" stripes, with which the COLDz observations overlap in their entirety.

image, with additional photometry being performed in 22 filters spanning the $U-$band to *Spitzer*/IRAC CH4. These observations are further extended by Momcheva et al. (2016), who determine the redshift for all 3D-HST entries by combining broadband photometry with *HST*/GRISM spectroscopic observations. In addition, Momcheva et al. (2016) determine dust-corrected star-formation rates by including information from *Spitzer*/MIPS $24\,\mu$m observations. The mass-completeness of the 3D-HST catalog has been assessed by Tal et al. (2014). They determine the catalog to be roughly 90% complete above stellar masses of $10^9\,M_\odot$, $10^{9.5}\,M_\odot$ and $10^{10.5}\,M_\odot$ out to $z \lesssim 1.8$, $z \lesssim 2.5$ and $z \lesssim 3.5$, respectively. In total, 14,313 galaxies included in the 3D-HST catalog fall within the footprint of the COLDz/GOODS-N observations, within 20% of the peak primary beam sensitivity.

5.3 Methods

5.3.1 Radio Stacking

In this work we employ a stacking analysis in order to investigate the shape of the radio spectrum of typical star-forming galaxies between observed-frame $1.4 - 34$ GHz. To this end, we create small cutouts of 51×51 pixels ($25\farcs5 \times 25\farcs5$ at 34 GHz) around galaxy positions identified in optical/near-IR imaging within the various radio maps, and co-add them together to gain a census of their average radio emission. As star-forming sources are expected to be faint at high radio frequencies, a large number of sources are required to be averaged together in order to obtain a clear detection even in the stacks. This, in turn, requires co-adding sources across a relatively wide range in redshift. In this work, we therefore stack in luminosity as opposed to flux density, in order to fairly combine sources across different cosmic epochs. For a source at redshift z, with a flux density S_ν at observed-frame frequency ν, we probe a luminosity of

$$L_{\nu'} = \frac{4\pi D_L(z)^2}{1+z} S_\nu \,, \tag{5.1}$$

where $\nu' = \nu(1+z)$. However, to ensure we probe the same rest-frame frequency for all sources in a given redshift bin, we scale the flux density to probe $\overline{\nu}' = \nu(1+\overline{z})$, where $\overline{z}$ is the median redshift in the bin, prior to stacking. Since this rest-frame frequency is probed at an observed-frame frequency of $\nu(1+\overline{z})/(1+z)$ for a source at redshift z, and $S_\nu \propto \nu^\alpha$, this implies that

$$L_{\overline{\nu}'} = \frac{4\pi D_L(z)^2}{1+\overline{z}} \left(\frac{1+\overline{z}}{1+z}\right)^{1+\alpha} S_\nu \,. \tag{5.2}$$

As such, an assumption on the spectral index must be made a priori. However, given that there are by definition an equal number of sources in the redshift bin with $z > \overline{z}$ as there are with $z < \overline{z}$, any uncertainty induced as a result of this spectral scaling tends to be small. In addition, with the typical $\alpha = -0.70$ we assume (Condon 1992), the exponent $1+\alpha$ in Equation 5.2 constitutes only a relatively shallow power, further minimizing any uncertainty induced by the luminosity-stacking. We have verified that adopting any reasonable value of α between -0.30 and -1.10 does not change the corresponding stacked luminosity density within more than a few per cent.

In this work we adopt both a median and a mean-stacking analysis, for different purposes. We review the advantages and disadvantages of either method in Appendix 5.A, and briefly summarize our choice here. In Section 5.4, we set out to determine the typical radio spectrum of individually undetected star-forming galaxies. In this case, we adopt a median stacking analysis, in order to obtain a radio spectrum that is representative of the underlying galaxy population, and less susceptible to contamination from AGN.

One caveat that applies when adopting the median, however, is that its interpretation is complicated in the presence of noise. In particular, as shown by White et al. (2007), the stacked median tends to be "boosted" with respect to the true sample median when the noise in the radio maps used for stacking is similar to, or exceeds, the typical flux density of the underlying galaxy population (which a priori is unknown). We investigate the effect of median boosting by testing our stacking routine on realistically generated mock sources in Appendix 5.A, and calculate the deboosting factors required to accurately compare stacked flux densities. These correction factors are typically largest at low signal-to-noise (S/N), and may reach up to $f_{\rm boost} \approx 2$ for (simulated) low-mass galaxies at 34 GHz. Throughout this work, all quoted stacked flux densities and spectral luminosities are corrected for the effects of median boosting, unless explicitly stated otherwise.

In Section 5.5, we seek to place constraints on the cosmic star-formation history through free-free emission. In this case, we adopt a mean stacking

analysis, as we are not interested in the median star-formation rate of individual galaxies, but instead in the *total* amount of star-formation occurring in a given redshift slice. This total simply constitutes the product of the number of sources being stacked and their mean-stacked star-formation rate. A further advantage of the mean is that, compared to the median, it is straightforward to interpret, and is robust in the presence of noise, i.e., it does not require any deboosting corrections. However, in contrast, AGN contamination is more likely to affect the mean stacks. As such, we remove sources identified as likely radio AGN from the stacks in Section 5.4.

In our mean stacking approach, we need to ensure that the background level in the stacks is not significantly affected by bright neighboring galaxies. As such, we treat individually detected radio sources separately from the undetected population and stack in the residual radio images, from which all bright radio sources have been removed (following, e.g., Magnelli et al. 2015). These residual maps were created using PyBDSF (Mohan & Rafferty 2015), using the appropriate detection threshold to match that of the parent catalogs.[2] The radio-detected sources are added in a posteriori, via

$$\langle L_{\nu'} \rangle = \frac{N_{\rm undet} \times \langle L_{\nu',\rm undet} \rangle + \sum_{i=1}^{N_{\rm det}} L_{\nu',\rm det,i}}{N_{\rm undet} + N_{\rm det}} \, . \tag{5.3}$$

Here $N_{\rm det}$ ($N_{\rm undet}$) is the number of detected (undetected) radio sources used in the stacking, $L_{\nu',\rm undet}$ the stacked luminosity of the undetected sources at an average frequency ν', and $L_{\nu',\rm det,i}$ the luminosity of the $i^{\rm th}$ individually detected galaxy, at the same frequency ν'. We ensure the same rest-frame frequency ν' is probed for the stack and the detections – namely the aforementioned $\nu' = \nu(1+\overline{z})$, where $\overline{z}$ represents the median redshift across the detected and undetected sources combined – by adopting $\alpha = -0.70$ and scaling $L_{\nu'}$ accordingly. The error on the combined luminosity $\langle L_{\nu'} \rangle$ incorporates both the error on the stacked luminosity, and the uncertainty on the individually detected sources.

We perform photometry on the stacks using PyBDSF, following Algera et al. (2020a), which fits a 2D Gaussian to any significant emission in the center of the stack. We pass an estimate of both the background mean and RMS in the stacked cutout by simultaneously stacking random locations

[2] As an example, source detection in the 34 GHz radio maps was performed with a 3σ peak threshold (Algera et al. 2021), while the 3 and 10 GHz images in COSMOS used a 5σ threshold (Algera et al. 2020b).

within the radio images, which are mostly devoid of sources. Unless stated otherwise, we employ a 3σ detection threshold for the stacks. If no detection is found at this significance, a 3σ upper limit is adopted instead. When applying the median boosting corrections (Appendix 5.A), we also propagate the spread of the recovered mock source fluxes into the error on the true deboosted flux densities. This effectively takes into account variation among the input sample into the final uncertainty, with the key benefit that we do not explicitly need to perform a bootstrap analysis on the real stacks: as bootstrapping by construction involves duplicating sources within the input distribution, the error in the bootstrapped stack increases with respect to the original sample.[3] As our stacked luminosities typically have modest significance (S/N $\approx 3-5$), bootstrapping results in both an increased number of non-detections and a larger median boosting correction, and as such constitutes a suboptimal approach in the low-S/N regime. We emphasize that this procedure requires the distribution of mock sources to match the true galaxy distribution with a high accuracy, which we ensure to be the case in Appendix 5.A.

5.3.2 Radio Spectral Decomposition

The radio spectrum of star-forming galaxies is frequently modelled as the sum of two power-law processes: synchrotron and free-free emission (e.g., Condon 1992). The former has a power-law slope with a typical value of $\alpha_{\rm NT} = -0.85$ (Niklas et al. 1997; Murphy et al. 2012), though observations of high-redshift sources indicate substantial scatter ($\sigma_{\alpha_{\rm NT}} = 0.3-0.5$, Smolčić et al. 2017b; Calistro Rivera et al. 2017). Free-free emission, on the other hand, has a well-known and nearly flat spectral index of $\alpha_{\rm FF} = -0.10$ (Condon 1992; Murphy et al. 2011). The radio spectrum can therefore be written as

$$S_\nu = \left(1 - f^{\rm th}_{\nu_0}\right) S_{\nu_0} \left(\frac{\nu}{\nu_0}\right)^{\alpha_{\rm NT}} + f^{\rm th}_{\nu_0} S_{\nu_0} \left(\frac{\nu}{\nu_0}\right)^{-0.1}, \tag{5.4}$$

where the thermal fraction $f^{\rm th}_{\nu_0}$ represents the relative contribution of free-free emission to the total radio emission at observed-frame frequency ν_0 (e.g., Tabatabaei et al. 2017). In turn, the radio spectrum can be fully characterized by three parameters: $f^{\rm th}_{\nu_0}$, $\alpha_{\rm NT}$ and an overall normalization S_{ν_0}.

[3] For a large number of sources N, the RMS noise in the bootstrapped stack is larger than that in the original stack by a factor of $\sqrt{2}$.

We adopt $\nu_0 = 1.4/(1+z)$ GHz in this work, in order to directly probe rest-frame 1.4 GHz where the thermal fraction is typically defined (Condon 1992; Tabatabaei et al. 2017). We run a Monte Carlo Markov Chain (MCMC) fitting routine to determine these parameters, as well as accurate uncertainties. We adopt flat priors on $f_{\rm th}$ and S_{ν_0}, and allow unphysical negative values in order to assess whether a thermal component is preferred by the fitting. We further adopt a Gaussian prior on $\alpha_{\rm NT}$ centered on a mean value of $\mu = -0.85$, with a spread of $\sigma = 0.30$. This spread is smaller than the $\sigma = 0.50$ adopted by Algera et al. (2021), as they model the radio spectra of individual sources, whereas in this work we consider only stacked radio spectra. For a stacked sample of sources, the average synchrotron slope is expected to regress towards the typical value of $\alpha_{\rm NT} \approx -0.85$, justifying the assumption of a narrower prior. For further details on the spectral fitting routine, we refer the reader to Algera et al. (2021).

Throughout this work, we compare our results with a simple but widely used model for the radio spectrum, namely that of prototypical starburst galaxy M82. M82 has a star-formation rate of SFR $\sim 10 - 20\,M_{\odot}\,{\rm yr}^{-1}$ (Förster Schreiber et al. 2003), which is similar to the typical SFRs of the galaxy population analyzed in this work (Section 5.5.1). The radio spectrum of M82 can be well described by a combination of free-free and synchrotron emission (Condon 1992), and as such forms the natural comparison to our high-redshift galaxy sample. We will in the following refer to an "M82-like" model for the radio spectrum as having a thermal fraction of $f_{\rm th}(1.4\,{\rm GHz}) = 0.1$ (Condon 1992), and a synchrotron spectral index of $\alpha_{\rm NT} = -0.85$ (Niklas et al. 1997; Murphy et al. 2012). While more complex forms of the radio spectrum – in particular in very luminous starburst galaxies – have been observed (e.g., Galvin et al. 2018), the M82-like model remains the most commonly assumed shape of the radio spectrum in the absence of wide multi-frequency radio coverage (e.g., Delhaize et al. 2017; Murphy et al. 2017; Tabatabaei et al. 2017; Klein et al. 2018; Penney et al. 2020; Algera et al. 2021).

5.4 Results

5.4.1 The Typical Radio Spectrum of Radio-selected Galaxies

Historically, radio surveys have predominantly been undertaken at low frequencies, where sources tend to be brighter and the field of view is large.

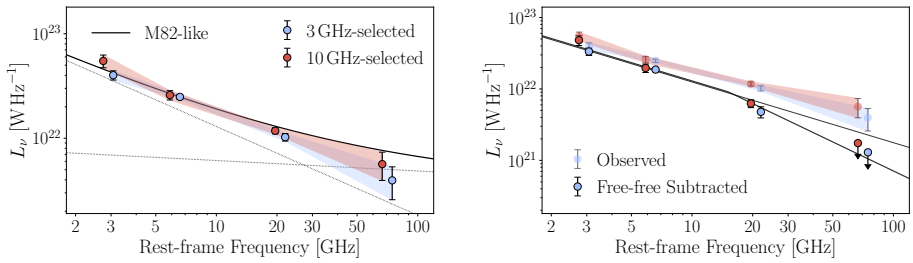

Figure 5.1: Left: The stacked radio spectrum for 53 (29) galaxies selected at 3 GHz (10 GHz) in COSMOS, spanning observed-frame $1.4 - 34$ GHz (rest-frame $2.7 - 75$ GHz). Compared to the M82 model for the radio spectrum normalized at 3 GHz (black line; the grey lines represent synchrotron and free-free emission), the luminosity densities steepen by a factor of $\sim 1.5 - 2\times$ at $\nu \sim 70$ GHz. At this frequency, the radio luminosity density is consistent with being solely due to free-free emission. **Right:** The same radio spectrum as in the left panel, now with the M82-like free-free component subtracted. The upper limits at observed-frame 34 GHz are 2σ, and arise because the radio luminosity remaining after subtraction of the free-free spectrum is consistent with zero within 1σ. The solid black line represents a steepened synchrotron spectrum, with a putative spectral break placed at rest-frame $\nu_b = 15$ GHz.

As a result, the nature of the high-frequency radio spectrum of distant star-forming galaxies remains poorly constrained. In order to assess the typical shape of the high-frequency radio spectrum of radio-selected galaxies, we employ a median stacking analysis on the 3- and 10 GHz positions of faint star-forming galaxies detected in the COSMOS-XS survey. The 3 GHz selected sample, which is based on slightly deeper data, comprises 53 sources, while the 10 GHz selected stack includes 29 galaxies (which are all individually detected at 3 GHz). The galaxies span a redshift range of $0.3 < z < 3.6$, although the 3 GHz selected sample lies at a slightly higher redshift of $\overline{z} \approx 1.2$ compared to the median redshift of $\overline{z} \approx 1.0$ for the 10 GHz selected sample.[4] the median stellar mass of both samples equals $M_\star \approx 10^{10.5}\,M_\odot$. Prior to stacking, radio AGN were explicitly removed from both samples. These AGN were identified by Algera et al. (2020b) as sources that are offset by more than 2.5σ from the high-redshift far-infrared/radio correlation from Delhaize et al. (2017). While radio-quiet AGN are as such not explicitly removed from this sample, these tend to show radio emission similar to the star-forming population (Delvecchio

[4]A single galaxy at $z = 5.3$ was excluded, as due its high-redshift nature the 34 GHz observations are likely probing dust emission; see Algera et al. (2021).

et al. 2017; Algera et al. 2020a,b). Additionally, the fraction of radio-quiet AGN decreases strongly towards faint radio flux densities (Smolčić et al. 2017a; Algera et al. 2020b), thereby making it unlikely that such AGN significantly bias our analysis.

The median stacked radio spectra are shown in the left panel of Figure 5.1. We further compare these spectra to an M82-like radio spectrum, which we normalize to our highest S/N measurement at 3 GHz. This therefore allows for a direct comparison of the observed high-frequency radio emission with the typically assumed shape for the radio SED.

The 10 GHz and 3 GHz selected samples show little variation in their average stacked spectra: in both cases the $3 - 10$ GHz spectral index is in agreement with the value expected from the M82-like SED. At higher-frequencies, however, the stacked $10 - 34$ GHz spectral index appears to steepen in comparison to this model radio spectrum. At the rest-frame frequencies probed by the 34 GHz observations, the model radio spectrum overpredicts the stacked luminosity density by a factor of $1.9^{+1.0}_{-0.5}$ and $1.3^{+0.6}_{-0.3}$ for the 3 GHz and 10 GHz selected samples, respectively. As a result, a simple extrapolation of an M82-like SED may not be valid for radio-detected high-redshift star-forming galaxies beyond $\nu' \approx 20$ GHz, and the typical radio spectrum may instead steepen by a typical factor of $\sim 1.7^{+0.6}_{-0.3}$ out to $\nu' \approx 70$ GHz. At this frequency, the remaining radio luminosity is consistent with being solely due to radio free-free emission, indicative of a deficit in high-frequency synchrotron emission. This, in turn, may be due to spectral steepening of the synchrotron spectrum.

If we suppose that the free-free component is well described by the M82 model normalized at 3 GHz, we may subtract it from the measured radio luminosities in order to highlight the remaining synchrotron contribution. Assuming that the synchrotron emission steepens by $\Delta\alpha = -0.5$ beyond a break frequency ν_b, as in the standard synchrotron ageing model (Kardashev 1962), we require that $\nu_b \lesssim 20$ GHz in order to match the observed radio luminosities at observed-frame 34 GHz. While we cannot currently fit the radio spectrum with a break due to insufficient sampling of the radio SED, a putative spectral break at 15 GHz constitutes a natural explanation for the high-frequency flux deficit (Figure 5.1; right panel). We discuss this possibility further in Section 5.5.2.

5.4.2 Free-free Emission in Optically-selected Galaxies

We next set out to constrain the average radio spectrum of representative star-forming galaxies, which are typically not individually detected even

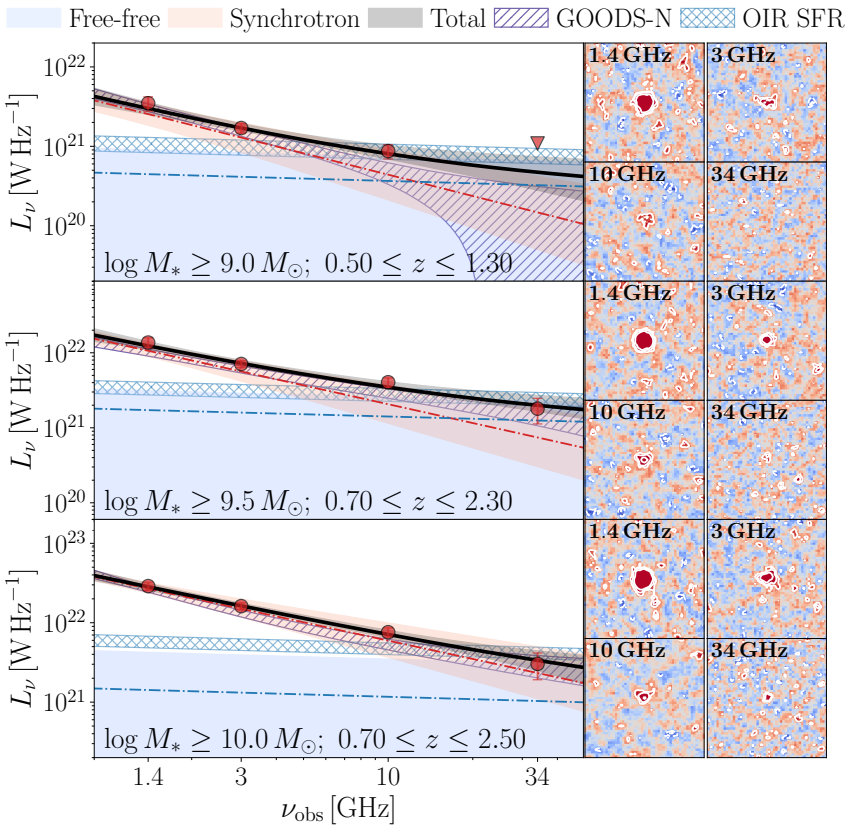

Figure 5.2: Median-stacked radio spectra (left) and stacked cutouts (51×51 pixels; right) in the COSMOS field, for the three different mass-complete bins highlighted in Table 5.1. The blue and red shaded regions in the radio spectra show the 1σ confidence intervals on the fitted free-free and synchrotron emission, respectively. The black line and grey shading comprises the total fitted emission, and the hatched blue region represents the predicted free-free luminosity given the typical SFR derived from the optical/infrared data for the galaxies. The purple hatched region represents the best fit to the stacked radio spectrum in GOODS-N (Figure 5.3), and is shown to allow direct visual comparison of the fields. In the stacks, contours are shown at the $\pm 2, \pm 3$ and $\pm 5\sigma$ levels, where σ is the RMS in the stack. Negative contours are indicated via dashed lines, and the color scale runs from -3σ to $+3\sigma$. High-frequency radio emission at 34 GHz is detected in two out of three bins, at a significance of 3.5σ and 3.9σ.

in deep radio observations. In COSMOS, we adopt prior galaxy positions from the COSMOS2015 catalog and remove all galaxies within $0\farcs9$ that are identified as radio AGN in the COSMOS-XS survey (Algera et al. 2020b).

Table 5.1: Mass-complete bins constructed from the COSMOS2015 and 3D-HST catalogs.

Bin	z_1	z_2	$\overline{z}$	$>\log M_\star$	$\langle\log M_\star\rangle$	$N_{\rm COS}$	$N_{\rm GN}$
M-low	0.5	1.3	0.92	9.0	9.5	122	440 (638)
M-med	0.7	2.3	1.36	9.5	9.9	113	360 (546)
M-high	0.7	2.5	1.38	10.0	10.3	57	157 (245)

Note. — (1) Bin identifier; (2), (3), (4) Lower, upper and median redshift of the bin, combining both fields; (5), (6) Minimum and median stellar mass; (7), (8) Number of sources in the bin in COSMOS and GOODS-N (combining the 10 & 34 GHz areas; $N_{\rm GN}$ within the full COLDz field of view is included in parentheses).

We additionally ensure the remaining galaxies are star-forming based on their position in the NUV $-$ r, $r-J$ color-color diagram, following Ilbert et al. (2013).

In the GOODS-N field, we adopt prior positions from the 3D-HST catalog. We limit ourselves to the area where the 10 GHz observations from Murphy et al. (2017) and the COLDz 34 GHz continuum data overlap, and perform the stacking analysis at four frequencies (1.4, 5, 10 and 34 GHz). For the majority of the radio-detected population in GOODS-N, however, there is no available information on whether the radio emission is likely originating from star-formation or from an AGN. In order to still exclude radio AGN, we adopt the results from the COSMOS-XS survey (Algera et al. 2020b). They find that, at $S_3 \approx 30\,\mu$Jy, the radio population consists of $\gtrsim 90\%$ star-forming galaxies, which corresponds to a flux density at 1.4 GHz of $S_{1.4} \approx 50\,\mu$Jy given $\alpha = -0.70$. In order to minimize any bias arising from AGN contamination, we therefore exclude all 3D-HST detections with a radio counterpart from Owen (2018) in excess of $S_{1.4} = 50\,\mu$Jy from our stacking analysis. Given that we are employing a median stacking analysis, any residual contamination from AGN is unlikely to significantly affect our results. We additionally ensure the remaining galaxies are star-forming based on their position in the UVJ-diagram (e.g., Williams et al. 2009), adopting the rest-frame magnitudes provided by Skelton et al.

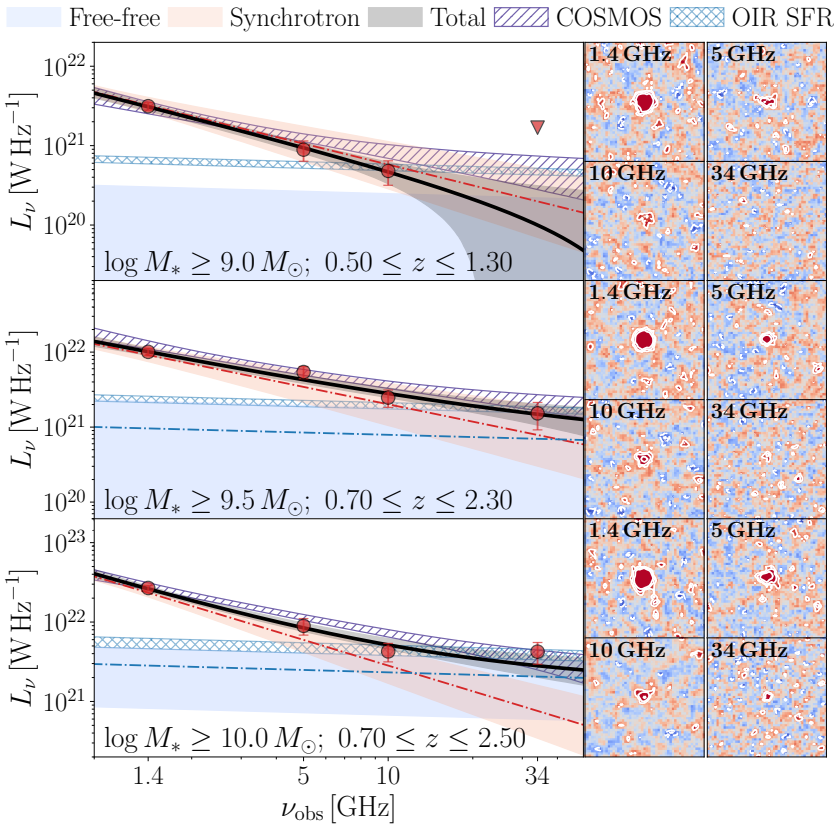

Figure 5.3: Similar to Figure 5.2, now showing the median-stacked radio spectra (left) and stacked cutouts (right) in mass-complete bins across the GOODS-N field. We detect stacked 34 GHz continuum emission in two out of three bins, at a significance of 3.0σ and 3.8σ.

(2014).

We subsequently divide the galaxies into three wide, mass-complete redshift bins, removing all sources for which the cutout does not fully lie within the COLDz footprint. The low ($> 10^9\,\mathrm{M}_\odot$), medium ($> 10^{9.5}\,\mathrm{M}_\odot$) and high-mass ($> 10^{10}\,\mathrm{M}_\odot$) bins (henceforth referred to as $M-$low, $M-$med and $M-$high, respectively) extend to the maximum redshift where both the COSMOS2015 and 3D-HST catalogs are complete. This, in turn, allows for a direct comparison of the results across both fields in Section 5.5. The precise binning we adopt and the number of sources per bin are given in Table 5.1. We note that the bins partially overlap in redshift, and are therefore not fully independent of one another. However, in order to obtain a stacked high-frequency detection at sufficient S/N, adopting wide bins is

essential.

We show the median stacked cutouts and the corresponding multi-frequency radio spectra for the COSMOS and GOODS-N fields in Figures 5.2 and 5.3, respectively. In COSMOS, we detect the stacked 34 GHz continuum emission at 3.9σ and 3.5σ significance in bins M-med and M-high, respectively, while for bin M-low we can only place a 3σ upper limit. In the GOODS-N field, we detect stacked 34 GHz emission at 3.0σ and 3.8σ significance in bins M-med and M-high, respectively, while similarly no significant emission is detected in M-low. The stacked luminosities in COSMOS and GOODS-N, as well as the adopted deboosting factors, are presented in Table 5.3 in the Appendix. The values for both fields are in good agreement, verifying that similar galaxy populations are probed in COSMOS and GOODS-N.

We additionally show the free-free luminosity expected from star formation in Figures 5.2 and 5.3, and compare this to the stacked luminosity density at 34 GHz. We adopt the star-formation rates derived from spectral energy distribution fitting of optical/infrared (OIR) data from the COSMOS2015 and 3D-HST catalogs by Laigle et al. (2016) and Momcheva et al. (2016), respectively, which account for a potential contribution from dust-obscured star formation via deep *Spitzer*/MIPS $24\,mu$m observations. We subsequently convert the OIR SFRs to an expected free-free luminosity via the conversion from Murphy et al. (2012), adapted for a Chabrier (2003) IMF. We then calculate the OIR-predicted thermal fraction as $f_{\rm th}^{\rm pred}\,(34\,{\rm GHz}) = \langle L_{34}^{\rm SFR}\rangle / L_{34}^{\rm obs}$, that is, as the ratio of the expected free-free luminosity and the observed 34 GHz luminosity. Following this procedure, we predict OIR thermal fractions of $f_{\rm th}^{\rm pred} \approx 1.2^{+0.8}_{-0.4}$ for the two COSMOS bins in which we detect 34-GHz emission, and can further place a lower limit of $f_{\rm th}^{\rm pred} \gtrsim 0.7$ for the lower-mass bin.[5]

In the GOODS-N field, we predict thermal fractions of $f_{\rm th}^{\rm pred} = 1.0^{+0.4}_{-0.2}$ and $f_{\rm th}^{\rm pred} = 0.8^{+0.4}_{-0.2}$ for bins M-med and M-high, respectively. As such, based on a comparison with the optical-infrared star formation rates, we expect the observed luminosity at 34 GHz to be dominated by free-free emission. We discuss this further in Section 5.5.1, where we analyze the two fields jointly.

[5]While in practice the thermal fraction evidently cannot exceed unity, we here quote the formal errors on the OIR predicted value which combines the uncertainty on $\langle L_{34}\rangle$ and the spread on the OIR SFRs.

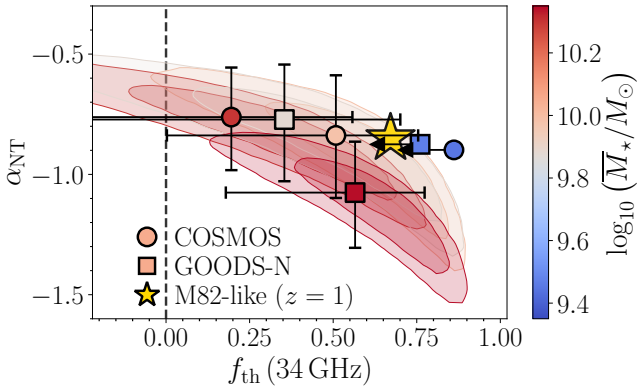

Figure 5.4: Synchrotron spectral index versus thermal fraction at observed-frame 34 GHz for the COSMOS (circles) and GOODS-N (squares) median stacks. Points are colored by their median stellar mass, and the 34 GHz thermal fraction and synchrotron slope for an M82-like radio spectrum at $z = 1$ is indicated via the yellow star. The shaded contours represent the 1σ (dark) and 2σ (light) confidence intervals on the spectral parameters, which are somewhat degenerate at this low S/N. In case of a non-detection at 34 GHz, we place an upper limit on the thermal fraction at the median $\alpha_{\rm NT}$ comprising 84% of the sampled values for $f_{\rm th}$ (equivalent to a 1σ upper limit). The recovered thermal fractions are a factor of $\sim 1.5 - 2$ lower than predicted from an M82-like radio spectrum.

5.5 Discussion

5.5.1 Radio Star-formation Rates

In the previous Sections, we sampled the radio spectrum of star-forming galaxies in COSMOS and GOODS-N through a multi-frequency stacking technique. We now jointly analyze the results across these fields, and investigate the nature of synchrotron and free-free emission in faint star-forming galaxies.

At rest-frame frequencies $\nu \gtrsim 30$ GHz, radio free-free emission is expected to dominate the radio spectrum (e.g., Condon 1992; Klein et al. 2018). To test this, we decompose the stacked multi-frequency radio spectra in COSMOS and GOODS-N into their synchrotron and free-free components, using the fitting routine outlined in Section 5.3. The decomposed radio spectra are shown in Figures 5.2 and 5.3, and the resulting fitted synchrotron spectral indices $\alpha_{\rm NT}$ and thermal fractions $f_{\rm th}$ are shown in Figure 5.4 and additionally tabulated in Table 5.3. At typical rest-frame

frequencies of $\nu' \approx 60 - 80$ GHz, we recover relatively low thermal fractions of $f_{\rm th} \approx 0.2 - 0.5$. For comparison, a simple extrapolation of the M82 radio SED predicts a thermal fraction of $f_{\rm th} \approx 0.7$ in this frequency regime, while the OIR predicted thermal fractions imply even larger values of $f_{\rm th} \approx 0.8 - 1$. Accordingly, the fitted thermal fractions appear to be a factor of $\sim 1.5 - 2$ lower than expected. In addition, in four out of the six bins, the thermal fraction at 34 GHz is consistent with zero within 1σ. In these bins, the combined fit to the radio spectrum is in turn primarily composed of the power-law synchrotron component.

We proceed by determining synchrotron and free-free star-formation rates from the stacked radio luminosities. In each of the mass-complete bins, we have a clear stacked detection at 1.4 and 3 or 5 GHz. We adopt the corresponding spectral index $\alpha_{3/5}^{1.4}$ in order to calculate the K-corrected luminosity density at rest-frame 1.4 GHz, which is the conventional normalization frequency of the far-infrared/radio correlation. We then adopt the recent mass-dependent parameterization of the far-infrared/radio correlation from Delvecchio et al. (2021) to calculate radio star formation rates, which we compare with the OIR SFRs in the left panel of Figure 5.5. The COSMOS and GOODS-N galaxy samples span a similar range of star formation rates, ranging from SFR $\approx 3 - 30\,M_{\odot}$ yr^{-1} in the low and high mass bins, respectively. The synchrotron SFRs correlate well with the optical-IR SFRs, supporting the robustness of our stacking analysis. However, we find the synchrotron SFRs to be slightly lower than the optical SFRs by an average of -0.13 dex (scatter of 0.08 dex). This may be related to the uncertain nature of far-infrared/radio correlation in low-mass galaxies at high redshift, as these are typically not individually detected even in deep radio imaging. Nevertheless, the offset in SFRs falls within the typical scatter of the local far-infrared/radio correlation of $0.17 - 0.26$ dex (Bell 2003; Molnár et al. 2021), and as such, we conclude that the radio and optical-IR SFRs are in reasonable agreement.

We additionally present the free-free star-formation rates, adopting the fitted thermal fractions (Figure 5.5; left panel). As expected from the low thermal fractions, the free-free SFRs tend to be significantly lower than the optical-infrared SFRs, although the individual uncertainties on the former are large. We discuss this apparent deficit of high-frequency radio emission in Section 5.5.2. However, it is interesting to additionally consider the free-free star formation rates we would infer when assuming a simple default value for the thermal fraction, as one may do when no multi-frequency radio data are available for a spectral decomposition. Upon adopting an

M82-like starburst model ($f_{\rm th} \sim 0.7$) we find good agreement between the synchrotron and free-free star-formation rates (Figure 5.5; right panel). This, in turn, indicates that the true thermal fraction exceeds the values derived from the spectral decomposition.

While free-free and synchrotron emission trace star formation on different timescales, our stacking analysis ensures we average across the star-formation histories of our galaxy sample. In turn, we can assume the free-free and synchrotron star-formation rates equal one another, and use this to determine the thermal fraction via $\mathrm{SFR}_{\rm FFE}\,(f_{\rm th} = 1) = f_{\rm th} \times \mathrm{SFR}_{1.4\,\rm GHz}$. A linear fit through the SFRs in Figure 5.5 (right panel) results in a thermal fraction of $f_{\rm th} = 0.84^{+0.23}_{-0.18}$ at observed-frame 34 GHz. This is consistent with the expected thermal fraction from an M82-like radio spectrum at $z = 1$, which predicts $f_{\rm th} \approx 0.70$ at observed-frame 34 GHz. While we probe slightly different rest-frame frequencies across the bins (Table 5.1), the variation in the thermal fraction of an M82-like SED between $z = 0.9$ and $z = 1.4$ – the typical redshift of bins M-low and M-high – is only $\Delta f_{\rm th} \approx 0.04$, well within the errors of our fitted thermal fraction.

While our fitting routine prefers relatively low thermal fractions at 34 GHz, resulting in low free-free SFRs, the above analysis indicates that a typical thermal fraction of $f_{\rm th} = 0.7 - 1.0$ produces SFRs that are in better agreement with SFRs derived from synchrotron emission and optical-infrared SED-fitting. We discuss this finding in detail in the following Section.

5.5.2 A Lack of High-frequency Emission

In Section 5.4.1 we identify a deficit of high-frequency radio emission in the typical spectrum of radio-selected galaxies with respect to M82, and in Section 5.5.1 we similarly find that the typical thermal fractions of mostly radio-undetected star-forming galaxies range between $f_{\rm th} \approx 0.2 - 0.5$ at 34 GHz. At this frequency, we probe a typical rest-frame frequency of $\nu' \approx 60 - 80$ GHz, where a simple extrapolation of the M82 radio SED predicts typical thermal fractions of $f_{\rm th} \approx 0.7$. Upon adopting the fitted thermal fractions, we determine free-free star-formation rates that are systematically lower than estimated from more established tracers, and also lower than the predicted thermal fractions based on optical-infrared SFRs (Section 5.4.2). However, instead adopting a canonical M82-like value for the thermal fraction ensures the various SFRs are in agreement. This apparent lack of high-frequency radio emission can arise in two possible ways. It is possible that the faint, star-forming population may be deficient in high-frequency free-free emission. Alternatively, this population may lack high-

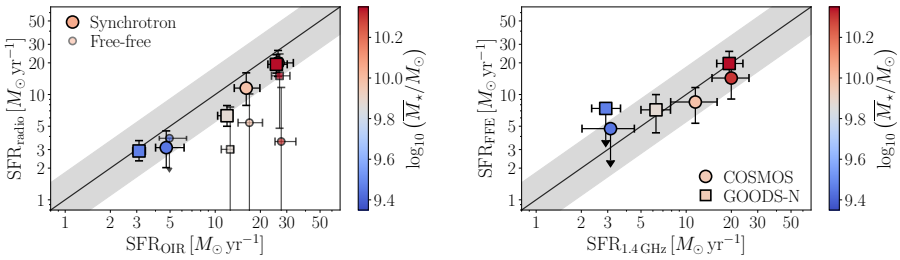

Figure 5.5: Left: Comparison of the radio-based star-formation rates and those from SED-fitting in the COSMOS (circles) and GOODS-N (squares) fields. The grey shading indicates the scatter about the local far-infrared/radio correlation from Bell (2003). While the synchrotron star-formation rates are in reasonable agreement with the optical-IR SFRs, the free-free SFRs are significantly lower when the fitted thermal fractions are adopted. **Right:** Comparison of the radio and free-free star-formation rates when an M82-like SED (thermal fraction of $f_{\mathrm{th}}(34\,\mathrm{GHz}) \approx 0.7$) is assumed. Given this thermal fraction, the radio-based SFRs are in excellent agreement.

frequency synchrotron emission, which is indicative of a more complex radio spectrum than the canonical M82 starburst model. In what follows, we discuss both of these possibilities.

A Lack of Free-Free Emission

First, we discuss our findings in light of a deficit of high-frequency free-free emission. The simplest explanation of such a deficit requires a non-negligible optical depth of free-free emission, τ_ν^{FF}, at the frequencies probed. However, given the strong frequency dependence of $\tau_\nu^{\mathrm{FF}} \propto \nu^{-2.1}$, free-free emission is certainly optically thin at observed-frame 34 GHz. Alternatively, the low radio frequencies could be affected by free-free absorption. In this regime, the radio spectrum is dominated by synchrotron emission, and hence any significant free-free absorption should give rise to shallower synchrotron spectra. This, in turn, may cause the high-frequency radio spectrum, where free-free absorption does not play a role, to be steeper relative to the low frequencies where the optical depth is not negligible, throwing off the spectral fitting.

This interpretation, however, appears unlikely as we find typical synchrotron slopes ($\alpha_{\mathrm{NT}} \sim -0.85$) for our stacks, while any free-free absorption should flatten this value. In addition, optical depth effects are generally limited to $\nu \ll 1\,\mathrm{GHz}$ for modestly star-forming galaxies (Condon

1992), as probed in this work. Even for brighter star-forming galaxies, such as the local (U)LIRGs studied by Murphy (2013), the typical frequency at which the spectrum turns over is $\nu \sim 1\,\mathrm{GHz}$. In addition, bright $z \sim 2$ submillimeter-detected starbursts show typical radio spectra of $\alpha \sim -0.80$ between observed-frame frequencies of $610\,\mathrm{MHz} - 1.4\,\mathrm{GHz}$ (roughly probing rest-frame $2 - 5\,\mathrm{GHz}$; Ibar et al. 2010; Thomson et al. 2014; Algera et al. 2020a), and hence do not show any evidence for spectral flattening due to free-free absorption. Using sensitive 150 MHz observations of high-redshift starbursts, Ramasawmy et al. (2021) further find that free-free absorption is typically limited to rest-frame frequencies $\nu \lesssim 1\,\mathrm{GHz}$. Given that we probe more modestly star-forming galaxies in this work ($\mathrm{SFR}_{1.4\,\mathrm{GHz}} \approx 3 - 30\,M_{\odot}\,\mathrm{yr}^{-1}$) at rest-frame frequencies $\nu \geqslant 2\,\mathrm{GHz}$, we conclude that free-free absorption is unlikely to significantly affect the frequencies sampled in this work, and as such the low-frequency radio spectra should be well-described by a combination of power-law free-free and synchrotron emission.

The low fitted thermal fractions could alternatively point towards a synchrotron excess in galaxies. For example, Murphy (2013) determine a typical thermal fraction of $f_{\mathrm{th}}(1.4\,\mathrm{GHz}) \approx 0.05$ for a sample of 31 local ULIRGs, which is lower than the canonical M82-like value. They interpret this through dynamical effects, whereby merging systems form synchrotron bridges between the individual galaxies (see also Condon et al. 1993). While not reducing a galaxy's free-free luminosity, such a synchrotron excess naturally results in lower thermal fractions. However, while the local ULIRG population tends to be dominated by merging systems (e.g., Armus et al. 1987), less than 10% of galaxies on the $z \lesssim 2$ star-formation main-sequence (Brinchmann et al. 2004; Noeske et al. 2007) appear to be major mergers (e.g., López-Sanjuan et al. 2009; Ventou et al. 2017; Cibinel et al. 2019). In addition, a comparison of synchrotron star-formation rates with those from SED-fitting (Section 5.5.1) does not show any evidence for a synchrotron excess. As such, we disfavor the scenario whereby the low thermal fractions are the result of an excess in synchrotron emission.

Alternatively, a deficit of free-free emission may arise when Lyman continuum photons are absorbed by dust still within the star-forming regions (Inoue et al. 2001; Dopita et al. 2003), or instead when a significant fraction of ionizing photons leaks out of the regions (see also Querejeta et al. 2019). However, in local modestly star-forming galaxies, free-free emission is observed to correlate well with dust-corrected SFRs from Hα and $24\,\mu$m emission (Tabatabaei et al. 2017). At high redshift, Murphy et al.

(2017) determine typical thermal fractions based on $1.4 - 10$ GHz spectral indices that are consistent with the expected level of free-free emission from an M82-like radio spectrum. Similarly, Algera et al. (2021) determine free-free star-formation rates for a 34 GHz selected sample that are in good agreement with those from synchrotron emission and SED-fitting. Moreover, while free-free emission is only affected by dust attenuation within HII-regions, SFR tracers using ionized gas at shorter wavelengths, such as the Balmer lines, should be affected by dust attenuation throughout the entire galaxy. However, with the possible exception of highly dust-obscured starbursts (Chen et al. 2020), the Balmer lines have been shown to agree both with panchromatic SFRs derived via SED-fitting (Shivaei et al. 2016) and SFRs from radio synchrotron emission (Duncan et al. 2020) at $z \sim 2$. Given that free-free emission is less affected by dust than Hα, it seems unlikely that high-redshift galaxies with modest star-formation rates exhibit a systematic deficit of free-free emission.

A Lack of Synchrotron Emission

The observed lack of high-frequency emission may instead be due to a deficit of synchrotron emission at 34 GHz. This is supported by the fact that in all stacks the observed-frame 34 GHz luminosities are in good agreement with the free-free luminosities predicted based on optical-infrared star formation rates. This, therefore, is indicative of a large thermal contribution, and hence a lack of synchrotron emission. A high-frequency deficit of synchrotron emission is most readily interpreted as synchrotron ageing: high-energy cosmic rays, which emit predominantly at high frequencies, are the first to radiate their energy via synchrotron emission. Such synchrotron cooling has been invoked to explain steep synchrotron spectra in local spiral galaxies (Tabatabaei et al. 2017), as well as spectral steepening in bright starbursts, both locally (e.g., Colbert et al. 1994; Clemens et al. 2008) and at high redshift (Thomson et al. 2019).

As this work investigates the radio spectra of faint star-forming galaxies, we are limited by both the signal-to-noise ratio at high-frequencies, and by the sampling of the radio SED at four distinct frequencies across both the COSMOS and GOODS-N fields. This, in turn, makes it difficult to fit a more complex prescription of the radio spectrum to the available photometry. However, we may improve the sampling of our spectra by combining the available radio data across COSMOS and GOODS-N. Given that we adopt identical mass-complete bins in both fields, we expect to trace the same underlying galaxy population. This is additionally supported by the

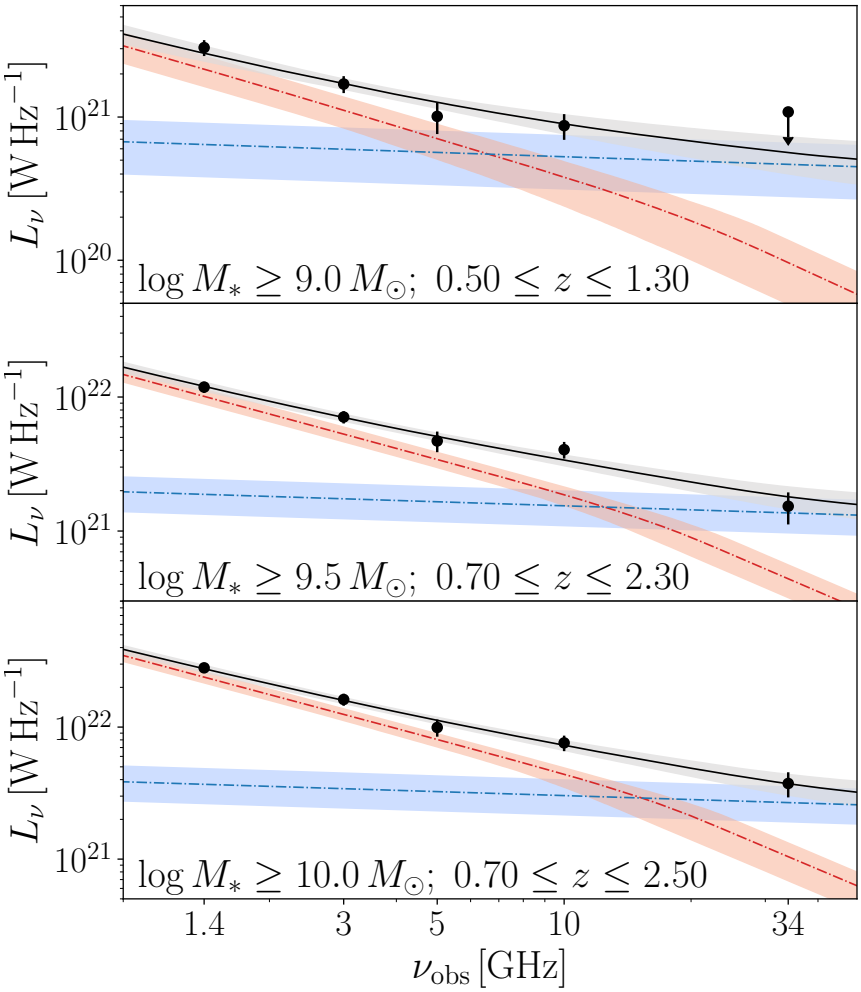

Figure 5.6: Stacked radio spectra, combining the photometry across the COSMOS and GOODS-N fields (Figures 5.2 and 5.3) to sample the radio spectrum at five distinct frequencies. This additional constraint enables fitting the combined spectrum (grey) with a model of free-free emission (blue) and synchrotron emission including a break (red). In contrast to the fits that do not incorporate a break, we now find that the observed-frame 34 GHz luminosity is likely dominated by free-free emission.

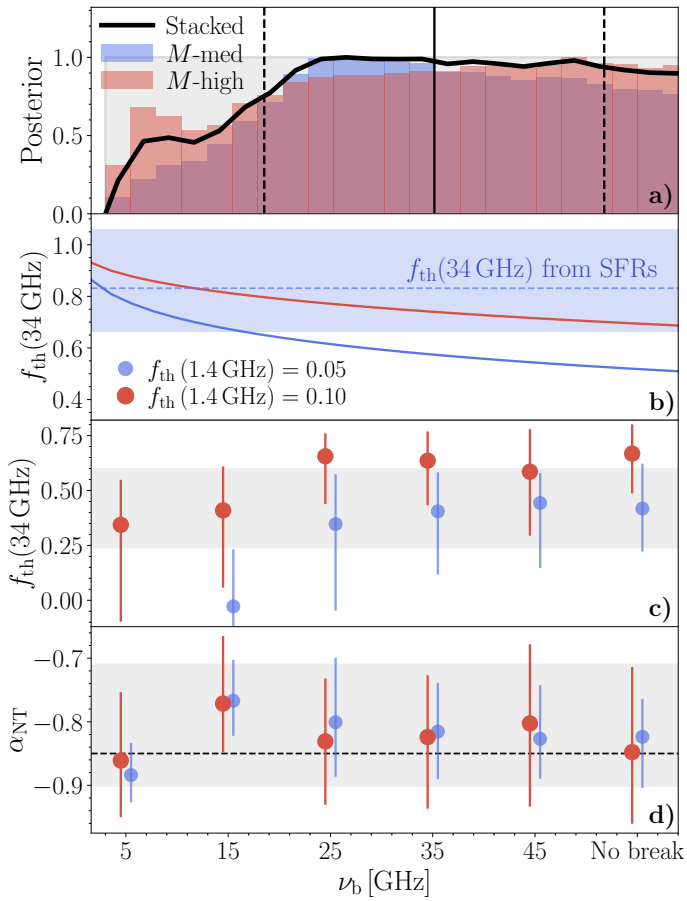

Figure 5.7: A quantitative test of synchrotron ageing in the radio spectra of typical high-redshift star-forming galaxies. **a)** Posterior distributions of the break frequency ν_b in bins M-med and M-high, obtained after explicitly including a spectral break in the fitting. The combined posterior is shown through the solid black line, while the prior is shown through the grey rectangle. The solid and dashed vertical lines indicate the median and $16-84^{\rm th}$ percentiles from the combined posterior, respectively. High break frequencies $\nu_b \gtrsim 15$ GHz are favored by the fitting routine. **b)** The 34 GHz thermal fraction as a function of ν_b for an M82-like spectrum at $z = 1$, given a 1.4 GHz thermal fraction of 10% (as in M82; red line) and 5% (as in Murphy 2013; blue line). The shaded blue region shows the expected thermal fraction based on the stacked synchrotron SFRs. A 5% thermal fraction at 1.4 GHz requires the existence of a low-frequency break ($\nu_b \lesssim 20$ GHz) in order to match the measured $f_{\rm th}(34\,{\rm GHz})$. This, however, is disfavored by the posterior in panel a). **c) & d)** Illustration of the biases induced when fitting complex spectra with a simple model. The recovered thermal fractions (c) and synchrotron spectral indices (d), obtained from fitting simulated radio spectra, are shown as a function of break frequency. The colored points indicate the median recovered value among the simulations, given an input thermal fraction at rest-frame 1.4 GHz, and the 16-84 percentile spread. The grey bands indicate the observed range of 34 GHz thermal fractions and synchrotron slopes when fitting the combined COSMOS and GOODS-N stacks with our model in Equation 5.4. A break in the radio spectrum is plausible when the observed and simulated spread among both $f_{\rm th}$ and $\alpha_{\rm NT}$ are similar, though the latter parameter does not provide meaningful constraints. A combination of either $f_{\rm th}(1.4\,{\rm GHz}) = 0.05$ and $\nu_b \gtrsim 30$ GHz or $f_{\rm th}(1.4\,{\rm GHz}) = 0.10$ and $15\,{\rm GHz} \lesssim \nu_b \lesssim 25\,{\rm GHz}$ provides a reasonable match between simulations and observations. Upon combining the constraints across the four panels, we qualitatively infer that the radio spectrum of star-forming galaxies can be characterized by a typical thermal fraction ($f_{\rm th}(1.4\,{\rm GHz}) \sim 0.10$) and a spectral break at $\nu_b \sim 15-25$ GHz.

measured radio luminosities across both fields, which are in good agreement. In what follows, we combine the spectra shown in Figures 5.2 and 5.3 by averaging the radio luminosities at 1.4 and 34 GHz across both fields. We additionally adopt the available 3 and 10 GHz radio luminosities from the COSMOS field, and the stacked 5 GHz luminosity in GOODS-N.[6] As such, combining the two fields amalgamates radio continuum data across five frequencies within 1.4 - 34 GHz.

We first re-fit the combined radio spectra with our simple model of free-free and synchrotron emission (Equation 5.4). In the two bins with a stacked detection at 34 GHz, M-med and M-high, we determine thermal fractions of $f_{\rm th}(34\,{\rm GHz}) = 0.26^{+0.32}_{-0.55}$ and $0.44^{+0.22}_{-0.35}$, respectively. These values are consistent with the thermal fractions determined for the COSMOS and GOODS-N fields individually, and are hence lower than expected from an M82-like spectrum. However, as the combined spectra span five frequencies, we can attempt to fit a more complex model to the available photometry, incorporating spectral ageing. We adopt the standard synchrotron ageing model whereby the non-thermal spectral index steepens to $\alpha_{\rm NT} - 0.5$ beyond a break frequency ν_b (Kardashev 1962). We note that this model is a simplification, and assumes the galaxy star-formation histories may be characterized by a single burst of star formation. However, more complicated continuous star-formation histories induce similar spectral behavior (Thomson et al. 2019; Algera et al. 2020a). The resulting functional form of the radio spectrum may be written as

$$S_\nu = \begin{cases} S_{\nu_0}\left[\left(1 - f^{\rm th}_{\nu_0}\right)\left(\frac{\nu}{\nu_0}\right)^{\alpha_{\rm NT}} + f^{\rm th}_{\nu_0}\left(\frac{\nu}{\nu_0}\right)^{-0.1}\right] & \nu \leqslant \nu_b \\ S_{\nu_b}\left[\left(1 - f^{\rm th}_{\nu_b}\right)\left(\frac{\nu}{\nu_b}\right)^{\alpha_{\rm NT}-0.5} + f^{\rm th}_{\nu_b}\left(\frac{\nu}{\nu_b}\right)^{-0.1}\right] & \nu > \nu_b \end{cases} \tag{5.5}$$

where the various parameters have the same meaning as in Equation 5.4, and $\nu_b > \nu_0$ is assumed. The modest S/N of our high-frequency data does not allow us to freely vary all parameters in the fitting. In what follows, we therefore adopt a fixed $\alpha_{\rm NT} = -0.85$. As before, we assume a flat prior on the thermal fraction and overall normalization, and in addition we now adopt a flat prior on the break frequency of $\nu_b \in [3, 60]$ GHz. This range was adopted to constrain the break frequency within the typical range of rest-frame frequencies sampled by our stacks at $z \sim 0.8 - 1.5$. We show

[6] By not including the 10 GHz data in GOODS-N, we are able to stack in the full 34 GHz footprint, thereby improving our high-frequency S/N.

the radio stacks combining the COSMOS and GOODS-N fields and their decomposition into free-free and (steepened) synchrotron emission in Figure 5.6.

In the bins with a stacked 34 GHz detection, M-med and M-high, we find typical break frequencies of, respectively, $\nu_b = 35^{+16}_{-15}$ GHz and $\nu_b = 35^{+17}_{-19}$ GHz. In addition, we recover thermal fractions of $f_{\rm th}(1.4\,{\rm GHz}) = 0.09 \pm 0.03$ and $f_{\rm th}(1.4\,{\rm GHz}) = 0.07^{+0.03}_{-0.02}$ for the two bins, in agreement with the canonically assumed thermal fraction of M82. However, given that we place a flat prior on the break frequency, we would expect that when the break does not significantly affect the fitting, we recover our prior distribution, and hence a fitted spectral break around the average frequency of $\nu_b \sim 30$ GHz. To investigate whether this is indeed the case, we show the individual and combined posterior distributions on the break frequency in bins M-med and M-high in the upper panel of Figure 5.7. A break at low frequencies ($\nu_b \lesssim 15$ GHz) is disfavored, while at higher frequencies the posterior distribution is flat, indicating a wide range of plausible break frequencies. As such, while we cannot precisely determine the location of a spectral break, we may conclude that if a break exists, it is likely to arise at a frequency $\nu_b \gtrsim 15$ GHz.

Next, we turn to our constraints on the 34 GHz thermal fraction based on a comparison of synchrotron and free-free star-formation rates. Under the assumption that the free-free and synchrotron SFRs are identical, we determined a thermal fraction of $f_{\rm th}(34\,{\rm GHz}) = 0.84^{+0.23}_{-0.18}$ (Section 5.5.1). We compare this value with the expected high-frequency thermal fraction as a function of break frequency in panel b) of Figure 5.7. For an M82-like radio spectrum at $z = 1$ with $f_{\rm th} = 0.10$ at 1.4 GHz, we expect a 34 GHz thermal fraction consistent with the predicted value for any given frequency of a spectral break. However, for a low thermal fraction of $f_{\rm th}(1.4\,{\rm GHz}) = 0.05$, a break frequency at $\nu_b \lesssim 20$ GHz is required to match the predicted high-frequency thermal fraction. This constraint is therefore rather orthogonal to the constraints on ν_b from the posterior distributions in Figure 5.7a.

Finally, we investigate whether the existence of a spectral break can indeed result in low thermal fractions when unaccounted for in the fitting. To this end, we simulate the radio spectra of faint star-forming sources with a spectral break at frequency ν_b. We then fit the resulting simulated radio spectrum with a simple combination of free-free and synchrotron emission, as in Equation 5.4. This model by construction cannot capture any spectral ageing, and as such simulates how any complexities in the radio spectra of star-forming galaxies might leave their imprint when modelled by our sim-

ple fitting routine. For the radio spectra we adopt an M82-like model, but with a synchrotron component that steepens beyond ν_b, and fix the S/N at 34 GHz to be similar to what is observed in our stacks (S/N $\approx 3-5$). Using this model for the radio spectrum, we further sample the fluxes of the simulated spectra at 1.4, 3, 5 and 10 GHz, and vary all fluxes within their corresponding uncertainties. We subsequently fit the simulated radio fluxes with our simple model a total of 400 times each for a range of assumed break frequencies spanning $\nu_b = 5 - 45$ GHz.

We show the recovered thermal fractions and synchrotron spectral indices as a function of break frequency for the simulated sources in panels c) and d) of Figure 5.7. We can naturally reproduce our low recovered thermal fractions by using an M82-like radio SED without any spectral break, provided that the input thermal fraction is low ($f_{\rm th} \sim 0.05$ at 1.4 GHz). In this case, a thermal fraction of $f_{\rm th} \sim 0.50$ at 34 GHz is expected. However, as is evident from panel b), this underestimates the predicted thermal fractions based on a comparison of the stacked free-free and synchrotron SFRs. Instead, a larger thermal fraction at rest-frame 1.4 GHz, in combination with a spectral break, can similarly give rise to modest fitted thermal fractions, while the true thermal fraction is significantly higher. Indeed, these simulations indicate that a likely value for the thermal fraction is $f_{\rm th}(1.4\,{\rm GHz}) > 0.05$, with a combination of $f_{\rm th}(1.4\,{\rm GHz}) = 0.10$ and $\nu_b \approx 15 - 25$ GHz being able to explain the observed spectral parameters.

Summarizing, we have tested whether the presence of a break in the synchrotron spectrum can plausibly explain the low fitted thermal fractions. Directly constraining the location of the spectral break via fitting a more complex radio spectrum to the available photometry indicates $\nu_b \gtrsim 15$ GHz. A comparison of the synchrotron and free-free SFRs points towards either a low thermal fraction and a low-frequency spectral break, or an overall high thermal fraction. Simulations that involve fitting radio spectra with a break using a model that does not account for spectral ageing indicates a high thermal fraction and a break at $\nu_b \approx 15 - 25$ GHz. Upon combining these constraints, we qualitatively conclude that the radio spectrum of typical star-forming galaxies may be described with a typical low-frequency thermal fraction ($f_{\rm th} \approx 0.10$), and a spectral break at moderately high-frequencies ($\nu_b \approx 15-25$ GHz). If indeed the result of spectral ageing, such a break reflects a population of older, cooled cosmic ray electrons and hence provides a rough proxy of a galaxy's recent star formation history (e.g., Thomson et al. 2019).

However, we caution that while this interpretation qualitatively explains the observed deficit of high-frequency radio emission, at present we cannot test it in detail. Instead, testing this hypothesis will require an increased sampling of the radio SED at high frequencies, in particular around observed-frame 20 GHz, allowing for more complex models for the radio spectrum to be fit to the data. At present, such analyses have remained limited to relatively nearby starburst galaxies (e.g., Galvin et al. 2018). However, extending such studies to higher redshifts will be crucial in order to establish free-free emission as an SFR indicator in the early Universe.

5.5.3 The Cosmic Star-formation History

In Section 5.4.2, we detect multi-frequency radio continuum emission in star-forming galaxies in COSMOS and GOODS-N, based on a median stacking analysis. We now perform a mean stacking analysis in order to measure the average radio luminosity of star-forming galaxies at 34 GHz, and in turn compute their corresponding average star-formation rate. Given that we are stacking on mass-complete galaxy samples within a known cosmic volume, we can directly constrain the cosmic star-formation rate density with free-free emission.

However, as we discussed in Section 5.5.2, the fitted thermal fractions may be underestimated if synchrotron ageing affects the radio spectrum, which in turn results in underestimated cosmic star-formation rates. As such, in what follows, we calculate star-formation rates in three different ways, assuming either 1) the fitted thermal fractions combining the COSMOS and GOODS-N fields from Section 5.5.2; 2) a fixed thermal fraction of unity or; 3) the thermal fraction obtained from comparing the free-free and synchrotron SFRs in Section 5.5.1. In the first case, we are likely underestimating the true cosmic SFRD, while the measurements from case three are not fully independent of the synchrotron-derived cosmic SFRD. In turn, the most direct and unbiased constraints on the SFRD from radio free-free emission are provided by case two, which constitute an upper limit on the total rate of cosmic star formation.

We first perform a mean stacking analysis to obtain the average radio luminosity at 34 GHz, using the same mass-complete bins as originally defined in Table 5.1. Note that we adopt the full COLDz footprint in GOODS-N, as in Section 5.5.2. We combine the cutouts around sources in both COSMOS and GOODS-N into a single cube of $N_{\rm COS} + N_{\rm GN}$ sources, and

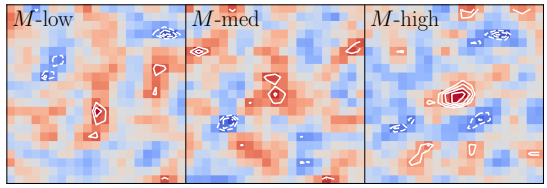

Figure 5.8: Mean stacks at 34 GHz for the mass-complete bins combining the COSMOS and GOODS-N fields. Only the central 21×21 pixels are shown for clarity, and the contours represent 2σ to 4σ in steps of 0.5σ. Continuum emission in the stacks is detected at 2.9σ and 4.2σ in the medium and high-mass bins, while no significant in M-low is observed at the 2.5σ level.

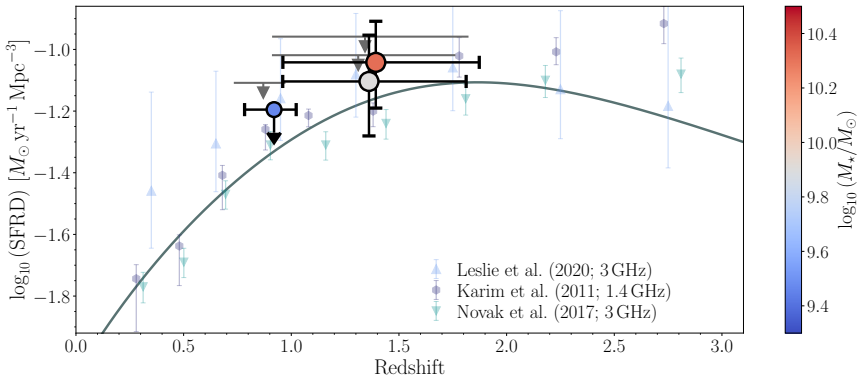

Figure 5.9: Constraints on the cosmic star-formation history from free-free emission. A thermal fraction of $f_{\rm th}(34\,{\rm GHz}) = 0.84^{+0.23}_{-0.18}$ is adopted, as determined through a comparison of synchrotron and free-free SFRs (Section 5.5.1). Upper limits assuming a thermal fraction of unity are additionally shown via grey arrows. The horizontal errorbars show the interquartile ranges for the corresponding redshift bins. The canonical Madau & Dickinson (2014) cosmic SFRD is shown through the grey curve, and various radio-based studies, using non-thermal synchrotron emission as a star-formation tracer, are additionally overplotted. Similar to this work, Karim et al. (2011) and Leslie et al. (2020) utilize a radio stacking analysis at low frequencies (1.4 and 3 GHz, respectively), while Novak et al. (2017) use radio-detected sources. Our constraints are in good agreement with those from commonly adopted star-formation tracers at high redshift, and show that radio free-free emission can be used to constrain cosmic star-formation.

take a simple unweighted mean across the entire sample.[7] The resulting stacks are shown in Figure 5.8. As the two fields have a slightly different beam, we do not fit the stacked emission with a 2D Gaussian as we did when median stacking, but simply extract the peak luminosity density within a radius of one pixel ($0\farcs5$) from the center of the stack. In the medium and high-mass bins, we detect mean-stacked 34 GHz emission at a significance of 2.9σ and 4.2σ, respectively, while in the low-mass bin we do not detect significant continuum emission and instead adopt a 2.5σ upper limit. We subsequently add in the galaxies individually detected at 34 GHz via Equation 5.3. Out of the seven star-forming galaxies detected in the COLDz observations by Algera et al. (2021), only the two COSMOS sources need to be added in a posteriori, as the five galaxies in GOODS-N were conservatively excluded based on their 1.4 GHz luminosities in excess of $S_{1.4} \gtrsim 50\,\mu$Jy, where AGN contamination may become important (Section 5.4.2). We then determine an upper limit on the mean 34 GHz luminosity of $L_{34} < 1.2 \times 10^{21}\,\mathrm{W\,Hz^{-1}}$ in M-low, and measure stacked luminosities of $L_{34} = (4.4 \pm 1.5) \times 10^{21}\,\mathrm{W\,Hz^{-1}}$ and $L_{34} = (10.7 \pm 2.5) \times 10^{21}\,\mathrm{W\,Hz^{-1}}$ in bins M-med and M-high, respectively.

Given the fitted or fixed thermal fractions, we subsequently calculate free-free star-formation rates. The cosmic star-formation rate density SFRD is then determined via

$$\mathrm{SFRD}(\overline{z}) = C(M_*) \times \langle \mathrm{SFR} \rangle \times N_{\mathrm{stack}} \times V(z)^{-1}\,, \tag{5.6}$$

where $\langle \mathrm{SFR} \rangle$ is the average free-free star-formation rate, N_{stack} is the number of sources used for stacking, combining detections and non-detections, $V(z)$ is the total cosmic volume probed by the 34 GHz mosaic spanning the full redshift range of the bin, and $C(M_\star)$ is a numerical factor that corrects for the fact that some star-formation occurs below the stellar masses where we assume to be complete. In order to determine this correction, we adopt the stellar mass functions for active galaxies from Davidzon et al. (2017), and assume a linear relation between stellar mass and star-formation rate, as is appropriate for low-mass ($M \lesssim 10^{10.5}\,M_\odot$) galaxies on the star formation main-sequence (Speagle et al. 2014; Schreiber et al. 2015; Leslie et al. 2020). The correction factor equals $C \approx 1.05$ and $C \approx 1.37$ for mass completeness limits of $10^9\,M_\odot$ and $10^{10}\,M_\odot$, respectively, when integrating the stellar mass function down to $10^5\,M_\odot$ (following Karim et al. 2011).

[7] We note that the COSMOS and GOODS-N radio maps have the same pixel scale of $0\farcs5$, such that the stacks may easily be co-added.

We note that, while the stellar mass function does evolve with redshift, the characteristic mass and low-mass slope for star-forming galaxies do not vary significantly within the redshift range probed in this work (Davidzon et al. 2017). As a result, the correction factor $C(M_\star)$ is mostly independent of redshift.

We plot our free-free constraints on the cosmic star-formation history in Figure 5.9. For each bin, we show both the SFRD given a thermal fraction of $f_{\rm th}(34\,{\rm GHz}) = 0.84^{+0.23}_{-0.18}$ (case 3) and an upper limit when a value of unity is assumed (case 2). We additionally provide the numerical values for the SFRD when assuming the fitted thermal fractions in Table 5.2.

When adopting the fixed case 3) thermal fraction, our cosmic star formation rates obtained via free-free emission are in good agreement with the canonical SFRD from Madau & Dickinson (2014). This is consistent with the fact that the SFRD derived from low-frequency radio observations similarly agrees with the Madau & Dickinson (2014) relation (Novak et al. 2017; Leslie et al. 2020; see also below). In addition, adopting a thermal fraction of unity places robust upper limits on the SFRD which are fully consistent with the Madau & Dickinson (2014) constraints. As expected, adopting the fitted thermal fractions (case 1) provides cosmic SFRs that are consistently biased low compared to the canonical SFRD, further highlighting that a thermal fraction of $f_{\rm th}(34\,{\rm GHz}) \sim 0.8$ is a good assumption for star-forming galaxies at $z \sim 1$.

We caution that the normalization of the star formation main-sequence increases with redshift (e.g., Speagle et al. 2014), and in turn varies across our relatively wide redshift bins. Since we adopt a luminosity stacking technique, the stacks are therefore weighted towards the on average more luminous high-redshift population within each bin. As a result, the luminosity-weighted mean redshift within the bins exceeds the median redshift of the sample shown in Figure 5.9. Qualitatively, if the luminosity-weighted redshift is adopted instead, the agreement between the SFRD from free-free emission and the Madau & Dickinson (2014) relation improves further, as the typical redshift probed now more closely approaches the peak of cosmic star-formation at $z \sim 2$.

We finally compare our constraints with radio-based studies of cosmic star-formation, which use low-frequency radio synchrotron emission. Both Karim et al. (2011) and Leslie et al. (2020) utilize stacking analyses in the COSMOS field, at 1.4 GHz and 3 GHz, respectively, while Novak et al. (2017) consider individually detected radio sources. These radio-based studies may hint towards a slight excess in the SFRD compared to Madau

Table 5.2: Constraints on the cosmic star-formation rate density from free-free emission

Bin	$\log[\mathrm{SFRD}(f_{\mathrm{th,obs}})]$	$\log[\mathrm{SFRD}(f_{\mathrm{th}}=1)]$	$\log\left[\mathrm{SFRD}(f_{\mathrm{th}}=0.84^{+0.23}_{-0.18})\right]$
	$[M_\odot\,\mathrm{yr}^{-1}\,\mathrm{Mpc}^{-3}]$	$[M_\odot\,\mathrm{yr}^{-1}\,\mathrm{Mpc}^{-3}]$	$[M_\odot\,\mathrm{yr}^{-1}\,\mathrm{Mpc}^{-3}]$
M-low	–	<-1.11	<-1.20
M-med	<-1.26	$-1.02^{+0.11}_{-0.14}$	$-1.10^{+0.15}_{-0.18}$
M-high	$-1.34^{+0.21}_{-0.62}$	$-0.96^{+0.09}_{-0.11}$	$-1.04^{+0.13}_{-0.15}$

Note. — (1) Bin matches that in Table 5.1; (2) cosmic star-formation rate density when the fitted thermal fraction is used. When the thermal fraction is consistent with zero a 1σ upper limit on f_{th} is used; (3) cosmic SFRD when a thermal fraction of unity is assumed; (4) cosmic SFRD when the thermal fraction predicted from synchrotron SFRs is used (Section 5.5.1).

& Dickinson (2014) at $z \gtrsim 2.5$, although the uncertain conversion from radio synchrotron emission into star-formation rates at high redshift complicates such interpretations. While free-free emission does not require adopting such a conversion, at present it remains difficult to probe beyond the peak of cosmic star-formation even via stacking analyses. In the future, radio observations at lower frequencies (for example at 10 GHz, probing $\nu \gtrsim 30$ GHz at $z \gtrsim 2$) may provide better constraints in this high redshift regime, owing to the increased source brightness and larger field of view. Such observations may subsequently be used to distinguish between a cosmic star-formation rate that follows the high-redshift decline of the Madau & Dickinson (2014) relation, or remains relatively flat, as might be expected if the current high-redshift UV- and optical-based constraints underestimate dust corrections (e.g., Casey et al. 2018, but see also the constraints on the SFRD from Bouwens et al. 2020 and Zavala et al. 2021).

5.6 Conclusions

We have performed a multi-frequency radio stacking analysis using deep VLA observations across the well-studied COSMOS and GOODS-N fields in order to investigate the shape of the radio spectrum of faint star-forming galaxies. The deep 34 GHz observations from the COLDz survey form the foundation of this work, and are augmented by deep archival data at 1.4, 3,

5, and 10 GHz. We construct three mass-complete bins from near-infrared selected galaxy catalogs across COSMOS and GOODS-N, and remove sources that are unlikely to be star-forming based on their optical/near-IR colors and radio emission. We stack at the known positions of the star-forming galaxies at all available frequencies, and decompose the resulting radio spectra into free-free and synchrotron components.

We detect stacked 34 GHz emission in the medium ($> 10^{9.5}\,\mathrm{M}_\odot$) and high-mass ($> 10^{10}\,\mathrm{M}_\odot$) bins, and place upper limits on the radio luminosity in the low-mass bin ($> 10^{9}\,\mathrm{M}_\odot$; Figures 5.2 and 5.3). Surprisingly, the fitted fractional contribution of free-free emission to the total radio emission at 34 GHz – the thermal fraction – is a factor of $\sim 1.5-2$ lower compared to the canonically assumed model for the radio SED (M82-like; Figure 5.4). However, in all cases the stacked 34 GHz luminosities are consistent with the predicted radio luminosity from free-free emission, when assuming the the star formation rates derived from optical-infrared data for the galaxies in the parent catalogs. This points towards a deficit in synchrotron emission at high frequencies (rest-frame $60 - 80$ GHz), while the contribution from free-free emission is as expected. Accordingly, this implies a high thermal fraction of $f_{\mathrm{th}} \sim 0.8$ in this frequency range.

Such a synchrotron deficit can plausibly be the result of synchrotron ageing of high-energy cosmic rays. Upon combining the radio continuum data across COSMOS and GOODS-N, we fit a more complex model to the radio spectrum including a spectral break. While a precise break frequency can not be robustly ascertained, a break at rest-frame $\nu \gtrsim 15$ GHz is favored. We supplement this analysis with realistic simulations of mock radio spectra, and verify that a spectral break at a rest-frame frequency of $\nu_b \sim 15-25$ GHz, in combination with a typical thermal fraction of $f_{\mathrm{th}}(1.4\,\mathrm{GHz}) = 0.10$, can explain the observed high-frequency deficit (Figure 5.7).

Finally, we perform a mean stacking analysis at 34 GHz, which allows us to constrain the cosmic star-formation rate density with free-free emission at $0.5 \leqslant z \leqslant 2.5$ We find good agreement between the constraints from high-frequency radio emission with canonical star-formation rate tracers, including radio synchrotron emission (Figure 5.9). This, in turn, demonstrates that free-free emission can reliably be used as a tracer of star formation in the early Universe.

Our current analysis remains limited by the 34 GHz observations, which cover a relatively small area on the sky. In addition, the individual stacks are of modest signal-to-noise, which complicates the spectral decomposition, and hence the determination of thermal fractions and subsequent

free-free star-formation rates. Finally, the radio spectra of normal star-forming galaxies may be more complicated than is typically assumed, such that an improved sampling of the radio SED through matched depth multi-frequency observations is required to make further progress. Future radio telescopes, such as the Square Kilometre Array Phase-1 (SKA-1), and in particular the next-generation VLA (ngVLA), will allow for more robust measurements of high-frequency radio emission in distant star-forming galaxies, and will provide more stringent constraints on cosmic star formation through free-free emission (e.g., Murphy et al. 2015; Barger et al. 2018).

Acknowledgements

The authors would like to thank F. Owen for sharing the 1.4 GHz radio image of GOODS-N. The National Radio Astronomy Observatory is a facility of the National Science Foundation operated under cooperative agreement by Associated Universities, Inc. H.S.B.A. and J.A.H. acknowledge support of the VIDI research programme with project number 639.042.611, which is (partly) financed by the Netherlands Organization for Scientific Research (NWO). D.R. acknowledges support from the National Science Foundation under grant Nos. AST-1614213 and AST- 1910107. D.R. also acknowledges support from the Alexander von Humboldt Foundation through a Humboldt Research Fellowship for Experienced Researchers. I.R.S. acknowledges financial support from STFC (ST/T000244/1). M.A. acknowledges support from FONDECYT grant 1211951, "CONICYT + PCI + INSTITUTO MAX PLANCK DE ASTRONOMIA MPG190030" and "CONICYT+PCI+REDES 190194". B.M. acknowledges support from the Collaborative Research Centre 956, sub-project A1, funded by the Deutsche Forschungsgemeinschaft (DFG) – project ID 184018867.

Appendix

5.A Stacking

Stacking is the art of co-adding small cutouts around a priori known galaxy positions in order to obtain a census of their typical emission at a different wavelength. Median stacking is often favored over mean stacking in the literature, as it reduces any biases from outliers, and is more repre-

sentative of the (radio-)undetected population (e.g., Condon et al. 2013 show the mean tends to be skewed towards sources close to the detection threshold). As a result, the median stacked spectrum is not dominated by a few bright, strongly star-forming galaxies, which may show relatively complex radio spectra (Tisanić et al. 2019; Thomson et al. 2019). In addition, a median stacking analysis renders one less susceptible to contamination from radio AGN , which constitute a minority of the population at faint radio fluxes (Smolčić et al. 2017a; Algera et al. 2020b). A further advantage is that, when adopting the median and stacking in luminosity as opposed to flux density, the resulting stacks typically have higher signal-to-noise ratios compared to when the mean is adopted. This is due to the luminosity distance, by which the stacks are multiplied (Equation 5.2), being a strongly increasing function of redshift. In turn, the RMS noise of stacks in units of luminosity density at high redshift is larger than that of the low-redshift population. A simple mean stacking analysis up-weights these noisy stacks, while a noise-weighted mean approach instead down-weights the high-redshift population. Finally, a median stacking analysis allows one to treat individually detected sources and non-detections homogeneously by stacking them together, whereas a mean stacking technique requires additional care to be taken when dealing with bright outliers or neighboring galaxies.

However, one caveat that applies when using the median is typically not addressed: White et al. (2007) show that, given a set of point-source flux densities S_i in an image with local RMS-noise σ_i, the stacked median $\tilde{S}_{\rm stack}$ does not necessarily represent the true sample median $\tilde{S}_{\rm true}$. In particular, when $S_i \ll \sigma_i$, the stacked median tends towards the true sample mean, i.e., $\tilde{S}_{\rm stack} \rightarrow \overline{S}_{\rm true}$. In the opposite scenario, where $S_i \gg \sigma_i$, the stacked median tends towards the true sample median $\tilde{S}_{\rm stack} \rightarrow \tilde{S}_{\rm true}$. In practice, the typical flux density of the sources is likely to be similar to the RMS, i.e., $S_i \sim \sigma_i$: if the sources are much brighter, stacking is likely unnecessary, while if the sources are substantially fainter, a significant number of galaxies is required to get a stacked detection.[8] This, in turn, implies that the stacked median will probe a value somewhere between the true median and true mean, complicating its interpretation. For a typical distribution of flux densities the mean will exceed the median. As a result, when performing a stacking analysis, the median is "boosted" compared to the true

[8] For example, if the median flux density is just $0.1\sigma_i$, this requires $\sim 10^3$ sources to be stacked for a detection at S/N ≈ 3, assuming that the noise decreases as $1/\sqrt{N}$. In the stacking analysis in this work, a sample of a $\sim 60 - 600$ galaxies is typical (Table 5.1).

sample median. The mean does not suffer from this difficulty, and needs not be deboosted, but is instead subject to the previously mentioned drawbacks.

What truly complicates this picture, however, is that the extent to which the median is boosted depends on the typical ratio S_i/σ_i. While the (local) noise properties of the image, σ_i, are known, the typical flux densities S_i of course are not – otherwise, one would not be stacking! Nevertheless, correcting for median boosting is particularly important in the multi-frequency stacking analysis we perform in this work: radio sources typically are fainter at higher rest-frame frequencies, and the radio maps used for stacking are of varying depths. As a result, the level of boosting is dependent on the properties of the individual radio images, and hence stacked flux densities cannot directly be compared, as they do not trace the quantity we would like to compare, $\tilde{S}_{\text{true}}$. What is needed, then, is an estimate of the boosting factor $f_{\text{boost}} = \tilde{S}_{\text{stack}}/\tilde{S}_{\text{true}}$, which can be used to correct stacked flux densities back to the true sample median.

In order to estimate the boosting factor, we perform a stacking analysis on simulated sources, for which the true sample median and mean are known a priori. Since the level of median boosting depends on the quantity S_i/σ_i, it is crucial that the distribution of flux densities S_i be realistic. For that reason, we generate mock sources by assigning radio flux densities to galaxies in the COSMOS2015 or 3D-HST catalogs. For each set of mass-complete bins in the COSMOS and the GOODS-N field, we randomly draw the redshift z and stellar mass $M_\star$ for a large number of galaxies within the corresponding catalogs. We then adopt the main-sequence from Schreiber et al. (2015) to assign these mock galaxies a star-formation rate, and include a realistic scatter of 0.25 dex. We subsequently convert these star-formation rates to radio luminosities $L_{1.4}$ at rest-frame 1.4 GHz via the far-infrared/radio correlation from Bell (2003), including their measured scatter of 0.26 dex about the correlation. We then randomly draw radio spectral indices from a normal distribution with a mean of -0.70 and a scatter of 0.30, and use these to calculate the flux densities of each of the mock sources. We assign these to unresolved mock sources which are subsequently inserted into the residual radio maps at randomly selected positions, using a Gaussian beam matching the resolution and position angle of the restoring clean beam. We opt for inserting mock sources into the residual images as to ensure we are not artificially approaching the confusion limit, but are still including realistic noise properties in our analysis. We further include small offsets in RA and Dec, normally distributed around

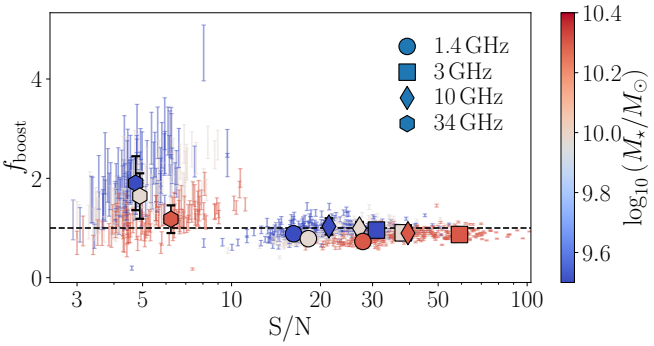

Figure 5.10: Median boosting as a function of S/N for stacks of simulated sources drawn from the bins defined in Table 5.1. Points are colored by their stellar mass – at fixed redshift, lower mass galaxies are typically fainter, and hence will show a greater level of median boosting. The correction factor is around unity at 1.4, 3 and 10 GHz, but reaches $f_{\rm boost} = 1.9$ ($\sigma = 0.5$) for the low-mass bin at 34 GHz. All median-stacked flux densities presented in this work are corrected for boosting.

zero, with a scatter of $0\farcs30$, between the true and catalogued mock sources positions, in order to capture realistic spatial offsets between sources. Finally, we stack the mock sources, and compare their input and output median luminosity densities. The ratio of these two quantities then defines the boosting factor, which is used to correct the luminosities probed in the real stacks.

As an example, we show the level of boosting for the COSMOS2015 catalog (Section 5.4.2) in Figure 5.10. The correction factor is typically around unity at high-S/N, and may in fact be slightly lower than one when the peak flux underestimates the true flux density of the stacked mock sources. However, for low-mass galaxies at 34 GHz, which on average have lower star-formation than their high-mass counterparts and hence a lower typical S_i/σ_i, the boosting correction may reach up to $f_{\rm boost} \approx 2$. All median-stacked flux densities and spectral luminosities presented in this work are corrected for boosting, based on realistic simulations such as the COSMOS one presented here. The boosting factors for the stacks in Figures 5.2 and 5.3 are additionally reported in Table 5.3. The uncertainty on the stacked luminosities further includes the spread across the recovered boosting corrections.

5.B The COSMOS $z = 5.3$ Protocluster

The COLDz COSMOS observations were designed to overlap with a prominent $z = 5.3$ protocluster, of which AzTEC.3 is the brightest member (Capak et al. 2011; Riechers et al. 2014). While this source is individually detected in the COLDz observations, an additional 17 protocluster members remain undetected at 34 GHz yet are observed in Lyman-α emission in VLT/MUSE spectroscopy (Guaita et al., in preparation). We median stack on all members at 1.4, 3, 10 and 34 GHz – in flux density as opposed to luminosity, as all sources lie at the same approximate redshift. However, we find no detection in the stacks at any frequency, and can therefore only place upper limits on the typical high-frequency continuum emission from the protocluster galaxies. At 10 and 34 GHz, respectively, we place 3σ upper limits of $S_{10} \lesssim 0.46\,\mu\mathrm{Jy\,beam^{-1}}$ and $S_{34} \lesssim 1.7\,\mu\mathrm{Jy\,beam^{-1}}$.

The 10 GHz stack probes a rest-frame frequency of $\nu' \approx 63$ GHz at $z = 5.3$. As such, it directly places constraints on the typical level of free-free emission in the protocluster members. The upper limit for the flux density at 10 GHz translates into a limit on the luminosity density of $L_{\nu'} < 2.2 \times 10^{22}\,\mathrm{W\,Hz^{-1}}$. Given a thermal fraction of $f_{\mathrm{th}}(\nu') = 0.70$, as is expected at this rest-frame frequency for an M82-like SED (Condon 1992), we determine an upper limit of SFR $< 100\,M_\odot\,\mathrm{yr^{-1}}$ for the protocluster members. This is consistent with the findings from Capak et al. (2015), who determine typical star-formation rates of $\sim 40\,M_\odot\,\mathrm{yr^{-1}}$ for a subset of the protocluster members used for stacking in this work, based on their combined UV and far-infrared emission. While the 34 GHz data are a factor of $\sim 3-4\times$ less sensitive than the 10 GHz stack, we may expect thermal emission from dust to become important at these frequencies ($\nu' \approx 210$ GHz). Indeed, Algera et al. (2021) find that the 34 GHz continuum emission observed for AzTEC-3 is likely dominated by a combination of dust emission and the CO(2-1) emission line. To estimate the expected contribution from dust emission at 34 GHz for the protocluster members, we assume a star-formation rate of SFR $= 100\,M_\odot\,\mathrm{yr^{-1}}$ and a grey body with $\beta = 1.8$ and $T_{\mathrm{dust}} = 35$ K for the dust SED (e.g., Casey et al. 2014). Given that the assumed star-formation rate is an upper limit, this translates into an upper limit on the 34 GHz flux density due to dust of $S_{34}^{\mathrm{dust}} < 1.0\,\mu\mathrm{Jy\,beam^{-1}}$, which is consistent with our stacked upper limit of $S_{34} = 1.7\,\mu\mathrm{Jy\,beam^{-1}}$, under the assumption that dust contributes $\gtrsim 50\%$ of the emission at rest-frame $\nu' \gtrsim 200$ GHz.

Table 5.3: Stacked luminosities and deboosting factors in COSMOS (upper three rows) and GOODS-N (lower).

Bin	$f_{\rm boost}(1.4)$	$L_{1.4}$	$f_{\rm boost}(3\text{ or }5)$[a]	$L_{3\text{ or }5}$[a]	$f_{\rm boost}(10)$	L_{10}	$f_{\rm boost}(34)$	L_{34}	$f_{\rm th}(34)$[b]	$\alpha_{\rm NT}$[b]
–	–	10^{21} W Hz^{-1}	–	10^{21} W Hz^{-1}	–	10^{21} W Hz^{-1}	–	10^{21} W Hz^{-1}	–	–
M-low	0.88 ± 0.13	3.5 ± 0.7	0.96 ± 0.10	1.7 ± 0.2	1.03 ± 0.16	0.9 ± 0.2	–	< 1.1	< 0.86	$-0.90^{+0.25}_{-0.29}$
M-med	0.79 ± 0.10	13.7 ± 2.1	0.90 ± 0.09	7.1 ± 0.7	0.99 ± 0.13	4.0 ± 0.6	1.64 ± 0.46	1.8 ± 0.7	$0.51^{+0.25}_{-0.51}$	$-0.84^{+0.25}_{-0.26}$
M-high	0.73 ± 0.07	28.9 ± 3.5	0.87 ± 0.09	16.2 ± 1.7	0.90 ± 0.11	7.6 ± 1.0	1.18 ± 0.28	3.0 ± 1.1	$0.20^{+0.36}_{-0.65}$	$-0.76^{+0.36}_{-0.22}$
M-low	1.21 ± 0.10	3.1 ± 0.3	1.64 ± 0.25	0.9 ± 0.3	1.90 ± 0.33	0.5 ± 0.2	–	< 1.7	< 0.76	$-0.88^{+0.82}_{-0.28}$
M-med	1.01 ± 0.10	10.1 ± 1.1	1.26 ± 0.17	5.4 ± 1.0	1.35 ± 0.20	2.5 ± 0.6	2.43 ± 0.45	1.5 ± 0.6	$0.35^{+0.35}_{-0.70}$	$-0.77^{+0.35}_{-0.26}$
M-high	0.91 ± 0.06	26.9 ± 2.1	0.92 ± 0.16	9.0 ± 2.1	1.07 ± 0.17	4.3 ± 1.1	1.67 ± 0.23	4.2 ± 1.3	$0.57^{+0.21}_{-0.39}$	$-1.08^{+0.21}_{-0.23}$

[a] Deboosting factors and luminosities are given at 3 GHz for COSMOS and 5 GHz for GOODS-N; see text.

[b] The errors on $f_{\rm th}$ and $\alpha_{\rm NT}$ are degenerate (Figure 5.4; see also Algera et al. 2021). We here quote the one-dimensional uncertainties, but adopt the full posterior probability distributions in this work to accurately propagate the uncertainties.

Note. — (1) Bin identifier, matching that in Table 5.1; (2), (4), (6), (8) Boosting factors at 1.4, 3 or 5, 10 and 34 GHz; (3), (5), (7), (9) Median-stacked deboosted luminosities at observed-frame 1.4, 3 or 5, 10 and 34 GHz; (10) Thermal fraction at observed-frame 34 GHz; (11) Synchrotron spectral index.

Bibliography

Alexander, D. M., Bauer, F. E., Chapman, S. C., et al. 2005, ApJ, 632, 736
Algera, H. S. B., Hodge, J. A., Riechers, D., et al. 2021, ApJ, 912, 73
Algera, H. S. B., Smail, I., Dudzevičiūtė, U., et al. 2020a, ApJ, 903, 138
Algera, H. S. B., van der Vlugt, D., Hodge, J. A., et al. 2020b, ApJ, 903, 139
Aravena, M., Murphy, E. J., Aguirre, J. E., et al. 2013, MNRAS, 433, 498
Aretxaga, I., Wilson, G. W., Aguilar, E., et al. 2011, MNRAS, 415, 3831
Armus, L., Heckman, T., & Miley, G. 1987, AJ, 94, 831
Ashby, M. L. N., Willner, S. P., Fazio, G. G., et al. 2013, ApJ, 769, 80
Bañados, E., Venemans, B. P., Morganson, E., et al. 2015, ApJ, 804, 118
Baldwin, J. A., Phillips, M. M., & Terlevich, R. 1981, PASP, 93, 5
Barger, A. J., Cowie, L. L., Sanders, D. B., et al. 1998, Nature, 394, 248
Barger, A. J., Kohno, K., Murphy, E. J., Sargent, M. T., & Condon, J. J. 2018, arXiv e-prints, arXiv:1810.07143
Barger, A. J., Wang, W. H., Cowie, L. L., et al. 2012, ApJ, 761, 89
Basu, A., Wadadekar, Y., Beelen, A., et al. 2015, ApJ, 803, 51
Battisti, A. J., da Cunha, E., Grasha, K., et al. 2019, ApJ, 882, 61
Baugh, C. M., Gonzalez-Perez, V., Lagos, C. d. P., et al. 2019, MNRAS, 483, 4922
Beck, R. 2012, Space Sci. Rev., 166, 215
Beck, R. & Wielebinski, R. 2013, Magnetic Fields in Galaxies, ed. T. D. Oswalt & G. Gilmore, Vol. 5 (Dordrecht: Springer), 641
Bell, E. F. 2003, ApJ, 586, 794
Bennett, C. L., Halpern, M., Hinshaw, G., et al. 2003, ApJS, 148, 1
Berta, S., Lutz, D., Santini, P., et al. 2013, A&A, 551, A100
Bertoldi, F., Carilli, C., Aravena, M., et al. 2007, ApJS, 172, 132
Best, P. N., Kaiser, C. R., Heckman, T. M., & Kauffmann, G. 2006, MNRAS, 368, L67

Beswick, R. J., Muxlow, T. W. B., Thrall, H., Richards, A. M. S., & Garrington, S. T. 2008, MNRAS, 385, 1143
Biggs, A. D., Ivison, R. J., Ibar, E., et al. 2011, MNRAS, 413, 2314
Biggs, A. D., Younger, J. D., & Ivison, R. J. 2010, MNRAS, 408, 342
Birkin, J. E., Weiss, A., Wardlow, J. L., et al. 2021, MNRAS, 501, 3926
Blain, A. W., Smail, I., Ivison, R. J., Kneib, J. P., & Frayer, D. T. 2002, Phys. Rep., 369, 111
Bonaldi, A., Bonato, M., Galluzzi, V., et al. 2019, MNRAS, 482, 2
Bondi, H. & Gold, T. 1948, MNRAS, 108, 252
Bondi, M., Ciliegi, P., Schinnerer, E., et al. 2008, ApJ, 681, 1129
Bondi, M., Zamorani, G., Ciliegi, P., et al. 2018, A&A, 618, L8
Bonzini, M., Padovani, P., Mainieri, V., et al. 2013, MNRAS, 436, 3759
Bothwell, M. S., Smail, I., Chapman, S. C., et al. 2013, MNRAS, 429, 3047
Bouwens, R., González-López, J., Aravena, M., et al. 2020, ApJ, 902, 112
Bouwens, R. J., Bradley, L., Zitrin, A., et al. 2014, ApJ, 795, 126
Bouwens, R. J., Illingworth, G. D., Franx, M., et al. 2009, ApJ, 705, 936
Bouwens, R. J., Illingworth, G. D., Oesch, P. A., et al. 2015, ApJ, 803, 34
Bouwens, R. J., Oesch, P. A., Labbé, I., et al. 2016, ApJ, 830, 67
Bouwens, R. J., Smit, R., Schouws, S., et al. 2021, arXiv e-prints, arXiv:2106.13719
Brammer, G. B., van Dokkum, P. G., & Coppi, P. 2008, ApJ, 686, 1503
Brammer, G. B., van Dokkum, P. G., Franx, M., et al. 2012, ApJS, 200, 13
Brandt, W. N. & Alexander, D. M. 2015, A&A Rev., 23, 1
Braun, R., Bonaldi, A., Bourke, T., Keane, E., & Wagg, J. 2019, arXiv e-prints, arXiv:1912.12699
Bressan, A., Silva, L., & Granato, G. L. 2002, A&A, 392, 377
Brinchmann, J., Charlot, S., White, S. D. M., et al. 2004, MNRAS, 351, 1151
Bromm, V. & Loeb, A. 2004, New A, 9, 353
Bromm, V. & Yoshida, N. 2011, ARA&A, 49, 373
Bruzual, G. 2010, Philosophical Transactions of the Royal Society of London Series A, 368, 783
Bruzual, G. & Charlot, S. 2003, MNRAS, 344, 1000
Burgarella, D., Buat, V., Gruppioni, C., et al. 2013, A&A, 554, A70
Butler, B., Grammer, W., Selina, R., Carilli, C., & Murphy, E. J. 2019, in American Astronomical Society Meeting Abstracts, Vol. 233, American Astronomical Society Meeting Abstracts #233, 361.10
Byler, N., Dalcanton, J. J., Conroy, C., & Johnson, B. D. 2017, ApJ, 840, 44
Cai, Z.-Y., Lapi, A., Bressan, A., et al. 2014, ApJ, 785, 65
Cai, Z.-Y., Lapi, A., Xia, J.-Q., et al. 2013, ApJ, 768, 21

Calistro Rivera, G., Lusso, E., Hennawi, J. F., & Hogg, D. W. 2016, ApJ, 833, 98
Calistro Rivera, G., Williams, W. L., Hardcastle, M. J., et al. 2017, MNRAS, 469, 3468
Capak, P., Aussel, H., Ajiki, M., et al. 2007, ApJS, 172, 99
Capak, P. L., Carilli, C., Jones, G., et al. 2015, Nature, 522, 455
Capak, P. L., Riechers, D., Scoville, N. Z., et al. 2011, Nature, 470, 233
Cardamone, C. N., Urry, C. M., Schawinski, K., et al. 2010, ApJ, 721, L38
Carilli, C. L. & Barthel, P. D. 1996, A&A Rev., 7, 1
Carilli, C. L., Perley, R. A., Dreher, J. W., & Leahy, J. P. 1991, ApJ, 383, 554
Carilli, C. L. & Yun, M. S. 1999, ApJ, 513, L13
Casey, C. M., Narayanan, D., & Cooray, A. 2014, Phys. Rep., 541, 45
Casey, C. M., Zavala, J. A., Spilker, J., et al. 2018, ApJ, 862, 77
Ceraj, L., Smolčić, V., Delvecchio, I., et al. 2018, arXiv e-prints, arXiv:1811.02966
Chabrier, G. 2003, PASP, 115, 763
Chapman, S. C., Blain, A. W., Smail, I., & Ivison, R. J. 2005, ApJ, 622, 772
Chen, C.-C., Harrison, C. M., Smail, I., et al. 2020, A&A, 635, A119
Chevance, M., Kruijssen, J. M. D., Hygate, A. P. S., et al. 2020, MNRAS, 493, 2872
Cibinel, A., Daddi, E., Sargent, M. T., et al. 2019, MNRAS, 485, 5631
Civano, F., Marchesi, S., Comastri, A., et al. 2016, ApJ, 819, 62
Clemens, M. S., Vega, O., Bressan, A., et al. 2008, A&A, 477, 95
Colbert, E. J. M., Wilson, A. S., & Bland-Hawthorn, J. 1994, ApJ, 436, 89
Condon, J. J. 1984, ApJ, 287, 461
Condon, J. J. 1989, ApJ, 338, 13
Condon, J. J. 1992, ARA&A, 30, 575
Condon, J. J. 1997, PASP, 109, 166
Condon, J. J., Anderson, M. L., & Helou, G. 1991a, ApJ, 376, 95
Condon, J. J. & Broderick, J. J. 1986, AJ, 92, 94
Condon, J. J. & Broderick, J. J. 1991, AJ, 102, 1663
Condon, J. J., Cotton, W. D., Greisen, E. W., et al. 1998, AJ, 115, 1693
Condon, J. J., Helou, G., Sanders, D. B., & Soifer, B. T. 1993, AJ, 105, 1730
Condon, J. J., Huang, Z. P., Yin, Q. F., & Thuan, T. X. 1991b, ApJ, 378, 65
Condon, J. J., Kellermann, K. I., Kimball, A. E., Ivezić, Ž., & Perley, R. A. 2013, ApJ, 768, 37
Condon, J. J. & Mitchell, K. J. 1984, AJ, 89, 610
Cotton, W. D., Condon, J. J., Kellermann, K. I., et al. 2018, ApJ, 856, 67
Crain, R. A., Schaye, J., Bower, R. G., et al. 2015, MNRAS, 450, 1937
Croton, D. J., Springel, V., White, S. D. M., et al. 2006, MNRAS, 365, 11
da Cunha, E., Charlot, S., & Elbaz, D. 2008, MNRAS, 388, 1595

da Cunha, E., Walter, F., Smail, I. R., et al. 2015, ApJ, 806, 110
Daddi, E., Dannerbauer, H., Krips, M., et al. 2009, ApJ, 695, L176
Danielson, A. L. R., Swinbank, A. M., Smail, I., et al. 2017, ApJ, 840, 78
Davidzon, I., Ilbert, O., Laigle, C., et al. 2017, A&A, 605, A70
De Jong, T., Klein, U., Wielebinski, R., & Wunderlich, E. 1985, A&A, 147, L6
Decarli, R., Walter, F., Aravena, M., et al. 2016, ApJ, 833, 70
Decarli, R., Walter, F., Carilli, C., et al. 2014, ApJ, 782, 78
Decarli, R., Walter, F., Gónzalez-López, J., et al. 2019, ApJ, 882, 138
Del Moro, A., Alexander, D. M., Mullaney, J. R., et al. 2013, A&A, 549, A59
Delhaize, J., Smolčić, V., Delvecchio, I., et al. 2017, A&A, 602, A4
Delvecchio, I., Daddi, E., Sargent, M. T., et al. 2021, A&A, 647, A123
Delvecchio, I., Gruppioni, C., Pozzi, F., et al. 2014, MNRAS, 439, 2736
Delvecchio, I., Smolčić, V., Zamorani, G., et al. 2018, MNRAS, 481, 4971
Delvecchio, I., Smolčić, V., Zamorani, G., et al. 2017, A&A, 602, A3
Dicke, R. H., Peebles, P. J. E., Roll, P. G., & Wilkinson, D. T. 1965, ApJ, 142, 414
Dickinson, M., Giavalisco, M., & GOODS Team. 2003, in The Mass of Galaxies at Low and High Redshift, ed. R. Bender & A. Renzini, 324
Donley, J. L., Koekemoer, A. M., Brusa, M., et al. 2012, ApJ, 748, 142
Dopita, M. A., Groves, B. A., Sutherland, R. S., & Kewley, L. J. 2003, ApJ, 583, 727
Downes, D. & Solomon, P. M. 1998, ApJ, 507, 615
Draine, B. T. 2003, ARA&A, 41, 241
Dudzevičiūtė, U., Smail, I., Swinbank, A. M., et al. 2020, MNRAS, 494, 3828
Duncan, K. J., Shivaei, I., Shapley, A. E., et al. 2020, MNRAS, 498, 3648
Elbaz, D., Dickinson, M., Hwang, H. S., et al. 2011, A&A, 533, A119
Elbaz, D., Leiton, R., Nagar, N., et al. 2018, A&A, 616, A110
Evans, A. S., Solomon, P. M., Tacconi, L. J., Vavilkin, T., & Downes, D. 2006, AJ, 132, 2398
Fabbiano, G. 2006, ARA&A, 44, 323
Fanali, R., Caccianiga, A., Severgnini, P., et al. 2013, MNRAS, 433, 648
Fanaroff, B. L. & Riley, J. M. 1974, MNRAS, 167, 31P
Farrah, D., Afonso, J., Efstathiou, A., et al. 2003, MNRAS, 343, 585
Farrah, D., Smith, K. E., Ardila, D., et al. 2019, Journal of Astronomical Telescopes, Instruments, and Systems, 5, 020901
Farrah, D., Urrutia, T., Lacy, M., et al. 2012, ApJ, 745, 178
Förster Schreiber, N. M., Genzel, R., Lutz, D., & Sternberg, A. 2003, ApJ, 599, 193
Frayer, D. T., Koda, J., Pope, A., et al. 2008, ApJ, 680, L21
Galvin, T. J., Seymour, N., Filipović, M. D., et al. 2016, MNRAS, 461, 825
Galvin, T. J., Seymour, N., Marvil, J., et al. 2018, MNRAS, 474, 779

Garrett, M. A. 2002, A&A, 384, L19
Geach, J. E., Dunlop, J. S., Halpern, M., et al. 2017, MNRAS, 465, 1789
Gehrels, N. 1986, ApJ, 303, 336
Giavalisco, M., Ferguson, H. C., Koekemoer, A. M., et al. 2004, ApJ, 600, L93
Gim, H. B., Yun, M. S., Owen, F. N., et al. 2019, ApJ, 875, 80
Gruppioni, C., Béthermin, M., Loiacono, F., et al. 2020, A&A, 643, A8
Gruppioni, C., Mignoli, M., & Zamorani, G. 1999, MNRAS, 304, 199
Gullberg, B., Smail, I., Swinbank, A. M., et al. 2019, MNRAS, 490, 4956
Gunn, J. E., Knapp, G. R., & Tremaine, S. D. 1979, AJ, 84, 1181
Haarsma, D. B., Partridge, R. B., Windhorst, R. A., & Richards, E. A. 2000, ApJ, 544, 641
Hainline, L. J., Blain, A. W., Smail, I., et al. 2011, ApJ, 740, 96
Hardcastle, M. J., Ching, J. H. Y., Virdee, J. S., et al. 2013, MNRAS, 429, 2407
Hashimoto, T., Laporte, N., Mawatari, K., et al. 2018, Nature, 557, 392
Heckman, T. M. & Best, P. N. 2014, ARA&A, 52, 589
Heger, A., Fryer, C. L., Woosley, S. E., Langer, N., & Hartmann, D. H. 2003, ApJ, 591, 288
Helou, G., Soifer, B. T., & Rowan-Robinson, M. 1985, ApJ, 298, L7
Herrera Ruiz, N., Middelberg, E., Deller, A., et al. 2017, A&A, 607, A132
Hoaglin, D. C., Mosteller, F., & Tukey, J. W. 1983, Understanding robust and exploratory data anlysis
Hodge, J. A., Carilli, C. L., Walter, F., et al. 2012, ApJ, 760, 11
Hodge, J. A. & da Cunha, E. 2020, Royal Society Open Science, 7, 200556
Hodge, J. A., Karim, A., Smail, I., et al. 2013, ApJ, 768, 91
Hodge, J. A., Swinbank, A. M., Simpson, J. M., et al. 2016, ApJ, 833, 103
Hoyle, F. 1948, MNRAS, 108, 372
Hubble, E. 1929, Proceedings of the National Academy of Science, 15, 168
Hubble, E. P. 1926, ApJ, 64, 321
Hughes, D. H., Serjeant, S., Dunlop, J., et al. 1998, Nature, 394, 241
Hummel, E. 1981, A&A, 93, 93
Huynh, M. T., Emonts, B. H. C., Kimball, A. E., et al. 2017, MNRAS, 467, 1222
Ibar, E., Ivison, R. J., Best, P. N., et al. 2010, MNRAS, 401, L53
Ibar, E., Ivison, R. J., Biggs, A. D., et al. 2009, MNRAS, 397, 281
Ilbert, O., Arnouts, S., McCracken, H. J., et al. 2006, A&A, 457, 841
Ilbert, O., Capak, P., Salvato, M., et al. 2009, ApJ, 690, 1236
Ilbert, O., McCracken, H. J., Le Fèvre, O., et al. 2013, A&A, 556, A55
Ilbert, O., Salvato, M., Le Floc'h, E., et al. 2010, ApJ, 709, 644
Inoue, A. K., Hirashita, H., & Kamaya, H. 2001, ApJ, 555, 613

Ivison, R. J., Alexander, D. M., Biggs, A. D., et al. 2010a, MNRAS, 402, 245
Ivison, R. J., Magnelli, B., Ibar, E., et al. 2010b, A&A, 518, L31
Ivison, R. J., Smail, I., Le Borgne, J. F., et al. 1998, MNRAS, 298, 583
Jarvis, M. J., Smith, D. J. B., Bonfield, D. G., et al. 2010, MNRAS, 409, 92
Jiménez-Andrade, E. F., Magnelli, B., Karim, A., et al. 2019, A&A, 625, A114
Jiménez-Andrade, E. F., Murphy, E. J., Heywood, I., et al. 2021, ApJ, 910, 106
Jin, S., Daddi, E., Liu, D., et al. 2018, ApJ, 864, 56
Jin, S., Daddi, E., Magdis, G. E., et al. 2019, ApJ, 887, 144
Kardashev, N. S. 1962, Soviet Ast., 6, 317
Karim, A., Schinnerer, E., Martínez-Sansigre, A., et al. 2011, ApJ, 730, 61
Karim, A., Swinbank, A. M., Hodge, J. A., et al. 2013, MNRAS, 432, 2
Kellermann, K. I., Bouton, E. N., & Brandt, S. S. 2020, Open Skies; The National Radio Astronomy Observatory and Its Impact on US Radio Astronomy
Kellermann, K. I. & Wall, J. V. 1987, in IAU Symposium, Vol. 124, Observational Cosmology, ed. A. Hewitt, G. Burbidge, & L. Z. Fang (Dordrecht: Reidel), 545–562
Kennicutt, R. C. & Evans, N. J. 2012, ARA&A, 50, 531
Kennicutt, Jr., R. C. 1998, ARA&A, 36, 189
Kereš, D., Katz, N., Weinberg, D. H., & Davé, R. 2005, MNRAS, 363, 2
Kimball, A. E., Knapp, G. R., Ivezić, Ž., et al. 2009, ApJ, 701, 535
King, A. & Pounds, K. 2015, ARA&A, 53, 115
Klein, U., Lisenfeld, U., & Verley, S. 2018, A&A, 611, A55
Kocevski, D. D., Hasinger, G., Brightman, M., et al. 2018, ApJS, 236, 48
Kormendy, J. & Ho, L. C. 2013, ARA&A, 51, 511
Kovács, A., Chapman, S. C., Dowell, C. D., et al. 2006, ApJ, 650, 592
Kriek, M., Shapley, A. E., Reddy, N. A., et al. 2015, ApJS, 218, 15
Krumholz, M. R. & Tan, J. C. 2007, ApJ, 654, 304
Lacki, B. C. & Thompson, T. A. 2010, ApJ, 717, 196
Lacki, B. C., Thompson, T. A., & Quataert, E. 2010, ApJ, 717, 1
Lacy, M., Storrie-Lombardi, L. J., Sajina, A., et al. 2004, ApJS, 154, 166
Laigle, C., McCracken, H. J., Ilbert, O., et al. 2016, ApJS, 224, 24
Le Fèvre, O., Tasca, L. A. M., Cassata, P., et al. 2015, A&A, 576, A79
Le Floc'h, E., Aussel, H., Ilbert, O., et al. 2009, ApJ, 703, 222
Lee, S.-K., Ferguson, H. C., Somerville, R. S., Wiklind, T., & Giavalisco, M. 2010, ApJ, 725, 1644
Lehmer, B. D., Alexander, D. M., Bauer, F. E., et al. 2010, ApJ, 724, 559
Lemaître, G. 1927, Annales de la Société Scientifique de Bruxelles, 47, 49
Leroy, A. K., Evans, A. S., Momjian, E., et al. 2011, ApJ, 739, L25

Leslie, S. K., Schinnerer, E., Liu, D., et al. 2020, ApJ, 899, 58
Licquia, T. C. & Newman, J. A. 2015, ApJ, 806, 96
Lilly, S. J., Le Brun, V., Maier, C., et al. 2009, ApJS, 184, 218
Lilly, S. J., Le Fèvre, O., Renzini, A., et al. 2007, ApJS, 172, 70
Linden, S. T., Murphy, E. J., Dong, D., et al. 2020, ApJS, 248, 25
Lindner, R. R., Baker, A. J., Omont, A., et al. 2011, ApJ, 737, 83
Lisenfeld, U., Völk, H. J., & Xu, C. 1996, A&A, 306, 677
Liu, D., Daddi, E., Dickinson, M., et al. 2018, ApJ, 853, 172
Liu, D., Schinnerer, E., Groves, B., et al. 2019, ApJ, 887, 235
López-Sanjuan, C., Balcells, M., Pérez-González, P. G., et al. 2009, A&A, 501, 505
Lusso, E., Comastri, A., Vignali, C., et al. 2011, A&A, 534, A110
Lutz, D., Poglitsch, A., Altieri, B., et al. 2011, A&A, 532, A90
Lynden-Bell, D. 1969, Nature, 223, 690
Lyu, J. & Rieke, G. H. 2017, ApJ, 841, 76
Madau, P. & Dickinson, M. 2014, ARA&A, 52, 415
Magnelli, B., Ivison, R. J., Lutz, D., et al. 2015, A&A, 573, A45
Magnelli, B., Lutz, D., Berta, S., et al. 2010, A&A, 518, L28
Magnelli, B., Popesso, P., Berta, S., et al. 2013, A&A, 553, A132
Magorrian, J., Tremaine, S., Richstone, D., et al. 1998, AJ, 115, 2285
Mahatma, V. H., Hardcastle, M. J., Williams, W. L., et al. 2018, MNRAS, 475, 4557
Maini, A., Prandoni, I., Norris, R. P., Giovannini, G., & Spitler, L. R. 2016, A&A, 589, L3
Mancuso, C., Lapi, A., Cai, Z.-Y., et al. 2015, ApJ, 810, 72
Mao, M. Y., Huynh, M. T., Norris, R. P., et al. 2011, ApJ, 731, 79
Marchesi, S., Civano, F., Elvis, M., et al. 2016a, ApJ, 817, 34
Marchesi, S., Lanzuisi, G., Civano, F., et al. 2016b, ApJ, 830, 100
Mason, B. S., Weintraub, L., Sievers, J., et al. 2009, ApJ, 704, 1433
Massardi, M., Bonaldi, A., Negrello, M., et al. 2010, MNRAS, 404, 532
Matthee, J. & Schaye, J. 2019, MNRAS, 484, 915
McAlpine, S., Smail, I., Bower, R. G., et al. 2019, MNRAS, 488, 2440
McBride, J., Quataert, E., Heiles, C., & Bauermeister, A. 2014, ApJ, 780, 182
McBride, J., Robishaw, T., Heiles, C., Bower, G. C., & Sarma, A. P. 2015, MNRAS, 447, 1103
McCracken, H. J., Milvang-Jensen, B., Dunlop, J., et al. 2012, A&A, 544, A156
McKinnon, M., Beasley, A., Murphy, E., et al. 2019, in Bulletin of the American Astronomical Society, Vol. 51, 81
McNamara, B. R. & Nulsen, P. E. J. 2012, New Journal of Physics, 14, 055023
Michałowski, M. J. 2015, A&A, 577, A80

Michałowski, M. J., Dunlop, J. S., Cirasuolo, M., et al. 2012, A&A, 541, A85
Middelberg, E., Deller, A. T., Norris, R. P., et al. 2013, A&A, 551, A97
Miettinen, O., Delvecchio, I., Smolčić, V., et al. 2017, A&A, 597, A5
Mohan, N. & Rafferty, D. 2015, PyBDSF: Python Blob Detection and Source Finder, Astrophysics Source Code Library
Molnár, D. C., Sargent, M. T., Delhaize, J., et al. 2018, MNRAS, 475, 827
Molnár, D. C., Sargent, M. T., Leslie, S., et al. 2021, MNRAS, 504, 118
Momcheva, I. G., Brammer, G. B., van Dokkum, P. G., et al. 2016, ApJS, 225, 27
Momjian, E., Wang, W.-H., Knudsen, K. K., et al. 2010, AJ, 139, 1622
Morganti, R., Fogasy, J., Paragi, Z., Oosterloo, T., & Orienti, M. 2013, Science, 341, 1082
Morrison, G. E., Owen, F. N., Dickinson, M., Ivison, R. J., & Ibar, E. 2010, ApJS, 188, 178
Murphy, E. J. 2009a, ApJ, 706, 482
Murphy, E. J. 2009b, ApJ, 706, 482
Murphy, E. J. 2013, ApJ, 777, 58
Murphy, E. J., Bolatto, A., Chatterjee, S., et al. 2018, in Astronomical Society of the Pacific Conference Series, Vol. 517, Science with a Next Generation Very Large Array, ed. E. Murphy, 3
Murphy, E. J., Bremseth, J., Mason, B. S., et al. 2012, ApJ, 761, 97
Murphy, E. J. & Chary, R.-R. 2018, ApJ, 861, 27
Murphy, E. J., Chary, R. R., Alexander, D. M., et al. 2009, ApJ, 698, 1380
Murphy, E. J., Condon, J. J., Schinnerer, E., et al. 2011, ApJ, 737, 67
Murphy, E. J., Dong, D., Leroy, A. K., et al. 2015, ApJ, 813, 118
Murphy, E. J., Hensley, B. S., Linden, S. T., et al. 2020, ApJ, 905, L23
Murphy, E. J., Momjian, E., Condon, J. J., et al. 2017, ApJ, 839, 35
Murray, N. 2011, ApJ, 729, 133
Muxlow, T. W. B., Richards, A. M. S., Garrington, S. T., et al. 2005, MNRAS, 358, 1159
Muxlow, T. W. B., Thomson, A. P., Radcliffe, J. F., et al. 2020, MNRAS, 495, 1188
Muzzin, A., Marchesini, D., Stefanon, M., et al. 2013, ApJS, 206, 8
Nagar, N. M., Falcke, H., Wilson, A. S., & Ho, L. C. 2000, ApJ, 542, 186
Neugebauer, G., Habing, H. J., van Duinen, R., et al. 1984, ApJ, 278, L1
Niklas, S., Klein, U., & Wielebinski, R. 1997, A&A, 322, 19
Noeske, K. G., Weiner, B. J., Faber, S. M., et al. 2007, ApJ, 660, L43
Novak, M., Smolčić, V., Delhaize, J., et al. 2017, A&A, 602, A5
Novak, M., Smolčić, V., Schinnerer, E., et al. 2018, A&A, 614, A47
Ocran, E. F., Taylor, A. R., Vaccari, M., et al. 2020, MNRAS, 491, 5911

Oesch, P. A., Bouwens, R. J., Illingworth, G. D., et al. 2013, ApJ, 773, 75
Oesch, P. A., Bouwens, R. J., Illingworth, G. D., Labbé, I., & Stefanon, M. 2018, ApJ, 855, 105
Offringa, A. R., McKinley, B., Hurley-Walker, N., et al. 2014, MNRAS, 444, 606
Ogle, P., Whysong, D., & Antonucci, R. 2006, ApJ, 647, 161
Oke, J. B. & Gunn, J. E. 1983, ApJ, 266, 713
Oliver, S. J., Bock, J., Altieri, B., et al. 2012, MNRAS, 424, 1614
Owen, F. N. 2018, ApJS, 235, 34
Padovani, P., Alexander, D. M., Assef, R. J., et al. 2017, A&A Rev., 25, 2
Padovani, P., Bonzini, M., Kellermann, K. I., et al. 2015, MNRAS, 452, 1263
Padovani, P., Mainieri, V., Tozzi, P., et al. 2009, ApJ, 694, 235
Padovani, P., Miller, N., Kellermann, K. I., et al. 2011, ApJ, 740, 20
Panessa, F., Baldi, R. D., Laor, A., et al. 2019, Nature Astronomy, 3, 387
Pavesi, R., Riechers, D. A., Capak, P. L., et al. 2016, ApJ, 832, 151
Pavesi, R., Sharon, C. E., Riechers, D. A., et al. 2018, ApJ, 864, 49
Penner, K., Pope, A., Chapin, E. L., et al. 2011, MNRAS, 410, 2749
Penney, J. I., Blain, A. W., Assef, R. J., et al. 2020, MNRAS, 496, 1565
Planck Collaboration, Aghanim, N., Akrami, Y., et al. 2020, A&A, 641, A6
Pope, A., Borys, C., Scott, D., et al. 2005, MNRAS, 358, 149
Prandoni, I., Guglielmino, G., Morganti, R., et al. 2018, MNRAS, 481, 4548
Prandoni, I. & Seymour, N. 2015, Advancing Astrophysics with the Square Kilometre Array (AASKA14), 67
Priester, W. 1958, ZAp, 46, 179
Querejeta, M., Schinnerer, E., Schruba, A., et al. 2019, A&A, 625, A19
Ramasawmy, J., Geach, J. E., Hardcastle, M. J., et al. 2021, A&A, 648, A14
Read, S. C., Smith, D. J. B., Gürkan, G., et al. 2018, MNRAS, 480, 5625
Reines, A. E., Sivakoff, G. R., Johnson, K. E., & Brogan, C. L. 2011, Nature, 470, 66
Richstone, D., Ajhar, E. A., Bender, R., et al. 1998, Nature, 385, A14
Riechers, D. A., Bradford, C. M., Clements, D. L., et al. 2013, Nature, 496, 329
Riechers, D. A., Carilli, C. L., Capak, P. L., et al. 2014, ApJ, 796, 84
Riechers, D. A., Hodge, J. A., Pavesi, R., et al. 2020, ApJ, 895, 81
Riechers, D. A., Pavesi, R., Sharon, C. E., et al. 2019, ApJ, 872, 7
Robishaw, T., Quataert, E., & Heiles, C. 2008, ApJ, 680, 981
Rovilos, E. & Georgantopoulos, I. 2007, A&A, 475, 115
Rowan-Robinson, M., Benn, C. R., Lawrence, A., McMahon, R. G., & Broadhurst, T. J. 1993, MNRAS, 263, 123
Rujopakarn, W., Nyland, K., & Kimball, A. E. 2018, arXiv e-prints,

arXiv:1810.07098
Rybak, M., Calistro Rivera, G., Hodge, J. A., et al. 2019, ApJ, 876, 112
Ryle, M. & Clarke, R. W. 1961, MNRAS, 122, 349
Sabater, J., Best, P. N., Hardcastle, M. J., et al. 2019, A&A, 622, A17
Saintonge, A., Catinella, B., Cortese, L., et al. 2016, MNRAS, 462, 1749
Salpeter, E. E. 1955, ApJ, 121, 161
Salvato, M., Ilbert, O., Hasinger, G., et al. 2011, ApJ, 742, 61
Sanders, D. B. & Mirabel, I. F. 1996, ARA&A, 34, 749
Sanders, D. B., Salvato, M., Aussel, H., et al. 2007, ApJS, 172, 86
Santini, P., Maiolino, R., Magnelli, B., et al. 2014, A&A, 562, A30
Sargent, M. T., Schinnerer, E., Murphy, E., et al. 2010, ApJ, 714, L190
Schaye, J., Crain, R. A., Bower, R. G., et al. 2015, MNRAS, 446, 521
Schinnerer, E., Sargent, M. T., Bondi, M., et al. 2010, ApJS, 188, 384
Schinnerer, E., Smolčić, V., Carilli, C. L., et al. 2007, ApJS, 172, 46
Schleicher, D. R. G. & Beck, R. 2013, A&A, 556, A142
Schmidt, M. 1963, Nature, 197, 1040
Schouws, S., Stefanon, M., Bouwens, R. J., et al. 2021, arXiv e-prints, arXiv:2105.12133
Schreiber, C., Pannella, M., Elbaz, D., et al. 2015, A&A, 575, A74
Scoville, N., Aussel, H., Brusa, M., et al. 2007, ApJS, 172, 1
Selina, R. J., Murphy, E. J., McKinnon, M., et al. 2018, in SPIE Astronomical Telescopes and Instrumentation conference, Vol. 10700, Ground-based and Airborne Telescopes VII, ed. H. K. Marshall & J. Spyromilio (New York: Curran Associates, Inc.), 107001O
Seymour, N., McHardy, I. M., & Gunn, K. F. 2004, MNRAS, 352, 131
Shankar, F., Weinberg, D. H., & Miralda-Escudé, J. 2009, ApJ, 690, 20
Shivaei, I., Kriek, M., Reddy, N. A., et al. 2016, ApJ, 820, L23
Simpson, J. M., Smail, I., Dudzevičiūtė, U., et al. 2020, MNRAS, 495, 3409
Simpson, J. M., Smail, I., Swinbank, A. M., et al. 2015, ApJ, 799, 81
Simpson, J. M., Swinbank, A. M., Smail, I., et al. 2014, ApJ, 788, 125
Skelton, R. E., Whitaker, K. E., Momcheva, I. G., et al. 2014, ApJS, 214, 24
Smail, I., Ivison, R. J., & Blain, A. W. 1997, ApJ, 490, L5
Smail, I., Ivison, R. J., Owen, F. N., Blain, A. W., & Kneib, J. P. 2000, ApJ, 528, 612
Smith, D. J. B., Haskell, P., Gürkan, G., et al. 2020, arXiv e-prints, arXiv:2011.08196
Smolčić, V. 2009, ApJ, 699, L43
Smolčić, V., Delvecchio, I., Zamorani, G., et al. 2017a, A&A, 602, A2

Smolčić, V., Novak, M., Bondi, M., et al. 2017b, A&A, 602, A1
Smolčić, V., Schinnerer, E., Zamorani, G., et al. 2009, ApJ, 690, 610
Soifer, B. T., Neugebauer, G., & Houck, J. R. 1987, ARA&A, 25, 187
Solomon, P. M., Downes, D., Radford, S. J. E., & Barrett, J. W. 1997, ApJ, 478, 144
Sparre, M., Hayward, C. C., Springel, V., et al. 2015, MNRAS, 447, 3548
Speagle, J. S., Steinhardt, C. L., Capak, P. L., & Silverman, J. D. 2014, ApJS, 214, 15
Springel, V., Di Matteo, T., & Hernquist, L. 2005, MNRAS, 361, 776
Stach, S. M., Dudzevičiūtė, U., Smail, I., et al. 2019, MNRAS, 487, 4648
Steidel, C. C., Giavalisco, M., Pettini, M., Dickinson, M., & Adelberger, K. L. 1996, ApJ, 462, L17
Swinbank, A. M., Simpson, J. M., Smail, I., et al. 2014, MNRAS, 438, 1267
Symeonidis, M., Georgakakis, A., Page, M. J., et al. 2014, Monthly Notices of the Royal Astronomical Society, 443, 3728
Tabatabaei, F. S., Schinnerer, E., Krause, M., et al. 2017, ApJ, 836, 185
Tabatabaei, F. S., Schinnerer, E., Murphy, E. J., et al. 2013, A&A, 552, A19
Takagi, T., Vansevicius, V., & Arimoto, N. 2003, PASJ, 55, 385
Tal, T., Dekel, A., Oesch, P., et al. 2014, ApJ, 789, 164
Thompson, T. A., Quataert, E., Waxman, E., Murray, N., & Martin, C. L. 2006, ApJ, 645, 186
Thomson, A. P., Ivison, R. J., Owen, F. N., et al. 2015, MNRAS, 448, 1874
Thomson, A. P., Ivison, R. J., Simpson, J. M., et al. 2014, MNRAS, 442, 577
Thomson, A. P., Ivison, R. J., Smail, I., et al. 2012, MNRAS, 425, 2203
Thomson, A. P., Smail, I., Swinbank, A. M., et al. 2019, ApJ, 883, 204
Tisanić, K., Smolčić, V., Delhaize, J., et al. 2019, A&A, 621, A139
Van der Kruit, P. C. 1971, A&A, 15, 110
Van der Kruit, P. C. 1973, A&A, 29, 263
van der Vlugt, D., Algera, H. S. B., Hodge, J. A., et al. 2021, ApJ, 907, 5
van der Wel, A., Franx, M., van Dokkum, P. G., et al. 2014, ApJ, 788, 28
Varenius, E., Conway, J. E., Martí-Vidal, I., et al. 2016, A&A, 593, A86
Ventou, E., Contini, T., Bouché, N., et al. 2017, A&A, 608, A9
Völk, H. J. 1989, A&A, 218, 67
Wagg, J., Carilli, C. L., Aravena, M., et al. 2014, ApJ, 783, 71
Walter, F., Carilli, C., Neeleman, M., et al. 2020, ApJ, 902, 111
Walter, F., Decarli, R., Aravena, M., et al. 2016, ApJ, 833, 67
Wang, F., Yang, J., Fan, X., et al. 2019, ApJ, 884, 30
Wang, R., Carilli, C. L., Neri, R., et al. 2010, ApJ, 714, 699
Wang, S. X., Brandt, W. N., Luo, B., et al. 2013, ApJ, 778, 179

Weiß, A., Kovács, A., Coppin, K., et al. 2009, ApJ, 707, 1201
Whitaker, K. E., Pope, A., Cybulski, R., et al. 2017, ApJ, 850, 208
White, R. L., Helfand, D. J., Becker, R. H., Glikman, E., & de Vries, W. 2007, ApJ, 654, 99
Williams, R. J., Quadri, R. F., Franx, M., van Dokkum, P., & Labbé, I. 2009, ApJ, 691, 1879
Wilman, R. J., Miller, L., Jarvis, M. J., et al. 2008, MNRAS, 388, 1335
Xu, J., Sun, M., & Xue, Y. 2020, ApJ, 894, 21
Xue, Y. Q., Luo, B., Brandt, W. N., et al. 2016, ApJS, 224, 15
Yoast-Hull, T. M., Gallagher, J. S., & Zweibel, E. G. 2016, MNRAS, 457, L29
Yun, M. S., Hibbard, J. E., Condon, J. J., & Reddy, N. 1999, Ap&SS, 266, 29
Yun, M. S., Reddy, N. A., & Condon, J. J. 2001, ApJ, 554, 803
Zamojski, M. A., Schiminovich, D., Rich, R. M., et al. 2007, ApJS, 172, 468
Zavala, J. A., Casey, C. M., Manning, S. M., et al. 2021, ApJ, 909, 165

Summary

When observed from a dark place on Earth, the night sky appears as a vast white band of stars, stretched out as far as the eye can see. This collection of stars, in addition to several constituents that are not so readily visible with the human eye (gas, dust, and the mysterious dark matter), is known as the *Milky Way*. It wasn't until the mid 1920s that astronomers realized the Milky Way is but one in a sea of many millions of other "Milky Ways", referred to as *galaxies*.

The earliest galaxies formed already within the first few hundred million years after the beginning of the Universe – the *Big Bang*, which in turn occurred some 13.8 billion years ago. Nowadays, we observe galaxies to take on a wide variety of shapes and sizes (as illustrated in Figure 1.2 in Chapter 1). If, for example, we could look at the Milky Way as an outside observer, we would see it to resemble a flat blue spiral disk. Other galaxies, however, may appear red and elliptical in nature, while even others are so enshrouded in cosmic dust that they are (nearly) invisible to the human eye. One of the major questions in astronomy, therefore, is to understand how galaxies evolve from the small, young systems that form in the early Universe to the varied population we observe today.

Studying the evolution of galaxies, however, is complicated by the fact that individual galaxies evolve very, very slowly. The Sun, for example, takes over 200 million years to orbit around the Milky Way just once. Indeed, the timescales involved are far too large for astronomers to watch galaxies evolve in real time. Instead, it is necessary to observe many different galaxies, at different stages in their lives, and compare the way they look. Nature, as luck would have it, provides a very useful way of looking at the youngest galaxy populations: since the speed of light is finite and – in the grand scheme of things – relatively slow, it takes the light emitted by distant galaxies a long time to reach our telescopes on Earth. In turn, observing the earliest formed galaxies is equivalent to observing the most distant ones. By then observing galaxies at various distances, across various cosmic epochs, we can attempt to infer and stitch together their evolutionary pathways.

Figure 1: The Orion nebula, the nearest – and quite possibly also most famous – star-forming region to Earth, as observed by the *Hubble Space Telescope* at various visible and infrared wavelengths. Nebulae such as Orion form the birthplace of stars in galaxies. Credit: NASA, ESA, M. Robberto (STSCI/ESA) and the Hubble Space Telescope Orion Treasury Project Team.

One of the crucial parameters describing the evolution of galaxies is their *star formation rate*, which is a measure of the average yearly mass formed in stars. These stars themselves are born out of the molecular gas in galaxies, in large stellar nurseries such as the famous Orion Nebula (Figure 1). However, star formation itself is also a lengthy process, spanning a timescale of millions of years. In addition, in distant galaxies it is generally impossible to observe individual stellar birth clouds, let alone individual stars. As such, measuring the buildup of stars in galaxies requires more sophisticated techniques, which not only encompass the light visible to the human eye, but also light at a variety of other wavelengths, such as the energetic ultraviolet light, and the low-energy infrared, millimeter and radio wavelengths.

Young, massive stars, for example, emit copious amounts of ultraviolet radiation, and in turn observing a galaxy that is bright at these wavelengths

is a surefire sign it is actively forming stars. Some of the most strongly star-forming galaxies, however, are actually surprisingly faint in the ultraviolet, as they are heavily obscured by cosmic dust. Dust gets heated when it absorbs light emitted at short wavelengths, and subsequently radiates its energy at infrared wavelengths. Indeed, over half of all star formation in galaxies is in fact *dust-obscured*. Infrared-bright galaxies, in turn, can be some of the most strongly star-forming galaxies in the Universe, possibly attaining star formation rates in excess of 1000 times that of the Milky Way. Combined, ultraviolet and infrared observations have mapped the *cosmic star formation rate density* – the average star formation rate of galaxies in the Universe – all the way back to the first billion years after the Big Bang (Figure 1.7).

However, both ultraviolet and infrared-based measurements of star formation are plagued by some issues that limit their ability to accurately probe star formation in the early Universe. Sensitive ultraviolet telescopes can probe star formation even in faint, distant galaxies, but are heavily susceptible to attenuation by dust. Infrared telescopes, on the other hand tend to not be sensitive enough to detect galaxies in the very early Universe, and have poorer resolution, meaning they cannot see galaxies as sharply. Observations at radio wavelengths provide a means to circumvent these issues, and form the main topic of this thesis.

Galaxies at Radio Wavelengths

The most powerful radio telescopes are so-called *radio interferometers*. Such telescopes consist of multiple individual radio dishes, which all work in unison in order to create the sharpest view of the radio sky. In addition, having multiple dishes increases the collecting area, in turn allowing for observations of fainter objects. The radio telescope most instrumental to this thesis, the 27 dish-strong Very Large Array (VLA) in New Mexico, USA, is shown in Figure 2.

Radio emission from galaxies may be powered through star formation, as well as through a supermassive black hole hosted in the galaxy center known as an *active galactic nucleus* (AGN). Star-forming galaxies tend to be faint at radio wavelengths, whereas AGN are generally significantly brighter. As such, previous studies of the radio sky have predominantly been limited to either nearby or strongly star-forming galaxies and bright AGN, whereas the typical galaxy population has mostly remained undetected (see also Figure 1.8). With the 2012 upgrade of the VLA, which improved its sensitivity by an order of magnitude, the *faint radio sky* is now

Figure 2: The Karl G. Jansky Very Large Array (VLA), originally built in the 1970s in New Mexico, USA, remains the most productive radio telescope of all time, and is instrumental to this thesis. While rendering any optical telescope mostly useless, the cloud cover seen in this image cannot deter the VLA. Credit: National Radio Astronomy Observatory.

finally within reach, and constitutes the topic of this thesis.

A star-forming galaxy emits radio waves via two processes: *synchrotron emission* and *free-free emission*. Free-free emission is produced directly upon the formation of young, massive stars, while synchrotron radiation is the result of these same stars ending their lives in powerful *supernova* explosions. While free-free emission is therefore clearly a more direct, and hence more powerful, tracer of recent star formation, it is very difficult to study in the early Universe, as it is considerably fainter than the synchrotron component (Figure 1.5). Synchrotron emission, in turn, has been much more widely utilized as a tracer of star formation, despite being more complex to interpret. The structure of this thesis reflects this: in Chapters 2 & 3, we study the synchrotron emission of faint, star-forming galaxies, while we present two pioneering studies of free-free emission in Chapters 4 & 5. We summarize our findings in these chapters below.

This Thesis

In this thesis, we take advantage of the "revolution" that is currently taking place within radio astronomy: within the last decade, various new radio telescopes have been constructed, while others have been significantly upgraded, providing new, sensitive observations and revolutionizing our understanding of the radio sky. **Chapter One** introduces the current state of the field, and discusses this revolution in detail, in addition to providing the necessary background information for the subsequent chapters.

In **Chapter Two**, we analyze the faint radio population discovered in the sensitive *COSMOS-XS* survey. Carried out with the upgraded VLA, COSMOS-XS provides some of the deepest radio observations to date, at two different frequencies. We utilize the new 3 GHz data, in addition to multi-wavelength observations spanning the X-ray to sub-millimeter regime, to study the composition of the radio sky and classify the radio population as either star-forming or AGN. Among the more than 1500 galaxies detected at 3 GHz, over 90% show radio emission powered by star formation. In turn, we show that the fraction of star-forming galaxies depends strongly on the flux limit of the parent survey, with fainter galaxy populations more likely to be dominated by star formation as opposed to AGN activity. In addition, we discover an interesting subset of galaxies that remain undetected even in deep optical and near-infrared observations. Through a stacking technique, we argue that these galaxies are likely very distant in nature (with a typical redshift of $z \sim 4-5$), implying these may contribute significantly to cosmic star formation.

Chapter Three presents a detailed analysis of the *far-infrared/radio correlation* in dusty star-forming galaxies. This link between the radio and infrared luminosities of galaxies, which has been observed across a wide variety of galaxy types, as well as out to high redshift, provides the crucial recipe needed for converting radio synchrotron luminosities into star formation rates. However, its theoretical origins remain poorly understood, and likely hinges on a variety of physical processes in galaxies "conspiring". Dusty star-forming galaxies form the perfect laboratory for studies of the far-infrared/radio correlation, as they allow for an investigation of the correlation in extreme physical conditions, mostly unbiased by selection effects.

Upon combining deep observations from the *Atacama Large Millimeter Array* for nearly 700 dusty star-forming galaxies with deep radio ob-

servations from the VLA, we determine the far-infrared/radio correlation to be independent of cosmic time in these dusty starbursting systems. This is in contrast to previous studies of the correlation for more heterogeneous – and therefore likely more biased – galaxy samples. In addition, we determine the correlation for dusty star-forming galaxies in the early Universe to be offset from the correlation in local starburst galaxies, which we attribute to the different physical conditions between these systems.

In **Chapter Four** we perform a pioneering study of radio free-free emission in the early Universe. Making use of new observations taken at 34 GHz as part of the COLDz survey, in addition to radio observations spanning multiple lower frequencies, we have an unprecedented view of the *radio spectra* of the faint galaxy population. We detect 18 galaxies in the new 34 GHz observations, seven of which are star-forming galaxies. Utilizing the multi-frequency radio observations, we disentangle the radio spectra of the star-forming systems into their synchrotron and free-free emission, allowing us to use the latter as a tracer of star formation in the early Universe. We show that the star formation rates obtained from free-free emission are in agreement with those from canonically used tracers, and elaborate how next-generation radio telescopes will revolutionize studies of free-free emission in distant galaxies.

Chapter Five expands the scope of the previous chapter to significantly larger galaxy samples through the powerful technique of *stacking*. While individual galaxies are generally too faint to detect at high observing frequencies, our stacking analysis combines the emission from large numbers of distant sources and allows for a census of the average radio spectra of star-forming galaxies. This, in turn, allows us to study free-free emission in faint, representative galaxies.

We find that galaxies in the early Universe tend to be fainter at high frequencies than would be expected from a naive extrapolation of local observations. We attribute this to *spectral ageing* at high frequencies, causing a deficit of synchrotron emission in a mature starburst. We subsequently utilize the high-frequency free-free component to determine the cosmic star formation rate density, thereby providing the first such constraints with radio free-free emission.

Samenvatting

Wanneer deze wordt waargenomen vanaf een donkere locatie op Aarde, lijkt de nachtelijke hemel te bestaan uit een langgerekte, witte wolk van sterren, zo ver als men kan zien. Deze verzameling sterren, plus een aantal andere ingrediënten die niet zo goed met het blote oog te zien zijn (kosmisch gas, stof en een mysterieuze substantie die we als donkere materie bestempelen), noemen we de *Melkweg*. Pas in de jaren '20 van de vorige eeuw beseften sterrenkundigen dat de Melkweg slechts één van een gigantisch aantal andere "Melkwegen" is. Onze Melkweg, evenals de vele soortgelijke objecten in het heelal, noemen we *sterrenstelsels*.

Al snel na het ontstaan van het helaal in de zogeheten *Oerknal*, die grofweg 13.8 miljard jaar geleden plaatsvond, vormden de eerste sterrenstelsels (ter vergelijking, de Aarde en de Zon zijn ongeveer 4.5 miljard jaar oud). Sindsdien hebben sterrenstelsels een divers aantal vormen en groottes aangenomen, zoals is te zien in Afbeelding 1.2 in Hoofdstuk 1. Als het mogelijk was geweest om de Melkweg van een afstand te bekijken, zouden we haar waarnemen als een blauwe schijf met daarin een karakteristieke spiraalstructuur. Andere stelsels, echter, ogen rood, en zijn nagenoeg rond of elliptisch. Er bestaan zelfs sterrenstelsels die omhuld zijn in zoveel kosmisch stof, dat (bijna) al het licht wordt uitgezonden op golflengten die niet met het blote oog te zien zijn. Wat sterrenkundigen daarom graag zouden begrijpen is hoe sterrenstelsels evolueren van kleine, jonge stelsels in het vroege Universum, tot aan de verscheidenheid van stelsels die we vandaag de dag met telescopen kunnen waarnemen.

Het begrijpen van de evolutie van sterrenstelsels wordt echter bemoeilijkt door het feit dat de evolutie van individuele stelsels een erg langzaam proces is. De tijd die de Zon nodig heeft om eenmaal de Melkweg te doorkruisen is ongeveer 200 miljoen jaar, oftewel, de laatste keer dat de Zon zich op haar huidige positie bevond, bewandelden de dinosauriërs nog de Aarde. De evolutie van sterrenstelsels kan daarom niet simpelweg begrepen worden door stelsels langere tijd te bekijken. In plaats daarvan is het nodig om een groot aantal verschillende sterrenstelsels te bestuderen – zowel jonge als oude stelsels – en deze met elkaar te vergelijken. Alleen op deze

manier kunnen mogelijke evolutionaire paden waarop sterrenstelsels de tijd doorkruisen worden begrepen. Gelukkig is dit mogelijk binnen de sterrenkunde, omdat de natuur ons een handje helpt. De snelheid van licht is niet oneindig, en is zelfs redelijk langzaam op de schaal van het Universum. Het licht dat wordt uitgezonden door verafgelegen sterrenstelsels heeft daarom een lange tijd nodig om onze telescopen te bereiken. Het waarnemen van de verste sterrenstelsels vormt dus de manier om ook de jongste stelsels te bestuderen en te begrijpen, en maakt het mogelijk om een theorie van de evolutie van sterrenstelsels op te bouwen.

Één van de meest nuttige parameters die de evolutie van sterrenstelsels beschrijft is de *stervormingssnelheid*, welke meet hoeveel zonsmassa's in sterren er jaarlijks worden gevormd in een sterrenstelsel. Sterren zelf worden geboren uit gigantische stofwolken, zoals de prachtige Orionnevel, getoond in Afbeelding 3. Zelfs de geboorte van individuele sterren, echter, is een tijdrovend proces wat miljoenen jaren in beslag neemt. Bovendien is het doorgaans onmogelijk om zulke individuele stofwolken waar te nemen in verafgelegen sterrenstelsels, laat staan individuele sterren. Het is daarom nodig om meer geraffineerde technieken te gebruiken om stervorming in verre sterrenstelsels te meten. Zulke technieken maken niet alleen gebruik van de golflengten waarop het menselijk oog werkt, maar ook van ultraviolet licht, alsmede infrarode en radio golflengten.

Jonge, massieve sterren, bijvoorbeeld, zijn veel heter dan de Zon, en stralen vele malen meer ultraviolet licht uit. Van een sterrenstelsel dat helder is op ultraviolette golflengten kunnen we daarom veronderstellen dat het op hoge snelheid sterren aan het vormen is. De meest stervormende sterrenstelsels zijn echter verrassend zwak in het ultraviolet, omdat ze omgeven zijn door grote hoeveelheden kosmisch stof. Zulk stof absorbeert ultraviolet licht, en zendt het weer uit op infrarode golflengten. Op deze manier kan stervorming ook worden gemeten door middel van het infrarode licht van sterrenstelselsels. Gezamelijk hebben ultraviolette en infrarode metingen aan sterrenstelsels de *kosmische stervormingssnelheid* weten te bepalen; dit is de gemiddelde stervormingssnelheid van alle sterrenstelsels in het heelal, op een gegeven ogenblik in het kosmisch verleden. Vandaag de dag hebben metingen aan de kosmische stervormingssnelheid deze weten te bepalen tot aan de eerste miljard jaar na de Oerknal (Afbeelding 1.7).

Ultraviolette en infrarode metingen van stervorming zijn echter niet zonder problemen. Zoals genoemd zijn ultraviolette waarnemingen erg

Figure 3: De dichtstbijzijnde – en hoogstwaarschijnlijk ook meest beroemde – stervormingsnevel; Orion. Deze foto is genomen met de ruimtetelescoop Hubble, en maakt gebruik van verschillende optische en infrarode golflengten. Gaswolken zoals de Orionnevel vormen de geboorteplaats van sterren in sterrenstelsels. Bron: NASA, ESA, M. Robberto (STSCI/ESA) en het Hubble Space Telescope Orion Treasury Project Team.

vatbaar voor de aanwezigheid van kosmisch stof, en kunnen erg stofrijke sterrenstelsels niet op deze golflengten worden waargenomen. Telescopen die gebruik maken van infrarood licht zijn echter vaak minder gevoelig, waardoor het vaak onmogelijk is om de meest afgelegen sterrenstelsels waar te nemen. Bovendien zien infrarode telescopen vaak minder scherp, wat waarnemingen van jonge, kleine sterrenstelsels verder bemoeilijkt. Een mogelijke oplossing die deze problemen weet te omzeilen, is het waarnemen van sterrenstelsels met radiostraling.

Sterrenstelsels op Radiogolflengten

De meest krachtige radiotelescopen zijn zogeheten *interferometers*. Zulke interferometers bestaan uit meerdere kleinere telescopen die allen samenwerken om een scherp beeld van de radiohemel te produceren. Bovendien schaalt de gevoeligheid van een interferometer met het aantal telescopen

Figure 4: De Karl G. Jansky Very Large Array (VLA), oorspronkelijk gebouwd in the de jaren '70 van de 20ste eeuw in de Verenigde Staten, is de meest productive (én iconische) radiotelescoop ter wereld. Hoewel het wolkendek hangende boven de telescoop elke optische waarnemingen zou verhinderen, is dit geen probleem voor een radiotelescoop. Bron: National Radio Astronomy Observatory.

waaruit deze bestaat, zodat een grote interferometer in staat is om zwakke en afgelegen sterrenstelsels waar te nemen. De radiotelescoop die voor dit proefschrift het meest essentieel is geweest, is de *Very Large Array* (VLA) in de Verenigde Staten, bestaande uit 27 telescopen elk met een diameter van 25 meter. De VLA is te zien in Afbeelding 4.

De radiostraling afkomstig van sterrenstelsels heeft twee mogelijke oorsprongen: een superzwaar zwart gat (EN: *supermassive black hole*) in het centrum van sterrenstelsels kan een bron van sterkre radiostraling zijn, in welk geval het een *Active Galactic Nucleus* (AGN; actieve galactische kern) genoemd wordt. Radiostraling kan ook het gevolg zijn van stervorming, hoewel stervormende sterrenstelsels vaak vele malen zwakker zijn dan AGN. Als gevolg daarvan zijn waarnemingen met radiogolven in het verleden vooral beperkt gebleven tot heldere AGN, nabijgelegen sterrenstelsels, en extreem heldere stelsels in het vroege Universum. 'Gewone' sterrenstelsels zijn een stuk zwakkere radiobronnen, en waren daarom niet waarneembaar met oudere telescopen (zie ook Afbeelding 1.8). Echter, nadat de VLA in 2012 een grote upgrade is ondergaan, is de gevoeligheid van de telescoop met een orde van grootte verbeterd. Sindsdien is het eindelijk mogelijk om

de *faint radio sky* – de lichtzwakke radiohemel – waar te nemen, welke het onderwerp vormt van dit proefschrift.

Een stervormend sterrenstelsel zendt radiogolven uit via twee processen: *synchrotronstraling* en *free-free straling*. De laatste wordt geproduceerd bij de vorming van zware sterren, terwijl synchrotronstraling wordt uitgezonden wanneer een zware ster sterft in een krachtige *supernova-explosie*. Free-free straling biedt daarom een directe meting van recente stervorming, maar is erg lastig waar te nemen in verre sterrenstelsels, aangezien het een stuk zwakker is dan de ook aanwezige synchrotronstraling (zie bijvoorbeeld Afbeelding 1.7). Vandaar wordt synchrotron veel meer gebruikt om stervorming te meten, ondanks dat dit eigenlijk de dood van sterren meet, en niet het ontstaan ervan. Dit proefschrift begint daarom met twee hoofdstukken die de synchrotronstraling van lichtzwakke sterrenstelsels bestuderen (Hoofdstukken 2 & 3). Daaropvolgend beschrijven we in Hoofdstukken 4 & 5 twee onderzoeken waarin voor het eerst systematisch naar free-free straling in het vroege heelal wordt gekeken.

Dit Proefschrift

In het afgelopen decennium heeft de radiosterrenkunde een heuse revolutie doorgaan: diverse nieuwe radiotelescopen zijn (of worden nog) gebouwd, en anderen, zoals de eerdergenoemde VLA, zijn flink gemoderniseerd. De steeds gevoeligere waarnemingen die hierdoor mogelijk zijn vervolledigen ons begrip van de lichtzwakke radiohemel. In **Hoofdstuk Één** beginnen we dit proefschrift met een gedetailleerde uitleg over de evolutie van sterrenstelsels en de radiosterrenkunde, en beschrijven we de benodigde achtergrondinformatie voor de latere hoofdstukken.

In **Hoofdstuk Twee** introduceren we gevoelige waarnemingen van de vernieuwde VLA als onderdeel van de zogeheten *COSMOS-XS survey*. COSMOS-XS verschaft radiowaarnemingen op twee verschillende frequenties, beiden een van de meest gevoelige die tot op heden bestaan. We maken gebruik van de waarnemingen op 3 GHz, in combinatie met observaties op een hoop andere golflengten van röntgenstraling tot microgolven, om de samenstelling van de radiohemel te onderzoeken, en sterrenstelsels in te delen als AGN of stervormend. We vinden dat meer dan 90% van de 1500 sterrenstelsels die zijn gedetecteerd in COSMOS-XS radiostraling uitzenden die afkomstig is van stervorming, en dat dit percentage oploopt voor zwakkere stelsels. Daarnaast ontdekken we ook een aantal sterrenstelsels

die niet gedetecteerd zijn in gevoelige waarnemingen op optische en infrarode golflengten. Door middel van een zogeheten *stacking* techniek, waarbij we de gemiddelde emissie van deze stelsels kunnen meten, laten we zien dat deze "donkere" stelsels waarschijnlijk erg verafgelegen zijn en een roodverschuiving van $z \sim 4 - 5$ hebben, wat inhoudt dat ze een belangrijk aandeel kunnen vormen in de kosmische stervormingssnelheid in het vroege Universum.

Hoofdstuk Drie betreft een uitvoerige studie van de *ver-infrarood/radio correlatie* in extreem stervormende en stofrijke sterrenstelsels in het jonge Universum. Deze relatie tussen ver-infrarood en radiostraling, die standhoudt in een verscheidenheid aan sterrenstelsels – van dwergsystemen tot massieve, stervormende sterrenstelsels – alsmede op hoge roodverschuiving, is cruciaal om radio synchrotronstraling te gebruiken als een maat voor stervorming. De theoretische onderbouwing van deze relatie is tot op heden echter enigszins onduidelijk gebleken, en wordt verondersteld het gevolg te zijn van een scala aan fysische processen. Snel snervormende sterrenstelsels vormen nuttige laboratoria om de ver-infrarood/radio correlatie te bestuderen, omdat deze hier kan worden getest in extreme fysische omstandigheden, zonder te worden geteisterd door systematische selectie-effecten.

Door het combineren van gedetailleerde observaties van de *Atacama Large Millimeter Array* voor ongeveer 700 stofrijke sterrenstelsels met gevoelige radiowaarnemingen van de VLA, meten we dat de ver-infrarood/radio correlatie niet afhankelijk is van roodverschuiving. Dit is in tegenstelling tot eerdere onderzoeken naar de correlatie, die minder homogene verzamelingen van sterrenstelsels bekeken, en daardoor meer last hebben van selectie-invloeden. Desalniettemin vinden we dat de correlatie voor stofrijke sterrenstelsels op hoge roodverschuiving verschilt van die van stervormende stelsels in het huidige Universum, waaronder die voor de nabije stofrijke stelsels. Dit is waarschijnlijk vanwege de veranderende fysische omstandigheden in sterrenstelsels in het verre Universum.

In **Hoofdstuk Vier** presenteren we een pionerende studie naar free-free straling in sterrenstelsels in het jonge Universum. Door middel van nieuwe waarnemingen van de VLA op 34 GHz als onderdeel van het COLDz project, alsmede waarnemingen op verschillende lagere frequenties, verkrijgen we een ongekend inzicht in de *radiospectra* van lichtzwakke sterrenstelsels. We detecteren 18 sterrenstelsels in de nieuwe waarnemingen op

34 GHz, waarvan we zeven classificeren als stervormende stelsels. Gebruik makende van de bestaande data op diverse radiofrequenties, extraheren we de synchrotron- en free-free straling uit de totale radiospectra. Op die manier kan de free-free straling gebruikt worden om stervorming in het vroege Universum te meten. We tonen aan dat de stervormingssnelheden verkregen van de free-free straling overeenkomen met deze van meer gebruikelijke meetmethoden, en beschrijven hoe de volgende generatie radiotelescopen cruciaal zullen zijn om onderzoek naar free-free straling te vervolgen.

Hoofdstuk Vijf bouwt voort op het onderzoek beschreven in het voorgaande hoofdstuk door gebruik te maken van een *stackinganalyse*, welk inzicht verschaft in veel grotere (en nog lichtzwakkere) verzamelingen sterrenstelsels. Op deze manier kunnen de gemiddelde radiospectra van sterrenstelsels met slechts bescheiden stervorming – de meest veelvoorkomende stelsels in het Universum – worden bestudeerd.

We tonen aan dat sterrenstelsels in het jonge Universum lichtzwakker zijn op hoge frequenties dan verwacht op basis van een extrapolatie van een typisch radiospectrum, welk vaak wordt aangenomen in de literatuur. We veronderstellen dat dit het resultaat is van het "verouderen" van de spectra, wat de afname van synchrotronstraling in oudere sterrenstelsels tot gevolg heeft. De free-free straling is hierdoor echter onaangetast, zodat we deze gebruiken om de kosmische stervormingssnelheid te bepalen – de eerste meting op deze manier, die in de toekomst hoogstwaarschijnlijk gangbaar zal zijn.

Publications

First Author

4. **Algera, H.S.B.**, Hodge, J. A., Riechers, D., Leslie, S.K., Smail, I., Aravena, M., Da Cunha, E., Daddi, E., Decarli, R., Dickinson, Gim, H.B., Magnelli, B., Murphy, E. J., Pavesi, R., Sargent, M., Sharon, C. E., Wagg, J., Walter, F., Yun, M., "*COLDz: Probing Cosmic Star Formation with Free-free Emission*", ApJ submitted (2021)

3. **Algera, H.S.B.**, Hodge, J. A., Riechers, D., Murphy, E. J., Pavesi, R., Aravena, M., Daddi, E., Decarli, R., Dickinson, M., Sargent, M., Sharon, C. E., Wagg, J., "*COLDz: Deep 34 GHz Continuum Observations and Free-free Emission in High-redshift Star-forming Galaxies*", ApJ, 912, 73 (2021)

2. **Algera, H.S.B.**, Van der Vlugt, D., Hodge, J.A., Smail, I., Novak, M., Radcliffe, J.F., Riechers, D.A., Röttgering, H., Smolčić, V., and Walter, F., "*A Multi-wavelength Analysis of the Faint Radio Sky (COSMOS-XS): the Nature of the Ultra-faint Radio Population*", ApJ, 903, 139 (2020)

1. **Algera, H.S.B.**, Smail, I., Dudzevičiūtė, U., Swinbank, A.M., Stach, S., Hodge, J.A., Thomson, A.P., Almaini, O., Arumugam, V., Blain, A.W., Calistro-Rivera, G., Chapman, S.C., Chen, C.-C., da Cunha, E., Farrah, D., Leslie, S., Scott, D., Van der Vlugt, D., Wardlow, J.L., and Van der Werf, P., "*An ALMA Survey of the SCUBA-2 Cosmology Legacy Survey UKIDSS/UDS Field: The Far-infrared/Radio correlation for High-redshift Dusty Star-forming Galaxies*", ApJ, 903, 138 (2020)

Contributing Author

10. Schouws, S., Stefanon, M., Bouwens, R.J., Smit, R., Hodge, J.A., Labbé, I., **Algera, H.S.B**, Boogaard, L., Carniani, S., Fudamoto, Y., Hol-

werda, B.W., Illingworth, G.D., Maiolino, R., Maseda, M.V., Oesch, P.A., and van der Werf, P.P., "*Significant Dust-Obscured Star Formation in Luminous Lyman-break Galaxies at* $z\sim7-8$", submitted to ApJ, arXiv:2105.12133 (2021)

9. da Cunha, E., Hodge, J.A., Casey, C.M., **Algera, H.S.B.**, Kaasinen, M., Smail, I., Walter, F., Brandt, W.N., Dannerbauer, H., Decarli, R., Groves, B.A., Knudsen, K.K., Swinbank, A.M., Weiss, A., van der Werf, P., and Zavala, J.A., "*Measurements of the dust properties in z 1-3 SMGs with ALMA*", ApJ in press, 2021

8. Mandal, S., Prandoni, I., Hardcastle, M.J., Shimwell, T.W., Intema, H.T., Tasse, C., van Weeren, R.J., **Algera, H.S.B.**, Emig, K.L., Röttgering, H.J.A., Schwarz, D.J., Siewert, T.M., Best, P.N., Bonato, M., Bondi, M., Jarvis, M.J., Kondapally, R., Leslie, S.K., Mahatma, V.H., Sabater, J., Retana-Montenegro, E., and Williams, W.L., "*Extremely deep 150 MHz source counts from the LoTSS Deep Fields*", A&A, 648, A5 (2021)

7. Delvecchio, I., Daddi, E., Sargent, M.T., Jarvis, M.J., Elbaz, D., Jin, S., Liu, D., Whittam, I.H., **Algera, H.S.B.**, Carraro, R., D'Eugenio, C., Delhaize, J., Kalita, B., Leslie, S., Molnar, D.C., Novak, M., Prandoni, I., Smolcic, V., Ao, Y., Aravena, M., Bournaud, F., Collier, J.D., Randriamampandry, S.M., Randriamanakoto, Z., Rodighiero, G., Schober, J., White, S.V., and Zamorani, G., "*The infrared-radio correlation of star-forming galaxies is strongly* $M_\star$*-dependent but nearly redshift-invariant since* $z\sim4$", A&A, 647, A123 (2021)

6. Van der Vlugt, D., **Algera, H.S.B.**, Hodge, J.A., Novak, M., Radcliffe, J.F., Riechers, D.A., Röttgering, H., Smolčić, V., and Walter, F., "*An Ultra-deep Multi-band VLA Survey of the Faint Radio Sky (COSMOS-XS): Source Catalog and Number Counts*", ApJ, 907, 5 (2021)

5. Leslie, S.K., Schinnerer, E., Liu, D., Magnelli, B., **Algera, H.S.B.**, Karim, A., Davidzon, I., Gozaliasl, G., Jiménez-Andrade, E.F., Lang, P., Sargent, M.T., Novak, M., Groves, B., Smolčić, V., Zamorani, G., Vaccari, M., Battisti, A., Vardoulaki, E., Peng, Y., and Kartaltepe, J., "*The VLA-COSMOS 3 GHz Large Project: Evolution of Specific Star Formation Rates out to* $z\sim5$", ApJ, 899, 58 (2020)

Curriculum Vitae

I was born in the idyllic Dutch town of Sneek on September 8th, 1995, where I would later attend the Gymnasium of the RSG Magister Alvinus high school. At age thirteen, I faced the difficult decision of choosing my future career path. Switching at the very last moment from an academic track focused on economics and ancient Greek to mathematics and physics – it was said this would "leave more options open" – I graduated from the RSG in 2012. Once more without a clear vision on what to do next, I decided to follow a long-time friend in pursuing a Bachelor's degree in astronomy at the University of Leiden.

It was at Leiden that my passion for the Cosmos – which had certainly already been instilled in me from a young age, yet lay temporarily dormant – took full form. I was introduced to radio astronomy during my Bachelor's research when, together with fellow student Louis Cheung, I worked on *Atacama Large Millimeter Array* observations of the protoplanetary disk HL Tau in a project led by Dr. Michiel Hogerheijde and Dr. Mason Carney. Subsequently, I obtained my BSc *cum laude* in 2015.

Continuing onward with a Master's in Astronomy at Leiden University, thereby opting for the cosmology specialization, I first studied the (apparent lack of) X-ray pulsations in accreting millisecond pulsars under the supervision of Dr. Alessandro Patruno. My master's thesis then finally exposed me to the fascinating field of galaxy evolution, leading me to find and study high-redshift galaxies with extremely strong emission lines under the supervision of Dr. Rychard Bouwens. I obtained my MSc from Leiden University *summa cum laude* in 2017.

In the same year, I enrolled in the PhD programme at Leiden University, pursuing a study of the faint radio sky under the supervision of Dr. Jacqueline Hodge. Having come full circle, back to radio astronomy albeit now armed with valuable experience at other wavelengths, I was fortunate to present my thesis work at various conferences, and work within several different collaborations. In 2019, this led to a four month visit to the University of Durham, England, where I studied the combined infrared and radio properties of dusty star-forming galaxies under the supervision of Prof.

Ian Smail and Prof. Mark Swinbank, culminating in Chapter 3 of this thesis. Starting November 2021, I will move to the University of Hiroshima, Japan, where I will pursue a postdoc with Dr. Hanae Inami, studying some of the very same galaxies I investigated during my MSc, now from a radio perspective.

Acknowledgements

The last near-decade in Leiden turned out to be an amazing journey, which is in part thanks to you, dear reader. Many of you have come and gone during my time here, so my sincere apologies to anyone I may have forgotten.

First of all, I would like to acknowledge the scientific guidance from both Jackie and Huub throughout the last four years, as well as from Michiel, Ale and Rychard in the years prior. A heartfelt thank you also goes out to Hanae, who has been so welcoming and helpful even before we have had the opportunity to meet.

I would also like to thank the various support staff at the observatory, who make the day to day life at the Sterrewacht run smoothly. Alexandra, especially during the final stages of writing this thesis, you have been tremendously helpful. Evelijn, Els, Hafize, Marjan Monica, and the full computer group, thank you for always being available in time of need.

I greatly enjoyed being part of the various *dusty groups* during my time in Leiden. Matus, thank you for organizing Jackie's group meeting for as long as I can remember. I enjoyed our frantic writing of proposals, and I am looking forward to seeing Bon Iver with you in the late 2100s. Sarah, I always enjoyed our chats and your support with whatever I happened to be working on. More dusty thanks go out to Alex, Cristy, Dazhi, Gaby, Leindert, Paul, Sander, Serena, Shravya and others – thank you for making the meetings both fun and instructive.

Arguably the best part of life as an astronomer is the people you meet along the way, and the time you get to spend with them. Kirsty and Dieuwertje, I have so many fond memories of our post-conference trips, from speedrunning Meteor Crater and swimming near the fake Hoover dam to seeing awesome bands at Primavera festival in Porto. A special thank you goes out to Amber and Taylor, for taking the famous notion of American hospitality to the next level on the rare occasion I was traveling alone. Anna, it's hard to pick between snacking on trail mix at 8am during our Grand Canyon descent and doing it all over again a few days later for our impromptu hike in Zion. Anniek, Pooneh, with you I can also appreciate the lazy side of life, sipping unlimited cocktails (including newly-found favourite: the espresso gin & tonic) at a sunny Cretan beach. Marta, thank

you for showing us your roots during a beautiful expedition to southern Spain, and for not driving us off a cliff after the umpteenth mispronunciation of Maláága. Finally, Diana, thank you for showing me that it is not the destination one travels to that matters, but the person one is traveling with (not gonna lie though, the destinations weren't too shabby either).

Fraser, I'm glad our shared passion for music brought us together under the same roof. Thank you for all the concerts, Netflix nights, stroopwafels, and tolerating my constant bass playing. Dario and Łukasz, thank you for instead encouraging my constant bass playing as one of the original Monkeys. DJ Mantas, thank you for always being the light of the party, on the rare occasion you make an appearance. Lydia, thank you for randomly enjoying the view from that particular Leiden bridge during the early stages of the pandemic.

I would like to thank many more of you for making, or having made, the Observatory – and in particular the Kaiser Lounge – the great place it is, inlcuding Alessandro, Alex, Andrej, Andrés, Aswin, Bas, Dilovan, Eleonora, Elina, Evgenii, Folkert, Frits, Gabriella with a hard Dutch G, Iva, Jeroen, Jit, Josh, Kim, Lammin, Margot, Marina, Martijn, Matthieu, MC, Michał, Niccolò, Niloo, Olivier, Omar, Patrick, Roi, Roland, Sanjana, Stella, Stijn, Tommaso, Turgay, and Vanja. Many thanks also go out to all the folks in Durham, for showing me not one, not two, but all three pubs in town.

Of course I cannot forget my non-astro friends, who did their part in keeping me sane over the past four years. Marten, thank you for – in a way – starting all of this, and for all the great jam sessions. Marieke, my bestie basically since the day I was born. Isa, Kaya, Koen, Marlize, Matthijs, Peter, Simone, Thomas, thank you for the many rainy camping trips, the (not so) beautiful Christmas gifts and the sunny botanical garden lunches. A special grazie goes out to Zehui, for not only designing this beautiful cover, but also for your pazienza and the delicious tiramisu.

Robbie, je weet hoeveel ik onze gesprekken altijd waardeer, ondanks dat er vaak geen touw aan je ideeën vast te knopen is (grapje). Ik blijf het bijzonder vinden dat je de enige niet-astronoom bent die echt weet wat ik de afgelopen vier jaar heb uitgevoerd. Mam, het is dankzij jou dat ik vanaf kinds af aan al weet dat de wereld veel groter is dan alleen Nederland. Ik weet dat je de verhuizing naar Japan zowel geweldig als ietwat beangstigend vindt, maar ik weet ook dat jij degene zal zijn die me het meest op komt zoeken. Josanne, ik heb zoveel bewondering voor jou en voor de manier waarop jij in het leven staat. Zonder dat je het geweten hebt, ben je de afgelopen vier jaar een grote bron van inspiratie voor me geweest.